AN ABSTRACT OF THE DISSERTATION OF

Mahyar Sharifi Mood for the degree of Doctor of Philosophy in Civil Engineering presented on May 16, 2017.

Title:

Probabilistic Geospatial Analyses, Uncertainty Modeling, and Mapping of Seismically-induced Ground Failures

Abstract approved:

_____

Michael J. Olsen Daniel T. Gillins

Ground failures, in particular landsliding, liquefaction and lateral spreading can be triggered by seismic sources. The frequency, magnitude, and impact of these ground failures are highly dependent on the topography and geology of the site including its slope, depositional environment, and geotechnical properties as well as the proximity of the site to seismic sources. Many available models for estimating these variables have high epistemic uncertainty given the extreme challenge to fully characterize seismic sources and subsurface conditions. Nevertheless, this high uncertainty must be considered when mapping ground failure hazards for a large area using geologic, geotechnical, topographical, and seismic hazard data of limited availability.

Many hazard maps do not fully consider uncertainty from the seismic sources, subsurface testing, and empirical models developed for estimating ground failures. Often, previously

developed maps are qualitative based on judgment due to the lack of detailed subsurface geotechnical investigations.

This research presents new mapping methods to address these challenges, resulting in ground failure hazard maps for evaluation and risk assessment. It explores both deterministic and probabilistic methods of mapping ground failure hazards for large study areas. Available geospatial data are incorporated in this research including digital elevation models (DEMs) acquired from lidar and photogrammetric data, DEM derivatives such as slope, geologic mapping, shear wave velocity tests and other geotechnical subsurface investigations, and seismic hazard curves.

First, efficient algorithms were developed to map estimates of the peak ground acceleration, landslide and liquefaction triggering probability, and horizontal displacement as a result of landslides or lateral spreading across the state of Oregon for several earthquake scenarios associated with the Cascadia Subduction Zone (CSZ). These algorithms utilize site classification and site geology maps provided by the Oregon Department of Geology and Mineral Industries (DOGAMI).

Second, a performance-based, landslide-induced, displacement hazard mapping technique is proposed and implemented for Western Oregon. This approach computes landslide displacement hazard curves across the regional area. The approach utilizes a detailed landslide inventory database and high-resolution topographical data to estimate the soil strength and associated uncertainty in the general geologic units.

Third, in an effort to characterize the uncertainty of the geotechnical properties of geologic units, a geospatial geotechnical database was developed and evaluated. In this evaluation,

available geologic maps and geotechnical subsurface databases from three counties in the State of Utah were compiled. Then, several distributions of geotechnical properties for the general geologic units were developed, and these distributions enabled the determination of which geologic units were most susceptible to liquefaction and lateral spreading. A statistical approach was also developed to provide a framework for simplifying geologic units based on soil properties.

Lastly, a new and fully probabilistic framework is developed for mapping the liquefaction-induced lateral spread displacement hazard at a regional scale. This framework is demonstrated by producing lateral spread hazard maps for Utah County, Utah. By performing numerous Monte Carlo simulations, the method accounts for uncertainties in the soil properties, seismic loading, and the empirical models for predicting horizontal displacements due to lateral spreading.

Probabilistic Geospatial Analyses, Uncertainty Modeling, and Mapping of Seismically-induced Ground Failures

by

Mahyar Sharifi Mood

A DISSERTATION

submitted to

Oregon State University

in partial fulfillment of
the requirements for the
degree of

Doctor of Philosophy

Presented May 16, 2017
Commencement June 2017

Doctor of Philosophy dissertation of Mahyar Sharifi Mood presented on May 16, 2017.

APPROVED:

_____

Co-major Professor, representing Civil Engineering

_____

Co-major Professor, representing Civil Engineering

_____

Head of the School of Civil and Construction Engineering

_____

Dean of the Graduate School

I understand that my dissertation will become part of the permanent collection of Oregon State University libraries. My signature below authorizes release of my dissertation to any reader upon request.

_____

Mahyar Sharifi Mood, Author

ACKNOWLEDGEMENTS

Foremost, I would like to express my sincere gratitude to my advisor, Dr. Michael Olsen who introduced me to the wonders and frustrations of scientific research. I give my profoundest gratitude for all the time you spent week by week with me assisting and supporting me in Oregon State University. Without a doubt, you are an example of excellence as a researcher, mentor, instructor, and role model.

My most sincere thanks go to my second advisor and mentor, Dr. Daniel Gillins. I thank him for the continuous support during my study and in my research, for his patience, motivation, and enthusiasm. He helped me significantly through the research process and writing of this dissertation.

I would like to thank my minor research advisor, Dr. Michael Bailey for all the topics I learnt from his courses and for his constant passion and encouragement. In addition I would like to thank my committee members: Dr. Ben Leshchinskey, and Dr. Jay Noller for the time and effort they spent on reviewing my dissertation.

I appreciate the Oregon Department of Transportation (ODOT) (Project #SPR-740), U.S. Geological Survey (USGS), Department of the Interior (USGS award numbers G14AP00118 and G14AP00119), Utah Department of Transportation and the Central Utah Water Conservancy District for funding to support this research. I further acknowledge the Cascadia Lifeline Program (CLiP) who sponsored significant portion of my PhD studies here in OSU as a graduate research assistant. To Bill Burns and Ian Madin from DOGAMI, thank you for providing the data necessary for this dissertation. This research also utilized lidar topographic data provided by the Oregon Lidar Consortium.

Thanks to Leica Geosystems and David Evans and Associates for their contribution of equipment and software to geomatics program of Civil and Construction Engineering department.

A special thank goes to my siblings, Negar and Nima, for their invaluable support, humor and guidance.

It would take more than an acknowledgement to thank my parents for being there for me all the time, for their constant love, care and support. Thank you for raising me with the desire to seek knowledge and wisdom. I could not ask for better parents.

This last word of acknowledgment I have saved for my life teammate, Mahsa, who stands with me and brightens my life. I am blessed to share this accomplishment with her.

CONTRIBUTION OF AUTHORS

Dr. Michael Olsen assisted with code debugging and development for Chapter 2 as well as reviewing the output maps. He assisted with developing the methodology and writing the code as well as interpreting and validating the results presented in Chapter 3. He provided data and assisted with the analysis framework and data interpretation for Chapter 4. In Chapter 5, he provided guidance related to the probabilistic mapping framework. Additionally Dr. Olsen provided important review comments and editing for all chapters.

Dr. Daniel Gillins assisted with developing the analysis framework for Chapter 2 and oversaw the implementation of the data into the O-Help web GIS. In Chapter 3, he provided critical review of the results. He contributed to Chapters 4 and 5 by writing a portion of the code used in the analysis. He helped with the interpretation of outputs and further provided substantial comments and edits on the texts and contents of all chapters.

Ian Madin provided data necessary to complete the processes performed in Chapter 2. He also provided the initial scripts and workflows for the effort.

Rubini Santha Mahalingam assisted with data processing for the input information in Chapter 3.

Jasmyn Harper helped with collection of data and partial processing of the raw data in Chapters 4 and 5.

Kevin Franke provided helpful comments and a thorough review for Chapters 4 and 5.

Steven Bartlett assisted in revising Chapters 4 and 5 by providing important feedbacks and comments.

TABLE OF CONTENTS

TABLE OF CONTENTS (Continued)

Page

TABLE OF CONTENTS (Continued)

Page

TABLE OF CONTENTS (Continued)

Page

LIST OF FIGURES

LIST OF FIGURES (Continued)

LIST OF FIGURES (Continued)

LIST OF FIGURES (Continued)

Figure Page

LIST OF FIGURES (Continued)

LIST OF TABLES

LIST OF TABLES (Continued)

LIST OF TABLES (Continued)

Table | Page

1 INTRODUCTION

Landslide, liquefaction, and lateral spreading are important geo-hazards that can be triggered from strong, cyclical ground shaking. They are considered devastating natural hazards and can be responsible for significant social and economic losses. The magnitude and distribution of such hazards is highly correlated with topography and morphology. Thus, it is quite important to accurately model and analyze the surface of the earth to better assess the hazards associated with these geotechnical phenomenon, particularly within urban regions with high concentrations of population. Creation of hazard zonation studies, susceptibility and hazard maps along with identifying locations with the most significant problems are among the best ways to help planners and field engineers to avoid extreme loss and damage by implementing mitigation measures in unstable areas.

Careful assessment of geological hazard as a consequence of strong ground motion can lead to superior decision making in planning and preparation. Upon the presence of effective tools and accurate data, key actions in management can be performed. Vulnerable urbanized regions, lifeline routes and utilities can be delineated in hazard map products enabling governmental agencies to optimally allocate resources for mitigation. With the use of such products, policy makers, planners and engineers can plan safer routes, design more resilient structures, develop disaster preparation, response strategies, and identify sites that warrant more detailed monitoring and investigation.

Unfortunately, performing a regional hazard mapping task can be quite challenging when across a large area, such as a county or state, which holds considerable spatial and temporal uncertainty in the subsurface conditions and overall seismic hazard. In addition,

ground failure modeling in any form (landslide, liquefaction or lateral spreading) is a complex problem that is commonly accomplished with empirical models based on case history data. These models contain significant uncertainties and assumptions requiring a careful attention when performing ground failure mapping. Probabilistic techniques should be used when handling data with significant epistemic uncertainty.

The overarching objective of this dissertation is to develop probabilistic mapping methodologies that account for existing variabilities in inputs and effectively quantify the probability of seismically-induced ground displacements. The methods are expected to produce probabilistic hazard maps for large regions, providing useful insights for future prioritization of site-specific engineering evaluations and risk assessments.

Earthquakes can cause geo-hazards including strong ground shaking, landslides, liquefaction and horizontal displacements. This dissertation explores landslide hazards in western Oregon by developing and implementing a fully probabilistic hazard mapping methodology based on Newmark sliding block theory, a database of inventoried landslides and empirical equations for estimating landslide displacement. Furthermore, in order to assist with future hazard mapping efforts geotechnical properties of geologic units are characterized using available and compiled geotechnical subsurface databases. The dissertation also proposes a fully probabilistic method for mapping the liquefaction-induced lateral spreading hazard. As an example, this method was implemented in Utah County, Utah, using available geotechnical subsurface investigations, recently developed

empirical equations for estimating lateral spread displacements, and probabilistic seismic hazard analyses.

1.1 LANDSLIDES

Landslides are the result of the downward movement of earth and its materials including rocks and soils from a slope in the presence of applied loads (driving forces) and the strength (resisting forces) of the slope materials (USGS, 2004). Slope failure occurs when the resisting forces (i.e. shear strength) are less than the driving forces (e.g. earthquake applied load) resulting in downward relocation of slope materials (rocks and soils). Factors contributing to landslide phenomenon can be both internal and external. Internal parameters include rock or soil type and strength, subsurface geological data, interbedding between different soil layers, slope gradient and aspect (slope face direction), surface topography roughness, presence of vegetation, level of ground water table and pore water pressures. Furthermore, persistent rainfall, seismic activities and human disturbance (e.g., over-steepening of a cliff face for highway construction) are those considered as external sources of landsliding. Co-seismic slope failures can be a significant source of earthquake damage. Therefore understanding and design of engineered slopes are crucial to prevent loss and damage.

The first two manuscripts in this dissertation focus on state of Oregon, which is very susceptible to various natural hazards, including landslides. Landslides are ubiquitous along the entire coast range of Oregon as well as Cascades region. For example, “sunken grade” signs are frequently observed along various highways. In particular, the western

side of Oregon contains steep slopes of soils wetted by persistent rainfall during most of the year, and the ground water table in the valleys is often near the ground surface. Weak, sensitive and saturated soils and sediments from the Tyee formation cover a large section of Oregon coast range. Crustal seismic sources (e.g., Portland hills fault) as well as subduction zone seismic sources are both present in this area, which are capable of instigating strong ground motions with frequent, small moment magnitude or rarer, very high moment magnitude earthquakes, respectively (Goldfinger et al., 2012). Further, inertial loadings produced from the prevalent seismic hazard may result in new landslides or reactivation of dormant existing landslides (Schulz and Galloway, 2012).

1.2 LIQUEFACTION AND LATERAL SPREADING

During major earthquakes and cyclic loading, saturated or partially saturated soil significantly loses shear strength and stiffness and behaves like a liquid, which is defined as soil liquefaction. Soil liquefaction can result in catastrophic problems such as flow failure, lateral spreading, differential settlement, bearing capacity failure, and ground oscillation. It is considered a major concern for structures on sandy soils. Robertsen and Fear (1995) reflected on the Niigata earthquake in 1964 and its consequences as a turning point on how the world changed their view and focused on this phenomenon. High ground water table, proximity to active seismic sources and surficial water bodies and relatively high amounts of granular and/or silty soils near the ground surface contribute to liquefaction hazard.

Lateral spreading, horizontal displacements due to liquefaction, are considered as one of the most pervasive form of liquefaction-induced ground failure. In areas prone to

liquefaction, these horizontal movements can range from a few tenths of a meter to as large as several meters (Bartlett and Youd 1995; Youd et al. 2002). Development of engineering strategies, planning and hazard zone identification are important methods to identify potential damages from this phenomenon.

The second portion of this dissertation targets the development of a geospatial database which could be leveraged for mapping liquefaction hazard. It implements this development by compiling thousands of geotechnical investigations in three counties in Utah. One portion of this database relates to Utah County, Utah, which is used in Chapter 5 to produce a lateral spreading hazard map. Utah has a high potential for liquefaction and liquefaction-induced ground failure because of its proximity to the Wasatch Front fault and its intrinsic potential for major earthquakes. A substantial amount of the soils covering the populated valleys in Utah contain potentially liquefiable sediments including loose sand and sandy silt deposited by lakes and streams. Several researchers have produced liquefaction hazard maps to convey its consequences in different urban areas of Utah (e.g., Anderson et al. 1994a, Anderson et al. 1994b, Bartlett et al. 2005, Gillins 2012).

1.3 OUTLINE OF DISSERTATION

The dissertation follows the manuscript format as specified below:

Chapter 2 presents Manuscript 1 which describes the deterministic modeling of four Cascadia Subduction Zone (CSZ) earthquake scenarios and the geo-hazards associated with these models within the State of Oregon. Automated analysis tools were developed to produce a suite of maps of ground motion parameters such as peak ground acceleration

(PGA) along with natural geological hazards such as landslide probability, landslide displacement, liquefaction, lateral spreading are created using modified versions of the methodologies defined in HAZUS-MH (Hazards US, Multi-Hazard) and the Oregon Resilience Plan.

Chapter 3 presents Manuscript 2, which represents a performance-based, fully probabilistic approach to landslide displacement hazard mapping. This study has been revised from work completed in Sharifi-Mood (2013). This study models the entire probabilistic seismic hazard curve to map probabilities of triggering landslides and exceeding displacement thresholds in a performance-based design framework. Pre-existing landslides and detailed topographic information were incorporated to estimate soil strength for geologic units. It also captures uncertainty in soil strength. Detailed maps were produced for western Oregon.

Chapter 4 presents Manuscript 3 describing the compilation of a comprehensive geotechnical subsurface database in three counties within the State of Utah to quantify geotechnical properties of various geologic units. Several example applications are demonstrated. With the use of this database, geological units are statistically compared and grouped into simplified geological groups and their geotechnical parameters are quantitatively described. Common geologic units existed in different locales are compared from the stand point of various geotechnical information. Such databases are helpful in modern development of geo-hazard maps and in site investigation projects allowing detailed planning of a geotechnical investigation more efficiently.

Chapter 5 presents Manuscript 4, which introduces a new performance-based, fully probabilistic approach in lateral spreading assessment and mapping and its application in Utah County, Utah. Using a pre-defined lateral spreading empirical model and incorporating available seismic, geotechnical, geological and topographical data, careful assessment of lateral spreading has been made in regional scale.

Chapter 6 provides the general conclusions to the dissertation, discussing the outcomes of the four manuscripts and defines the general and scientific contribution of each. Potential uses of the databases, maps and results created in the previous chapters are described.

1.4 REFERENCES

Anderson, L.R., Keaton, J.R., and Bischoff, J.E. (1994a). Liquefaction Potential Map for Utah County, Utah, Logan, Utah State University Department of Civil and Environmental Engineering and Dames and Moore unpublished Final Technical Report prepared for the U.S. Geological Survey, National Earthquake Hazards Reduction Program Award No. 14-08-0001-21359, 46 p., 1986; published as Utah Geological Survey Contract Report 94-8, 1994.

Anderson, L.R., Keaton, J.R., and Eldredge, S.N. (1994b). Liquefaction-potential map for a part of Utah County, Utah: Utah Geological Survey Public Information Series 28, 1 sheet, 1:365,000.

Bartlett, S.F., and Youd, T.L. (1995). "Empirical prediction of liquefaction-induced lateral spread." J. Geotech. Eng., 121(4), 316-329.

Bartlett S. F., Olsen, M. J., and Solomon, B. J. (2005). "Lateral Spread Hazard Mapping of Northern Salt Lake County for a Magnitude 7.0 Scenario Earthquake," Technical Report submitted to the United States Geological Survey, NERHP Award No. 04HQGR0026, 218 p.

Goldfinger, C., and others (2012), Turbidite event history— Methods and implications for Holocene paleoseismicity of the Cascadia subduction zone: U.S. Geological Survey, Professional Paper 1661–F, 170 p. Web: http:// pubs.usgs.gov/pp/pp1661f/

Robertson, P. K., & Fear, C. E. (1995). Liquefaction of sands and its evaluation. In Proceedings of the 1st International Conference on Earthquake Geotechnical Engineering, Tokyo.

Schulz, W.H., Galloway, S.L. (2012). Evidence for Earthquake triggering of large landslides in coastal Oregon, USA. Geomorphology, 141: 88-98.

Sharifi Mood, M. (2013). Probabilistic analysis and mapping of seismically induced landslide deformation in Oregon. Oregon State University.

Youd, T. L., Hansen, C. M., and Bartlett S. F. (2002). Revised multilinear regression equations for prediction of lateral spread displacement." J. Geotech. Geoenviron. Eng. 128(12), 1007-1017.

Manuscript # 1

Complementary ground motion, ground deformation, and damage potential maps for deterministic scenarios of Cascadia subduction zone earthquake events

Mahyar Sharifi-Mood, Michael J. Olsen, Daniel T. Gillins and Ian P Madin

DOGAMI open file report O-17-XX

2 COMPLEMENTARY GROUND MOTION, GROUND DEFORMATION, AND DAMAGE POTENTIAL MAPS FOR DETERMINISTIC SCENARIOS OF CASCADIA SUBDUCTION ZONE EATHQUAKE EVENTS

2.1 ABSTRACT

The Cascadia Subduction Zone (CSZ) has the ability to generate earthquakes as powerful as 9 moment magnitude which will likely significantly damage structures and facilities in Oregon. Series of deterministic earthquake analysis are performed for M9.0, M8.7, M8.4 and M8.1 presenting persistent, long lasting shaking associated with other geological threats such as ground shaking, landslides, liquefaction-induced ground deformations, etc. These ground deformation endangers urban structures, foundations, bridges, roadways, pipelines and other lifelines.

In this report, two automated modules are introduced to perform site amplification of stated seismic scenario events and subsequently perform hazard and ground deformation mapping tasks relevant to these scenarios based on HAZUS-MH recommendation (FEMA, 2011). Series of statewide ground motion parameters and predicted ground failure hazard maps are created. Analysis of these scenarios and the resultant maps can help lifeline providers in Oregon, including private and public practices responsible for transportation, electric and gas utilities, water and wastewater, fuel, airports, and harbors to have a better understanding of this extreme seismic risk.

2.2 INTRODUCTION

The Cascadia Subduction Zone (CSZ) lies off the coast of Oregon, Washington, northern California and British Columbia and is capable of generating great moment magnitude earthquakes (M8.0-M9.0) similar to recent events in Chile and Japan. The last great earthquake in the CSZ with similar characteristics happened on January 26, 1700. Goldfinger et al. (2012) estimated that the return period for a great CSZ earthquake is 300-500 years and there is a 7-12% likelihood of a M9.0 subduction zone earthquake occurring within the next 50 years. Similarly, they estimated a 37-42% chance of an earthquake in southern margin of the CSZ within the same time period.

Various direct and indirect hazards threaten the communities and urban areas near the CSZ. Some potential hazards include tsunamis and various ground deformations (e.g. landslide, liquefaction, fault rupture), which can bring significant damage to lifelines, infrastructure, and buildings. Detailed and comprehensive analyses along with the creation of hazard maps should be completed in order to assist with making informed decisions on how to reduce the risk of loss of life as well as mitigate the inevitable cost of damage and recovery as a result of a great CSZ earthquake.

Unfortunately, many of today's building codes were based on lessons learned and research related to the experiences of smaller-magnitude earthquakes in California. A great CSZ earthquake is expected to last several minutes and cause more significant damage, similar to recent great earthquakes in Chile and Japan. The Oregon State Seismic Safety Policy Advisory Commission (OSSPAC, 2013) recently prepared a plan for Oregonians to increase

the state resiliency. Inside this report, damage exposures were assessed and policies and strategies were identified to address them. This study focused on a moment magnitude 9 earthquake scenario accompanied by a large tsunami. Volunteers from the engineering, planning, emergency management, architectural, business, and geoscience communities as well as members of the public and representatives of state and local government assessed the vulnerability of their respective sectors.

Among the workgroups of OSSPAC was the Cascadia Earthquake Scenario Working Group, which developed a series of hazard maps for likely ground motions and deformations expected in accordance to a M9.0 CSZ earthquake scenario. Open file report (O-13-06) (Madin and Burns 2013) explains the input data sources and methods used to prepare the various data products based on a M9.0 earthquake scenario.

To produce the M9.0 earthquake scenario hazard maps, Oregon Department of Geology and Mineral Industries, DOGAMI developed python scripts within Esri's ArcGIS software. These scripts performed site amplification calculations and later produced the final hazard maps related to earthquake ground motion and ground deformation associated with it. In this previous work, however, fault rupture was only modeled for a moment magnitude 9.0 event.

This new open file report builds upon those prior efforts and presents hazard maps for other earthquake scenarios, including for M8.7, M8.4 and M8.1 events on the CSZ. The motivation behind analyzing these series of events is that they provide the ability to analyze how potential events will affect infrastructure in different ways. In order to better

improve and complete the earthquake risk-based assessments, it is necessary to know what could potentially happen under different scenarios and how they would affect the state of Oregon Instead of focusing on planning for the "big one" and allocating all resources solely on this specific scenario, other scenarios events that are considered more probable based on Goldfinger et al. (2012) study are introduced with their associated hazard maps.

The methodologies that are used in this report are based upon the HAZUS-MH 2.0 (Hazards US for Multi-Hazard) technical manual developed by FEMA in 2011. It provides procedures and recommendations to compute various hazards across a regional scale for specific natural hazard scenarios. It is a nationwide, standardized approach that assesses prospective damages from strong ground motion as well as the geological consequences they bring.

The previous scripts from O-13-06 have also been updated and refined such that they can be utilized to compute various geo-hazard maps, including landslide and liquefaction probabilities for custom scenario events with minimal user input. When needed, some information describing the methods or datasets used is repeated from O-13-06 for clarity and completeness. In addition some typographical errors are corrected in this report.

The resolution of the input and output generated datasets is all within tens of meters. Hence, **these maps are not appropriate to be directly applied for site-specific investigations and analyses for engineering design.** Applying site-specific data and methodologies are likely to produce small-scale, detailed maps that are different from the

statewide maps presented in this report. **Rather, these maps are intended to support local and statewide planning and research purposes.**

2.3 FRAMEWORK

Peak ground acceleration (PGA) estimates were provided for bedrock using the *ShakeMap*® program developed by the USGS (2016). These estimates were generated for M8.1, 8.4, 8.7, and 9.0 events. These different magnitude events were created by applying the appropriate level of energy across different sections of the CSZ based on research by Goldfinger et al. (2012). Table 2.1 summarizes the fault parameters used for each CSZ scenario. Note that although the M9.0 hazard maps were generated in O-13-06, these hazard maps were re-developed herein using updated datasets. Figure 2-1 presents the extent of fault rupture zone for the different scenarios presented in this report.

Table 2.1: Moment magnitude earthquake scenario corresponding to fault rupture bounding parameters.

MW	South	North	East	West	Depth (km)
8.1	40.4	42.7	-124	-125.20	20
8.4	40.4	44.4	-124	-125.30	20
8.7	40.4	46.25	-124	-125.30	20
9.0	40.4	45.73	-124	-125.12	20

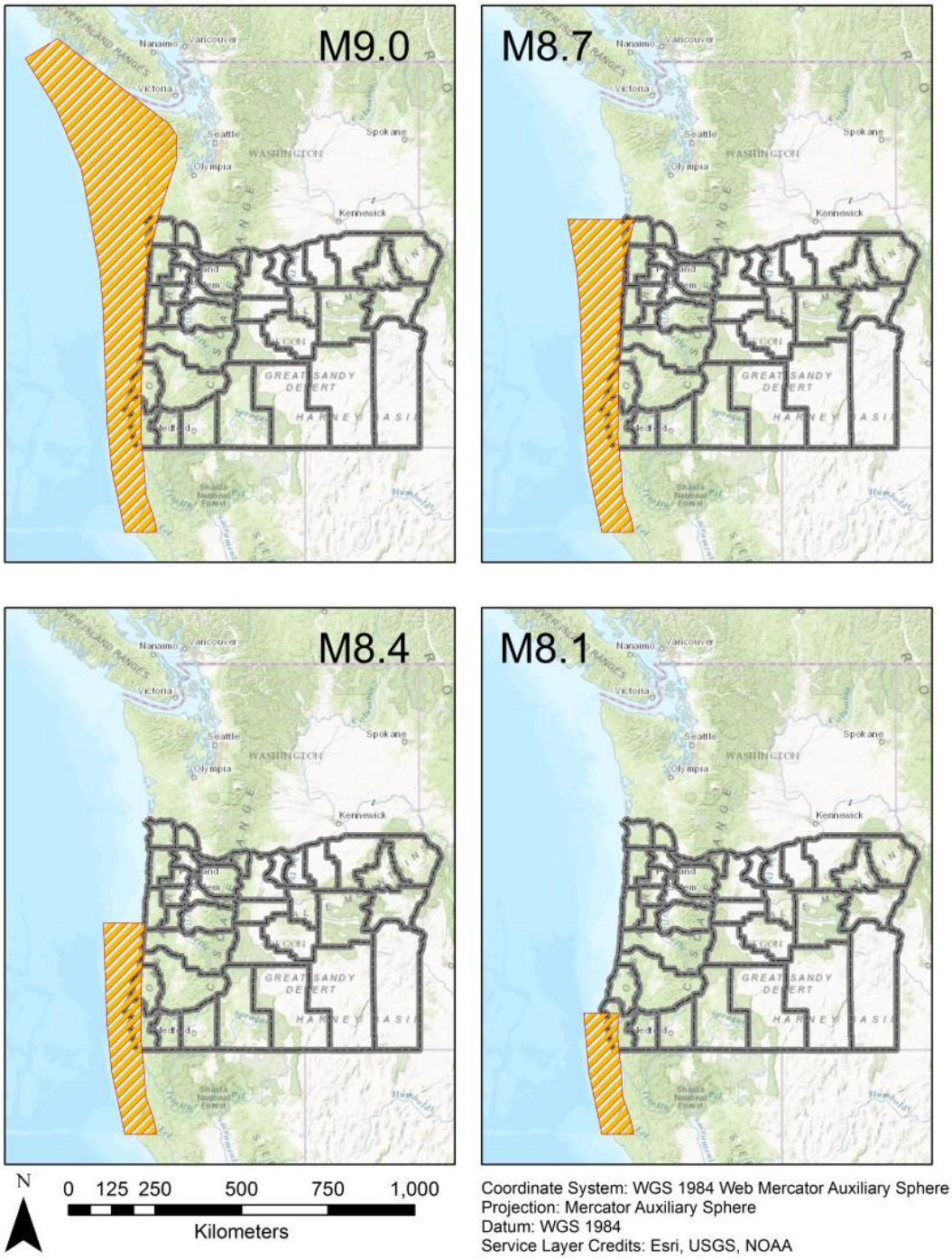

Figure 2-1: Fault rupture energy dissipation region in four CSZ earthquake scenarios.

Providing a scenario earthquake magnitude and a "bounding box" of latitudes/longitudes of these margins, the scenario ground motions for bedrock can be produced by using the USGS attenuation models. *Shakemap* outputs simulated bedrock (firm rock condition, Vs_{30} = 760 m/sec) ground motion values across 0.02 degree intervals in a point grid data format based on the input earthquake magnitude and fault rupture parameters. To improve processing efficiency with other datasets, these data were projected to the state-standard Oregon Lambert projection (EPSG 2292) and then converted to raster datasets with 30-m (98.4 ft) cell sizes.

Two consecutive modules were developed in order to compute the appropriate site amplification factors to scale the initial bedrock ground motion inputs to the top of the soil column and further perform various hazard assessments using HAZUS-MH recommendations (FEMA 2011). Figure 2-2 depicts an overview flowchart for these procedures. Each of the blocks in this flowchart is discussed in detail below.

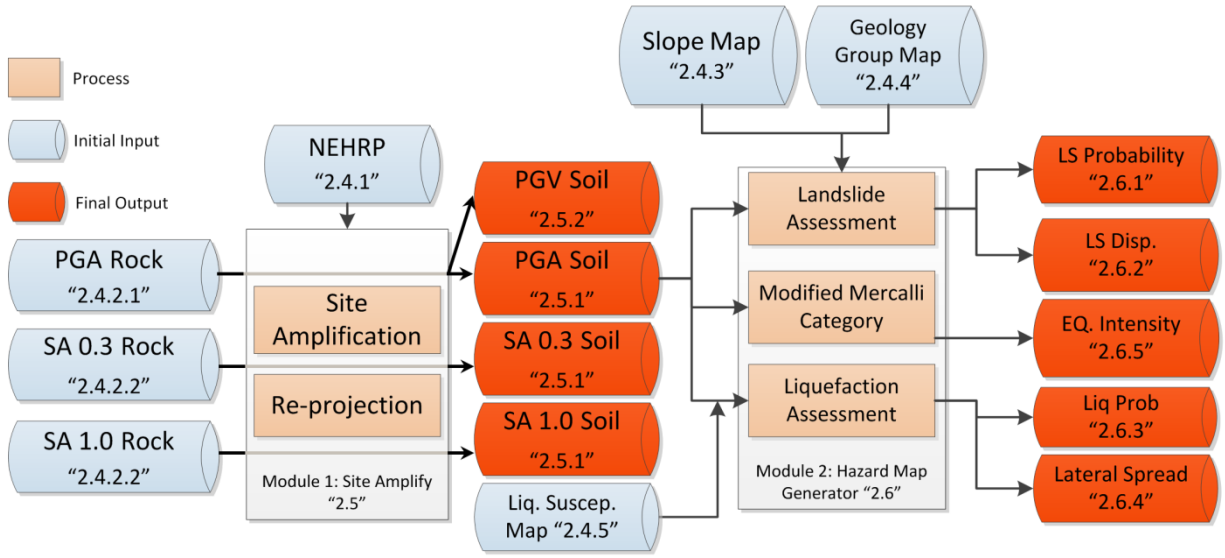

Figure 2-2: Overview flowchart introducing initial inputs and outputs and developed processes with intermediate input and final outputs (numbers in quotation represent the section where the item is discussed).

More specifically, two separate modules were created:

Module 1. Re-projection and site amplification

After re-projection of the bedrock spectral accelerations from the USGS, module 1 interpolates these grid values into a raster dataset and multiplies the spectral accelerations by site amplification factors using the method presented in Boore and Atkinson (2008). This module outputs raster datasets of estimates for PGA Soil (a_{max}), Peak Ground Velocity (PGV), and Spectral Acceleration (SA) for periods of 0.3 seconds and 1.0 seconds at the ground surface.

Module 2. Hazard map generator

After completion of module 1, module 2 uses the PGA soil (a_{max}) in conjunction with previously created susceptibility and topographic maps to generate additional hazard maps. The module

implements various models presented in the HAZUS-MH earthquake technical manual (FEMA, 2011) for the analysis. It outputs various raster datasets such as landslide triggering, landslide displacement, liquefaction triggering, and lateral spread displacement hazards.

2.4 INPUT DATA LAYERS

Several data layers were created or used for input in the two modules (Table 2.2). Some of these layers were originally created for the Oregon Resilience Plan or O-13-06. However, most of the layers were updated to take advantage of data from recent mapping and analysis efforts by DOGAMI.

The resultant maps were produced at 30 m resolution, similar to some of the source data. Table 2.2 summarizes the input layers used in both modules, identifying their source and providers.

Table 2.2: Input Datasets used for both modules and their sources and providers.

Input Layer	Used in Module	Source	Provider	Reference
NEHRP	*1 - site amplify*	The Oregon resilience plan	DOGAMI	BSSC (2000)
PGA Bedrock (4 Scenarios)	*1 - site amplify*	*ShakeMap*® scenarios	USGS	Wald and others (2005)
1 Second Spectral Acceleration Bedrock (4 Scenarios)	*1 - site amplify*	*ShakeMap*® scenarios	USGS	Wald and others (2005)
0.3 Second Spectral Acceleration Bedrock (4 Scenarios)	*1 - site amplify*	*ShakeMap*® scenarios	USGS	Wald and others (2005)
PGA soil (4 Scenarios)	*2 - Hazard Map Generator*	The output of *Module 1*.	OSU/DOGAMI	OSU/DOGAMI
Slope Classes	*2 - Hazard Map Generator*	Reclassified from a hybrid slope generated from USGS NED and lidar DEM.	DOGAMI	Madin and Burns (2013)
Geology Group	*2 - Hazard Map Generator*	Assigning OGDC units to HAZUS-MH geologic groups based on the percentage of the mapped units that intersect with inventoried landslides.	DOGAMI	Madin and Burns, (2013)
Liquefaction Susceptibility	*2 - Hazard Map Generator*	Estimating susceptibility for various geologic units in OGDC, SLIDO-2, and recently published lidar-based surficial geology maps.	DOGAMI	Madin and Burns (2013)

2.4.1 Statewide NEHRP site class (Vs_{30})

Geotechnical properties of the soil or bedrock in a given location contribute to the intensity of ground shaking during an earthquake. The Building Seismic Safety Council (BSSC, 2000) used numerous shear wave velocity tests along with other geotechnical properties to classify various building locations into different site classes to describe the general site response conditions. These classes are referred to as NEHRP (National Earthquake Hazard Reduction Program) Site Classes. The classification (Table 2.3) is based on shear wave

velocities in the upper 30 meters of the soil profile. The NEHRP site classification is widely accepted and is incorporated into many building codes in United States and around the world (Holzer et al. 2005).

Table 2.3: NEHRP site classes and their corresponding profile type and shear wave velocity (Holzer et al., 2005).

Site class	**Profile Type**	**Vs_{30} (m/s)**
A	Hard rock	> 1500
B	Rock	760 – 1500
C	Very dense soil/soft rock	360 – 760
D	Stiff soil	180 – 360
E	Soft soil	< 180
F	Special soils requiring site-specific investigations	-

DOGAMI has been compiling a shear wave velocity measurement database since the 1990s for the northeast section of Oregon. These Vs_{30} values were combined with a generalized geology map of the study area based on (OGDC) v5.0 to produce the NEHRP Site Class map (Figure 2-3).

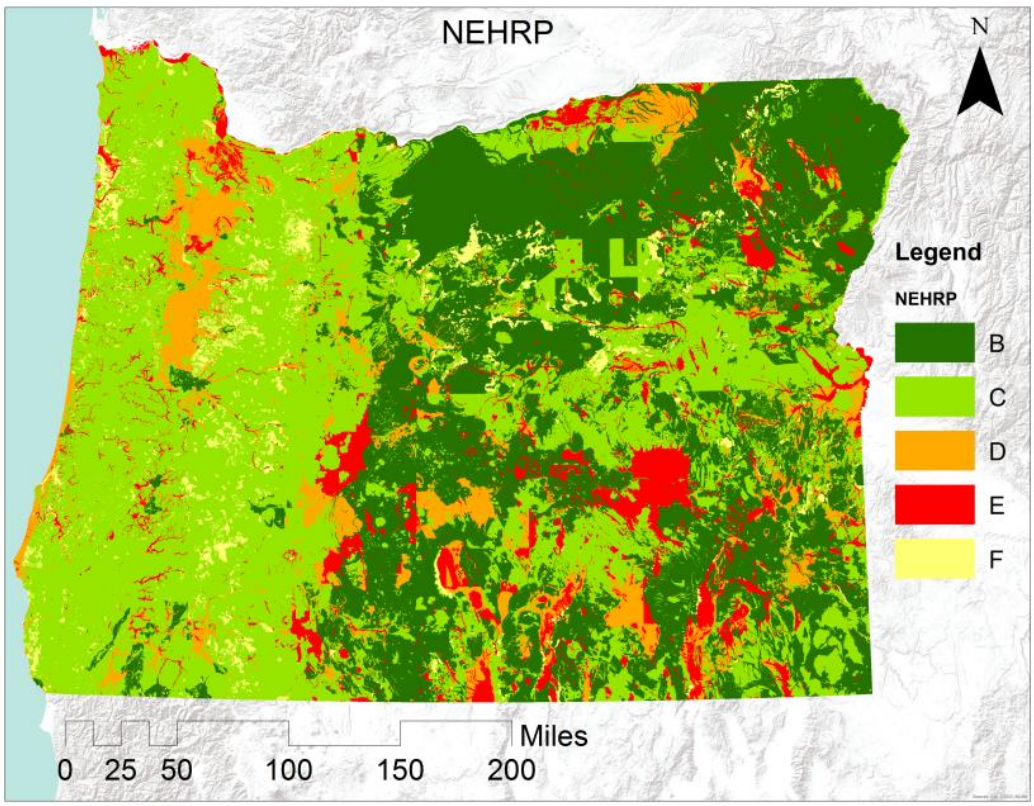

Figure 2-3: Updated NEHRP map developed for the state of Oregon based on Vs_{30} measurements correlated with geologic mapping by DOGAMI (Madin and Burns, 2013).

2.4.2 Ground motion maps

2.4.2.1 Bedrock Peak Ground Acceleration (PGA)

PGA is widely used in geotechnical and structural engineering as a measure of ground shaking. A series of bedrock peak ground acceleration maps were created by the USGS using *ShakeMap* for the four different rupture models described in Table 2.1. The simulated bedrock point data for Oregon was provided at 0.02 degree intervals in an ASCII Text file (longitude, latitude, and PGA bedrock).

In Module 1 of the developed tools, the Oregon Lambert Projection NAD 83 International Feet (EPSG: 2992) coordinate system was used for re-projection of the ground motion estimates. Interpolation was then performed using natural neighbor analysis to convert these points to raster datasets.

2.4.2.2 Bedrock Spectral Accelerations (SA01 – SA0.3)

Similar to PGA, the USGS used *ShakeMap* to compute gridded bedrock spectral acceleration for 1-second period (SA01) and 0.3-second period (SA0.3) for each scenario. Module 1 re-projects these grids into the Oregon Lambert coordinate system interpolates the spectral accelerations into raster datasets.

2.4.3 Categorized slope classes

The HAZUS-MH methodology requires a reclassified slope class map and a generalized geologic group table to compute the corresponding landslide susceptibility classes. A hybrid DEM was created by combining available lidar DEMs from the Oregon Lidar Consortium with the USGS National Elevation Dataset (NED) to fill in the gaps where lidar

data were not yet available. A slope map (Figure 2-4) was then created from this hybrid DEM and subsequently classified using the parameters in Table 2.4.

Table 2.4: Slope classes for landslide hazard analysis.

Slope Angle, degrees					
0-10	10-15	15-20	20-30	30-40	> 40

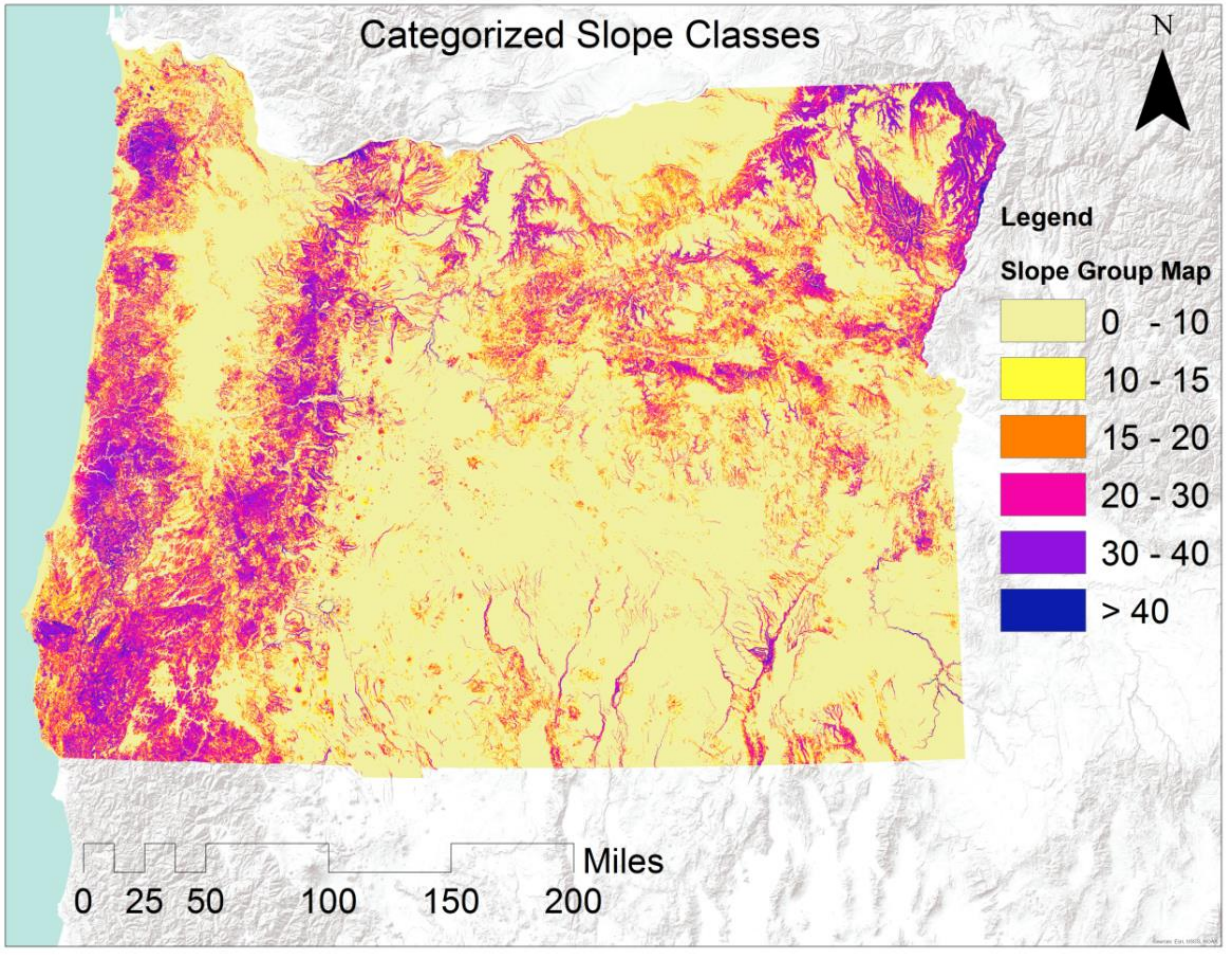

Figure 2-4: Categorized slope classes for state of Oregon.

2.4.4 Geology group map

Following the recommendation in HAZUS-MH for landslide susceptibility computations, DOGAMI created a geology “group map" that corresponds to the HAZUS-MH classification scheme (Table 2.5). This group map contains three geologic units (A,B,C) and the six slope classes (see Figure 2-4). Using expert judgement, DOGAMI divided the geologic units in the Oregon Geologic Data Compilation release 5 (OGDC-5, Ma et al., 2009) into the three geologic groups per definitions in Table 2.5. Depending on OGDC formation and rock type, the generalized geology groups in the OGDC were reclassified by DOGAMI to HAZUS-MH groups. Since the groups defined in HAZUS-MH were quite general, an empirical assessment of landslide susceptibility was performed by intersecting the inventoried landslide polygons from the SLIDO-2 database (Burns et al. 2011) with the OGDC polygons. Afterwards, the intersected percentage of each Geologic Merge Unit was calculated and resulted in the spatial association of 732 of 1923 OGDC units with existing landslides. Based on the association determined by the intersection of that unit with historical landslides, each merged unit was assigned by DOGAMI to a HAZUS-MH group (Table 2.6) and a corresponding map (Figure 2-5) was produced (see O-13-06, Madin and Burns (2013) for more details).

Table 2.5: Geologic group Landslide susceptibility based on HAZUS-MH 2.0 Table 4-15 (FEMA, 2011).

Geologic Group		Slope Angle, degrees					
		0 - 10	10 -15	15 - 20	20 - 30	30 - 40	> 40
(a) DRY (groundwater below level of sliding)							
A	**Strongly Cemented Rocks (crystalline rocks and well-cemented sandstone, c' = 300 psf, φ' = 35°)**	None	None	I	II	IV	VI
B	**Weakly Cemented Rocks and Soils (sandy soils and poorly cemented sandstone, c'=0, φ' = 35°)**	None	III	IV	V	VI	VII
C	**Argillaceous Rocks (shales, clayey soil, existing landslides, poorly compacted fills, c'=0, φ' = 20°)**	V	VI	VII	IX	IX	IX
(b) WET (groundwater level at ground surface)							
A	**Strongly Cemented Rocks (crystalline rocks and well-cemented sandstone, c' = 300 psf, φ' = 35°)**	None	III	VI	VII	VIII	VIII
B	**Weakly Cemented Rocks and Soils (sandy soils and poorly cemented sandstone, c'=0, φ' = 35°)**	V	VIII	IX	IX	IX	X
C	**Argillaceous Rocks (shales, clayey soil, existing landslides, poorly compacted fills, c'=0, φ' = 20°)**	VII	IX	X	X	X	X

Table 2.6: Geology group categories established by HAZUS-MH technical manual (FEMA 2011). The groups were classified according to the percentage of geologic unit polygons that intersected with inventoried landslides.

Percentage of polygons in contact:	HAZUS-MH Group	Rock type
0 to 20% intersection	**Group A**	Strongly cemented rocks
20% to 50% intersection	**Group B**	Weakly cemented rocks
Greater than 50% intersection	**Group C**	Argillaceous rocks

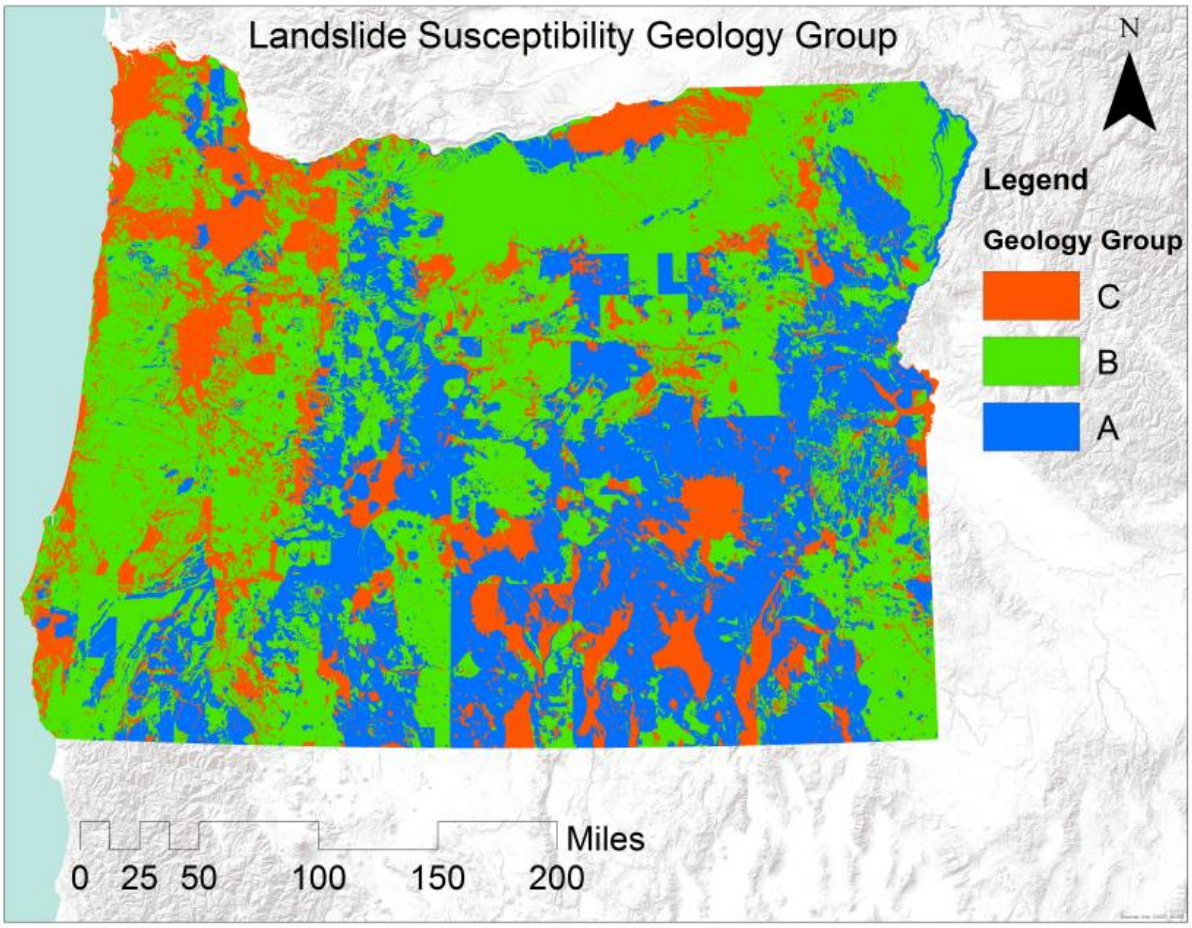

Figure 2-5: Geologic group map for HAZUS-MH landslide susceptibility by DOGAMI (Madin and Burns, 2013).

2.4.5 Liquefaction susceptibility map

Using the Youd and Perkins (1978) liquefaction susceptibility method, the OGDC geologic units were categorized into 5 different sub-groups. These groups were then modified by current understanding of Oregon geology as well as detailed hazard studies (Mabey et al., 1993; Madin and Wang, 1999 a,b,c; Wang and Wang, 2000), which consider data from site-specific in situ geotechnical tests, including SPT (Standard Penetration Test) logs and shear

wave velocity measurements. The final liquefaction susceptibility map (Figure 2-6) consists of 6 groups presenting “None” to “Very High” hazard levels.

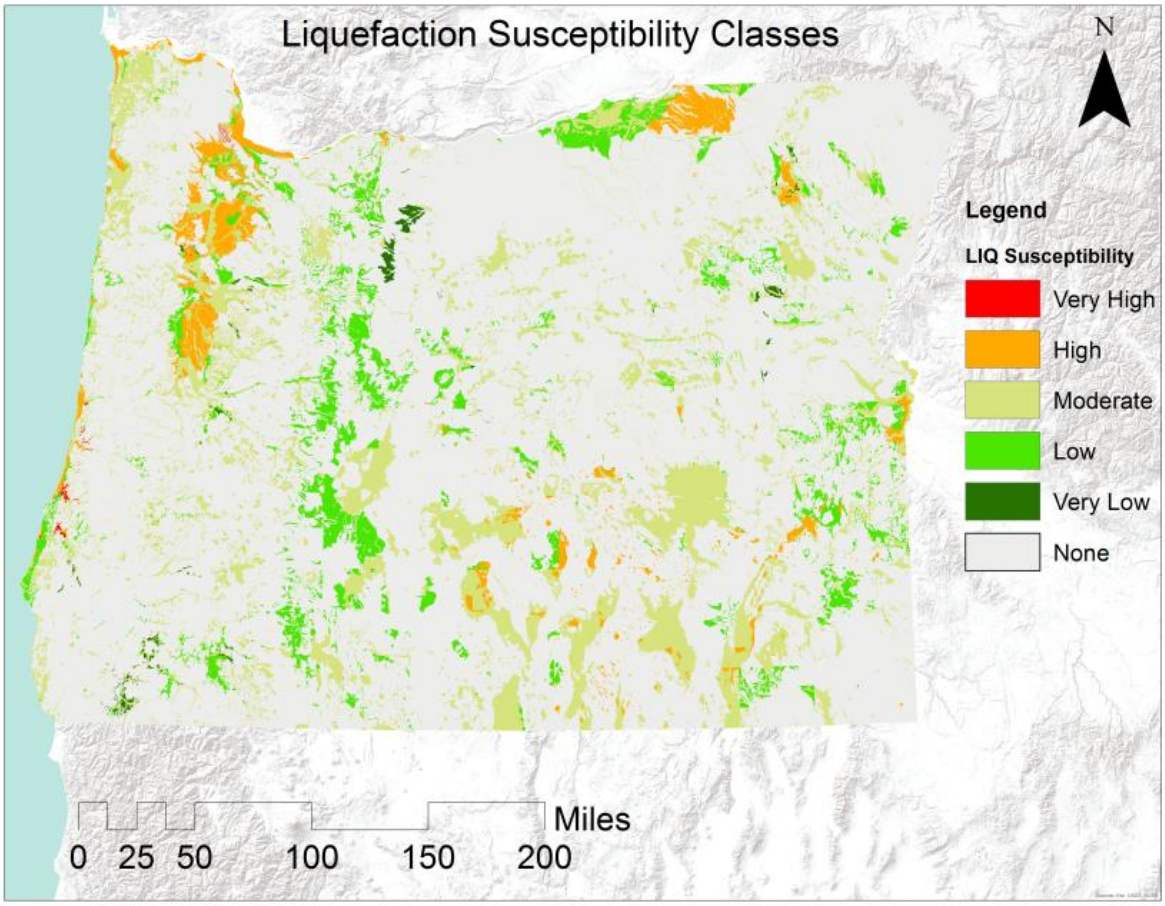

Figure 2-6: Liquefaction susceptibility class map of Oregon developed by DOGAMI (Madin and Burns, 2013).

2.5 SITE AMPLIFICATION METHODOLOGY

Module 1 is a custom program written in C++ language for amplifying or de-amplifying bedrock acceleration values produced by the USGS for a scenario seismic event using attenuation relationships in Boore and Atkinson (2008) and the NEHRP site class map introduced in Section 3. Module 1 outputs raster datasets of the ground accelerations at the soil surface. Boore and Atkinson (2008) proposed a site amplification expression as:

$$F_S = F_{LIN} + F_{NL} \quad (2\text{-}1)$$

where F_{LIN} is the linear portion which is computed by following equation:

$$F_{LIN} = b_{lin} \ln (Vs_{30}/V_{ref}) \quad (2\text{-}2)$$

and b_{LIN} is a coefficient related to period having a value of -0.36 for PGA (see Table 2.7 for other periods) and V_{ref} = 760 m/s. F_{NL} is a nonlinear term computed by one of the relationships given in equations below, depending on the value of PGA for bedrock:

For $PGA_b \leq 0.03$ g, $F_{NL} = b_{nl} [\ln (0.06 / 0.1)]$ (2-3)

For $PGA_b > 0.03$ g and ≤ 0.09 g, $F_{NL} = b_{nl} \ln (0.06 / 0.01) + c[\ln (PGA_b / 0.03)]^2 + d[\ln (PGA_b / 0.03)]^3$ (2-4)

For $PGA_b > 0.09$ g, $F_{NL} = b_{nl} \ln (PGA_b / 0.1)$ (2-5)

Coefficients c and d can be computed by:

$c = (3\Delta y - b_{NL}\Delta x)/\Delta x^2$ (2-6)

$d = (2\Delta y - b_{NL}\Delta x)/\Delta x^3$ (2-7)

where

$\Delta x = ln\left(\frac{0.09g}{0.03g}\right) = 1.0986$ (2-8)

$\Delta y = b_{nl} ln\left(\frac{0.09g}{0.06g}\right)$ (2-9)

and b_{nl} is computed by:

For Vs_{30} < 180 m/sec,

$b_{nl} = b_1$ (2-10)

For Vs_{30} > 180 m/sec and ≤ 300 m/sec,

$b_{nl} = (b_1 - b_2) \ln(Vs_{30} / 300) / \ln (180 / 300 \text{ m/sec}) + b_2$ (2-11)

For Vs_{30} > 300 m/sec ≤ 760 m/sec,

$b_{nl} = b_2 \ln (Vs_{30} / 760 \text{ m/sec}) / \ln (300 / 760 \text{ m/sec})$ (2-12)

where b_1 and b_2 are coefficients related to the period. For PGA, they are equal to -0.64 and -0.14, respectively (See Table 2.7 for the coefficients related to other periods).

Table 2.7: Boore and Atkinson (2008) period-dependent site-amplification coefficients.

Period	b_{lin}	b_1	b_2
PGA	-0.360	-0.640	-0.14
0.300	-0.440	-0.520	-0.14
1.000	-0.700	-0.440	0.00

After inputting the various Vs_{30} values from the site class map into the above equations, Table 2.8 presents the resulting Boore and Atkinson (2008) site amplification coefficients for PGA.

Table 2.8: Boore and Atkinson (2008) PGA site amplification coefficients for Vs_{30} values in the statewide Vs_{30} map.

Vs_{30} m/sec	b_{nl}	Δy	c	d	F_{LIN}
98	-0.6400	-0.2595	-0.0625	-0.1389	0.737406
163	-0.6400	-0.2595	-0.0625	-0.1389	0.554245
301	-0.1395	-0.0566	-0.0136	-0.0303	0.333435
464	-0.0743	-0.0301	-0.0073	-0.0161	0.177636
680	-0.0168	-0.0068	-0.0016	-0.0036	0.040041

2.5.1 Site ground motion parameters prediction maps

Figure 2-7 to Figure 2-9 present maps of site PGA, as well as site spectral accelerations for short (0.3 second) and long (1 second) periods for all four scenarios (output from Module 1). The raster datasets in these maps are later used as inputs for producing geo-hazard maps.

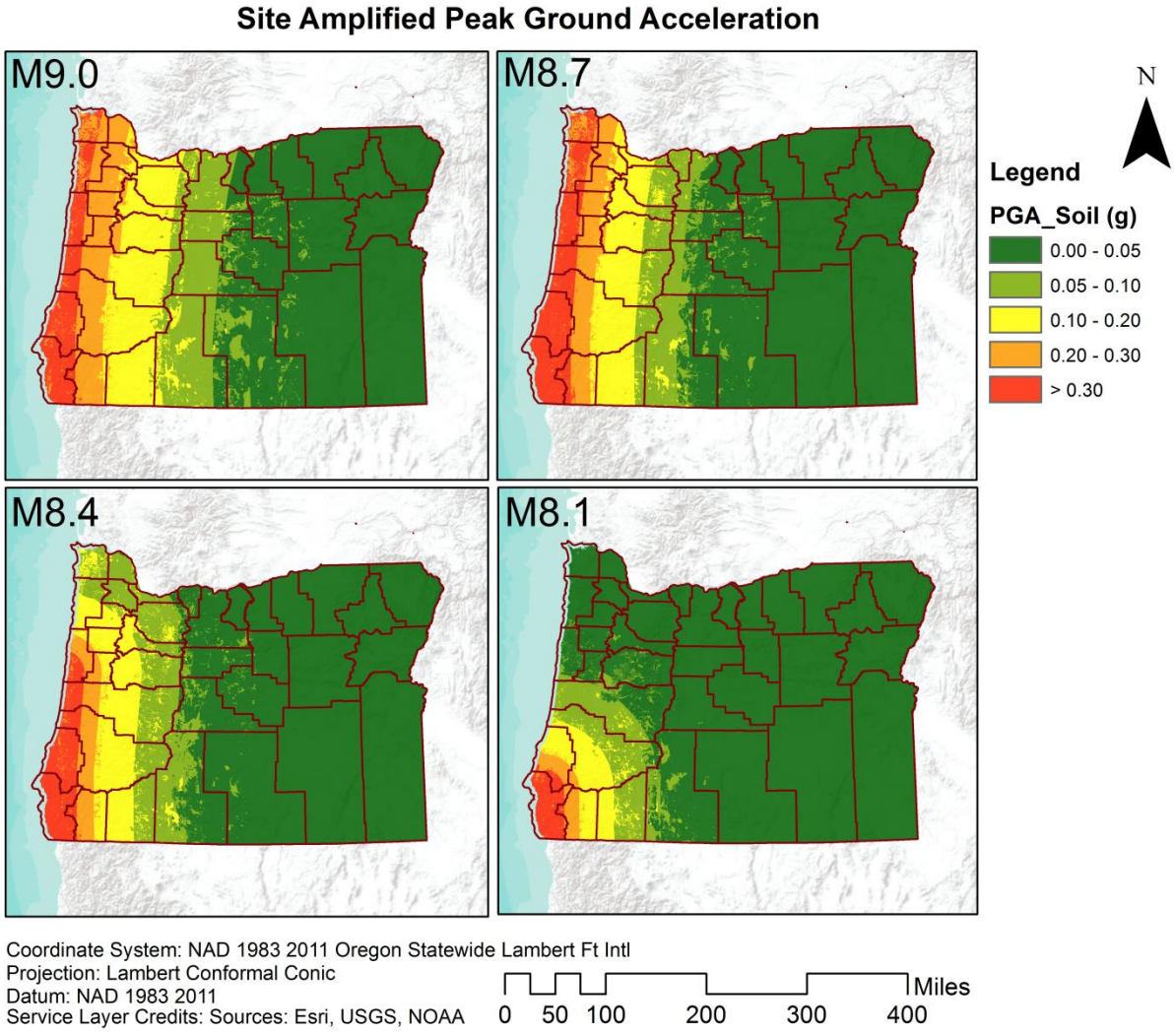

Figure 2-7: Site amplified Peak Ground Acceleration estimates for deterministic scenarios of a CSZ earthquake.

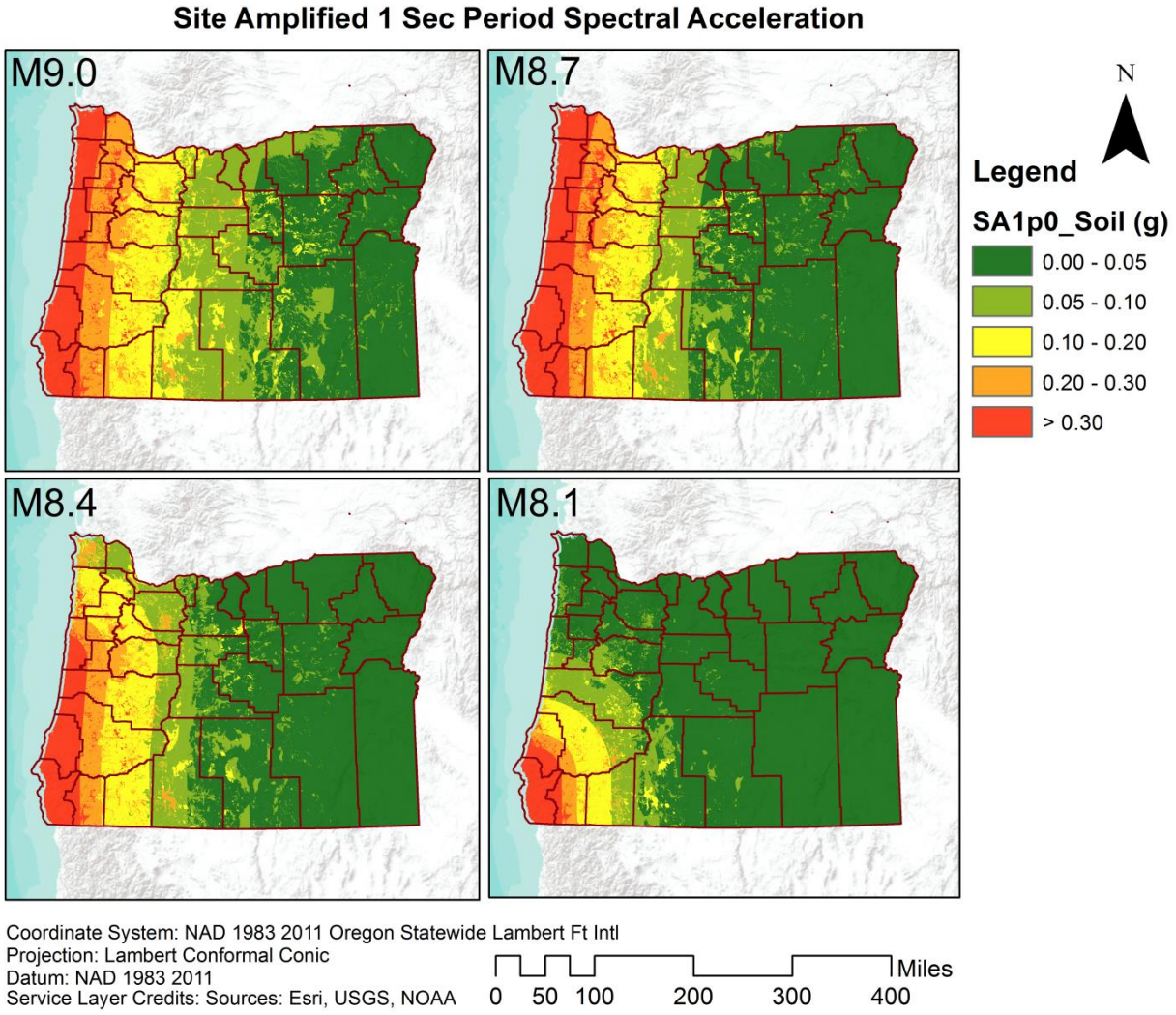

Figure 2-8: Site amplified long period (1 second) spectral acceleration maps for deterministic scenarios of a CSZ earthquake.

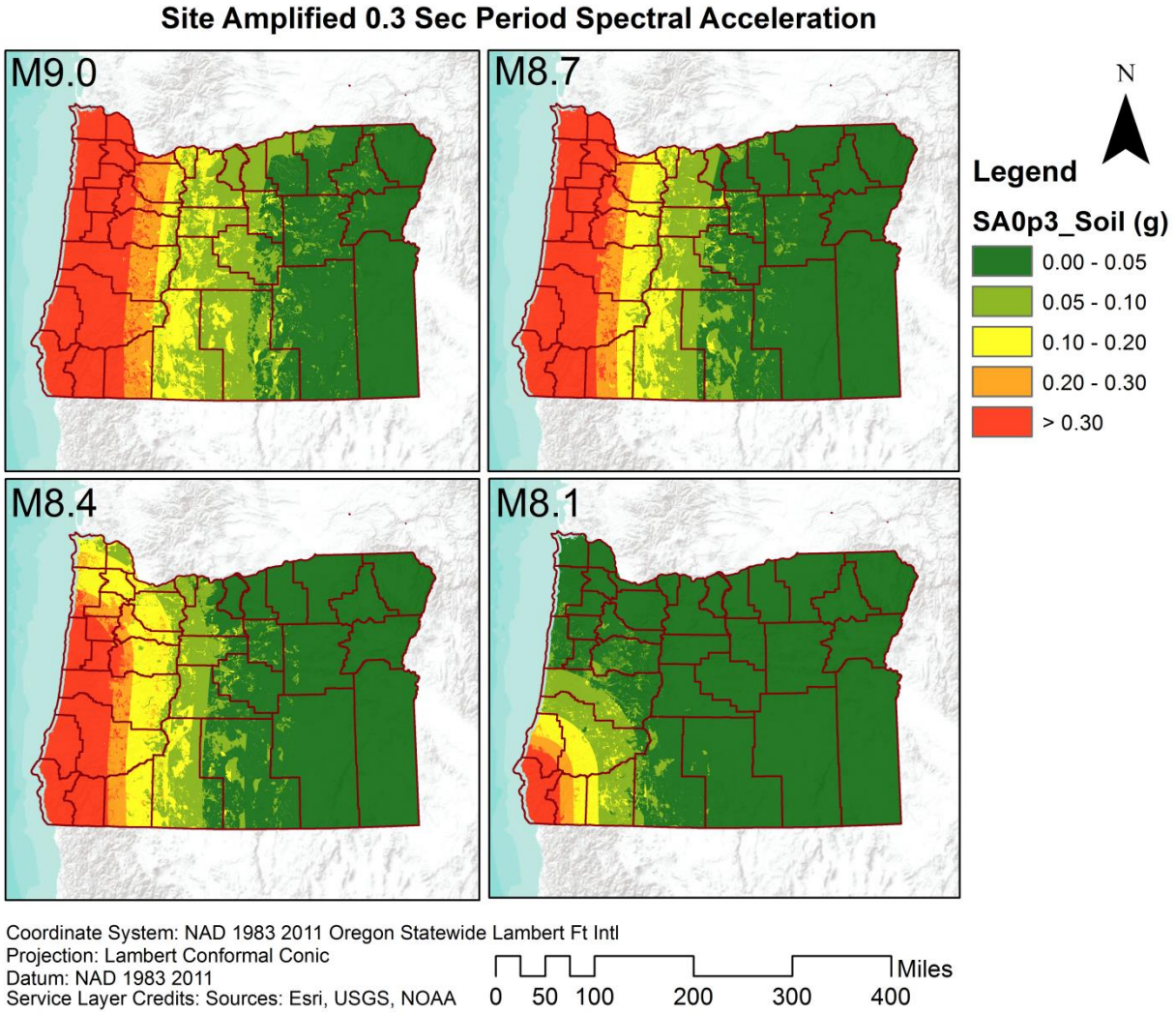

Figure 2-9: Site amplified short period (0.3 second) spectral acceleration maps for deterministic scenarios of a CSZ earthquake.

2.5.2 Peak Ground Velocity (PGV)

PGV values were also estimated for each of the four CSZ scenarios following relationships described in Newmark and Hall (1982) (i.e. converting 1-second period spectral acceleration (SA01) to PGV).

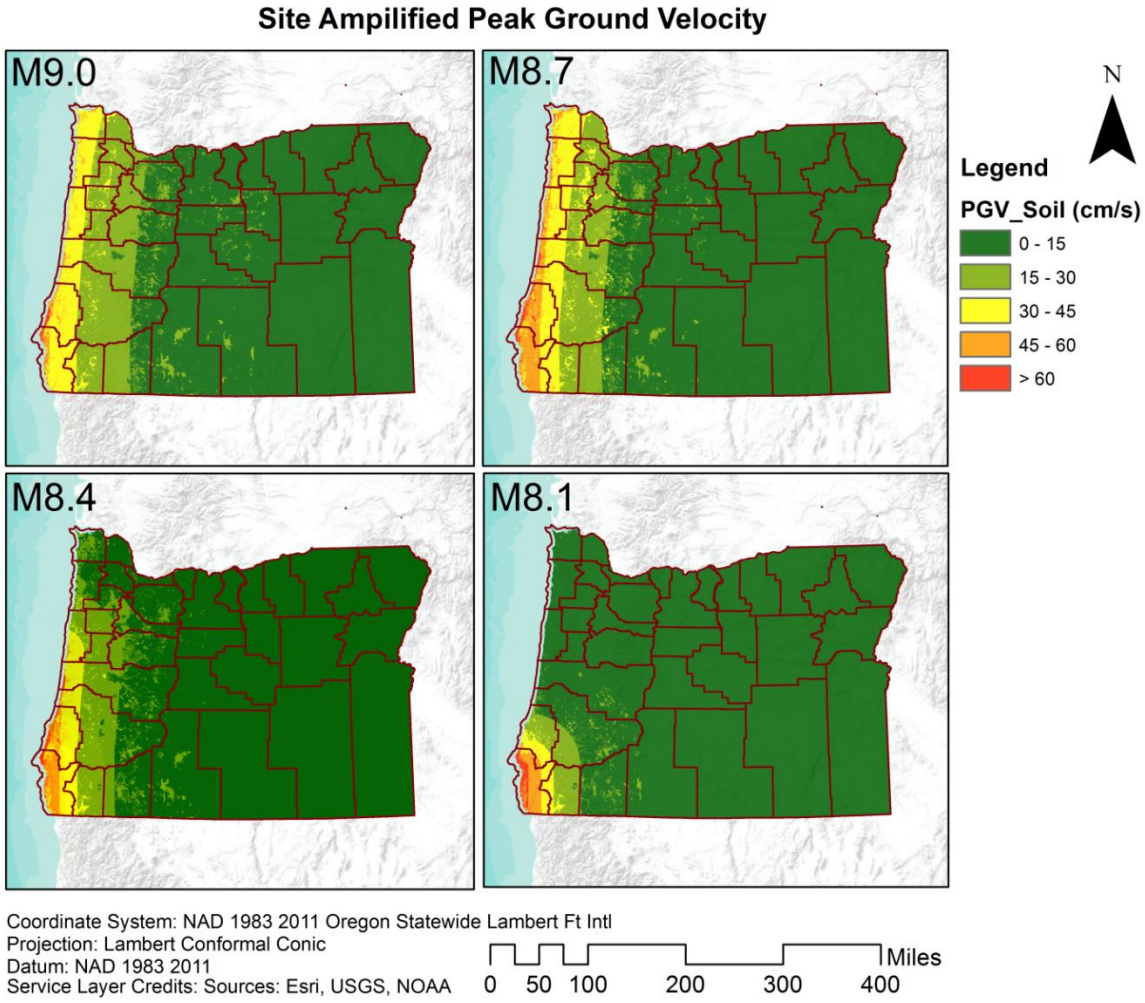

Figure 2-10: Site amplified Peak Ground Velocity (PGV) estimates for deterministic scenarios of CSZ.

Figure 2-10 presents PGV values for each scenario. To perform this conversion, the following equation was used:

PGV = SA01 x 94.666 (2-13)

where PGV is in centimeters per second and SA01 is in g.

2.6 HAZARD MAPPING METHODOLOGY

In addition to producing the spectral acceleration maps associated with the four deterministic seismic events, a series of hazard maps, such as landslide and liquefaction triggering probabilities with corresponding estimates of horizontal ground displacements were developed.

Using the input raster datasets described in sections 2.4.3 to 2.4.5, the site amplified peak ground acceleration raster datasets developed in section 2.5.1 and methods described in HAZUS-MH, Module 2 were written in C++ language to compute a series of statewide geo-hazard maps.

2.6.1 Landslide triggering probability

Following the Wilson and Keefer (1985) approach, landslide susceptibility categories were classified into 10 groups from I to X as a function of the geologic group (introduced in 2.4.4), groundwater conditions (assumed to be at the surface in Oregon given its wet climate), and categorized slope map (introduced in 2.4.3). Given the geology group map (Figure 2-5) in conjunction with Table 2.5, the landslide susceptibility group can be

defined. Next, per Table 2.9, map area percentage which was set to equal the landslide probability was assigned based on the susceptibility category.

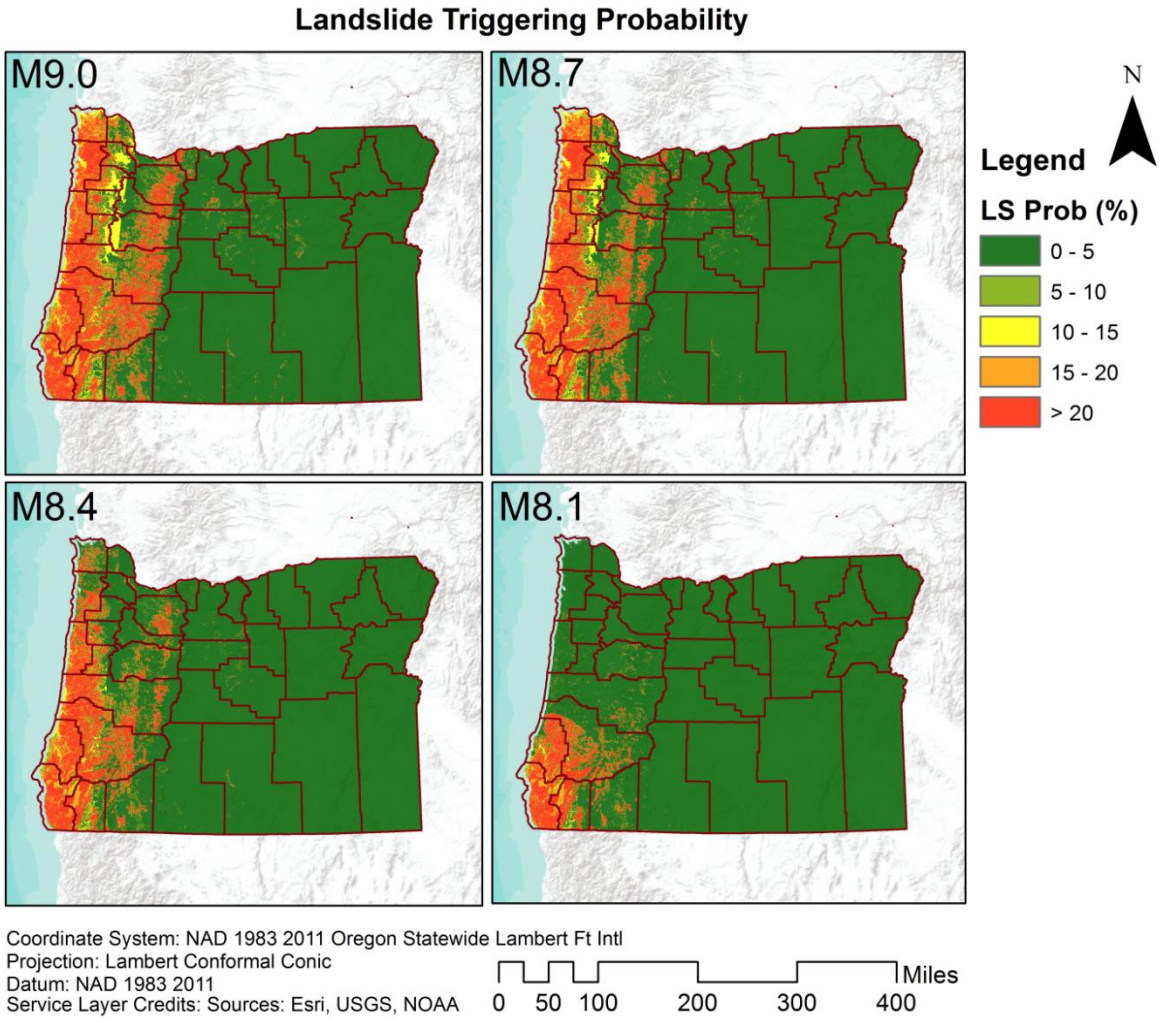

Figure 2-11: Landslide triggering probability corresponding to four deterministic scenarios of a CSZ earthquake.

Table 2.9 presents the critical acceleration values and corresponding landslide map area proposed in HAZUS-MH. Figure 2-11 shows maps of the landslide triggering probabilities for the four different seismic scenarios.

Table 2.9: Critical acceleration (a_C) and percentage of map area for susceptibility categories.

Susceptibility Category	None	I	II	III	IV	V	VI	VII	VIII	IX	X
Cr. Acceleration (g)	None	0.60	0.50	0.40	0.35	0.30	0.25	0.20	0.15	0.10	0.05
Map Area	0.00	0.01	0.02	0.03	0.05	0.08	0.10	0.15	0.20	0.25	0.30

2.6.2 Landslide displacement

HAZUS-MH proposes the following relationship to compute the expected permanent ground displacement [E(PGD)] in centimeters as a result of a landslide:

$$E(PGD) = E(d|a_{is}) \times a_{is} \times n \quad (2\text{-}14)$$

where

$E(d|a_{is})$ is the expected displacement factor, in cm per cycle, (see Figure 4.14 in HAZUS, earthquake technical manual, FEMA 2011) which can be calculated using equation 2-15,

$$E(d \mid a_{is}) = \begin{cases} 75.69 \times e^{-6.87x} & for \;\; 0.0 < x \leq 0.7 \\ 3681.22 \times e^{-12.42x} & for \;\; 0.7 < x \leq 1.0 \end{cases} \quad (2\text{-}15)$$

x is the ratio of critical acceleration and induced acceleration, a_{is} is the induced acceleration by seismic source (in decimal fraction of g's), and n is the number of cycles computed based on Seed and Idriss (1982) for a given earthquake moment magnitude (M) using the following empirical relationship:

$$n = 0.3419M^3 - 5.5214M^2 + 33.6154M - 70.7692 \quad (2\text{-}16)$$

The resulting landslide displacement maps for the four scenario events are presented in Figure 2-12.

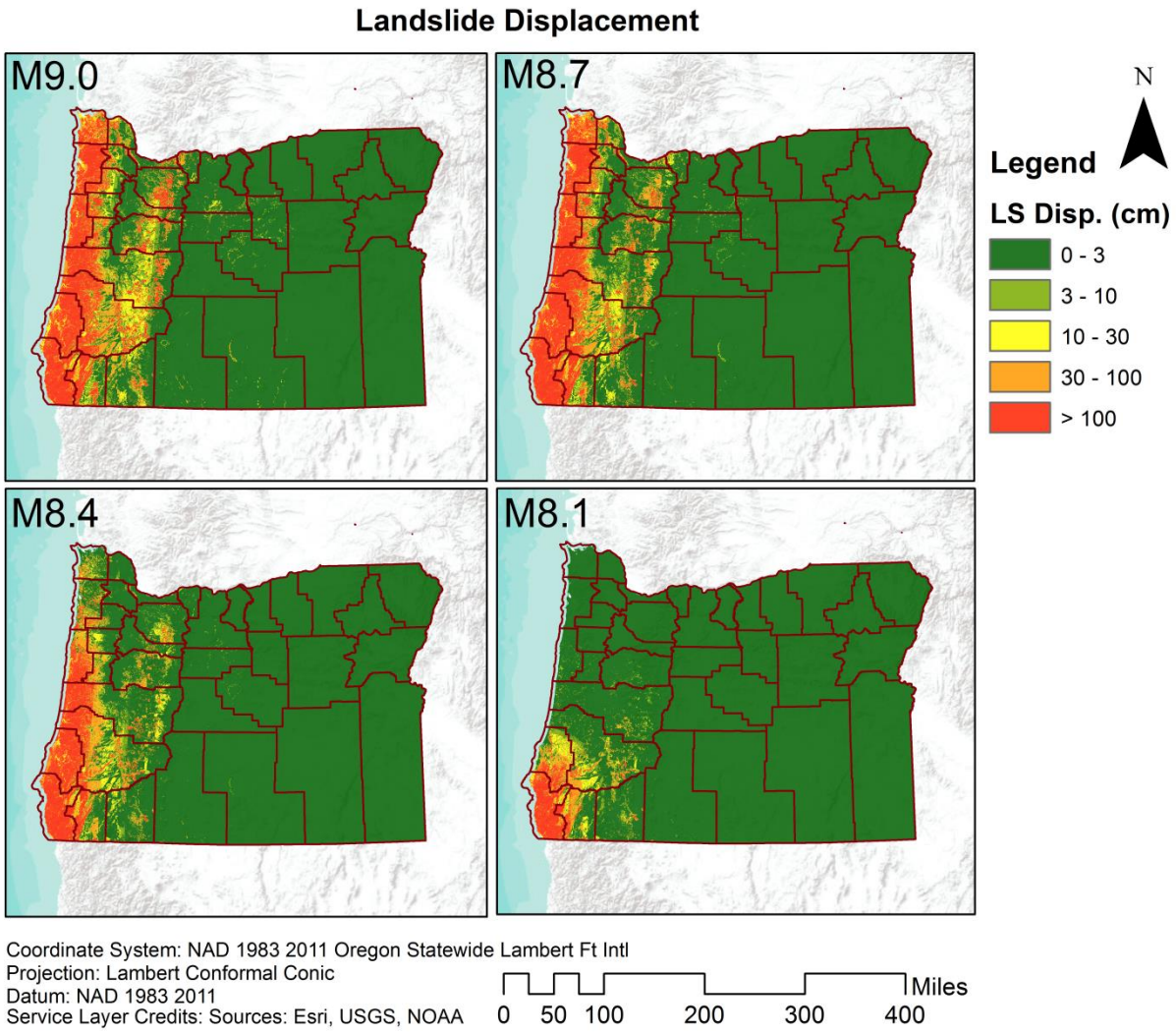

Figure 2-12: Landslide displacement corresponding to four deterministic scenarios of a CSZ earthquake.

2.6.3 Liquefaction triggering probability

Liquefaction potential is estimated in HAZUS-MH based on the susceptibility of the soil, the amplitude (i.e., estimated from peak ground acceleration, PGA) and duration of the ground shaking (i.e., estimated from the moment magnitude of the earthquake), and groundwater depth. Youd and Perkins (1978) correlate relative liquefaction susceptibility of soils within a particular geologic unit. Equation below presents the relationship for estimating the probability of liquefaction triggering for a given susceptibility category, $P\ [Liquefaction_{SC}]$:

$$P\ [Liquefaction_{SC}] = \frac{P\ [Liquefaction_{SC}|\ PGA=a]}{K_M \times K_W} \times P_{ml} \quad (2\text{-}17)$$

where $P\ [Liquefaction_{SC}|\ PGA = a]$ is the conditional liquefaction probability for a given susceptibility group (see Figure 2-6) at a given value of PGA equal to "a" at the soil surface for an earthquake with M=7.5 and where groundwater depth is assumed to be five feet (Table 2.10), and P_{ml} is the proportion of the unit susceptible to liquefaction (Table 2.11). These values are based on judgments from preliminary examination of soil data for geologic map units in regional liquefaction studies (e.g., Power et. al., 1982).

The following correction factors were used for correcting the conditional probability of liquefaction triggering for other earthquake magnitudes (other than M = 7.5) and groundwater depths (other than 5 feet) based on relationships in Seed and Idriss (1982), Seed et. al. (1985) and the National Research Council (1985).

K_M is the correction factor for moment magnitude calculated by the following equation:

$$K_M = 0.0027M^3 - 0.0267M^2 - 0.2055M + 2.9188 \quad (2\text{-}18)$$

K_W is the correction factor for the ground water determined by:

$$K_W = 0.022d_w + 0.93 \quad (2\text{-}19)$$

d_w is the depth to the groundwater in feet, and M is the earthquake moment magnitude.

Table 2.10: Equations for the conditional probability of liquefaction triggering for different liquefaction susceptibility categories (after Liao, et al., 1988).

Susceptibility Category (See Figure 2-6)	$\mathbf{P\,[Liq_{SC}|\,PGA = a]}$
Very High	0 ≤ 9.09 a – 0.82 ≤ 1.0
High	0 ≤ 7.67 a – 0.92 ≤ 1.0
Moderate	0 ≤ 6.67 a – 1.00 ≤ 1.0
Low	0 ≤ 5.57 a – 1.18 ≤ 1.0
Very Low	0 ≤ 4.16 a – 1.08 ≤ 1.0
None	0.0

Table 2.11: Map unit susceptibility to liquefaction according to HAZUS-MH (FEMA, 2011).

Mapped Relative Susceptibility	**Very High**	**High**	**Moderate**	**Low**	**Very Low**	**None**
Proportion of Map Unit	0.25	0.20	0.10	0.05	0.02	0.00

Figure 2-13 depicts the liquefaction triggering potential for the state of Oregon for the four deterministic earthquake scenarios.

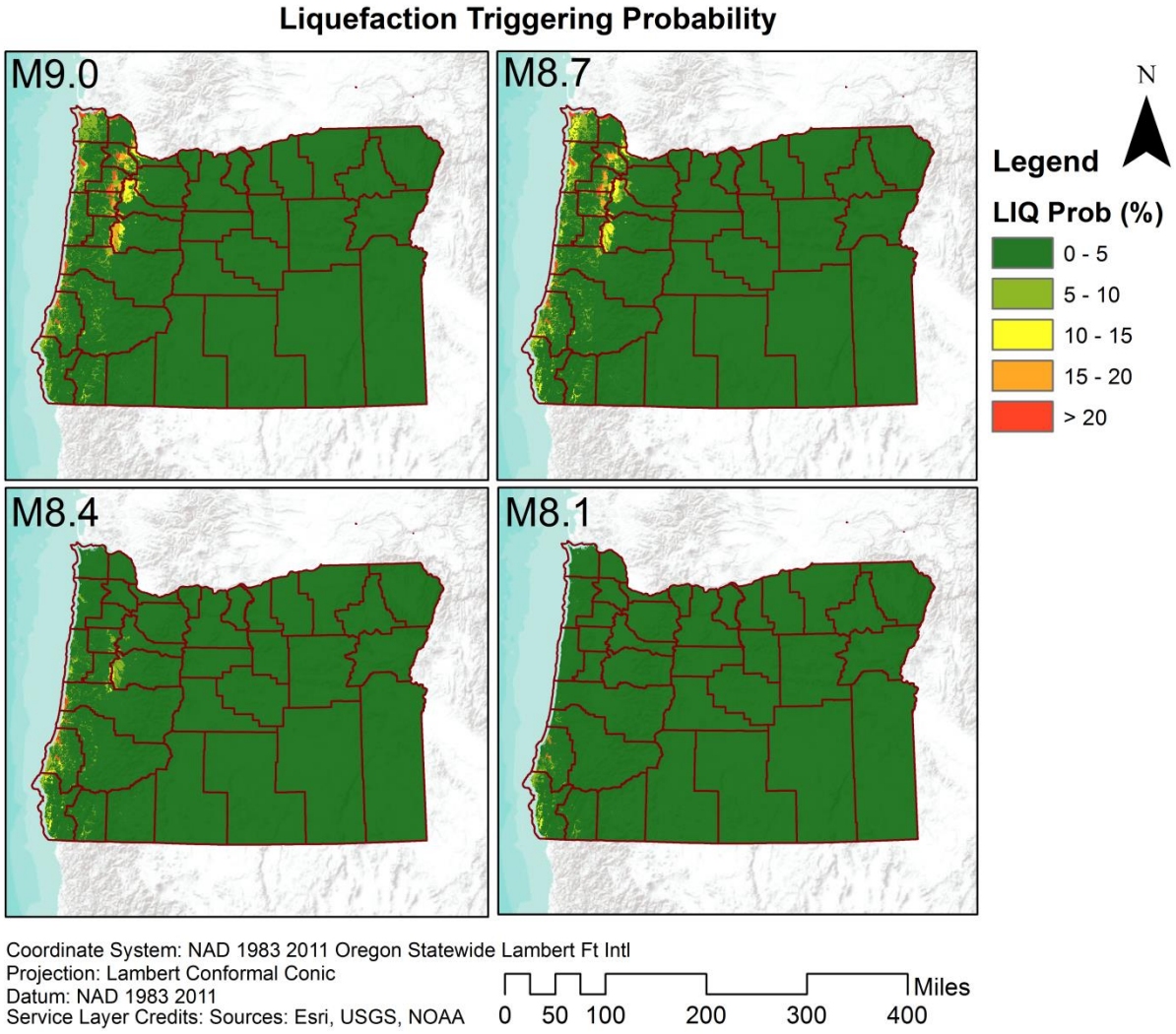

Figure 2-13: Liquefaction triggering corresponding to four deterministic scenarios of a CSZ earthquake.

2.6.4 Lateral spreading displacement

For estimating lateral spread displacements, HAZUS-MH recommends using the methodology in Joyner and Boore (1988) which combines the Liquefaction Severity Index (LSI), proposed in Youd and Perkins (1987), and a ground motion attenuation relationship developed by Sadigh et al. (1986). The following relationship is used to estimate the horizontal ground displacement (E[PGD_{SC}]), in inches, as a result of lateral spreading:

$$E\,[PGD_{SC}] = E[PGD|\left({}^{PGA}/_{PGA(t)}\right) = a] \times K_{\Delta} \quad (2\text{-}20)$$

where

$E[PGD|\left({}^{PGA}/_{PGA(t)}\right)$ is the expected permanent ground displacement for a given susceptibility group and a specific level of normalized ground shaking (PGA/PGA(t)) (see Figure 4.9 in HAZUS , earthquake technical manual, FEMA 2011). $PGA(t)$ is the ground acceleration threshold required to induce liquefaction per Table 2.12.

K_{Δ} is the correction factor for lateral spreading displacement for earthquakes other than a moment magnitude (M) of 7.5. After Seed & Idriss (1982), it is estimated as:

$$K_{\Delta} = 0.0086M^3 - 0.0914M^2 + 0.4698M - 0.9835 \quad (2\text{-}21)$$

Table 2.12: Ground acceleration required for inducing liquefaction with mentioned susceptibility category.

Susceptibility Category	Very High	High	Moderate	Low	Very Low	None
PGA(t)	0.09 g	0.12 g	0.15 g	0.21 g	0.26 g	N/A

Figure 2-14 presents estimates of lateral spreading displacement according to four different CSZ earthquake scenarios. Please note that a conversion from inches to centimeters has been made for these results.

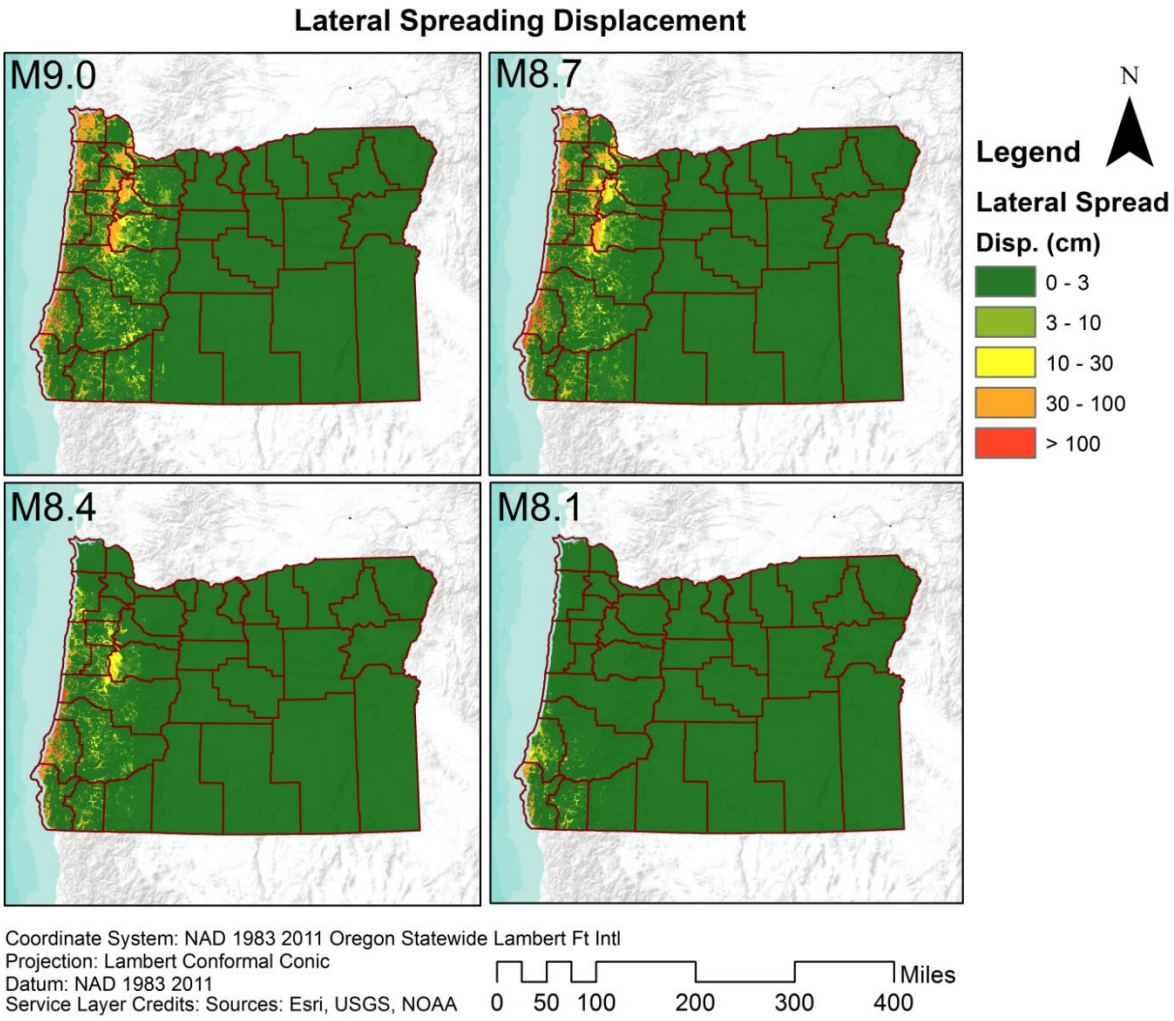

Figure 2-14: Lateral Spread displacement corresponding to deterministic scenarios of a CSZ earthquake.

2.6.5 Earthquake intensity

Wald et. al.,1999 proposed the following relationships for estimating an earthquake intensity value on the Modified Mercalli Intensity (MMI) scale using PGA at the soil surface (in cm/s^2).

$I_{mm} = 3.66\log(PGA) - 1.66$ for PGA > 70 cm/s^2 or $I_{mm} > V$,

$I_{mm} = 2.20\log(PGA) + 1.00$ for PGA i< 70 cm/s^2 or $I_{mm} > V$. (2-22)

Intensity values are rounded to the nearest integer and are commonly expressed as a Roman numeral. Figure 2-15 presents earthquake intensity maps for the four scenario events.

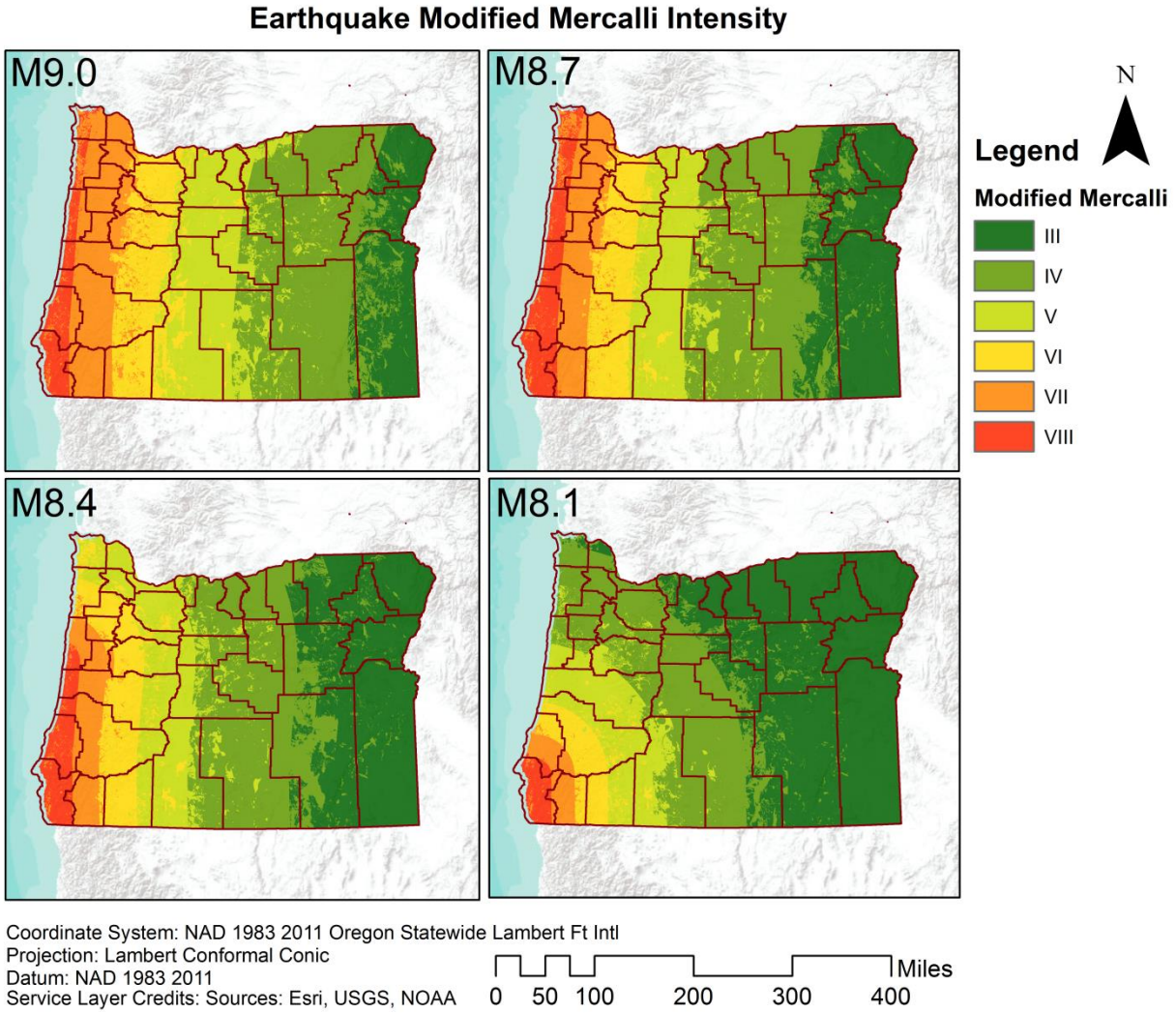

Figure 2-15: Earthquake Modified Mercalli intensity maps corresponding to deterministic scenarios of CSZ.

2.7 DISCUSSION

As can been seen in the output maps, the extent of the fault rupture and energy release of the event plays a critical role in the impending hazard associated with that modeled earthquake. In the case of a truncated fault rupture zone for southern Oregon (M8.1 scenario), PGA soil values as high as 0.40 g in PGA are expected within the southern Oregon Coast. These hazard maps also show a considerable amount of deformation from landslides along the southern Oregon Coast, whereas little to no effect from liquefaction is observed. Similarly, for a larger earthquake (M8.4), high PGA soil values extend along the coast from south to mid Oregon. As a result of this strong ground shaking, the hazard maps present some lateral spreading displacement in Oregon shores where the probability of liquefaction is much higher than the rest of the state. The landslide hazard maps follow the similar trends compared to those observed for PGA soil.

When directly comparing the M8.7 and M9.0 scenarios, higher PGA soil values are observed in the coastal regions. The reason behind this is that the energy from the fault rupture is dissipated along a much larger area (see Figure 2-1) in the M9.0 earthquake scenario resulting in a smaller PGA soil values and other ground motion parameter values for Oregon. Similar hazard maps from both landslide and liquefaction damages are observed for these four earthquake scenarios. Most of the coastal regions in Oregon are predicted to have high landslide triggering probability in both the M8.7 and M9.0 scenarios. Similarly, some of the Cascade Range Mountains are predicted to experience landslides. While the Cascade Range is mainly predicted to have moderate landslide displacement values (from

10 to 30 cm), most of coastal regions in landslide displacement hazard maps are covered with large displacement values higher than 1 meter. Liquefaction probability maps show significant liquefaction hazard in the northern Willamette valley (near I-5, Woodburn, Portland, Hillsboro). Moderate lateral spreading displacement is predicted to occur under these events within the Oregon coast and the Willamette Valley.

Since detailed site-specific data and methodologies were not applied to complement these maps, it is very important to be cautious when using these maps. These maps are important starting points to identify regional trends and approximate magnitudes of various hazards anticipated from a CSZ (or other) earthquake event for resilience planning or as a starting point for a site-specific engineering project.

2.8 DISTRIBUTION OF OUTPUTS

The resultant maps introduced in this report are primarily distributed in 2 different ways:

2.8.1 Streaming through OHELP website

These datasets are available for interactive viewing on the user friendly web-GIS entitled as the “Oregon Hazard Explorer for Lifelines Program (OHELP)”, which has been developed by the Cascadia Lifelines Program (CLIP) to assess earthquake hazards in Oregon (Gillins et al. 2015).

This website is intended to aid engineers to quickly acquire important seismic hazard data for their analyses. The website has a simple and powerful user interface, yet it does not require extensive knowledge of Geographic Information System (GIS) software. Within the

website, a tool is implemented to generate seismic hazard reports from the available published maps.

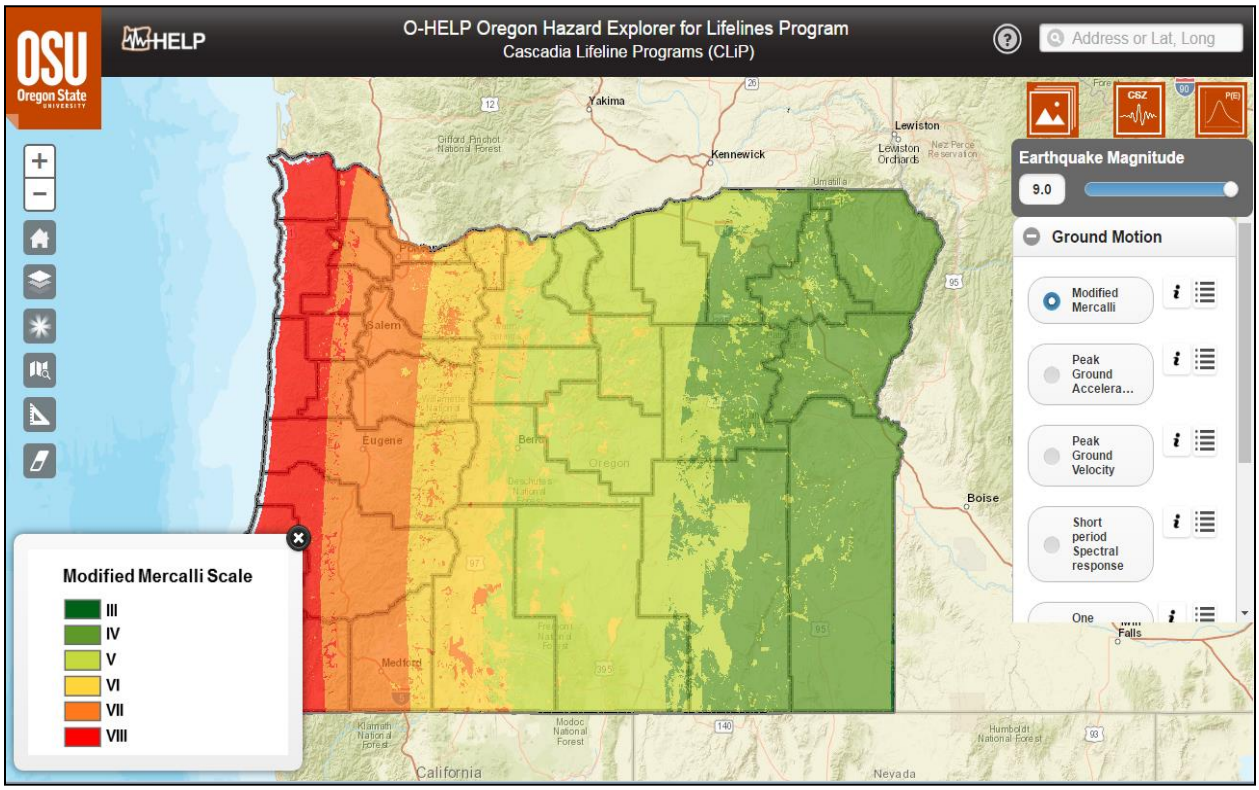

Figure 2-16: OHELP website in action showing Modified Mercalli map related to 9 moment magnitude CSZ earthquake.

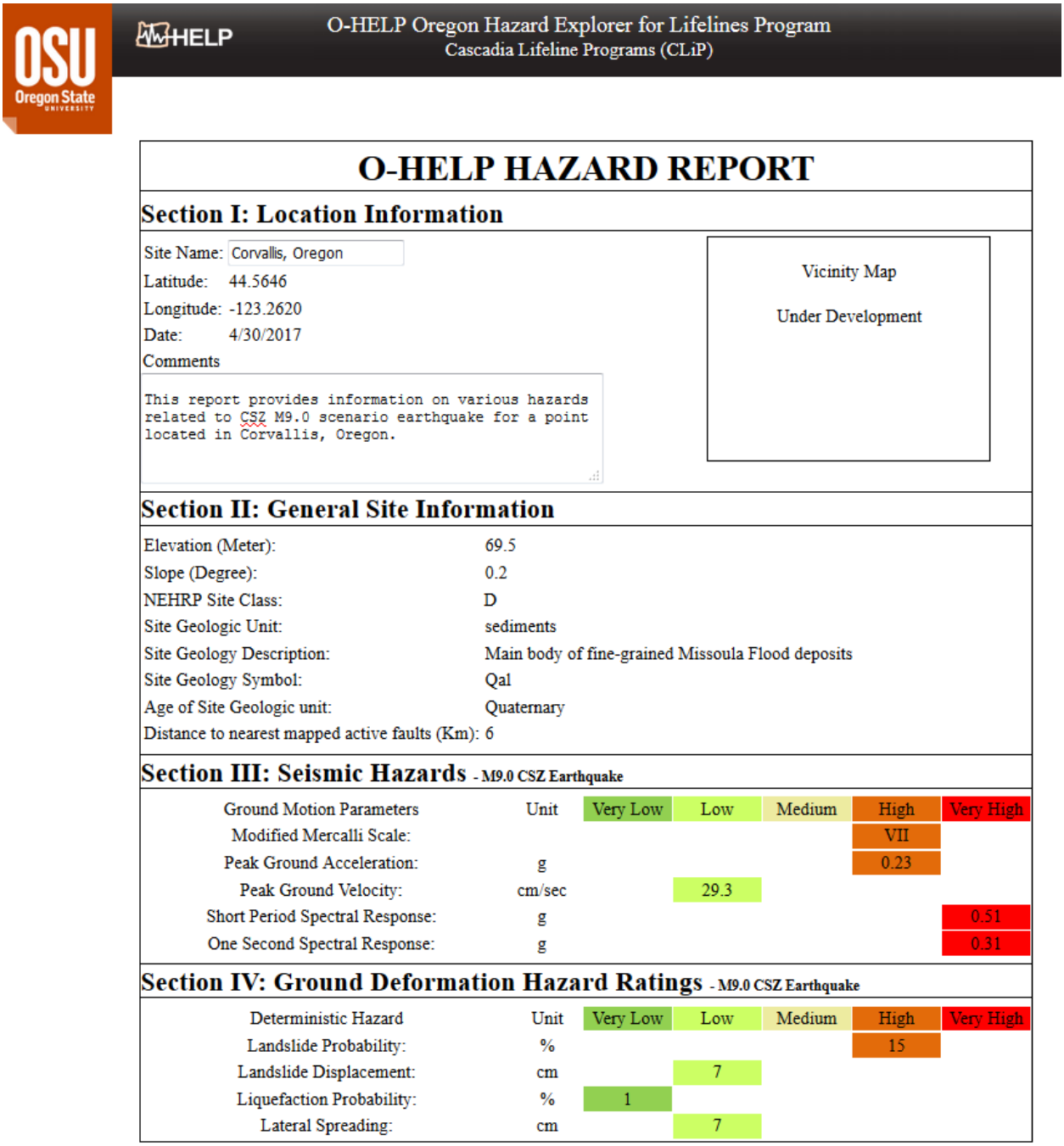

Figure 2-17: An example of OHELP Hazard report tool page.

2.8.2 Distribution through DOGAMI

All of the developed datasets and tools developed for this report are also available for distribution through DOGAMI's website in conjunction with this report.

2.9 CONCLUSION

This open file report was developed based upon previous efforts by DOGAMI to model hazards related to a M9.0 CSZ earthquake scenario event (Madin and Burns 2013). Re-projection, site amplification, and hazard map generation were performed by developing two separate yet consecutive modules. These modules output regional hazard data corresponding with a deterministic earthquake scenario from the CSZ.

In order to better delineate the hazards, a series of maps were developed given four scenario earthquake events (M9.0, 8.7, 8.4 and 8.1). Nevertheless, the methodology and supporting computer programs can be easily modified to consider other deterministic or pseudo-probabilistic scenarios in Oregon and other locales.

The maps provided in this report do not merely focus on considering the "big one." Instead, other smaller, yet more probable scenario events were considered in order to identify problematic regions for mitigation and recovery planning.

2.10 ACKNOWLEDGEMENT

The authors would like to thank Cascadia Lifeline Program (CLIP) for providing the funding and opportunity to explore this project. We thank members of the Oregon Resilience Plan

Cascadia Scenario workgroup for their assistance and input in the development of the scenario maps.

2.11 REFERENCES

Boore, D.M., and G.M. Atkinson. (2008). Ground-motion prediction equations for the average horizontal component of PGA, PGV, and 5%-damped PSA at spectral periods between 0.01 s and 10.0 s. Earthquake Spectra, Vol. 24, No. 1, 2008, pp. 99-138.

Building Seismic Safety Council (BSSC). (2000) Edition, NEHRP Recommended Provisions for Seismic Regulations for New Buildings and Other Structures, FEMA-368, Part1 (Provisions): developed for the Federal Emergency Management Agency, Washington, D.C, 2001.

Burns, W. J., Mickelson, K. A., Saint-Pierre, E. C. (2011), Statewide Landslide Information Database for Oregon, release 2 (SLIDO-2): Oregon Department of Geology and Mineral Industries.

Burns, W.J., R.J. Watzig, SLIDO-3.0, Statewide Landslide Information Database for Oregon (SLIDO), Release 3. http://www.oregongeology.org/sub/slido/data.htm#interim, Oregon Department of Geology and Mineral Industries. Portland, OR, 2014.

FEMA (Federal Emergency Management Administration). (2011), HAZUS®-MH 2.0, Multi-Hazard Loss Estimation Methodology, software and technical manual documentation. Web: http://www.fema.gov/plan/prevent/hazus; earthquake model technical manual: http://www.fema.gov/library/viewRecord.do?id=4713

Gillins, D. T., Olsen, M. J., Sharifi-Mood, M., Javadnejad, F., and Narayanan, R. (2015). "O-HELP: Oregon Hazard Explorer for Lifelines Program." Oregon State University, Corvallis, OR. http://ohelp.oregonstate.edu/.

Goldfinger, C., and others (2012), Turbidite event history— Methods and implications for Holocene paleoseismicity of the Cascadia subduction zone: U.S. Geological Survey, Professional Paper 1661–F, 170 p. Web: http:// pubs.usgs.gov/pp/pp1661f/

Holzer, T. L., Padovani, A. C., Bennett,M. J., Noce, T. E. and Tinsley J. C. (2005). Mapping NEHRP VS30 Site Classes. Earthquake Spectra: May 2005, Vol. 21, No. 2, pp. 353-370.

Joyner, W.B., and Boore D.M. (1988). Measurement, Characterization, and Prediction of Strong Ground Motion, Proceedings of Earthquake Engineering & Soil Dynamics II, pp.43- 102. Park City, Utah, 27 June 1988. New York: Geotechnical Division of the American Society of Civil Engineers.

Liao, S. S., Veneziano, D., & Whitman, R. V. (1988). Regression models for evaluating liquefaction probability. Journal of Geotechnical Engineering, 114(4), 389-411.

Ma, L., Madin, I. P., Olson, K. V., Watzig, R. J., Wells, R. E., Niem, A. R., and Priest G. R. (compilers), (2009), Oregon geologic data compilation (OGDC) release 5 (statewide): Oregon Department of Geology and Mineral Industries.

Mabey, M. A., Madin, I. P., Drescher, D. E., Uba, O. G., and Bosworth, M. (1993). Relative earthquake hazard map of the Portland 7-1/2-minute quadrangle, Oregon: Metropolitan Service District (Metro) and Oregon Department of Geology and Mineral Industries, Open-File Report O-93-14, 8 p., scale 1:24,000.

Madin, I., Burns, W. J. (2013). Ground Motion, Ground Deformation, Tsunami Inundation, Coseismic Subsidence, and Damage Potential Maps for the 2012 Oregon Resilience Plan for Cascadia Subduction Zone Earthquakes. Oregon Department of Geology and Mineral Industries, Open-File Report O-13-06.

Madin, I. P., and Wang, Z. (1999a). Relative earthquake hazard maps for selected urban areas in western Oregon, Canby-Barlow-Aurora, Lebanon, Silverton-Mt. Angel, Stayton-Sublimity-Aumsville, Sweet Home, Woodburn-Hubbard: Oregon Department of Geology and Mineral Industries, Interpretive Map Series IMS-8, 22 p., scale 1:24,000, GIS files.

Madin, I. P., and Wang, Z. (1999b). Relative earthquake hazard maps for selected urban areas in western Oregon: Dallas, Hood River, McMinnville-Dayton-Lafayette, Monmouth-Independence, Newburg-Dundee, Sandy, Sheridan-Willamina, St. Helens-Columbia City-Scappoose: Oregon Department of Geology and Mineral Industries, Interpretive Map IMS-7, 24 p., scale 1:24,000, GIS files.

Madin, I. P., and Wang, Z. (1999c). Relative earthquake hazard maps for selected urban areas in western Oregon: Ashland, Cottage Grove, Grants Pass, Roseburg, Sutherlin-Oakland: Oregon Department of Geology and Mineral Industries, Interpretive Map IMS-9, 21 p., scale 1:24,000, GIS files.

National Research Council (1985). Liquefaction of Soils During Earthquakes, Committee on Earthquake Engineering, Commission on Engineering and Technical Systems, National Academy Press, Washington, DC.

Newmark, N. M., and Hall W. J. (1982). Earthquake spectra and design, Engineering Monographs on Earthquake Criteria, Structural Design, and Strong Motion Records, Vol. 3: Berkeley, Calif., University of California, Earthquake Engineering Research Institute, 103 p.

Oregon Seismic Safety Policy Advisory Commission (OSSPAC) (2013). The Oregon Resilience Plan: Reducing Risk and Improving Recovery for the Next Cascadia Earthquake and Tsunami. Web: http://www.oregon.gov/OMD/OEM/osspac/docs/Oregon_Resilience_Plan_draft_Executive_Summary.pdf ,.

Power, M. S., Dawson, A. W., Streiff, D. W., Perman, R. C., & Haley, S. C. (1982). Evaluation of liquefaction susceptibility in the San Diego, California, urban area. In Proceedings 3rd International Conference on Microzonation, II(pp. 957-968).

Priest, G. R., and others (2013). DOGAMI Open-File Report O-13-19 Tsunami Inundation Scenarios for Oregon. Oregon Department of Geology and Mineral Industries, Portland, OR.

Sadigh, K., Egan, J. A., and Youngs, R. R. (1986). "Specification of Ground Motion for Seismic Design of Long Period Structures", Earthquake Notes, vol. 57, no. 1, p. 13, relationships are tabulated in Joyner and Boore (1988) and Youngs and others (1987).

Seed, H. B., and Idriss, I. M. (1982). Ground motions and soil liquefaction during earthquakes (Vol. 5). Earthquake Engineering Research Institute.

Seed, H. B., Tokimatsu, K., Harder, L. F., & Chung, R. M. (1985). Influence of SPT procedures in soil liquefaction resistance evaluations. Journal of Geotechnical Engineering, 111(12), 1425-1445.

USGS, (2016). Advanced National Seismic System (ANSS), ShakeMap, Global Region, Maps of ground shaking and intensity for event casc9.0_expanded_peak_se, Cascadia M9.0 Scenario (peak value). Edition: Map V4, Code V3.5, http://earthquake.usgs.gov/earthquakes/shakemap/global/shake/casc9.0_expanded_peak_se/ .

Wald, D. J., Quitorano, V., Heaton, T., and Kanamori, H. (1999). Relationships between peak ground acceleration, peak ground velocity, and modified Mercalli intensity in California. Earthquake Spectra, Vol. 15(3, pp. 557-564. Aug.).

Wald, D. J., Worden, B. C., Quitoriano, V., & Pankow, K. L. (2005). ShakeMap manual: technical manual, user's guide, and software guide (No. 12-A1).

Wang, Z., and Wang, Y. (2000), Relative earthquake hazard maps of ground motion amplification, liquefaction and slope instability for Klamath County, Oregon: Oregon Department of Geology and Mineral Industries, Interpretive Map Series IMS-20, 28 p, scales 1:500,000, 1:1,000,000.

Wilson, R. C., and Keefer, D. K. (1985). Predicting areal limits of earthquake-induced landsliding. Evaluating earthquake, 76.

Youd, T. L., and Perkins, D. M. (1978), Mapping liquefaction-induced ground failure potential: Journal of Geotechnical Engineering Division, v. 104, no. 4, 433-446.

Manuscript # 2

Performance-Based, Seismically-induced Landslide Hazard Mapping of Western Oregon

Mahyar Sharifi-Mood, Michael J. Olsen, Daniel T. Gillins and Rubini Mahalingam

Submitted to: Soil Dynamics and Earthquake Engineering journal, Elsevier

3 PERFORMANCE-BASED, SEISMICALLY-INDUCED LANDSLIDE HAZARD MAPPING OF WESTERN OREGON

3.1 ABSTRACT

Seismically-induced landslides can be detrimental to urban communities, often resulting in significant damage and repair costs, blockage of lifeline connection routes and utilities, environmental impacts, and potential for loss of life. Consistent, reliable hazard maps can assist agencies to efficiently allocate limited resources to prepare for these events. This paper presents methodology for evaluating and mapping seismically-induced landslide hazards across a large area utilizing performance-based design strategies. This approach scales site-specific seismic hazard curve analysis techniques to a regional scale evaluation by combining generally available data, including: previous landslide inventories, lidar and photogrammetric topographic data, geologic mapping, NEHRP site classifications based on shear wave velocity (Vs_{30}) measurements, and seismic hazard curves for the analysis. These maps can be combined with maps generated for other hazards (e.g., liquefaction) for a fully probabilistic, multi-hazard evaluation and risk assessment. To demonstrate the methodology, a series of landslide hazard maps showing the probabilities of exceeding different thresholds of movement (e.g., 0.1, 0.3, and 1.0 m) were generated for western Oregon. The study area contains weak, wet soils that experience land sliding regularly even without significant seismic activity. The maps show reasonable agreement with landslide inventory and susceptibility maps.

3.2 INTRODUCTION

Natural hazards such as landslides can result in significant material damage, economic loss, and loss of life. Landslides are mainly characterized by the movement of earth materials such as rocks, deposited soils, and manmade fills with downhill and outward failure directions (Schuster and Krizek, 1978; Varnes, 1978). Landslides can be triggered from seismic, climatic or lithospheric stress fields on slopes (Clague and Stead, 2012). Topographic (e.g., slope angle and geometry), hydrologic (e.g., groundwater level, rainfall, water flow), and geologic (e.g., lithology, age, structure, seismicity) conditions are common variables correlated with landslide occurrence (Sarkar and Kanungo, 2004; Turner and Schuster, 1996). However, an improved knowledge in the mechanism of landslide failure and the role of these contributing factors are necessary in order to determine locations likely to fail.

Generally, landslides are widespread in regions with steep slopes where the soil is weak, weathered, and near saturated due to heavy rainfall, and/or the groundwater table is relatively high. Furthermore, landslides can be generated as a result of seismic activities (Keefer, 1984; Keefer 1999). Keefer in 2002 suggested that many medium to large landslides are the result of either long-term rainfall buildup or seismic impacts. Anthropogenic terrain modifications such as cut slopes, fills, excavations, tree harvesting, and other loading also contribute to landslide triggering. For example, Xinpo and Siming (2009) discuss various types of landslides that occurred adjacent to highways after the Sichuan earthquake in 2008. They also note that a substantial portion of damages and

injuries from an earthquake are instigated by seismically-induced landslides. Espinosa et al., (1987) studied effects of landslides on lifeline routes after earthquakes including property loss, damaged utility services, delayed recovery, and structural failures.

Studying the influence of contributing factors such as slope, geology, source parameters and seismic hazard curve patterns is a first step to prepare for seismically-induced landslide hazards. Because landslides disrupt the earth's surface, detection of prone regions is enhanced through remote sensing, geospatial analysis, and mapping techniques. These data can be utilized to develop landslide inventories and identify vulnerable infrastructure to prepare for future events (Harp et al., 2011).

Oregon, in particular, is exceedingly prone to landslides due to its wet climate. Landslides in Oregon are estimated to cause $10 million in damages annually (Wang et al., 2002) and they are a challenge for infrastructure such as highways. For example, the coastal mountain range in western Oregon runs near the Pacific Ocean and contains U.S. route 101, which is the only viable road linking seaside communities to each other. During heavy rainfall, various sections of this route are subject to closure when landslides occur, leading to significant traffic delays and safety concerns. Other portions of the highway require frequent maintenance from damages from currently active landslides that are accelerated by wave erosion at the toe of the slopes (Schulz and Galloway, 2012). In addition, there are only a few routes connecting these coastal communities to more populated regions of the Willamette Valley (OSSPAC, 2013). All of these traverse through the steep, landslide prone terrain of the coast range. Hence, landslides occurring on these routes are expected to

result in significant economic and social impacts to rescue and recovery efforts during other hazards such as strong ground motion and shaking; soil liquefaction, settlement, and lateral spreading; tsunamis; and high intensity coastal storms.

Because of these aforementioned concerns, substantial landslide hazard mapping efforts have been completed in Oregon by the Department Of Geology And Mineral Industry, DOGAMI (Wang et al., 2002; Harvey and Peterson, 1998; Waters, 1973). The Statewide Landslide Information Database of Oregon (SLIDO – 3.2) (Burns and Watzig, 2014) represented in Figure 3-1 is an accumulation of reported landslides in Oregon and the result of detailed mapping with lidar technology. This database contains historical precipitation-induced landslide events represented as a point feature class as well as mapped landslide deposits and scarp flanks represented as polygons. DOGAMI frequently updates this database utilizing lidar technology (Burns and Madin, 2009), which improves the detection of landslides below the dense forests. Although these efforts have only captured a small portion of the study area; they have shown that significantly many more landslides exist than could be mapped with conventional techniques due to heavy vegetation cover. Hence, despite the fact that Figure 3-1 shows the lidar data availability in a large portion of the study area, only a few small sections and quadrangles (see SLIDO 3.2) have been analyzed by DOGAMI to produce more-detailed landslide inventory maps. As a result, it is likely that many landslides have not yet been inventoried than are included in the database.

Lin et al., 2008 shows that landslide distribution varies with respect to their triggering mechanism; however, recent studies (O'Banion and Olsen, 2014; Schulz and Galloway, 2012) indicate that there is strong likelihood that some of the landslides that have been mapped in Oregon were seismically induced. In many cases, it is unclear whether these landslides have seismic or precipitation origins because of the relative infrequency of significant earthquakes in recent centuries.

3.2.1 Objectives

To this end, the primary goal of this study is to develop a mapping methodology to quantify the likelihood of seismically-induced landslide occurrence as well as the probability of exceeding certain thresholds of ground displacement considering a wide range of potential earthquake events. While previous work takes significant steps towards the improvement of landslide mapping, the available methods do not achieve all of the objectives desired for this study to produce a methodology, which is:

- **Fully Probabilistic:** The method accounts for major uncertainty sources in the strong ground motion, local topography, and soil strength
- **Consistent:** The method can be implemented throughout other regions and across a wide range of scales without requiring significant modification. Results from one area should be able to be directly compared with results of a second location.
- **Simplistic:** The method should be based on readily available data while being interactive and user-friendly.

- **Extensive:** The approach can be applied across a large area without problems. Hence, it cannot be reliant on detailed time histories for site response characteristics.
- **Reliable:** The method can be verified by an existing landslide database.
- **Cost-efficient:** It does not rely on limited, expensive data like boreholes and in-situ or laboratory testing of soils, which are not available for an entire region.
- **Compatible:** This method can be integrated with other datasets and analysis (e.g., lateral spreading, flooding and settlement) for a complete hazard analysis.
- **Expandable:** The living maps can easily be updated when new information and data are available.

This methodology was tested for western Oregon (Figure 3-1). Mapping landslide hazards for such a large area is challenging because detailed, site-specific data are not available for the entire region.

3.3 EARTHQUAKE INDUCED DISPLACEMENT TECHNIQUES

Landslide displacements provide a better indicator of failure and damage potential than landslide triggering because the amount of deformation controls the serviceability of a slope and adjacent infrastructure after an earthquake (Kramer, 1996). Newmark, 1965 proposed a simple analysis procedure to model a landslide as a rigid block accelerated from equilibrium by an unbalanced force from the seismic loading. Any earthquake excitation exceeding a critical acceleration will overcome frictional resistance (i.e., shear strength) and initiate sliding of the block. Through two consecutive integrations on the

acceleration time-history (using area above the critical values), permanent displacements can be estimated (Wilson and Keefer, 1983).

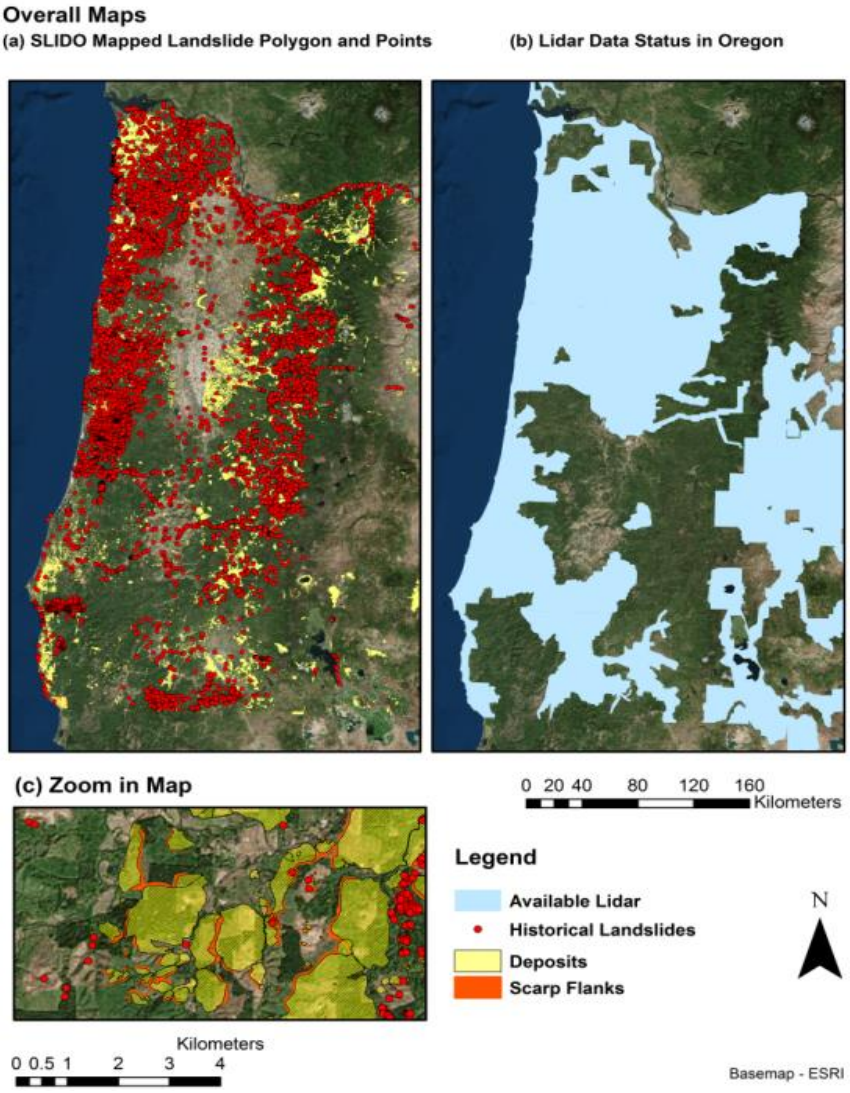

Figure 3-1: (a) Historical landslide database (SLIDO) including landslide deposits and scarp flanks provided by DOGAMI, (b) lidar data availability in western Oregon, (c) a detailed view of map (a) at a site in the city of Portland representing the detailed deposits and scarp flanks along with historical landslides in the SLIDO database.

Additional work has been performed to create new seismic slope displacement models such as the simplified rigid-block, decoupled and coupled methods, and other complicated models. For example, Saygili and Rathje, 2008, Jibson, 2007 and Miles and Ho, 1999 empirically assessed the likelihood of a seismically induced landslide based on this method. These relationships are typically multivariate regression equations of parameters calibrated to case history data including:

- Peak Ground Acceleration (PGA), the largest absolute acceleration measured in a strong ground motion,
- Peak Ground Velocity (PGV), the largest velocity measured in an earthquake,
- Spectral Acceleration (Sa), the acceleration measured on an object with given period,
- Equivalent number of cycles (Neq), number of cycles of ground shaking estimated from an earthquake scenario,
- RMS acceleration, defined as the effective acceleration over a given time,
- Yield acceleration (ay), defined as the minimum acceleration that puts the slope on the verge of failure,
- Earthquake magnitude (M), the maximum trace amplitude, which can be recorded on various seismometers,
- Arias intensity (Ia), a parameter representing all amplitude, frequency content and duration characteristics of a ground motion, and
- Predominant Period of sliding mass (T), the period associated with the highest Fourier amplitude spectrum.

These regression equations all have a probabilistic form to calculate the likelihood of exceeding a threshold displacement. Table 3.1 summarizes some of the available empirical seismic displacement methods and their necessary input parameters.

Strenk and Wartman, 2011 evaluated 16 techniques and have shown that these models performed similar to Newmark's method when compared to new case histories. It should be noted that in some cases, Newmark's model would underestimate the actual displacement; as strain increases with the displacement, undrained shear strength will drop to lower amounts in slightly sensitive materials resulting in a reduced critical acceleration (Cornforth, 2005). With any technique applied to regional mapping, it is important to realize that various types of landslides and triggering mechanisms will occur. Further, high quality datasets of soil properties are often unavailable at a regional scale. Hence, a generalized method is preferred to one that requires several parameters because detailed information is typically not available for a large region similar in size to the one studied in this paper.

Table 3.1: Example empirical predictive models for earthquake-induced sliding displacements of slopes and associated input parameters.

Method	Year	a_y	a_{max} (PGA)	I_a	M	T	Sa	N_{eq}	PGV
Makdisi & Seed	1977	●	●		●	●			
Ambraseys & Menu	1988	●	●						
Yegian et al.	1991	●	●			●		●	
Jibson	1994	●		●					
Jibson (Scalar)	2007	●	●						
Jibson (Vector)	2007	●	●	●	●				
Bray & Travasarou	2007	●	●		●	●	●		
Saygili & Rathje (Scalar)	2008	●	●						
Saygili & Rathje (Vector)	2008	●	●	●		●			●
Rathje & Saygili (1)	2011	●	●						●
Rathje & Saygili (2)	2011	●	●		●				

3.3.1 Performance based landslide displacement analysis

The performance-based framework is defined by a component associated with an engineering demand parameter to show how likely that parameter would be exceeded (Deierlein et al., 2003; Krawinkler, 2002; Cornell and Krawinkler, 2000). This approach was developed by Pacific Earthquake Engineering Research Center (PEER) to improve hazard and risk analyses. The performance-based seismic hazard analysis incorporates all known and plausible earthquake scenarios. Within a particular site, it assesses the hazard (e.g., landslide displacement) associated with the ground motion available from all seismic sources. Previously, Franke and Kramer, 2013 used a similar framework as part of seismic liquefaction hazard analysis to assess lateral spreading displacements. To develop a landslide displacement hazard curve, the mean annual rate of displacement exceedance is plotted against various displacement thresholds, similar to those developed for lateral spreading.

3.4 OVERVIEW OF AVAILABLE LANDSLIDE MAPPING METHODS

Various types of landslide mapping techniques are available to qualitatively or quantitatively investigate this threat across a regional scale, including:

- Inventory mapping - the documentation and reporting the locations of historical landslides without any analytical interpretation,
- Susceptibility mapping – quantifying the existing physical situation of the soil and site (e.g., slope and shear strength) in which slopes are likely to experience a landslide independent from a triggering effect,

- Potential mapping – the likelihood of external impacts and triggering sources (e.g., seismic activities and excessive rainfall) combined with susceptibility analyses to predict potential deformation or damage.

Further, potential maps can be generated utilizing either deterministic or probabilistic approaches.

3.4.1 Deterministic Mapping

Deterministic mapping can result in reliable results when provided with comprehensive datasets with detailed input information, such as hydrological and slope stability models. A combination of surface geology with slope gradient is used in most landslide mapping analyses to determine the appropriate hazard level. Deterministic models involve modification and updating input parameters. While slope values for a large study area can be processed from a Digital Elevation Model (DEM), it is unlikely to acquire detailed soil profiles and geotechnical properties at a very large regional scale. For regional mapping, numerous literatures such as Densham, 1991 as well as Stuart and Stocks, 1993 indicate that one can depict the pore pressure threshold by combining the simulation of time and variance in pore pressure with the slope stability model. In regional mapping, effects of weathering are difficult to model because such modeling requires detailed subsurface data which is not available across a wide region (Xie et al., 2004). Information at each point, such as the presence of pore water pressure, failure surface depth, strength parameters and limiting equilibrium slope stability information are essential for a deterministic analysis yet are difficult to obtain for large areas, leading to lower credibility in spatial variability. Hence, a deterministic model, which is fully physically based, is more suitable

for mapping of localized areas when potential failure depth, depth to ground water, and material strengths are well characterized.

As an example, Khazai and Sitar, 2000a integrated three factors to analyze seismic slope stability in a GIS environment: (1) the concentration of shaking at the site from attenuation relationships; (2) yield strength of the slope through traditional slope stability analyses by pseudo-static approach; and (3) deformation calculated from Newmark`s displacement method (Newmark, 1965).

Jibson, 1993 suggests that on a regional basis, Newmark`s method could be effectively applied in order to capture permanent ground deformation by either performing two sequential integrations of the area under the accelerogram record and the block`s velocity time period that exceeds the critical acceleration and velocity values respectively, or by deriving a regression equation from the ground motion to determine displacement. A possible downside to the second approach is that displacement at a particular location may not be calculated accurately with a mean displacement curve, and furthermore, local site responses are not accounted in analyses (Khazai and Sitar, 2000b).

Khazai and Sitar, 2000b created a program that enables a user to interact, modify and update inputs like slope map and estimated site response in order to produce a seismically-induced landslide susceptibility map for an area. The landslide inventory map, soil map and topography were analyzed within a pseudo-static analysis approach in combination with Newmark`s displacement model.

A somewhat different approach than the previous physical based modeling, Lee et al., 2008 introduced a Landslide Susceptibility Index (LSI) for each pixel using a summation of factors weighted linearly. In this study, which was done in Taiwan, an event-based landslide inventory map was created in addition to triggering elements. Correlation of the factors in regions susceptible and unsusceptible to landslides was calculated by statistical testing and evaluation of weights using discriminant analysis.

3.4.2 Probabilistic Mapping

Deterministic methodologies are the most common in hazard mapping; however, in order to incorporate the uncertainty associated with geotechnical, geological and geomorphological data, spatial analyses and advanced procedures are being developed in a form of probabilistic mapping. Rathje et al., 2014 compared both deterministic and probabilistic approaches in landslide hazard analysis, and found that the deterministic approach resulted in excessive underestimation of landslide displacement due to disregarding the aleatory variabilities in the movement mechanism of the sliding mass. Van Westen et al., 2006 defined hazard as the probability of occurrence within a time period, which is a function of both spatial likelihood and temporal probability influenced by static environmental factors like slope angle and dynamic factors such as rain input, drainage or ground shaking. Probabilistic models take numerous variables such as acceleration, strength parameters, pore pressure, distance and magnitude as random variables (Khazai and Sitar, 2000a). Geologic maps can be updated by geotechnical parameters gathered from laboratory tests (Refice and Capolongo, 2002). By determining the impact of ground motion parameters in slope failure along with the slope displacement corresponding to

existing geometrical and seismic properties, one could develop a probabilistic model (Bray and Travasarou, 2007).

Using datasets from the 1994 Northridge earthquake in a regional analysis, Harp and Jibson, 1996 produced an earthquake triggering landslide hazard map for Northern San Fernando Valley and Santa Susana Mountains. Jibson et al., 2000 used 200 strong motion records across the region, DEMs, geologic maps and engineering properties of geologic units to analyze seismically-triggered landslides. They introduced a dynamic model based on Newmark`s deformation analysis to calculate the landslide displacement at each pixel. Refice and Capolongo, 2002 introduced a simplified Newmark`s slope stability model on pixel by pixel basis. They used a Monte Carlo technique to simulate necessary samples from probability density function in all stages of the work. They developed a series of functions in Matlab to read the raster matrices and tabulated numerical values containing the statistical parameters of involved variables. The combination of the latter with the Monte Carlo simulation and Newmark`s equation generated the probabilistic map. The output was quite valuable in areas with common seismic activity.

A fully probabilistic landslide hazard analysis was first proposed by Del Gaudio et al., 2003 including the full seismic hazard curve. Saygili and Rathje, 2009 used a similar approach to the presented approach to identify regions with high seismically-induced landslide hazard. However, their approach ultimately only considers the threshold scenarios of 2% in 50 years and 10% in 50 years rather than a full performance-based design approach as completed in this study.

3.5 STUDY AREA

Western Oregon contains weak soils that experience heavy rainfall, resulting in high landslide susceptibility (e.g., Figure 3-1). For example, a large storm event in February 1996 individually led to $4 million in damages to the Portland urban area (Burns et al., 1998a, Burns et al., 1998b).

Oregon also experiences high seismicity. For example, the Scott Mills earthquake in 1993 (M 5.6), a shallow, crustal earthquake, resulted in $30 million in damages (Wong et al., 2001). However, the most severe earthquake hazard threatening Oregon is the Cascadia subduction zone (James et al., 2000). The most recent devastating earthquake occurred on January 26, 1700, with an estimated moment magnitude of 9.0. It has been estimated that there is a 40% chance of occurrence of such an earthquake within the next 50 years (Nelson et al., 2012). The Cascadia subduction zone is capable of producing great earthquakes which would likely produce large inertial loads that would trigger new landslides or reactivate existing landslides.

Figure 3-2 displays the study area that is bounded by the northern and southern borders of the state. Tectonic plates and volcanic activities formed many of the features across the landscape. As a result, the western section receives significantly more rainfall compared to the eastern section, consisting of high desert country that is predominately plutonic rocks. In between the coast range (sedimentary rock) and Cascades (volcanic rock), lies the Willamette Valley, which consists of alluvium with sedimentary or surficial soil deposits. The Tyee formation spans much of the coast range, which consists of very weak

sedimentary materials with interbedding of slick clay and silt seams between sandstone layers. Landslides are common in this formation.

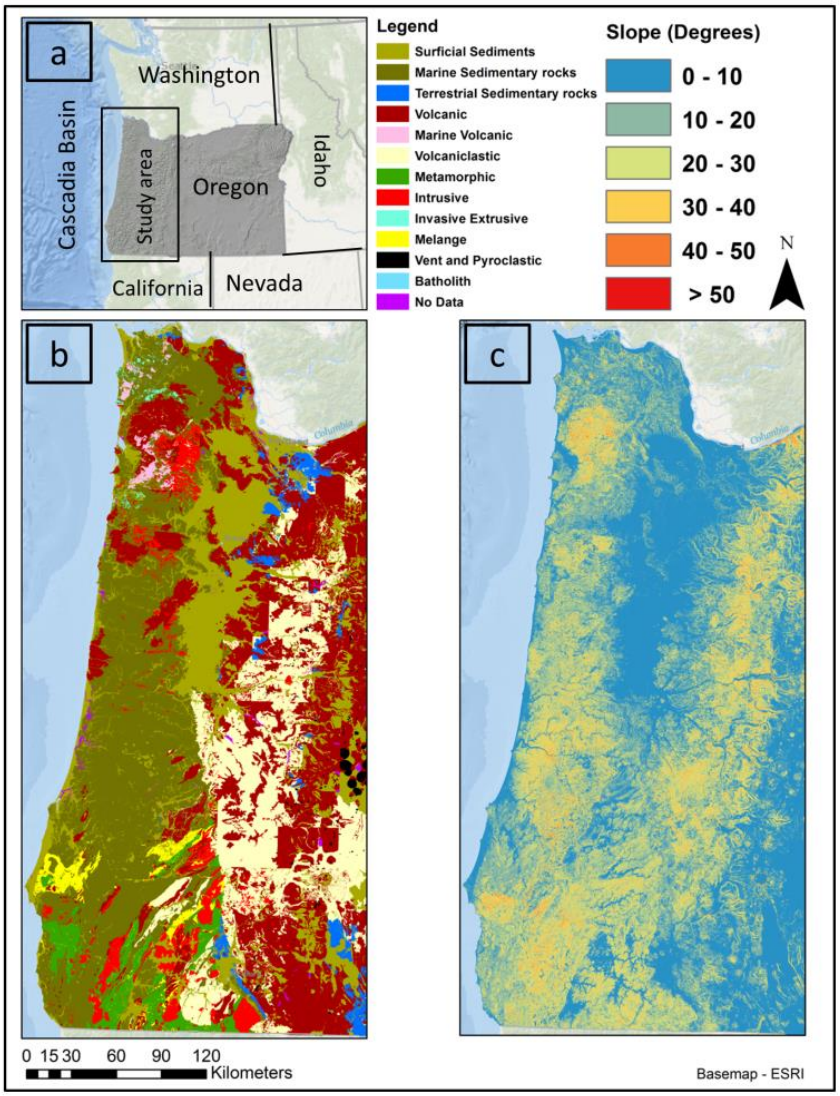

Figure 3-2: a) Extents of western Oregon selected as the study area, b) Geology map within the ranges of western Oregon, c) slope map from a hybrid DEM in the region.

3.6 DATA SOURCES

In landslide studies, there are several geospatial, geological, and geotechnical data sources which can be considered to determine hazard levels, including: topographic information (e.g., slope angle), ground water levels, soil properties, intensity, and probability of triggering sources such as earthquakes and rainfall (Soeters and van Westen, 1996).

For this project, slope gradient, generalized geology information, and site classification data were used along with the PGA de-aggregated hazard curves as a triggering event. These necessary datasets were acquired from numerous sources, which are summarized in Table 3.2.

Table 3.2: Datasets used for the landslide analysis and their source, provider and resolution.

Dataset	Source	Provider	Native Resolution	Computation Resolution
Hybrid Slope	[a]National Elevation Dataset [b]lidar DEM	[a]USGS [b]DOGAMI	[a]26.7 (m) [b]1 (m)	30 (m)
SLIDO-V3	Burns and Madin (2009), Special Paper 42	DOGAMI	N/A	N/A
PGA Exceedance probabilities	Seismic Hazard Curves Data	USGS NSHMP 2008	0.05 (deg) (i.e., 5.5 km in latitude and 4.0 km in longitude)	Bilinear Interpolation
NEHRP Site Class	The Oregon resilience plan	DOGAMI	Polygons 1:20,000	100 (m)
Geology	Ma et al., 2009 OGDC v 5.0	DOGAMI	Polygons 1:20,000	100 (m)

These datasets include:

- A DEM derived from aerial lidar data, available from the Oregon lidar consortium (see Figure 3-1)

- (DOGAMI, 2012), and the USGS National Elevation Dataset (NED), (USGS, 2006), for the remainder of the study area. The original resolution for lidar DEMs was 0.91 m which was then resampled to 26.7 m to match the USGS NED DEM. Slope values were then derived for each pixel from the DEM using a slightly larger 30 m pixel size.

- Historical landslide deposits and scarps in the Statewide Landslide inventory Database of Oregon (SLIDO-3) (Burns and Watzig, 2014) (previous versions: Burns and Madin, 2011; Burns et al., 2011) contain approximately 22,500 landslide polygons (Figure 3-1).

- While the database also includes many points digitizing the landslides from rain-fall events, this study only uses the polygons of landslide deposits and scarps describing the location of landslides, some of which were likely initiated by seismic effects.

- Grids of USGS NSHMP (2008) seismic hazard curves (Petersen et al., 2008, USGS, 2008) that include the mean annual rate of exceedance (λ) versus peak ground acceleration (PGA). The USGS provides the hazard curve values for various Vs_{30} measurements (180, 259, 360, 537 and 1150 m/s) based on NEHRP site classifications at 0.05 degree increments throughout the entire study area. An example of these curves at a grid point is shown in Figure 3-3. C++ code was developed to convert the available gridded text file to a GIS floating point grid format and separate various PGA intervals within the study area for efficient computation. During the probabilistic landslide analysis, bilinear interpolation was used to obtain finer cell increments.

- NEHRP site classification, which is based on the soil shear wave velocity in the upper 30 m (Vs_{30}) and average properties of soil in the upper 30 m, provided by the Oregon Resilience Plan (OSSPAC, 2013).

- Geologic mapping from the Oregon Geologic Data Compilation (OGDC v 5.0), (Ma et al., 2009), which provides the most current geologic and lithological mapping available in the study area.

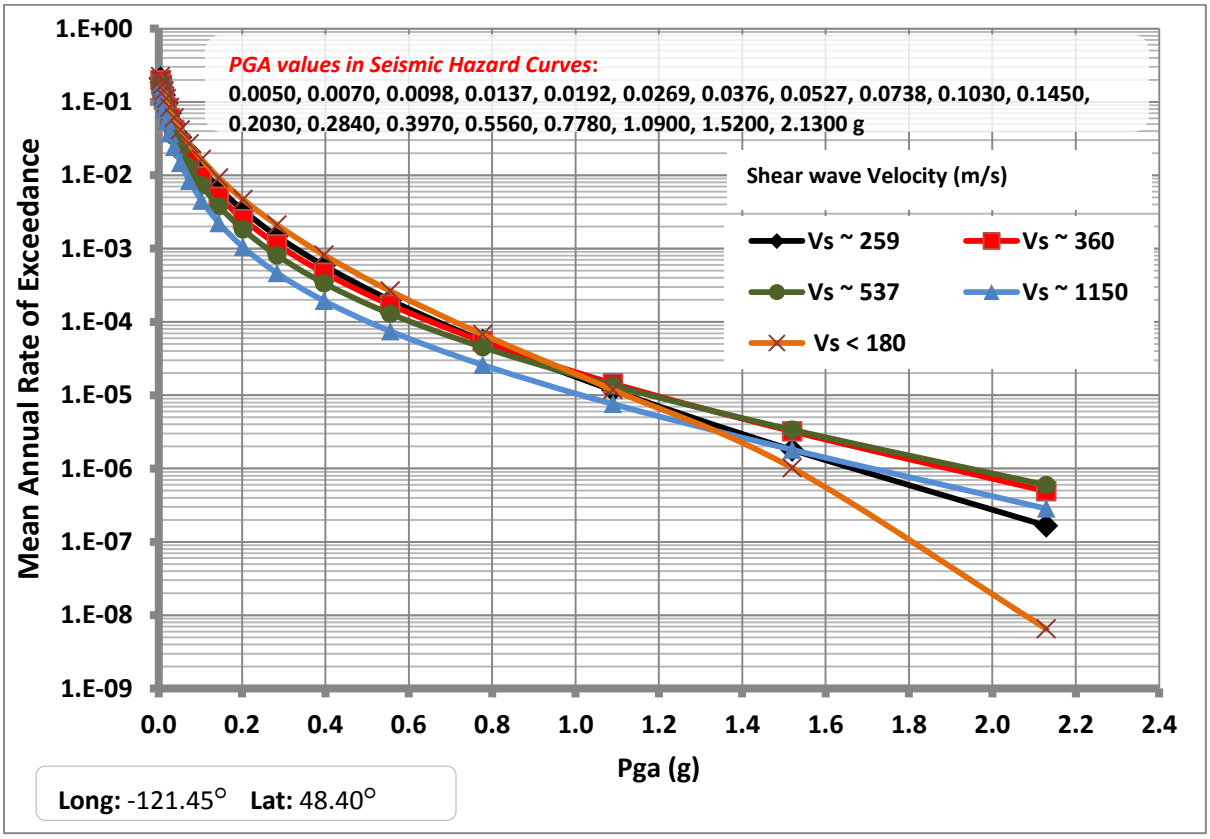

Figure 3-3: Example of seismic hazard curve at a specific location within the study area. Various curves present the hazard curves related to different site classes. The site class for this pixel is E, with shear wave velocity less than 180 m/s.

Both the NEHRP site classification and geology datasets were polygon vector feature classes mapped at a scale of 1:20,000. For efficient computation, they were converted into a grid format (with 100 m pixel size) at the expense of requiring additional disk storage space.

In regional analysis where the target is to map landslide hazard for an area as large as a state, it is unlikely to have access to detailed subsurface investigations and laboratory testing results to provide geotechnical properties such as soil strength to adequately characterize each geologic unit. There can also be a significant amount of spatial variability. In such analyses, it is important to distinguish the difference among geographical, topographical and geological features, which may correlate with soil strength (Sharifi-Mood et al. 2013). To this end, various approaches for regional geotechnical analysis were reviewed in the literature. However, in many cases, these values are simply estimated or applied using engineering judgement. Wang and Rathje, 2015 used a logic tree approach to pre-estimate the friction angle and cohesion factor in general geologic units to help account for this uncertainty; however, only three values are considered.

Expanding on the effort of Wang and Rathje, 2015, the presented approach develops cumulative distributions for each major geologic unit to serve as models of estimated soil strength. This approach assumes that the slope angle at the landslide failure locations (i.e., scarps or deposits) can be used as a proxy for soil strength (i.e., friction angle, φ, based on Mohr-Columb theory). While the authors recognize that there is not a perfect 1 to 1 relationship between the ground slope of the deposit and the friction angle because other factors such as dip angle are important, these slope distributions do provide a clear distinction between the geologic units and reasonable estimates of strength. The distributions were created by extracting slope values at each pixel within landslide deposits polygons in the SLIDO and subsequently categorized by each geologic unit. A similar analysis was completed for scarp flanks for comparison, which typically shift the

curves about 6 degrees. This correlation results in an estimated soil strength distribution (normalized by the total number of landslides in each unit) for each geologic unit.

Table 3.3 summarizes detailed information on landslide scarp and deposit coverage in the 12 distinct site geology units in the study area. Most of the study area was mapped in the volcanic geologic unit, but the marine sediment unit contains the most scarp coverage. Landslide deposits are primarily accumulated in the surficial sediments unit, providing evidence that soils within this unit are weaker than the other units.

Table 3.3: Table of various site geology units and their coverage in the study area, along with their scarp and landslide deposits coverage.

Generalized Geology	Total Area (km^2)	Coverage (%)	Scarp Coverage (km^2)	Scarp Coverage (%)	Deposits Coverage (km^2)	Deposits Coverage (%)
Surficial Sediments	181,744	19.4%	79	10.3%	27,889	35.0%
Marine Sediment	244,412	26.1%	371	48.0%	22,296	28.0%
Terrestrial Sediment	21,984	2.3%	47	6.0%	1,445	1.8%
Volcanic	257,302	27.4%	237	30.6%	12,567	15.8%
Marine Volcanic	4,960	0.5%	0	0.0%	743	0.9%
Volcanoclastic	137,034	14.6%	26	3.4%	10,827	13.6%
Metamorphic	28,423	3.0%	N/A	N/A	683	0.9%
Intrusive	37,641	4.0%	12	1.6%	1,002	1.3%
Invasive Extrusive	1,921	0.2%	1	0.1%	639	0.8%
Melange	12,716	1.4%	N/A	N/A	1,537	1.9%
Vent and Pyroclastic	6,304	0.7%	N/A	N/A	44	0.1%
Batholith	0	0.0%	N/A	N/A	0	0.0%
Unclassified	3,565	0.4%	0	0.0%	19	0.0%

While the approach requires the assumption that the slope angles of the scarp or deposits (repose) are representative of the soil strength (a conservative estimate), it presents some

important benefits. First, significant differences in strength are observed between different geologic units, enabling the methodology to appropriately distinguish the relative hazard between these units. For example, Figure 3-4 compares three different sedimentary geologic units, showing clear differences between the geologic units. Figure 3-5 shows these distributions for all of the generalized geologic units characterized in this study. Recorded values for these distributions are predominately within the range of 0 to 40 degrees, which correlate well with the limited testing available and typical values for soil friction angles. Second, the approach captures the variability observed in these observations. Note that some geologic units exhibit a much higher degree of variability (uncertainty) compared with others, which can be accounted for in the probabilistic analysis.

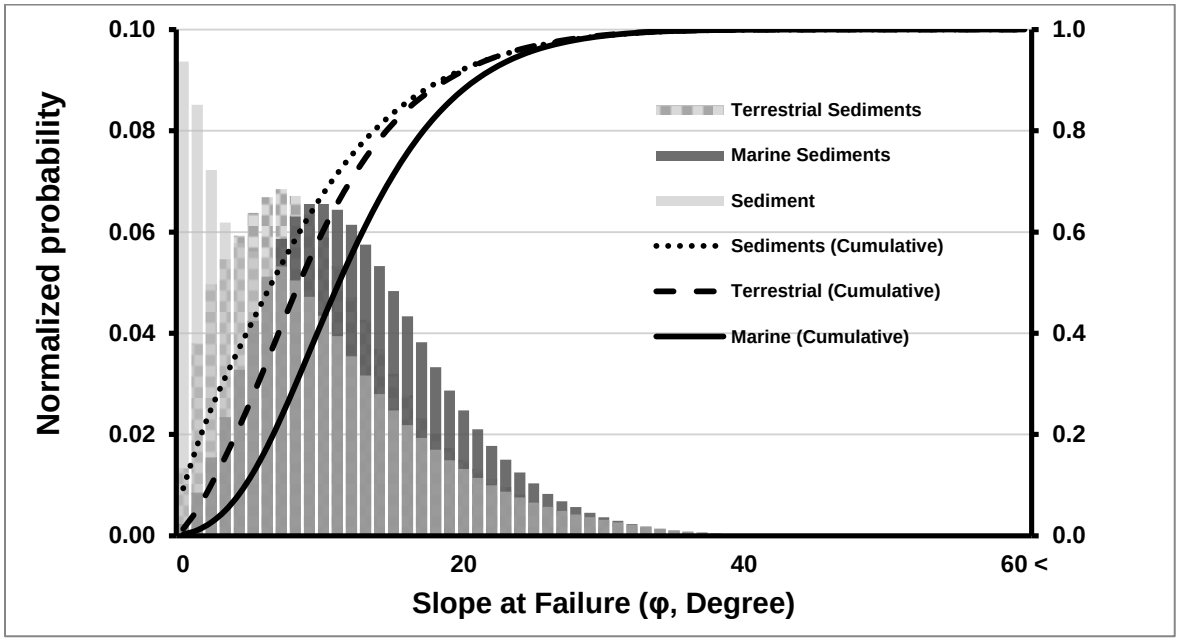

Figure 3-4: Comparison of distributions of slopes of pixels mapped as landslide deposits for surficial sediments, terrestrial and marine sediments geologic units.

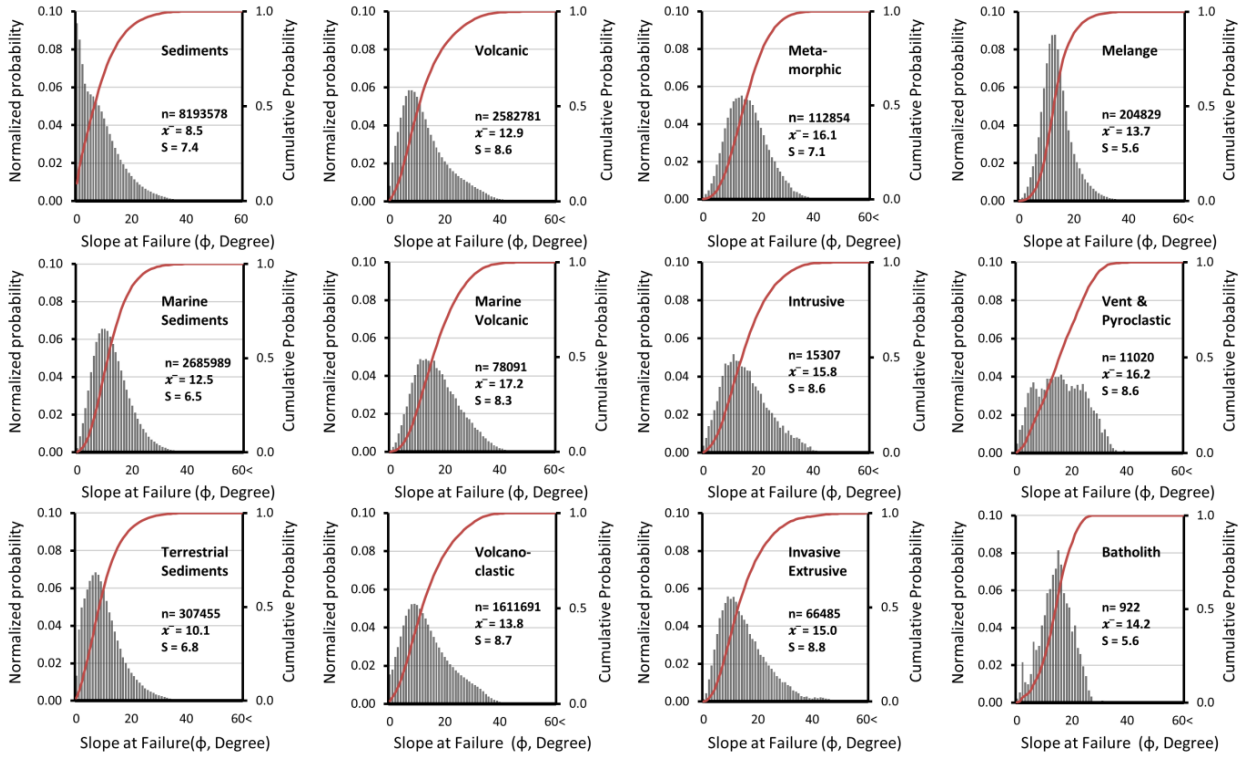

Figure 3-5: Distributions of slopes for pixels occupied by landslide deposits for each generalized geologic unit (computed for 1 degree bins).

3.7 METHODOLOGY

To facilitate the ability to create new maps when new, improved data are available (e.g., updates to the USGS seismic hazard curves), code was developed in C++ to efficiently process the probabilistic calculations for such a large spatial area. The code is also flexible such that one can alternate datasets, strength distributions, and run it for fully probabilistic calculations or for scenario events. The resulting probabilistic maps can be brought into a GIS platform for further analysis and visualization.

There are three main factors contributing to the seismically-induced landslide hazard, including slope, shear strength and peak ground acceleration. According to the chain rule in probability theory, conditional probabilities can be used over all possible member of joint distributions of a set of random variables (e.g., slope, PGA and slope at failure as a representative of residual shear strength) to calculate the aggregated probability of a landslide. The following expression can be used to calculate the exceedance probability of a landslide at a given location:

$$P_{LS|E,N} = \sum_{i=0}^{n} \sum_{j=0}^{90^{\circ}} P\left(PGA_i > a_{y(\varphi_j,\beta_{E,N})} \mid \varphi_j, \beta_{E,N}\right) \times P(\varphi_j) \times \Delta P_i \quad (3\text{-}1)$$

where:

i is an increment and *n* is the number of bins for the probability distribution function for PGA, provided in the USGS seismic hazard curves (e.g., Figure 3-6)

$P_{LS|E,N}$ is the exceedance probability of a seismically-induced landslide at a location with N and E representing northing and easting coordinates, respectively,

$\beta_{E,N}$ is the slope angle at location *N, E*,

PGA_i is the peak ground acceleration from the corresponding seismic hazard curve (based on NHERP site classification) at a location *N, E*, for bin increment *i*,

$a_{y(\varphi_j,\beta_{E,N})}$ is the minimum pseudo-static acceleration required to produce instability for the sliding block (yield acceleration), which is a function of friction angle and the slope calculated using Newmark's method (downhill equation),

$a_y = \tan(\varphi_j - \beta_{E,N}) \times g$ (3-2)

g is the acceleration due to gravity of Earth, equal to 9.807 m/s^2,

$P\left(PGA_i > a_{y(\varphi_j,\beta_{E,N})} \mid \varphi_j, \beta_{E,N}\right)$ is the probability of an earthquake with peak ground acceleration exceeding yield acceleration given the condition representing the pixel located at *N, E* with a slope of β degrees and estimated friction angle of φ from the appropriate distribution for the corresponding geologic unit (Figure 3-5).

$P(\varphi_j)$ is the probability of the soil having a given strength (friction angle), obtained from the probability distribution function in the corresponding geologic (Figure 3-5),

ΔP_i is the interval exceedance probability for an earthquake producing a peak ground acceleration from seismic hazard curve (based on site classification) for the location *N, E*, at bin *i* calculated by $\Delta P_i = e^{-\lambda_{k+1}} - e^{-\lambda_k}$.

λ_k is the mean annual rate of exceedance for an earthquake producing a peak ground acceleration *k* on the seismic hazard curve (based on NHERP site classification) for the location *N, E*.

The interval probability is computed such that all interval probabilities sum to 1. The highest PGA hazard level given in the seismic hazard curve downloaded from USGS website was 2.13 g, which has a very minimal value of mean annual rate of exceedance (i.e., a very large return period). Boundary situations are handled by closing the hazard curve to

perform the full integration of the area below the curve. For this reason, a P=1 for PGA=0 and P=0 for PGA=2.5 g was assumed. In other words, a PGA is always exceeding 0 by a slight amount. Since PGA never exceeded 2.13 g in the study area, setting the upper bound equal to 2.5 g seemed reasonable. Ultimately, the results are not sensitive to this upper value given its low probability of occurrence, but it is needed for mathematical completeness.

PGA values within each bin are defined as the mean value of the seismic hazard curve points describing that bin: $PGA_{i=1} = (\overline{PGA}_1 + \overline{PGA}_2)\ /2$. Figure 3-6 describes the methodology used to integrate over the seismic hazard curve.

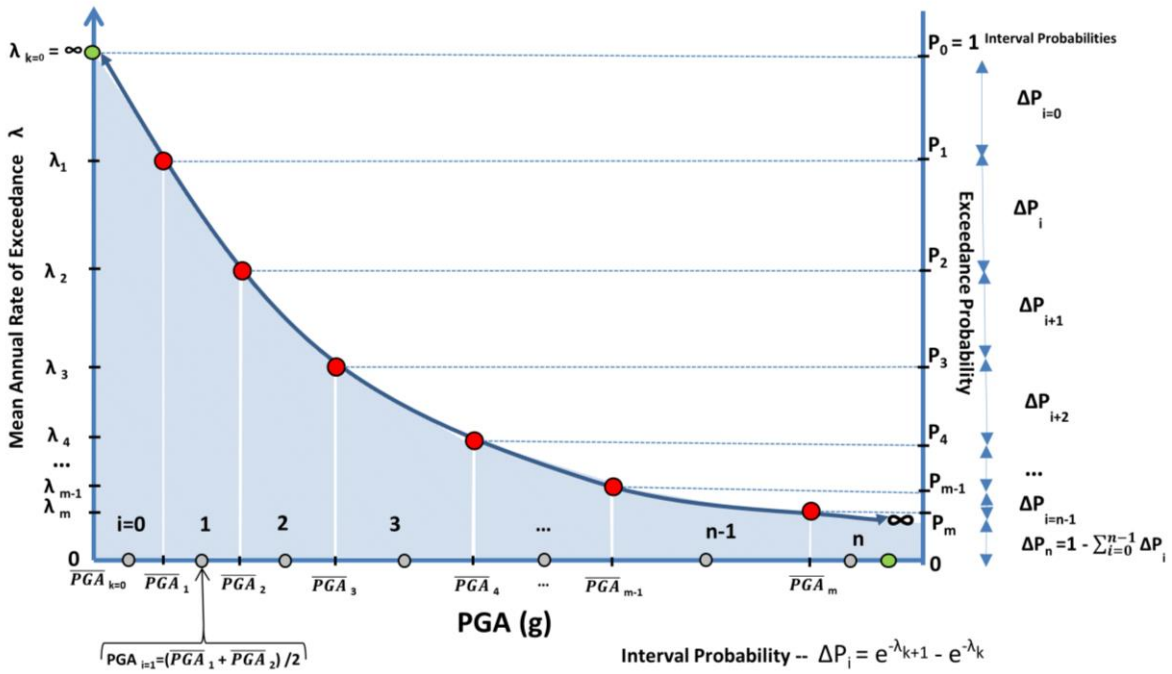

Figure 3-6: Schematic description of fully probabilistic approach for integration over the seismic hazard curve at each pixel. Red points are the defined values which are located on the seismic hazard curve. Green points are the boundary points added to the curve, and grey points are mean PGA values representing the intervals.

Calculations were performed for each 30 m x 30 m pixel (encompassing 900 m^2) in western Oregon. A related approach for modeling the hazard curve for PGA was used for liquefaction and lateral spread hazard mapping in Utah, (Olsen, 2005; Erickson, 2006; Gillins, 2012). Figure 3-7 depicts the methodology in a flowchart format.

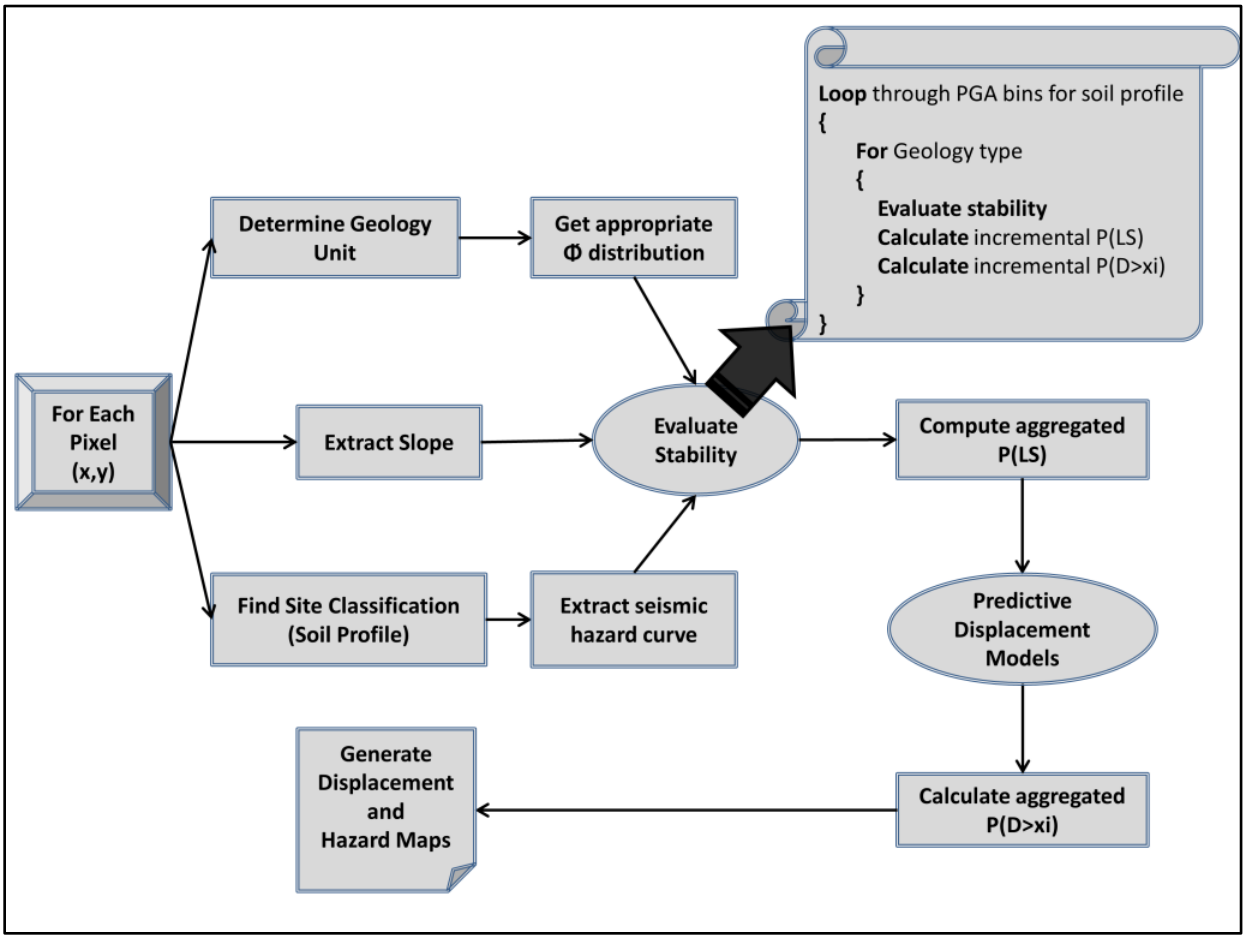

Figure 3-7: The methodology displayed as flowchart with simplified pseudo-code for stability evaluation.

Simultaneous with the landslide triggering analysis, probabilities of exceeding displacement thresholds of (0.1, 0.3, 1.0 m) are determined since they provide an indicator

of damage potential and are necessary for the performance-based design framework. The first threshold was selected as 0.1 m, which represents the lower threshold of Saygili and Rathje, 2008 regression model describing the initiation of landslide producing minimal damage which is likely to be easily repairable. The next threshold is 0.3 m, which is where significant damage may occur to structures (Olsen et al., 2007). Exceeding 1 meter threshold would likely create serious damage and could bring extensive problems for lifeline utilities.

When performing regional analysis over a large area, a simple displacement approach is needed since parameters such as number of cycles, predominant period, and arias intensity are not easily obtained for such a large area or require significant assumptions and computations to acquire, reducing their reliability. Scalar displacement models are regressed over a single ground motion parameter whereas vector models need multiple motion parameters. Hence, a method proposed in Saygili and Rathje, 2008 was selected from among the available methods discussed previously because it required only critical acceleration (a_y) and peak ground acceleration (a_{max}) to estimate permanent displacement (see Table 3.1).

$$\ln D_L = 5.52 - 4.43\,(a_y / PGA) - 20.39\,(a_y / PGA)^2 + 42.61\,(a_y / PGA)^3$$

$$- 28.74\,(a_y / PGA)^4 + 0.72\ln(PGA) \qquad \sigma_{lnD_L} = 1.13 \qquad (3\text{-}3)$$

where:

D_L is the amount of permanent displacement in cm,

a_y is the yield acceleration, in g,

PGA is the peak ground acceleration of the input motion, in g,

σ_{lnD_L} is the standard error for aforementioned regression equation, in cm.

The rate of displacement exceeding a threshold value $P\ [D_L > t]$ was computed within each cell by looping through possible acceleration intervals from the seismic hazard curve for that location and critical acceleration values. The standard errors of the regression model of Saygili and Rathje, 2008 were used to calculate the rate of exceedance for given values of a_y and PGA. Equations 3-2 and 3-3 were used to estimate D_L and exceedance probabilities were calculated from Equation 3-4:

$$P\ [(D_L>t) \mid a_y, PGA_i] = 1 - F_z(z) \qquad (3\text{-}4)$$

where:

t is a threshold value, equal to 3 different values: 0.1, 0.3, 1.0 m,

$F_z(z)$ is cumulative density function (CDF) for the standard normal variant, z, which can be calculated or taken from a CDF table of the standard normal distribution,

z can be computed from equation 3-5:

$$z = \frac{\overline{\ln(D_L = t)} - \ln(D_L)}{\sigma_{\ln(D_L)}} \qquad (3\text{-}5)$$

where:

ln(D_L) is the natural logarithm of the estimated displacement by Saygili and Rathje, 2008 model,

ln(D_L = t) is the natural log of the selected threshold displacement, t,

$\sigma_{ln(DL)}$ = 1.13, the standard error for the Saygili and Rathje, 2008 regression model.

In order to calculate the exceedance rates, equations 3-1 and 3-4 can be merged representing the following expression:

$$P[(D_L > t)]_{E,N} = \sum_{i=0}^{n} \sum_{j=0}^{90^\circ} P\left(LS_{E,N} \mid \varphi_j, \mathrm{PGA}_i\, \beta_{E,N}\right) \times P[(D_L > t) \mid \mathrm{a_y}, \mathrm{PGA_i}] \qquad (3\text{-}6)$$

The probability that D_L exceeds a given threshold can be calculated with Equation 3-6, which is a summation of PGA and friction angle with a given slope and computed yield acceleration in a particular cell. After the aggregation of all PGA values on the seismic hazard curve, the mean annual rate of exceedance of several displacement thresholds will be produced, resulting in the creation of a series of hazard maps, which will be discussed in the following section.

3.8 RESULTS AND DISCUSSION

Maps were created for western Oregon. To illustrate the value of these data, five different locations were selected to highlight the differences in seismicity across the study area. The Newport and the South Coast study sites are located in the very high seismicity region of the study area near to the surface expressions of the Cascadia subduction zone. The City of Portland and South Willamette Valley study sites have milder slopes and are located near

the central meridian of the study area. The Cascades Region was also selected because it is in a mountainous region with lower seismicity compared to the coastal regions. Within each of these locations, three sites with high, moderate and shallow slopes were selected and evaluated in order to study the effects of changes in terrain.

Figure 3-8 presents the landslide triggering map derived using Equation 3-1. Multiple sets of landslide displacement maps for thresholds of 0.01, 0.03, 0.05, 0.07, 0.1, 0.13, 0.15, 0.2, 0.4, 0.6, 1.0, 1.5, 2.0, 3.0, 5.0, 9.0 m were produced. The hazard level corresponding to these threshold intervals are later used to create landslide displacement seismic hazard curves. For brevity, Figure 3-9 presents the 0.1 m displacement threshold exceedance probabilities using the Saygili and Rathje, 2008 model. Note that the maximum value of the green (low hazard) to red (high hazard) legend bar varies between Figure 3-8 and Figure 3-9.

The produced landslide hazard map given in Figure 3-8 provides detailed information regarding the regions in Oregon and delineates domains extremely susceptible to landslides. While the hazard is very high, this map shows reasonable probability results when it is compared with landslide inventory datasets (SLIDO) (Figure 3-1) and susceptibility maps (Burns et al., 2016). Most of the regions where it is estimated to have a high level of hazard, already frequently experience landslides without significant seismic activity. In most cases, the high hazard level prediction inside the map is in accordance with existing landslide features including active and dormant steep slopes, which have historically failed. The displacement (calculated using Saygili and Rathje, 2008) maps show

a rational, decreasing order of likelihood of failure with increasingly detrimental deformations.

Figure 3-10 depicts the performance-based landslide displacement curves for the 5 different study sites for steep, moderate, and shallow slopes in the study area. An overall trend of higher hazard in more seismic regions is observed. For example, In Newport, the performance-based hazard curves for mountainous and hill sites are similar. Even though there is some change in slope from a hill site to a mountain site, the displacement hazard is similar for both sites because of the overall high seismic hazard in Newport due to its proximity to the Cascadia subduction zone.

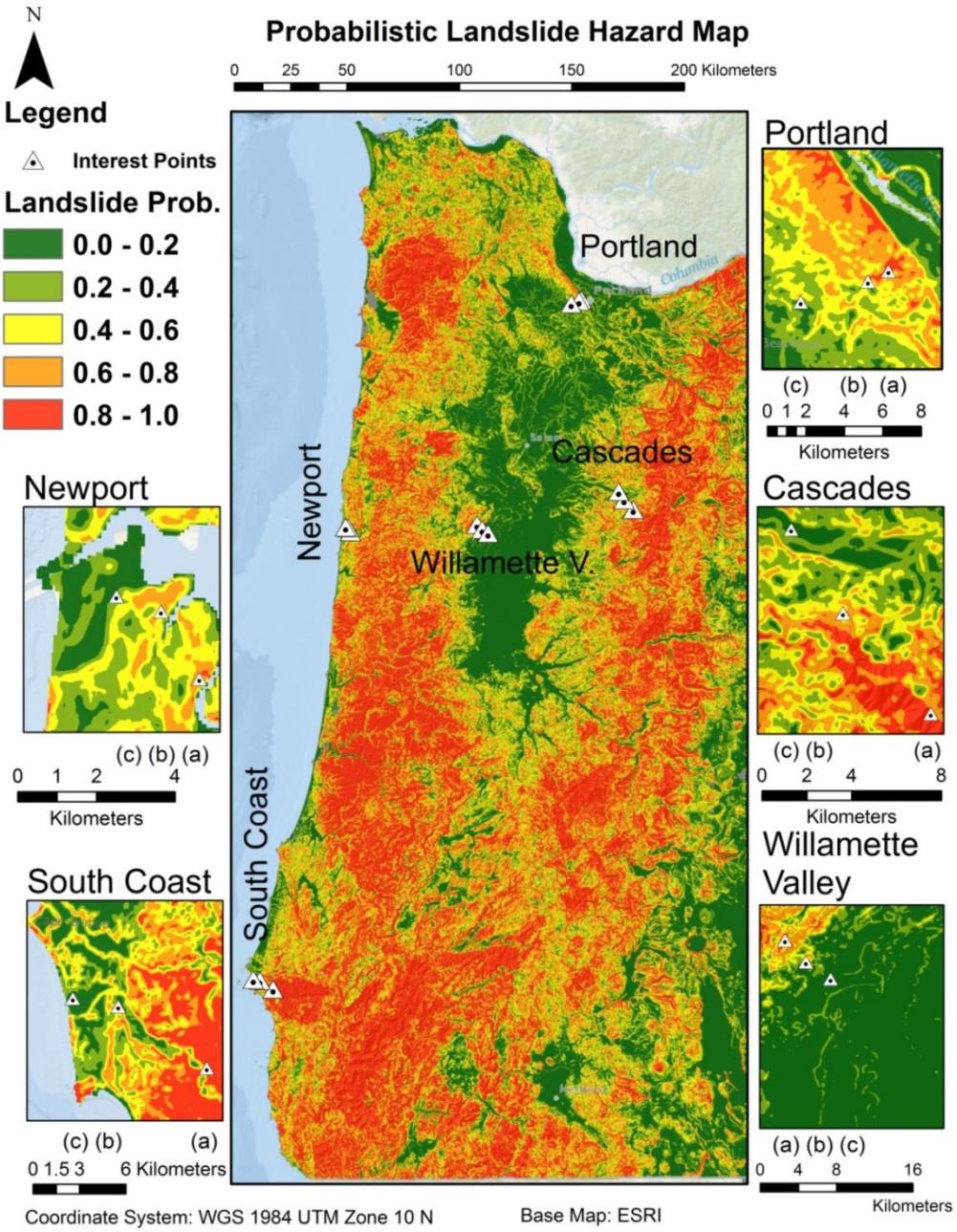

Figure 3-8: Fully probabilistic landslide hazard map for western Oregon using Newmark's slope stability model. The figure depicts the map in 5 selected regions in more detail. Interest points (a) are in steep slopes (slope > 38°), (b) in hill sites (10° < slope < 20°) and (c) in relatively flat sites (slope < 5°).

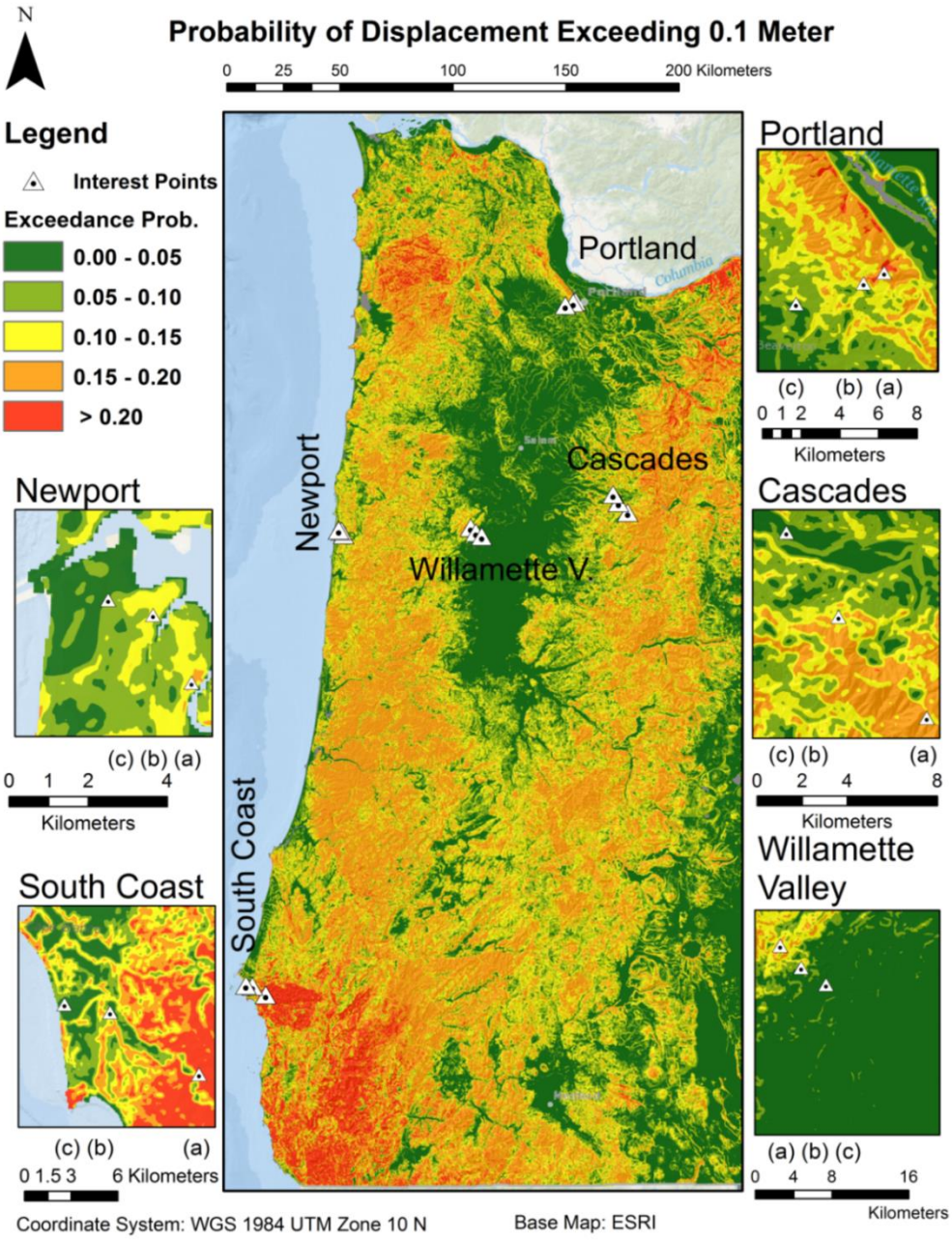

Figure 3-9: Probability of landslide displacement exceeding 0.1 meter using Saygili and Rathje, 2008 displacement prediction model. The figure depicts the map in 5 selected regions in more detail. Interest points (a) are in steep slopes (slope > 38°), (b) in hill sites (10° < slope < 20°) and (c) in relatively flat sites (slope < 5°).

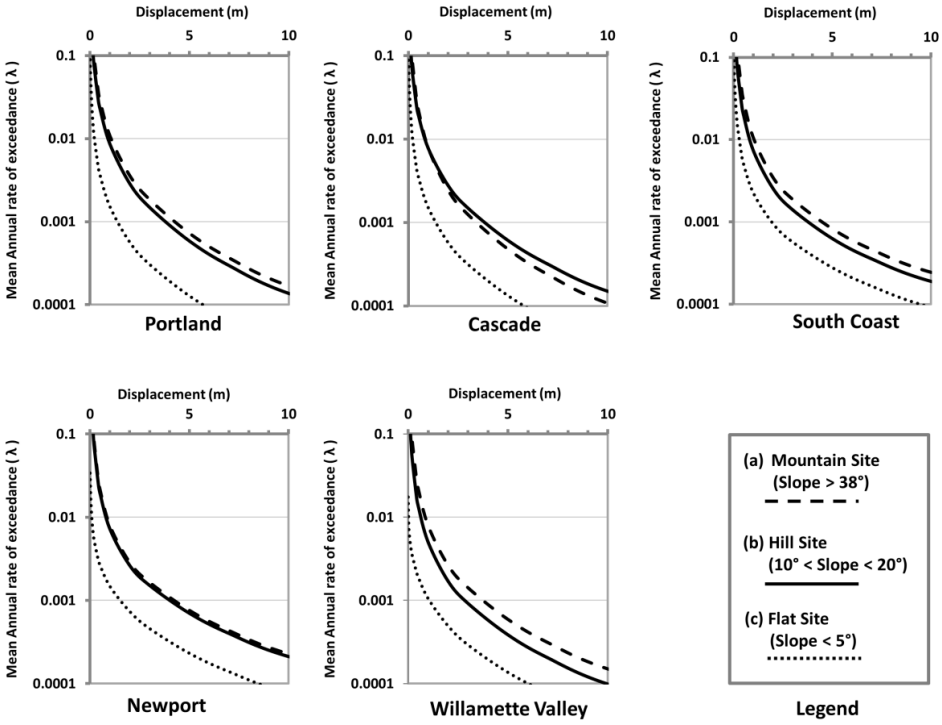

Figure 3-10: Performance based landslide displacement hazard curves for 5 selected regions (Portland, Cascade, South Coast, Newport and Willamette Valley) through 3 sites with different slope gradient going from mountainous to hill and flat regions (see Figure 3-8 and Figure 3-9).

3.9 VALIDATION

A post-earthquake landslide inventory does not exist for western Oregon. However, SLIDO provides a detailed dataset of existing landslides that have been inventoried. SLIDO is one of the most comprehensive statewide landslide inventories available in the world. Note that DOGAMI is continually updating portions of this database using lidar, which has dramatically improved the ability to detect and map landslides for inventorying. These updates, unfortunately, have only been completed for a very small section of the state. Hence, SLIDO only contains a subset of landslides that actually exist in the topography. The triggering mechanisms of the landslides (e.g., seismic or precipitation) are not identified; although prior research (O'Banion & Olsen, 2014) have begun to investigate likely triggering mechanisms of these landslides.

Despite these shortcomings in applying SLIDO to our study which considers seismically induced landslides, it still provides a sensible database to validate the created landslide probability map to ensure that reasonable results were obtained. While not all of these landslides in SLIDO represent seismically induced landslides, they provide an indication of where landslides would be expected to occur (i.e., seismic activities may re-trigger existing landslides and landslides often reoccur in locations where they have already occurred).

Burns et al., 2016 recently published a deterministic statewide landslide susceptibility map. Within this map, more than a third of the state of Oregon was identified as either very high or high susceptibility to landslide hazard. The categories in this study were low, moderate, high and very high. The first three categories were determined through a

decision process based on slope and other parameters, while the existing landslides in SLIDO are automatically classified in Burns et al., 2016 as very high.

Distributions of the landslide probability computed from this study are created for each category in the DOGAMI susceptibility map for comparison (Figure 3-11). The distributions show good agreement between the maps overall. As expected, a significant portion of the low susceptibility areas (more than 85%) have probabilities no more than 10%. Similarly, landslide probabilities for areas with moderate susceptibility are generally distributed from 20% to 40%. More than 60% of the areas described as high susceptibility have landslide probabilities greater than 70%. The last category in the susceptibility map is "very high" category, which is the existing landslides (SLIDO). Approximately, half of the pixels labeled as "very high" have a probability higher than 60 %. Note that one would expect to have this category be higher than the "high" category. However, one possible explanation for this discrepancy is that SLIDO is a compilation. While the newer landslide inventories are well constrained from detailed lidar topographic data, some older inventories demarcate large areas as landslide deposits which are, in actuality, several smaller landslide features intermixed between stable terrain.

Figure 3-12 and Figure 3-13 present two close-up maps of the landslide deposits and scarps from SLIDO plotted on the landslide probability map and DOGAMI's susceptibility map at Dixie Mountain and Pittsburg, Oregon. In these two quads detailed lidar data are available and a significant number of landslides are mapped. Scarps would be expected to fall in high landslide potential hazard locales since they represent steep locations with

weaker materials that have previously failed. Deposits are likely to be located adjacent to unstable slopes. Note that most of the scarps in both of the quads correlate well with the high or very high potential regions.

Nevertheless, some portion of previously captured landslide deposits are now categorized in low hazard regions in the maps, which can be considered as a shortcoming of the methodology. The methodology is successful in identifying scarps well, but is sometimes limited in identifying the locations where the material will relocate to (deposits). As an example, in the Pittsburg Quadrangle in Figure 3-13, a landslide deposit in the center of the map is categorized as a low hazard due to its very shallow slope. However, it would likely be impacted by failed material upslope. To overcome this limitation one could implement a buffer or focal statistics (maximum) approach to expand the high hazard locations to account for these areas. Alternatively, one could perform runout modeling. Nevertheless, such efforts are beyond the scope of this paper which focuses on identifying locations that are likely to fail.

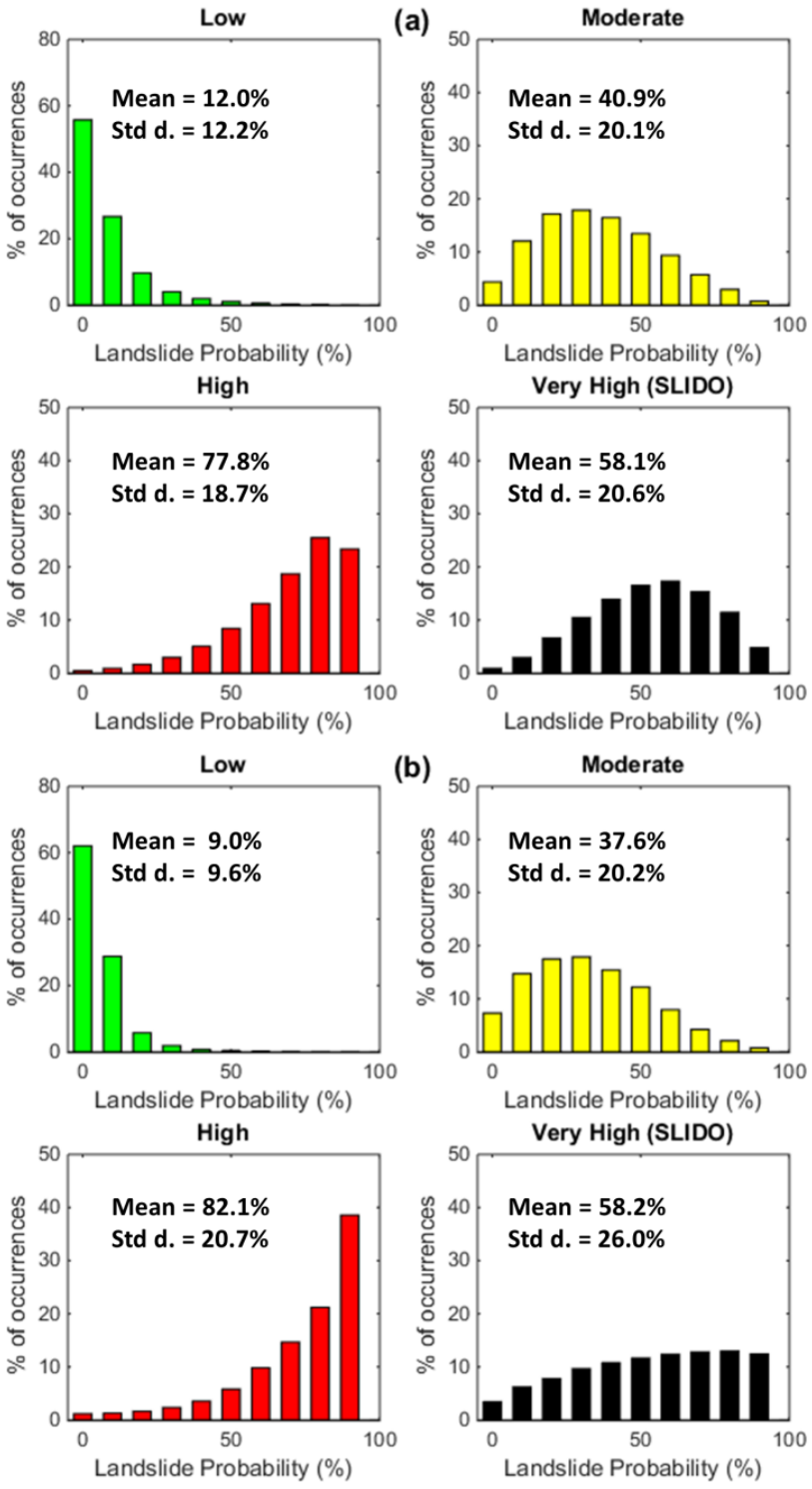

Figure 3-11: Landslide probability distribution at each susceptibility category per definition in Burns et al. (2016) (a) with focal statistics smoothing and (b) without.

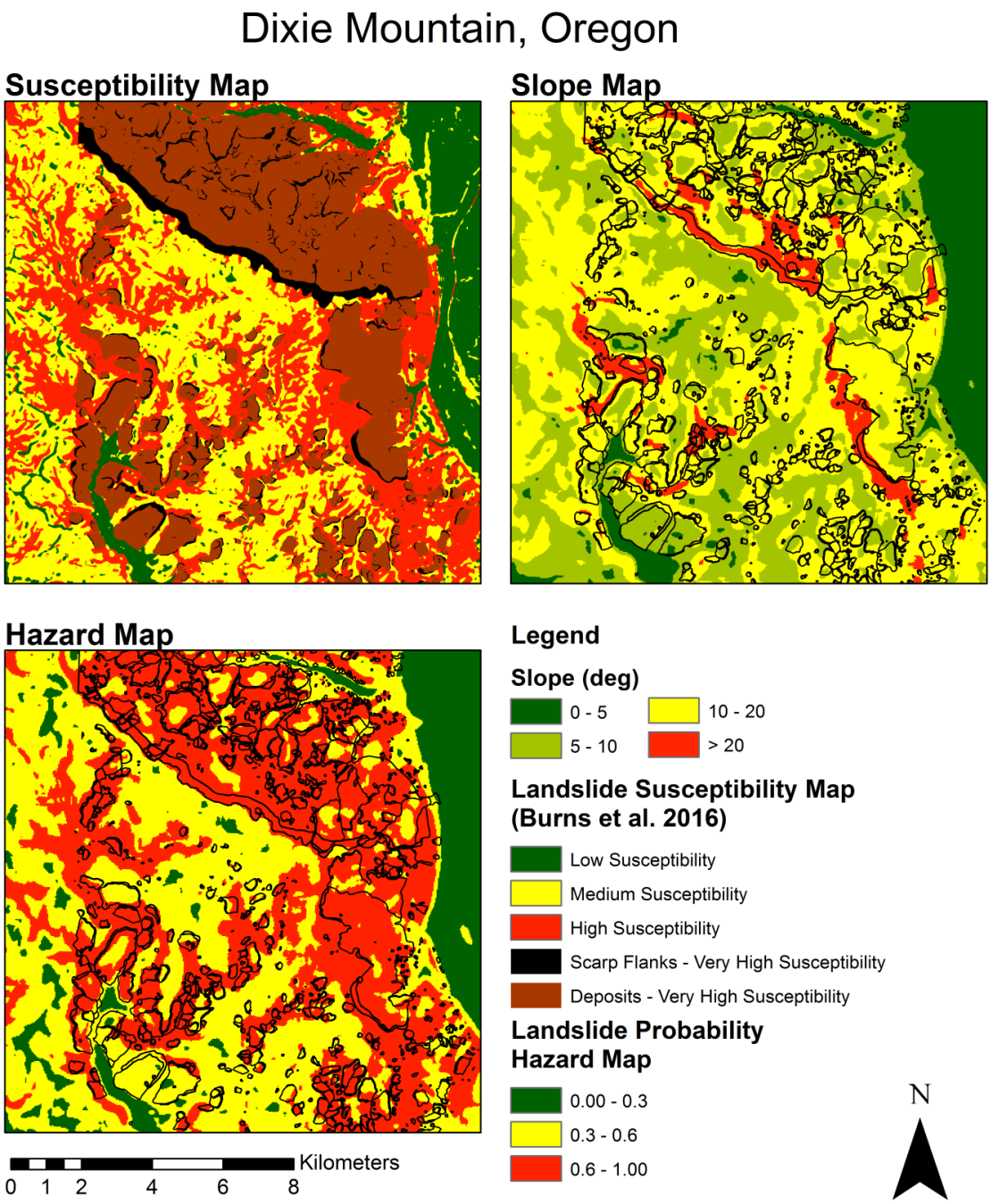

Figure 3-12: Landslide hazard map comparison with landslide susceptibility map by Burns et al. (2016) on top of landslide deposits and scarp flanks in Dixie Mountain, Oregon.

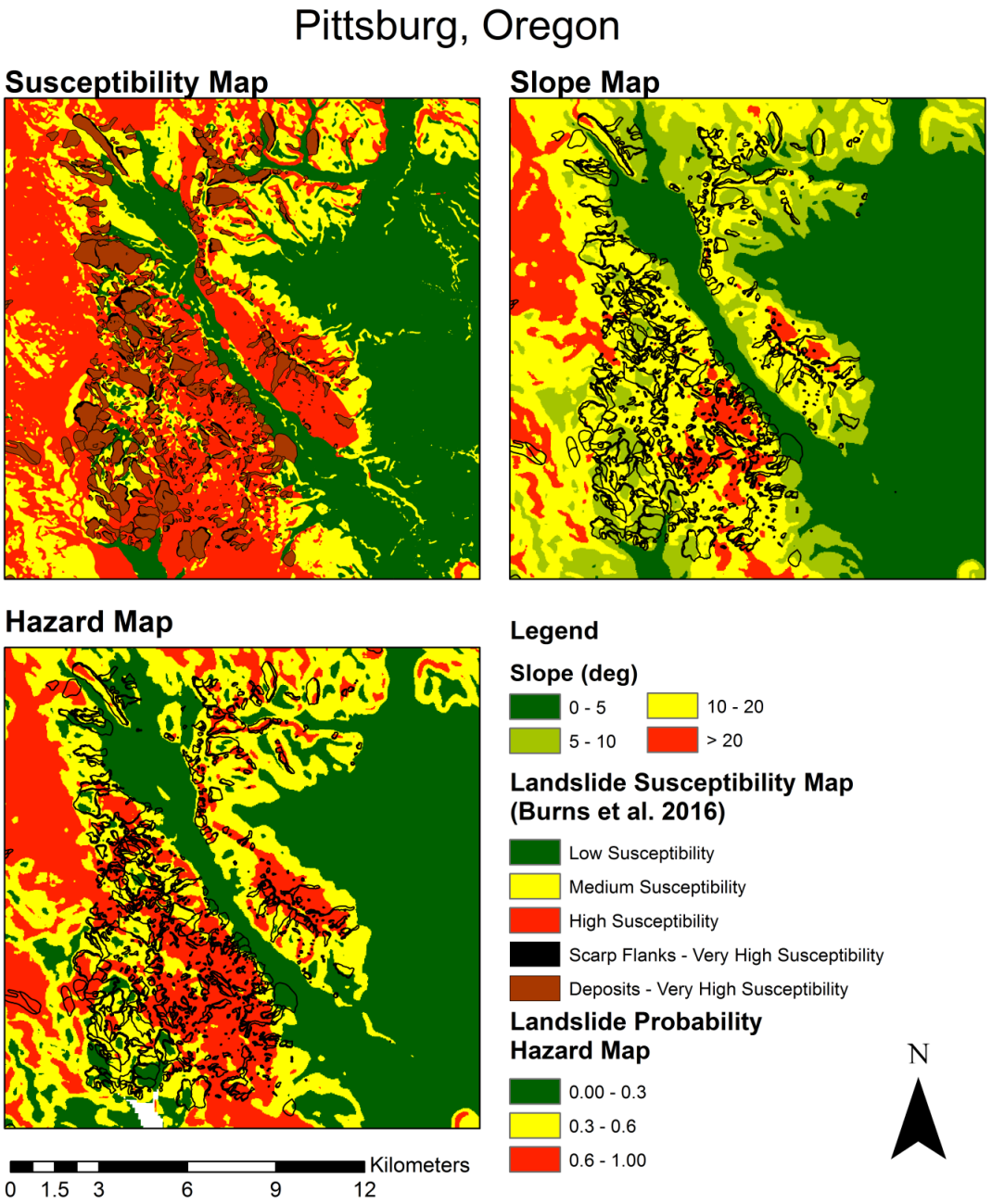

Figure 3-13: Landslide hazard map comparison with landslide susceptibility map Burns et al. (2016) on top of landslide deposits and scarp flanks in Pittsburg, Oregon.

3.10 CONCLUSION

3.10.1 Oregon`s Situation

The chronic, widespread nature of landslide movements within the western part of the state of Oregon is of extreme concern, particularly when exacerbated by seismic activity. While the soil strength estimate approach may be conservative, it agrees well with recent map analyses by DOGAMI using lidar technology, which has led to the discovery of many new landslides (Burns and Madin, 2009; Burns et al., 2016; Madin and Burns, 2006).

Given the results shown in the maps and the fact that Oregon contains very active seismic sources such as the Cascadia subduction zone, it can be concluded that the landslides are apparent hazards in quite a large portion of the state, endangering vital structures, utilities, and lifeline corridors.

3.10.2 Methodology Findings

A very significant limitation of performing a landslide regional assessment is the collection of accurate, detailed geotechnical data. It is quite challenging to use available data and systematically evaluate stability analysis and incorporate site-specific displacement regression models into regional analyses.

This study applies many of the site specific rigors (e.g., Saygili and Rathje model) to a regional assessment. It is thus critical to note that at the time of application, values from these maps should not be used for engineering design in site specific projects, but rather as a relative screening criterion for when more detailed site investigations and design

analyses should be completed. Further, earthquake shaking characteristics (e.g., peak ground acceleration and arias intensity or predominant period) are important parameters; hence, the expected motion in Oregon might differ with input motions used in empirical predictive displacement models, which will result in aleatory variability. Finally, the methodology was shown to produce fairly consistent results with the best available landslide inventories for comparison.

According the scale of this study area and because a lot of the landslide displacement empirical relationships are using regional earthquake data to calibrate and develop models for site specific projects or small regional studies instead of a statewide mapping project, results of this study should not be used for engineering design and instead can be beneficial for monitoring criteria.

3.11 FUTURE WORK

Several improvements can be made to the methodology, which is expandable, by design. One can include other factors (e.g., probability of soil being sufficiently saturated for a landslide to occur). The probabilistic seismic hazard routines written in C++ can be also implemented consistently where similar datasets are available. (Note that most of these datasets are available across the US). In addition, as more high-resolution lidar data are collected through the USGS 3D Elevation Program (3DEP: Sugarbaker et al., 2014), they can be easily integrated into the analysis for improved terrain detail.

Additional uncertainty in the source data could be incorporated into the methodology. For example, there is very limited shear wave velocity data to generate the NEHRP site

classification maps over such a large area. (There can also be significant local site effects within each geologic unit). This, in turn, leads to uncertainty when determining the appropriate seismic hazard curve to apply, based on the site amplification. Improved shear wave velocity data availability and modeling would enable this uncertainty to be added as another parameter considered in the probabilistic chain, similar to the slope distributions representing soil strength.

Further calibration and testing of the approach should be performed to validate the results of this study. Recent case histories of landslides triggered from major to great earthquakes would enable this analysis. As an example, the Tohoku, Japan, earthquake of 2011 is known to have approximately 3,477 seismically induced landslides (Wartman et al., 2011; Rathje et al., 2017). These landslides could be used to validate the proposed mapping method.

The developed map series can further be used in disaster management to minimize damages from landslides posing a hazard to western Oregon. For example, Oregon DOT utilized the results of this study, in conjunction with consideration of other variables, to determine priority lifeline corridors for resource allocation. The probabilistic nature of these maps also enables them to be combined with other hazards for a more complete hazard analysis.

3.12 ACKNOWLEDGEMENT

Financial support for this study was provided by the Oregon Department of Transportation (ODOT), under SPR-740 and the Cascadia Lifelines Program (CLiP). The authors acknowledge the helpful feedback from Curran Mohney, Matthew Mabey, and other

technical advisory committee members at ODOT. The Oregon Lidar Consortium provided the lidar data used in this project. We would like to express our gratitude to Bill Burns and Ian Madin from DOGAMI, in particular, for their assistance in providing datasets. The authors would also like to thank OSU's Civil Engineering, Geomatics research lab for their assistance. The authors also appreciate the reviewers who have provided constructive feedback to this manuscript.

3.13 REFERENCES

Ambraseys, N., Menu, J. (1988). Earthquake-induced ground displacements. Earthquake Engineering & Structural Dynamics, 16(7): 985-1006.

Bray, J.D., Travasarou, T. (2007). Simplified procedure for estimating earthquake-induced deviatoric slope displacements. Journal of Geotechnical and Geoenvironmental Engineering, 133(4): 381-392.

Burns, S.F., Burns, W.J, James, D.H., Hinkle, J.C. (1998a). Landslides in Portland. Oregon Metropolitan.

Burns, S.F., Burns, W.J., James, D.H., Hinkle, J.C. (1998b) Landslides in the Portland, Oregon metropolitan area resulting from the storm of February 1996: Inventory map, database and evaluation. Report prepared as fulfillment of Metro contract, 905828.

Burns, W.J., Madin, I.P. (2011). Statewide Landslide Information Database of Oregon (SLIDO)-Release 1, 2008 Joint Meeting of The Geological Society of America, Soil Science Society of America, American Society of Agronomy, Crop Science Society of America, Gulf Coast Association of Geological Societies with the Gulf Coast Section of SEPM.

Burns, W. J., Madin, I. (2009). Protocol for inventory mapping of landslide deposits from light detection and ranging (LiDAR) imagery. Oregon Department of Geology and Mineral Industries.

Burns, W. J., Mickelson, K. A., & Madin, I. (2016). Landslide Susceptibility Overview Map of Oregon.

Burns, W. J., Mickelson, K. A., Saint-Pierr, E. C. (2011). SLIDO-2, Statewide Landslide Information Database for Oregon, Release 2. Oregon Department of Geology and Mineral Industries. Portland, OR.

Burns, W. J.,Watzig, R. J. (2014). SLIDO-3.0, Statewide Landslide Information Database for Oregon, Release 3.0. Oregon Department of Geology and Mineral Industries. Portland, OR.

Clague, J.J., and Stead, D., (eds.) (2012). Landslides- Types, Mechanisms and Modeling, New York, Cambridge University Press, 420 p.

Cornforth, D.H. (2005). Landslides in practice. Wiley Hoboken.

Cornell, C.A. and Krawinkler, H. (2000). Progress and challenges in seismic performance assessment, PEER News, April, 1-3,

Deierlein, G.G., Krawinkler, H., and Cornell, C.A. (2003). A framework for performance-based earthquake engineering, Proceedings, 2003 Pacific Conference on Earthquake Engineering.

Del Gaudio, V., Pierri, P., & Wasowski, J. (2003). An approach to time-probabilistic evaluation of seismically induced landslide hazard. Bulletin of the Seismological Society of America, 93(2), 557-569.

Densham, P.J. (1991). Spatial decision support systems. Geographical information systems: Principles and applications, 1: 403-412.

DOGAMI, (2012). Lidar Collection and Mapping,

Erickson, G.L. (2006). Probabilistic liquefaction potential mapping of the Salt Lake Valley Book Thesis, University of Utah.

Espinosa, A., Egred, J., Garcla-Lopez, M., Crespo, E. (1991). Intensity and damage distribution. The March 5, 1987, Ecuador earthquakes: mass wasting and socioeconomic effects, 5: 42.

Franke, K. W., & Kramer, S. L. (2013). Procedure for the empirical evaluation of lateral spread displacement hazard curves. Journal of Geotechnical and Geoenvironmental Engineering.

Gillins, D.T. (2012). Mapping the Probability and Uncertainty of Liquefaction-induced Ground Failure, The University of Utah.

Harp, E.L., Jibson, R.W. (1996). Landslides triggered by the 1994 Northridge, California, earthquake. Bulletin of the Seismological Society of America, 86(1B): S319-S332.

Harp, E.L., Keefer, D.K., Sato, H.P., Yagi, H. (2011). Landslide inventories: the essential part of seismic landslide hazard analyses. Engineering Geology, 122(1): 9-21.

Harvey, A., Peterson, G. (1998). Water-Induced Landslide Hazards: Western Portion of the Salem Hills. Marion County, Oregon, Oregon Department of Geology and Mineral Industries Interpretive Map Series IMS-6.

James, T.S., Clague, J.J., Wang, K., Hutchinson, I. (2000). Postglacial rebound at the northern Cascadia subduction zone. Quaternary Science Reviews, 19(14): 1527-1541.

Jibson, R.W. (2007). Regression Models for estimating coseismic landslide displacement. Engineering Geology, 91(2): 209-218.

Jibson, R.W. (1993). Predicting earthquake-induced landslide displacements using Newmark's sliding block analysis. Transportation research record: 9-9.

Jibson, R.W. (2000). Harp, E.L., Michael, J.A., A method for producing digital probabilistic seismic landslide hazard maps. Engineering Geology, 58(3): 271-289.

Keefer, D.K. (1984). Landslides caused by earthquakes. Geological Society of American Bulletin, 95(4): 406-421.

Keefer, D.K. (1999). Earthquake-induced landslides and their effects on alluvial fans. Journal of sedimentary research, 69(1).

Keefer, D.K. (2002). Investigating landslides caused by earthquakes- a historical review. Surveys in Geophysics, 23(6): 473-510.

Khazai, B., Sitar, N. (2000a). Assessment of seismic slope stability using GIS modeling. Geographic Information Sciences, 6(2): 121-128.

Khazai, B., Sitar, N. (2000b). Landsliding in native ground: a GIS-based approach to regional seismic slope stability assessment report.

Kramer, S.L. (1996). Geotechnical earthquake engineering. Prentice-Hall Civil Engineering and Engineering Mechanics Series, Upper Saddle River, NJ: Prentice Hall.

Krawinkler, H. (2002). A general approach to seismic performance assessment. Proceedings, International Conference on Advances and New Challenges in Earthquake Engineering Research, ICANCEER, 2002, Hong Kong.

Lee, C. T., Huang, C. C., Lee, J. F., Pan, K. L., Lin, M. L., & Dong, J. J. (2008). Statistical approach to earthquake-induced landslide susceptibility. Engineering Geology, 100(1), 43-58.

Lin, G.W., Chen, H., Hovius, N., Horng, M.J., Dadson, S., Meunier, P., and Linesm M. (2008). Effects of earthquake and cyclone sequencing on landsliding and fluvial sediment transfer in a mountain catchment. Earthquake surface Processes and Landforms, 33, 1354-1373.

Ma, L., Madin, I. P., Olson, K. V., Watzig, R. J., Wells, R. E., & Priest, G. R. compilers. (2009). Oregon geologic data compilation [OGDC], release, 5.

Madin, I., Burns, W. (2006). Map of Landslide Geomorphology of Oregon City. Oregon and Vicinity Interpreted from lidar Imagery and Aerial Photographs, Oregon Department of Geology and Mineral Industries Open File Report O-06-27.

Makdisi, F. I., & Seed, H. B. (1977). Simplified procedure for estimating dam and embankment earthquake-induced deformations. In ASAE Publication No. 4-77. Proceedings of the National Symposium on Soil Erosion and Sediment by Water, Chicago, Illinois, Dec. 12-13.

Miles, S., Ho, C. (1999). Rigorous landslide hazard zonation using Newmark's method and stochastic ground motion simulation. Soil Dynamics and Earthquake Engineering, 18(4): 305-323.

Nelson, C. H., Morey, A. E., Johnson, J. E., Patton, J. R., Karabanov, E., Gutierrez-Pastor, J et al. (2012). Turbidite event history: Methods and implications for Holocene paleoseismicity of the Cascadia subduction zone. US Department of the Interior, US Geological Survey.

Newmark, N.M. (1965). Effects of earthquakes on dams and embankments. Geotechnique, 15: 139-160.

O'Banion, M.S., and Olsen, M.J. (2014). Predictive Seismically-Induced Landslide Hazard Mapping in Oregon Using a Maximum Entropy Model (MAXENT), National Conference on Earthquake Engineering.

Olsen, M.J., Bartlett, S.F., Solomon, B.J. (2007). Lateral Spread Hazard Mapping of the Northern Salt Lake Valley, Utah, for a M7. 0 Scenario Earthquake. Earthquake Spectra, 23(1): 95-113.

Olsen, M.J. (2005). Lateral spreading hazard mapping of northern Salt Lake County for a magnitude 7.0 scenario earthquake Book Thesis, University of Utah.

OSSPAC, (2013). The Oregon Resilience Plan, Reducing Risk and Improving Recovery for the Next Cascadia Eathquake and Tsunami, Salem, Oregon.

Petersen, M.D., Frankel, A.D., Harmsen, S.c., Mueller, C.S., Haller, K.M., Wheeler R.L., Wesson, R.L., Zeng, Y., Boyd, O.S., Perkins, D.M., Luco, N., Field, E.H., Wills, C.J., and Rukstales, K.S. (2008). Documentation for the 2008 Update of the United States National Seismic Hazard Maps: U.S. Geological Survey Open-File Report –1128, 61 p.

Rathje, E., Little, M., Wartman, J., Athanasopoulos-Zekkos, A., Massey, C. and Sitar, N. (2017). Preliminary Landslide Inventory for the 2016 Kaikoura, New Zealand Earthquake Derived from Satellite Imagery and Aerial/Field Reconnaissance, Quick Report 1, ver. 1 of the forthcoming NZ-US Geotechnical Extreme Events Reconnaissance (GEER) Association Report on the Geotechnical Effects of the 2016 M7.8 Kaikoura Earthquake. doi: 10.18118/G6NK57

Rathje, E.M., Saygili, G. (2011). Estimating fully probabilistic seismic sliding displacements of slopes from a pseudoprobabilistic approach. Journal of Geotechnical and Geoenvironmental Engineering, 137(3): 208-217.

Rathje, E.M., Wang, Y., Stafford, P.J., Antonakos, G., Saygili, G. (2014). Probabilistic assessment of the seismic performance of earth slopes. Bulletin of Earthquake Engineering, 12(3): 1071-1090.

Refice, A., Capolongo, D. (2002). Probabilistic modeling of uncertainties in earthquake-induced landslide hazard assessment. Computers & Geosciences, 28(6): 735-749.

Sarkar, S., and Kanungo, D.P. (2004). An integrated approach for landslide susceptibility mapping using remote sensing and GIS. Photogrammetric Engineering and Remote Sensing, 70(5): 617-625.

Saygili, G., Rathje, E.M. (2008). Empirical predictive models for earthquake-induced sliding displacements of slopes. Journal of Geotechnical and Geoenvironmental Engineering, 134(6): 790-803.

Saygili, G., Rathje, E.M. (2009). Probabilistically Based Seismic Landslide Hazard Maps: an application in Southern California. Engineering Geology, 109(3-4), 183-194.

Schulz, W.H., Galloway, S.L. (2012). Evidence for Earthquake triggering of large landslides in coastal Oregon, USA. Geomorphology, 141: 88-98.

Schuster, R.L., and Krizek, R.J. (eds.), (1978). Landslides-Analysis and Control: Transportation Research Board Special Report, 176, 234 p.

Sharifi-Mood, M., Santha Mahalingam., R., Olsen, M.J. (2013). Geospatial characterization of causative factors for recent landslides in the Oregon Coast Range, GeoCongress. ASCE, San Diego.

Soeters, R., van Westen, C.J. (1996). Slope instability recognition, analysis, and zonation, Chapter 8. In: Landslides: Investigation and mitigation. Transportation Research Board Special Report, 247.

Strenk, P.M., Wartman, J. (2011). Uncertainty in seismic slope deformation model predictions. Engineering Geology, 122(1): 61-72.

Stuart, N., Stocks, C. (1993). Hydrological modelling within GIS: an integrated approach. IAHS publication, 319-319.

Sugarbaker, L.J., Constance, E.W., Heidemann, H.K., Jason, A.L., Lukas, Vicki, Saghy, D.L., and Stoker, J.M. (2014). The 3D Elevation Program initiative—A call for action: U.S. Geological Survey Circular 1399, 35 p., https://dx.doi.org/10.3133/cir1399.

Turner, A.K., and Schuster, R.L. (eds.).(1996). Landslides-Investigation and Mitigation, Transportation Research Board Special Report. 247, 673 p.

USGS, (2006). National Elevation Dataset.

Petersen, Mark D., Frankel, Arthur D., Harmsen, Stephen C., Mueller, Charles S., Haller, Kathleen M., Wheeler, Russell L., Wesson, Robert L., Zeng, Yuehua, Boyd, Oliver S., Perkins, David M., Luco, Nicolas, Field, Edward H., Wills, Chris J., and Rukstales, Kenneth S. (2008). Documentation for the 2008 Update of the United States National Seismic Hazard Maps: U.S. Geological Survey Open-File Report 2008–1128, 61 p. https://pubs.usgs.gov/of/2008/1128/

USGS, (2008). United States National Seismic Hazard Maps.

Van Westen, C., Van Asch, T.W., Soeters, R. (2006). Landslide hazard and risk zonation—why is it still so difficult? Bulletin of Engineering Geology and the Environment, 65(2): 167-184.

Varnes, D.J., Slope movement types and processes, in Schuster, R.L., and Krizek, R.J. (eds.), (1978). Landslides-Analysis and Control: Transportation Research Board Special Report, 176, 11-33.

Wang, Y., Rathje, E.M. (2015). Probabilistic seismic landslide hazard maps including epistemic uncertainty. Engineering Geology, 196: 313-324.

Wang, Y., Summers, R.D., Hofmeister, R.J. (2002). Landslide loss estimation pilot project in Oregon. Department of Geology and Mineral Industries.

Wartman, J., Dunham, L., Tiwari, B., Pradel, D. (2013). Landslides in eastern Honshu induced by the 2011 Tohoku earthquake. Bulletin of the Seismological Society of America, 103(2B), 1503-1521.

Waters, A. (1973). The Columbia River Gorge—Basalt stratigraphy, ancient lava dams, and landslide dams. Beaulieu, JD, Geologic field trips in northern Oregon and southern Washington: Oregon Dept. of Geology and Mineral Industries Bulletin, 77: 133-162.

Wilson, R.C., Keefer, D.K. (1983). Dynamic analysis of a slope failure from the 6 August 1979 Coyote Lake, California, earthquake. Bulletin of the Seismological Society of America, 73(3): 863-877.

Wong, I.G., Hemphill-Haley, M.A., Liberty, L.M., Madin, I.P. (2001). The Portland Hills fault: an earthquake generator or just another old fault. Oregon Geology, 63(2): 39-50.

Xie, M., Esaki, T., Zhou, G. (2004). GIS-based probabilistic mapping of landslide hazard using a three-dimensional deterministic model. Natural Hazards, 33(2): 265-282.

Xinpo, L., Siming, H. (2009). Seismically induced slope instabilities and the corresponding treatments: the case of a road in the Wenchuan Earthquake hit region. Journal of mountain Science, 6(1): 96-100.

Yegian, M., Marciano, E., Ghahraman, V. (1991). Earthquake-induced permanent deformations: probabilistic approach. Journal of Geotechnical Engineering, 117(1): 35-50.

Manuscript # 3

Quantification of Geotechnical Properties of Surficial Geologic Units for Geo-hazard Assessments

Mahyar Sharifi-Mood, Daniel T. Gillins, Michael J. Olsen, Kevin Franke and Steven F. Bartlett

Target journal: Earthquake Spectra, EERI

4 QUANTIFICATION OF GEOTECHNICAL PROPERTIES OF SURFICIAL GEOLOGIC UNITS FOR GEO-HAZARD ASSESSMENTS

4.1 ABSTRACT

Geotechnical borehole information can be of highly variable quality and difficult to find after a project is completed. Typically, boring logs are provided as images in geotechnical reports rather than delivered in a database format. When these logs are digitized by engineers for analysis (typically into a spreadsheet), often only a small portion of the information of highest interest to the project and study are digitized. The objective of this paper is to demonstrate the value of compiling scattered geotechnical data into a consistent, organized database with uncertainty metrics describing the data quality. This paper describes the organizational structure of three available geotechnical borehole databases compiled in the state of Utah (Utah, Weber and Salt Lake counties). The geotechnical database of Utah (GeoDU) is subsequently used to quantify the engineering properties of soils within dominant geologic units. Geologic mapping is generally available (at least at coarse scales), whereas geotechnical data is more expensive and time-consuming to acquire and thus less available. Investigations have been completed to quantitatively group statistically similar geologic units which can simplify hazard assessments. Further, by developing correlations of soil properties to geologic groups where geotechnical investigations have occurred, one can utilize these correlations in locales that lack appropriate geotechnical data for geospatial hazard assessment. To this end, statistical distributions of soil properties such as $(N_1)_{60}$ and fines contents are

developed for simplified geologic groups. The resulting digital database is an important resource for future efforts with applications such as liquefaction, lateral spreading, and landslide hazard mapping efforts along with community data sharing and preliminary site investigations.

4.2 INTRODUCTION

Geologic maps serve a wide range of applications including landslide risk assessment, earthquake hazard analysis, ground-water quality evaluations, energy and mineral resources characterization, land management, land-use planning, and so forth (Soller, 2002 and Varnes, 1974). Similarly, site investigations provide geotechnical and mechanical properties of the native soil that are an important component for characterizing geo-hazards (El May et al., 2010). While often expensive and scarce, geologic maps are readily available for many locales, albeit at different resolutions.

A thorough geotechnical database compiled in a consistent platform is capable of providing scientists, engineers, and planners detailed information on the native soil properties. This information can be used for various applications including liquefaction hazard mapping. Unfortunately, soil investigations such as the standard penetration test (SPT) are performed with a wide range of quality. Further, most subsurface information are archived in hard copy or electronic document form only. Only a small portion of them are digitized into a consistent database. Even in these efforts, only the portion of the data of highest relevance to an existing project or study are digitized. This process can result in inconsistency and reduces the ability to utilize information between projects.

Currently there are different database formats available including commercial software such as gINT by Bentley in and web-based interfaces similar to Consortium of Organizations for Strong Motion Observation Systems (COSMOS, Swift et al., 2002 and Stepp et al., 2009). The gINT software supports centralized data management for geotechnical subsurface projects. The structure of gINT database consists of customizable tables with various fields to hold numerous geotechnical data. COSMOS, on the other hand, is an online interface for a geotechnical database created by a group of organizations including USGS. Geotechnical data can be input in this database and shared over the internet. The XML language format used within COSMOS was designed to store and transport data that is extensible, granting many users the ability to input their data in a compatible format or query data within an existing project for analyses.

A novel example of a geotechnical database is the Canterbury Geotechnical Database (CGD), which provides access to shared data provided by other engineers and their clients. Generally, imagery and spreadsheets of data collected from a site investigation are submitted and shared through the CGD. Established by Tonkin and Taylor, CGD is a well-developed online database, which was developed to assist earthquake recovery in Canterbury, New Zealand. To date, it contains over 22,500 CPT and 4,900 SPT records and was designed as a searchable source to share both new and existing geotechnical information.

Another example is the Department of Oregon Geology and Mineral Industry (i.e. DOGAMI) 3D drillhole database for Portland, Oregon. DOGAMI (Roe and Madin, 2013) published an

open file report that contained 3D geologic model of the Portland urban area along with other geologic and geotechnical data specifically for hazard studies. The primary purpose of this study was to produce new, detailed shear wave velocity and NEHRP site class maps for Portland metropolitan area. A total of 10,075 conventional drill holes are stored in this database. 8,392 of these are geotechnical boreholes (SPTs), water wells, or exploration wells. Additionally, 227 shear wave velocity tests along with 1,105 "pseudo" drill holes and 578 CPT are recorded in this database. The combination of these drill holes, subsurface interpretations, and shear-wave velocity measurements provided further possibilities in performing research on geologic and engineering properties of Portland area. However, a limitation to this database is that only a portion of the data on the borehole logs were digitized into attribute tables. Much of the geotechnical information (e.g., $(N_1)_{60}$ values) were not digitized since the database was primarily developed for geologic purposes.

While above databases are helpful to collect and share relevant geotechnical information for different projects, links between these geotechnical information and to geological mapping are often overlooked. However, geotechnical properties are related to the depositional environments (Youd and Perkins 1978). To this end, the purpose of this paper is to illustrate the value of compiling unorganized and scattered subsurface data into a cohesive database to provide this linkage between geology and geotechnical parameters. The geotechnical database of Utah (GeoDU) contains over 1935 SPT boreholes in Utah, Weber and Salt Lake counties and has been compiled over the last decade to support liquefaction mapping activities (Gillins 2012, Olsen et al. 2007, Gillins and Franke 2016 ,

Anderson et al. 1994). In this study we explore more potential applications of the data and explore the following questions:

I. Can we simplify/group geologic units based on common geotechnical properties?

II. Can we statistically quantify geotechnical parameters of a simplified geologic group?

III. Can we use geotechnical information from one locale in another region based on a common geologic group in the mapping?

The key motivation for these questions resides in the fact that there are often significant data limitations in geospatial analysis and mapping efforts over a large area. Often, in these efforts, geologic maps are simplified by combining similar units based on expert judgement. Alternatively, with a database, units can be grouped based on a statistical analysis. Further, by statistically quantifying a geologic unit, one can perform a detailed geospatial analysis without requiring boreholes to be spread throughout an entire geologic unit. Insufficient geotechnical information can be compensated by correlations to other boreholes in that geologic unit or a nearby area with similar geologic properties. In contrast to geotechnical data that are usually very expensive and unavailable, surficial geology maps are commonly available. A comparison between boreholes in the three counties shows the ability to utilize or supplement geotechnical data in different geographic regions with a similar geologic history.

4.3 GEOLOGIC SETTING

This study focuses on three representative counties within northern Utah (Figure 4-1) including Utah (Figure 4-2), Weber (Figure 4-3), and Salt Lake (Figure 4-4) Counties. The

Wasatch Mountains extend from central Utah northward for almost 200 miles. Potential large earthquakes as high as 7.5 moment magnitude from the Wasatch Fault are likely to generate strong ground shaking throughout the state of Utah, which is of significant concern to highly populated regions (Smith and Arabasz, 1991). Various seismically induced geo-hazards such as liquefaction, lateral spreading and landslides are anticipated due to the high seismicity and susceptible sandy soils present throughout the valleys.

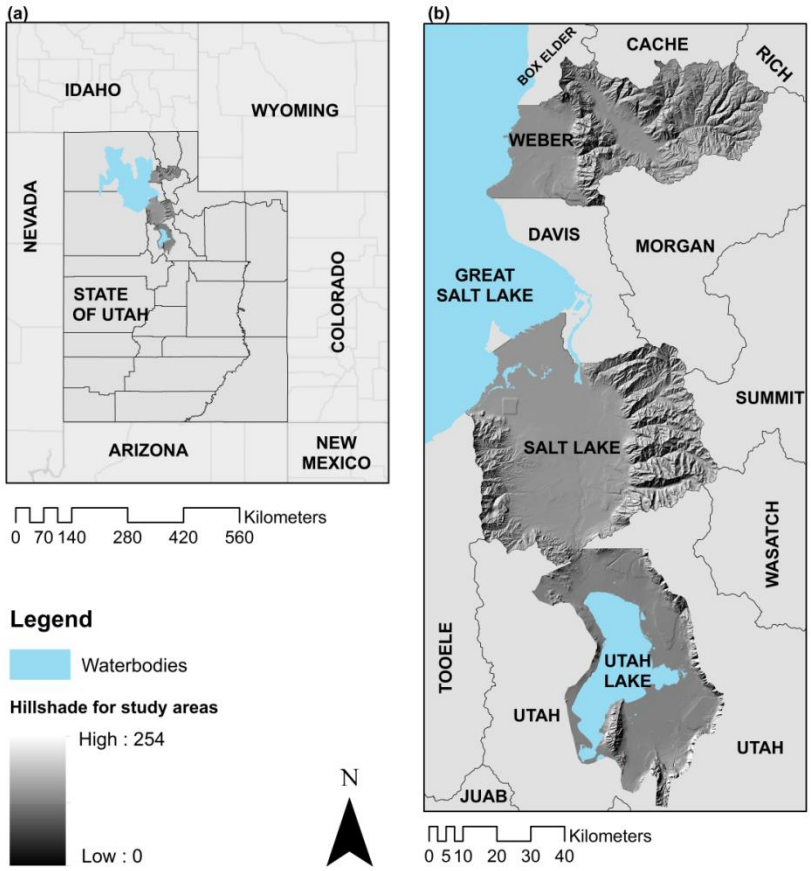

Figure 4-1: (a) Overview map for state of Utah, (b) geographical location of three counties (Utah, Salt Lake and Weber) residing in northern Utah.

A significant portion of these county boundaries follow distinct geologic or geographic features. For example, the northern and southern boundaries of Salt Lake County tend to follow mountain ridge lines and also occur in locales where the valley narrows substantially between the Wasatch and Oquirrh mountains to the south and the Wasatch mountains and Great Salt Lake in the north. Note that in other locales, division by counties may not be appropriate for such a study, since administrative boundaries may not follow geological features.

A substantial portion of northern Utah was covered by Lake Bonneville during the Pleistocene era. The loose, lacustrine sediment deposited by this lake later formed flat lake beds and valley floors. Today, the Great Salt Lake in Salt Lake County and Utah Lake in Utah County are the remains of Lake Bonneville, which dramatically receded as a result of the extended warm and dry climate over time. The Jordan River, the predominant river in Salt Lake County, present in the center of Figure 4-4 and in northwest section of

, flows slowly from Utah Lake to the Great Salt Lake at a very shallow slope. The Jordan River has deposited a significant amount of alluvial sediment along its meandering course. The Weber and Ogden Rivers, running within the center of Figure 4-3, are the primary rivers in Weber County that flow into the Great Salt Lake. In Utah County, the Provo River, Hobble creek, Spanish Fork River, and American Fork River are the dominant rivers in Utah County, all of which flow into Utah Lake.

The Utah Geological Survey (UGS) provides a detailed surficial geologic map for all three counties in the study area. Table 4.1 summarizes the geological mapping efforts done at each county within the study area.

Figure 4-2 through Figure 4-4 show the geologic maps for Utah, Weber and Salt Lake counties with the visual location of subsurface investigations respectively. All geologic maps are bounded by the Wasatch Mountains on the east, where the Utah segment of Wasatch Fault is visible.

Utah County is primarily filled by Holocene and upper Pleistocene alluvial, lacustrine, and deltaic sediment deposits. Constenius et al. 2011 compiled a series of multiple 7.5-minute quadrangles from the UGS, along parts of populous Wasatch Front and Utah Valley to produce surficial geology base maps (30 by 60 minute quadrangles) for entire Utah County.

Weber County is mainly dominated by Holocene and late Pleistocene sediments from the Weber and Ogden Rivers, Lake Bonneville, and later the Great Salt Lake. Weber County's geologic map is composed of the Ogden quadrangle (Yonkee and Lowe 2004), Roy quadrangle (Sack 2005), Plain City quadrangle (Harty and Lowe 2005) and north Ogden quadrangle (Harty and Lowe 2003).

The surficial geologic map for Salt Lake County combines several mapping efforts. Personius and Scott (1992) produced a geologic map for the eastern part of the valley. Solomon et al. (2007) mapped the Magna Quad on the west side. Extrapolation of geologic units from boundaries of previously mapped areas (Miller, 1980) was performed to finalize the geologic mapping of the north-western and western portion of Salt Lake County.

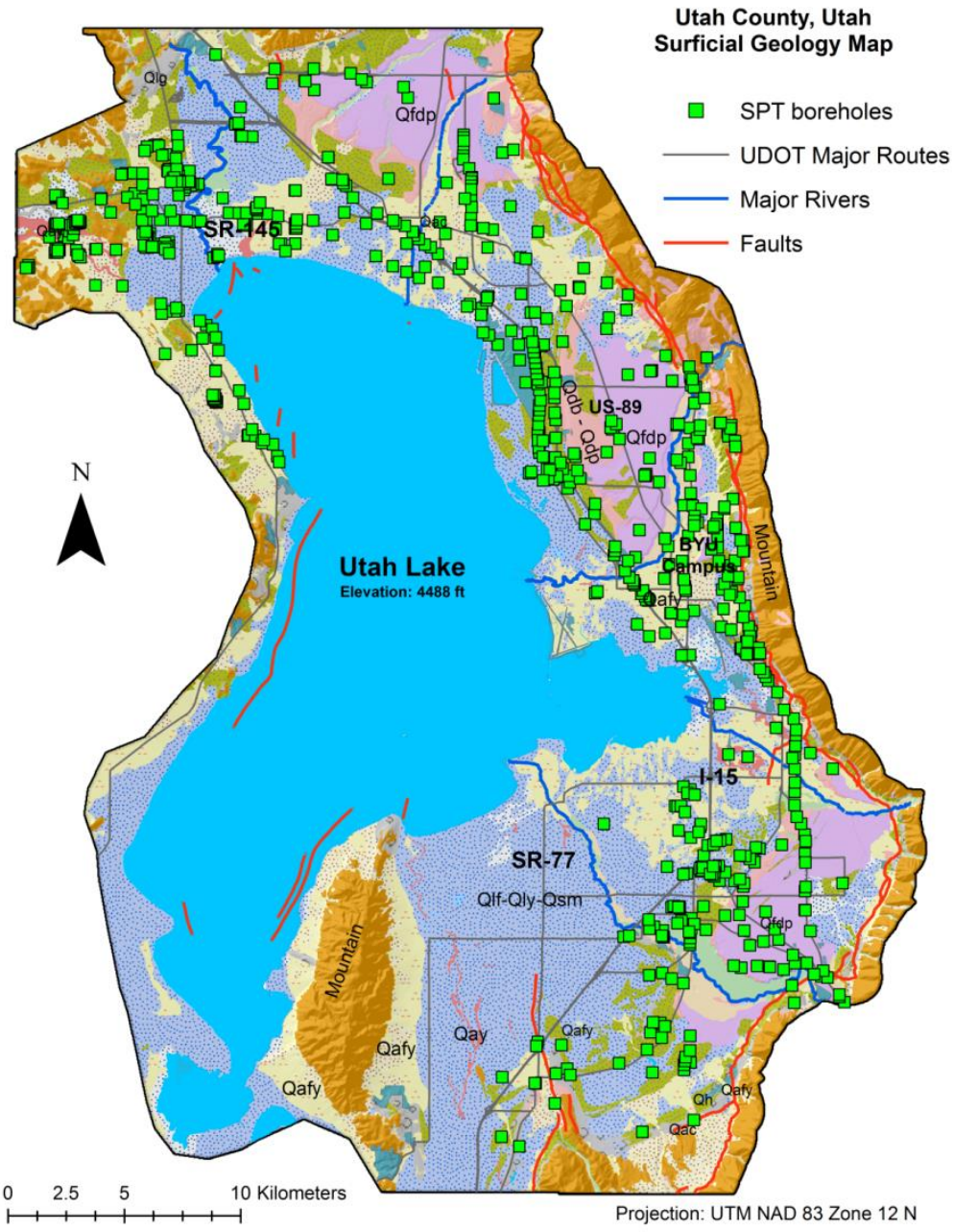

Figure 4-2: Surficial geology map of Utah County with locations of geotechnical investigations (Sharifi-Mood et al., Under Review).

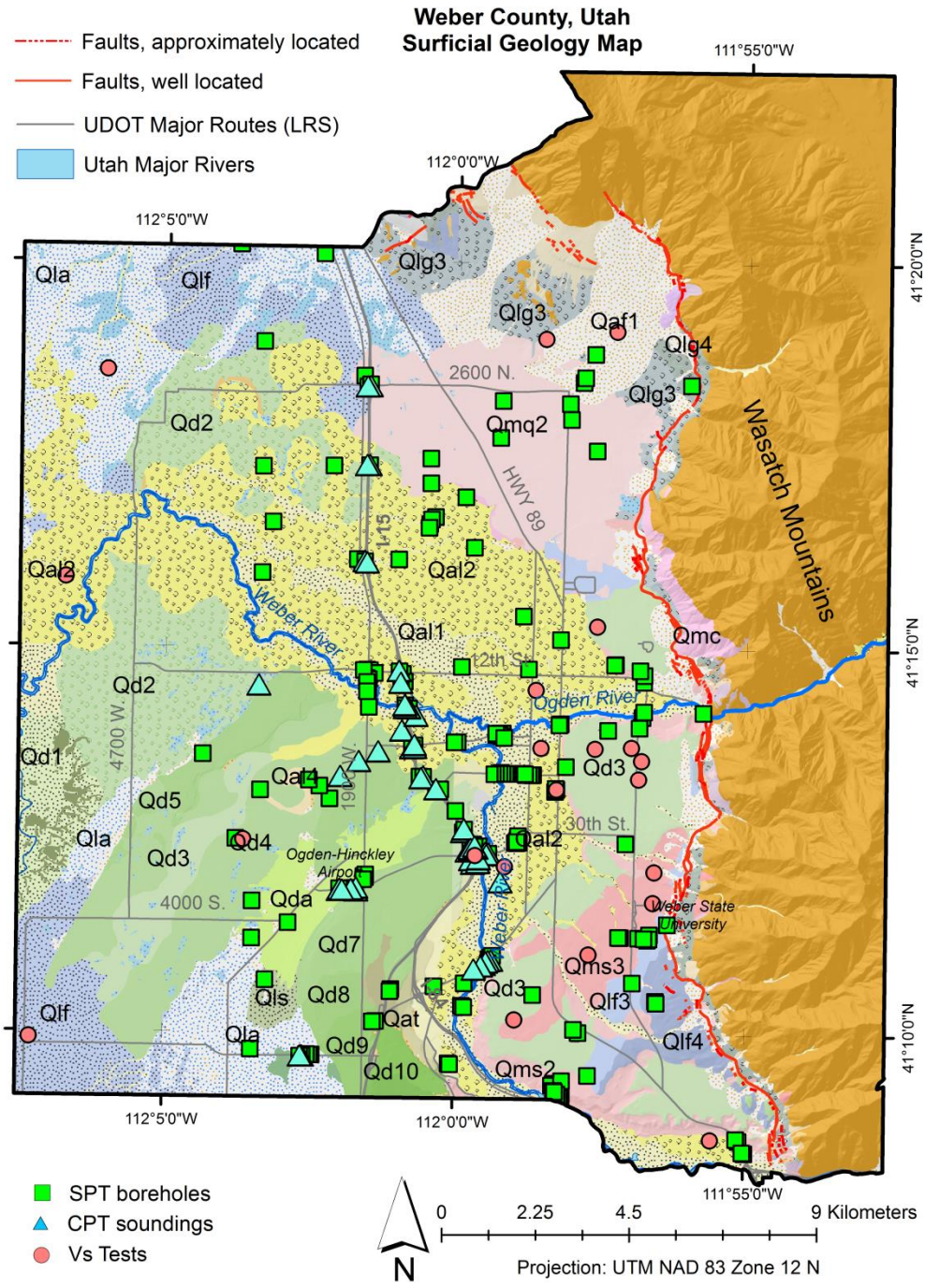

Figure 4-3: Surficial geology map of Weber County with locations of geotechnical investigations (from Gillins 2012).

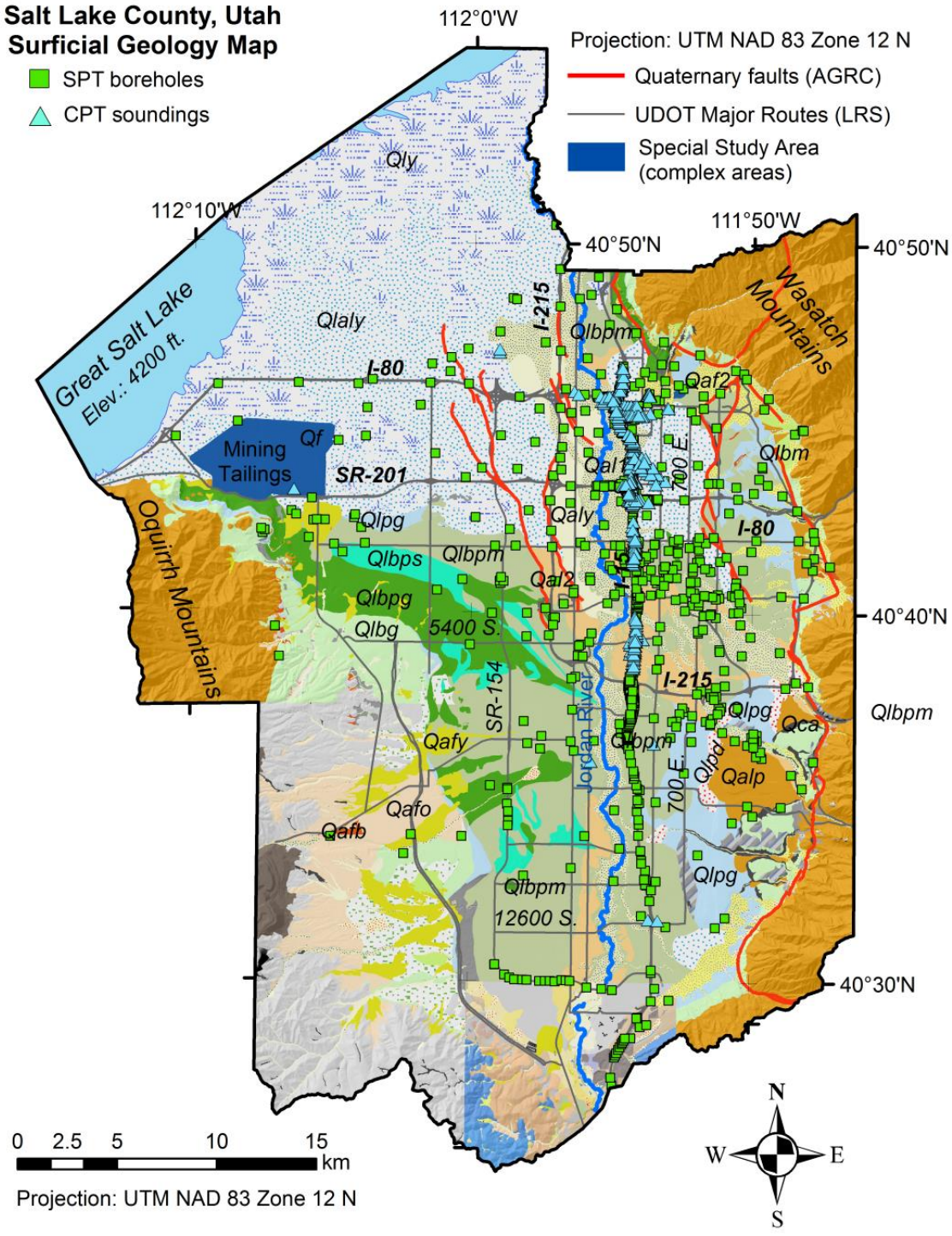

Figure 4-4: Surficial geology map of Salt Lake County with locations of geotechnical investigations.

Table 4.1: Summary of past geologic mapping efforts in state of Utah within each county.

County	Location	Quad. Resolution	Reference
Utah	Entire county	30' x 60'	Constenius et al. (2011)
Salt Lake	East Valley	7.5 min	Personius and Scott (1992)
	Magna	7.5 min	Solomon et al. (2007)
	Northwest and west Sections	7.5 min	Miller (1980)
Weber	North Ogden	7.5 min	Harty and Lowe (2003)
	Ogden	7.5 min	Yonkee and Lowe (2004)
	Roy	7.5 min	Sack (2005)
	Plain City	7.5 min	Harty and Lowe (2005)

Given the significant amount of geologic units covered throughout the study area, simplified geologic groups were created to capture the predominant geology (Sharifi-Mood et al., Under Review) as well as address naming differences between mapping efforts. These simplified geologic groups, their description and the number of subsurface tests available in the database at each county are all expressed in Table 4.2. Some of the selected categories include: stream alluvium, stream-terrace alluvium, old and young alluvial fans, fine-grained lacustrine, lacustrine sand and gravel. According to Youd and Perkins (1978), many of these deposits are moderately to very highly susceptible to liquefaction.

Table 4.2: Simplified geologic groups present in the study area with descriptions and the number of SPT boreholes in each unit.

Deposit Symbol	Description	Salt Lake	Utah	Weber	Total
1. Stream Alluvium - Young					
'Qal'	Modern stream alluvium	0	33	0	33
'Qal1'	Modern stream alluvium, currently or recently active	278	0	59	337
'Qal2'	Modern stream alluvium	100	0	65	165
'Qaly'	Young stream alluvium	10	0	0	10
2. Stream Alluvium - Old					
'Qalp'	Old stream alluvium	13	0	0	13
3. Stream-Terreace Alluvium					
'Qat1'	Stream-terrace alluvium, lowest terrace levels	0	7	0	7
'Qat2'	Stream-terrace alluvium, medium terrace levels	0	4	6	10
'Qat3'	Stream-terrace alluvium, highest terrace levels	0	1	0	1
'Qat7'	Fluvial terrace, below the Gilbert shoreline	0	0	1	1
4. Alluvial Fan - Young					
'Qaf'	Modern alluvial fan	0	0	3	3
'Qaf1'	Modern alluvial fan deposits 1	0	0	5	5
'Qaf2'	Modern alluvial fan deposits 2	30	0	0	30
'Qafy'	Younger alluvial-fan	7	171	0	178
5. Alluvial Fan - Old					
'Qafb'	Transgressive (Bonneville) Lake Bonneville-age	3	1	0	4
'Qafm'	Intermediate Lake Bonneville-age alluvial fan	0	21	0	21
'Qafo'	Older alluvial-fan deposits, undivided	2	0	0	2
'Qafp'	Regressive (Provo) Lake Bonneville-age alluvial fan	0	10	0	10
6. Alluvial Fan and Terrace					
'Qay'	Alluvial fan and terrace post-Provo shoreline of Lake Bonn.	0	13	0	13
7. Alluvial Fan and Delta					
'Qfdp'	Lake Bonneville alluvial-fan and delta, Provo stage	0	61	0	61
8. Alluvium and Colluvium					
'Qac'	Alluvium and colluvium, undivided	0	7	0	7
'Qca'	Colluvium and alluvium, undivided	1	0	0	1
9. Delta					
'Qd2'	Modern fine-grained delta	0	0	2	2
'Qd3'	Fine-grained delta of Gilbert shoreline age	0	0	12	12
'Qd4'	Fine-grained delta from Lake Bonneville's regressive phase	0	0	6	6
'Qd5'	Sand dominated delta from Lake Bonn.'s regressive phase	0	0	7	7
'Qd6'	Deltaic sand from early regressive phase of Lake Bonn.	0	0	1	1
'Qd9'	Deltaic sand from early regressive phase of Lake Bonn.	0	0	2	2
'Qda'	Undifferentiated delta and alluvium, sand-dominated	0	0	10	10
'Qdb'	Near Bonneville shoreline of Lake Bonneville	0	1	0	1
'Qdp'	Near and below Provo shoreline of Lake Bonneville	0	13	0	13
'Qlpd'	Deltaic deposit	6	0	0	6

10. Lacustrine Fine-Grained - Young					
'Qlf'	Mixed from Lake Bonneville and Great Salt Lake lacustrine	0	194	3	197
'Qlf3'	Fine-grained lacustrine from Lake Bonn.'s regressive phase	0	0	4	4
'Qlf4'	Fine-grained lacustrine from Bonn.'s transgressive phase	0	0	2	2
'Qly'	Young lacustrine less than 6 m thick and overlies Qlf unit	15	6	0	21
'Qsm'	Spring and marshes, undivided	0	1	1	2
11. Lacustrine Fine-Grained - Old					
'Qlbm'	Lacustrine clay and silt related to the Bonneville (transgressive) phase of the Bonneville lake cycle	3	0	0	3
'Qlbpm'	Lacustrine silt and clay of the Provo and Bonneville lake cycles, undivided	271	0	0	271
12. Lacustrine Gravel and Sand					
'Qlbpg'	Lacustrine gravel and sand of the Provo and Bonneville lake cycles, undivided	16	0	0	16
'Qlpg'	Lacustrine gravel and sand of the Provo	28	0	0	28
13. Lacustrine and Alluvial					
'Qla'	Lacustrine and alluvial, undivided	0	20	12	32
'Qlaly'	Young lacustrine, marsh, and alluvial deposits	126	0	0	126
14. Lacustrine Sand					
'Qlbps'	Lacustrine sand and silt of the Provo and Bonneville lake cycles, undivided	5	0	0	5
'Qlps'		1	0	0	1
'Qls'	Lacustrine sand below Bonneville and Provo shorelines	0	100	1	101
'Qes'	Eolian sand; 1-1.5 m thick and derived from Qls unit	0	7	0	7
15. Lacustrine Gravel					
'Qlbg'	Lacustrine gravel and sand related to the Bonneville (transgressive) phase of the Bonneville lake cycle	14	0	0	14
'Qlg'	Lacustrine gravel and sand near Bonn. and Provo shorelines	0	21	0	21
'Qlg4'	Lacustrine gravel from Lake Bonn.'s transgressive phase	0	0	2	2
16. Landslides					
'Qmq2'	Liquefaction-induced landslide (N. Ogden slide complex)	0	0	11	11
'Qms'	Modern landslide, currently or recently active	0	2	0	2
'Qms2'	Modern landslide	0	0	22	22
'Qms3'	Liquefaction- induced landslide (East Ogden slide complex)	0	0	6	6
'Qmsy'	Younger landslide deposits	0	6	0	6
17. Human Disturbance					
'Qf'	Artificial fill - historical	2	0	0	2
'Qh'	Human disturbance – fill for major interstate and highways	0	53	0	53

4.4 DATABASE DEVELOPMENT

The GeoDu geotechnical database is the compilation of several liquefaction mapping efforts requiring the digitization of borehole information. A total of 1,935 standard penetration test (SPT) boreholes are recorded in this database, including 753, 250 and 932 SPT boreholes from Utah, Weber and Salt Lake counties, respectively. Gillins and Franke (2016) and Sharifi-Mood et al. (2017) compiled the data for Utah County, Bartlett and Olsen (2005), Olsen et al. (2007), Erickson, (2006) compiled the data for Salt Lake County. Lastly, Gillins (2012) and Bartlett and Gillins (2013) compiled the data for Weber County. The Utah Department of Transportation (UDOT), UGS, and local engineering firms provided a large portion of these subsurface investigations. While this paper only focused on SPT boreholes, some cone penetration tests (CPT) and shear wave velocity tests (VS) were also integrated into this database. Discussion of these datasets are beyond the scope of this study.

Data for each county were compiled in a digital format stored in a Microsoft Access Database. For computational efficiency, the data were also converted to a Matlab format. While beyond the scope of this study, liquefaction analysis routines have been coded that populate the database with extra info beyond what is available on the soil boring logs.

A preliminary form of the database structure was first developed in Bartlett and Youd (1992) to support the development of lateral spread regression equations. The raw SPT data are summarized into two tables called SITE and BLOW, which are linked via a site identification number (SITEIDNO) field. The first table, SITE (Table 4.3), contains metadata

about the borehole site, including groundwater depth, approximate address, equipment type, data source, latitude and longitude of the test, elevation, etc. The second table, BLOW (Table 4.4), contains rows of data for each sample obtained during the SPT, including: sample depth, sampler properties, the soil description and classification, uncorrected SPT blow count, and any related laboratory test results, such as dry unit weight, moisture content, Atterberg limits, fines content, grain size distribution, etc. In addition to the rows of data for each sample, more rows in the BLOW table are added to show either the ending depth of each layer of a layer depicted on a SPT log as well as the ending depth of the SPT investigation.

Data quality indicators were assigned to the data in the BLOW table. Data with a rank of "1" is assigned for data extracted originally from the report or soil log. A rank of "2" is a reasonably estimated value from other samples in the same borehole or from nearby borehole logs at similar depths. A rank of "3" is provided for those fields where data was estimated from other borehole logs at differing depths, implying lower confidence in the data.

Table 4.3: SITE table structure with field descriptions and units (modified from Gillins and Franke, 2016).

Group	Field Name	Description	Units	Data Type
Location	SITEIDNO	Identification number assigned to SPT (link to BLOW table)	N/A	[int]
	SITENAME	Name of facility or address where SPT was performed	N/A	[text]
	LATITUDE	NAD 1983 latitude (in decimal degrees)	degree	[float]
	LATITEST	Quality indicator of measurements of latitude and longitude: 1 = directly from log; 2 = scaled from maps	N/A	[int]
	LONGITUDE	NAD 1983 longitude (in decimal degrees)	degree	[float]
	EASTING	NAD 1983, UTM Zone 12 easting	meters	[float]
	NORTHING	NAD 1983, UTM Zone 12 northing	meters	[float]
Borehole Characteristics	DATE	Date of borehole	N/A	[text]
	BORING	Identification of borehole listed on SPT log	N/A	[text]
	BOREELEV	Surface elevation of SPT borehole	feet	[float]
	ELEVEST	Quality indicator for elevation of borehole: 1 = directly from log; 2 = estimated from nearby log; 3 = from maps	N/A	[int]
Groundwater information	DEPTHGW	Depth to groundwater table	feet	[float]
	GWDATE	Date of depth to groundwater measurement	N/A	[text]
	GWEST	Quality indicator of depth to groundwater measurement; 1 = directly from log at least 24 hours after drilling; 2 = from log but date not listed; 3 = from nearby log	N/A	[int]
Drilling Information	DRILLER	Name of company who drilled the borehole	N/A	[text]
	DRILLMETH	Drilling method	N/A	[text]
	RIGTYPE	Type of drill rig used by drillers	N/A	[text]
	CE	Mean correction for hammer energy ratio : 1 = safety; 1.1 = automatic. Apply to correct raw SPT blow counts to $(N_1)_{60}$	N/A	[int]
	CB	Correction for borehole diameter. Apply to correct raw SPT blow counts to $(N_1)_{60}$	N/A	[int]
	HAMMER_TYP	Hammer type (i.e., safety, donut, or automatic)	N/A	[text]
	NCORR	True/False whether SPT N-values on logs were already corrected to $(N_1)_{60}$	N/A	[text]
	BoreDiam	Diameter of borehole	inches	[float]
	BoreDiamEs	Quality indicator of diameter of borehole: 1 = directly from log; 2 = from log drilled by same rig and driller	N/A	[int]
Other Info.	GEOLUNIT	Mapped surficial geologic unit where SPT was performed	N/A	[text]
	NOTES	Notes and other information	N/A	[text]
	REFERENCE	Name of folder containing scanned images of SPT logs	N/A	[text]
	REPORT	Name of report where SPT log can be found	N/A	[text]

Table 4.4: BLOW table structure with field descriptions and units. (Modified from Gillins and Franke, 2016).

Group	Field Name	Description	Units	Data Type
Location	SITEIDNO	Identification number assigned to SPT (link to SITE table)	N/A	[int]
	DEPTH	Depth to middle of sample or depth to boundary line between layers	feet	[float]
	BOREIDNO	Identification of boring listed on SPT log	N/A	[text]
	COMMENTS	Comments or additional information	N/A	[text]
Soil type info.	SOILTYPE	Description of soil sample from log; blank values indicate boundary lines between layers	N/A	[text]
	USCS	Unified Soil Classification System	N/A	[text]
	ESTUSCS	Quality indicator for classification of sample according to the Unified Soil Classification System	N/A	[int]
	SOIL_INDEX	Soil index of sample (SI)	N/A	[int]
Soil Properties	DRYUNIT	Dry unit weight of sample	kN/m3	[float]
	DRYUNITPCF	Dry unit weight of sample in pounds per cubic foot	pcf	[float]
	ESTDRY	Quality indicator for dry unit weight of sample	N/A	[int]
	WCLASS	Index assigned to sample for estimating its unit weight	N/A	[int]
	WETUNIT	Wet unit weight of sample	pcf	[float]
	ESTWET	Quality indicator for wet unit weight of sample	N/A	[int]
	FINES	Fines content of sample (percent of sample passing a U.S. Standard No. 200 sieve)	%	[float]
	ESTFINES	Quality indicator for fines content of sample	N/A	[int]
	MOISTURE_CONTENT	Moisture content of sample	%	[float]
	ESTMOIST	Quality indicator for moisture content of sample	N/A	[int]
	MCLASS	Index assigned to sample for estimating its moisture class	N/A	[int]
	SPGRAV	Specific gravity of sample	N/A	[int]
	SGCLASS	Index assigned to sample for estimating its specific gravity	N/A	[int]
Atterberg Limits	PLASTIC INDEX	Plastic index of sample	%	[float]
	PLASTICLIMIT	Plastic limit of sample	%	[float]
	LIQUIDLIMIT	Liquid limit of sample	%	[float]
	ESRATT	Quality indicator for Atterberg limits of sample	N/A	[int]
Size Dist.	PERGRAVEL	Percent of sample retained on a No. 4 sieve	%	[float]
	RERSAND	Percent of sample passing a No. 4 sieve and retained on a No. 200 sieve	%	[float]
Sampler Information	SAMPLER	Type of sampler: CS or MCAL = modified California; DM = Dames & Moore; SH = thin-walled Shelby tube; SS = split-spoon (standard for SPT)	N/A	[text]
	SAMLPLEREST	Quality indicator for properties of sampler	N/A	[int]
	SAMPLER_LENGTH	Length sample retained in the sampler	feet	[float]
	SAMPLER_OUTSIDE_DIAMETER	Outside diameter of sampler	inches	[float]
SPT Blow Counts Information	NVALUE	Uncorrected SPT blow counts for bottom 12 in. (0.3 m) of sample (more common than $(N_1)_{,60}$)	N/A	[int]
	ESTNM	Quality indicator for SPT blow counts for bottom 12 inches (0.3 m) of sample	N/A	[int]
	N60CE	SPT blow counts for bottom 12 in. (0.3 m) of sample, corrected for rod length, sampler liner, sampler type, and borehole diameter (but not for energy ratio, CE)	N/A	[int]
	N160	Corrected SPT blow counts $(N_1)_{,60}$ from borehole log for bottom 12 in. (0.3 m) of sample	N/A	[int]

4.5 METHODOLOGY

Distributions of expected soil properties for various geologic groups within these three counties in the study area can be developed with the use of GeodU. Uncertainty in the subsurface characterization can be modeled with the help of these distributions.

Prior work has developed basic histograms to describe the geotechnical properties within the geologic units for some of these locales. For example, Olsen 2005, Olsen et al. 2007, Gillins 2012, and Gillins and Franke 2016 created frequency histograms of geotechnical properties such as corrected SPT blow count, $(N_1)_{60}$, effective stress, σ′ and other parameters in correspondence to some geologic units. This study builds upon those preliminary efforts to more fully evaluate these statistical correlations as well consider all of the data from the combined database.

In this paper, the authors target to compare the geotechnical data for geologic groups in the context of liquefaction hazard analysis. Selected soil properties that were compared include: corrected SPT blow count, $(N_1)_{60}$, clean-sand equivalent corrected SPT blow count, $(N_1)_{60cs}$, average corrected SPT blow counts in the upper 30 meters, $\bar{N}$, fines content, FC, moisture content, MC, dry unit weight, UW, and the cumulative thickness of clean-sand equivalent saturated soil susceptible to liquefaction with corrected SPT blow counts less than 15, T_{15cs} (Gillins and Bartlett, 2013).

With an adequate number of SPT tests from GeodU within a geologic group, the distribution of the expected $(N_1)_{60}$ and other soil properties for various deposit layers can

be developed. Such distributions can provide information on anticipated behavior of soil layers during seismic events.

Clean-sand equivalent values of $(N_1)_{60}$ should be calculated as many studies show that soils with high fines content are more resistant to liquefaction (e.g., Youd et al. 2001; Cetin et al. 2004). To this end, $(N_1)_{60}$ and $(N_1)_{60cs}$ were computed using the Idriss and Boulanger (2008 and 2010) recommendations following computations of the total and effective stress profiles.

Additionally, moisture contents, fines contents, and unit weights distributions were developed using the recorded measurements on all SPT logs in the database (Figure 4-5 to Figure 4-7). A soil index value (SI, Table 4.5) was assigned to every layer on each SPT log according to the most general soil description or Unified Soil Classification System (USCS) symbol in order to account for variability of these parameters per soil type. As can be seen, soil property distributions at each soil index present sensible results. For example, one should expect to see higher fines contents in samples from clay and silty sands in contrast to lower fines contents in fine gravels. Moreover, distributions of soil properties look similar according to soil index, regardless of the source of the data from tests conducted in the different counties. Note that there are a few discrepancies in the soil type distributions compared with the strict definitions in the USCS that can be observed from the samples in the database. These discrepancies occur because of misclassifications when initial field classifications are not corrected with the more detailed results of the laboratory tests (e.g., grain size distribution analysis).

Table 4.5: Soil indices and description (after Gillins and Bartlett 2013).

SI	Group	Definition
1	Fine Gravels	Silty gravel with sand, silty gravel, fine gravel
2	Gravels and Sands	Coarse to very coarse sand, sand and gravel, gravelly sand
3	Clean Sands	Sand, medium to fine sand, sand with some silt
4	Silty Sands	Fine to very fine sand, sand with silt, silty sand, dirty sand
5	Sandy Silts	Sandy silt, silt with sand
6	Clays	Non-liquefiable such as cohesive soil or soil with high plasticity

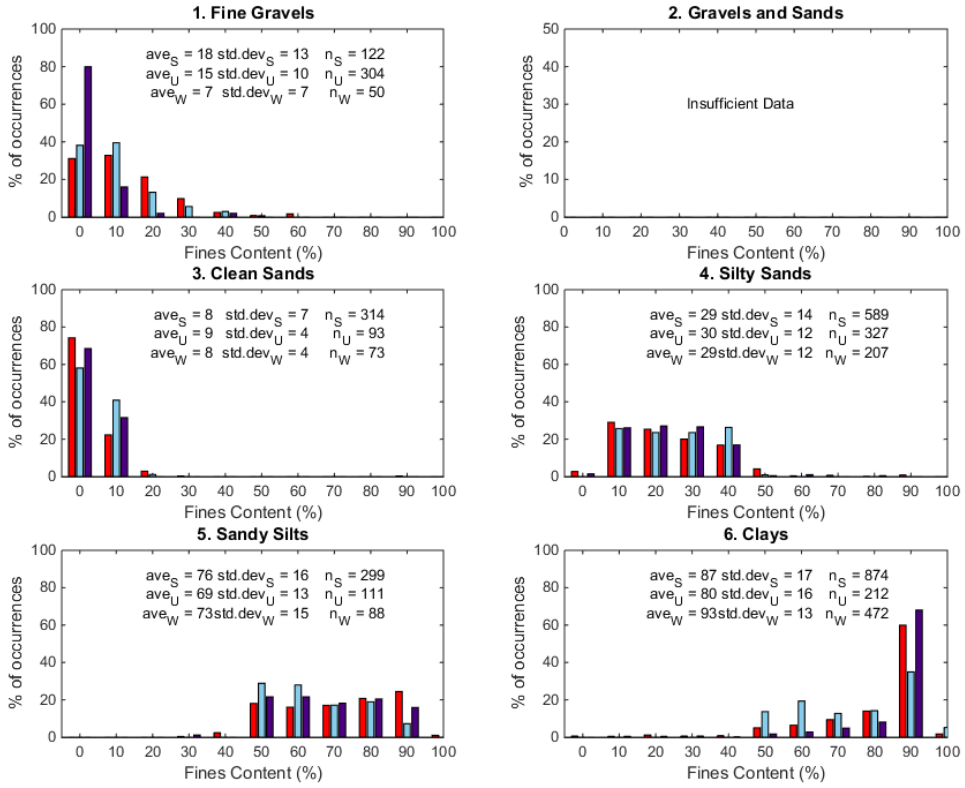

Figure 4-5: Fines content distributions for samples classified by different soil types in Utah (blue), Weber (purple) and Salt Lake (red) counties.

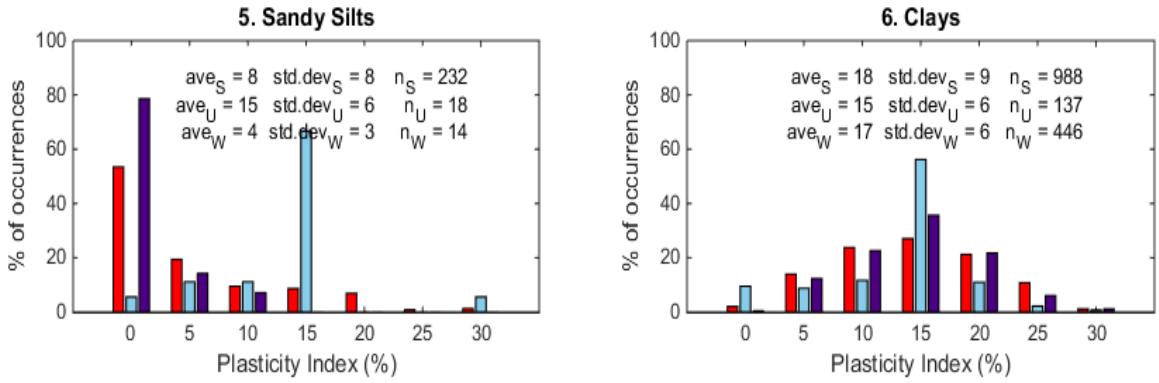

Figure 4-6: Plasticity index distributions for samples classified by different soil types (sandy silts and clays) in Utah (blue), Weber (purple) and Salt Lake (red) counties.

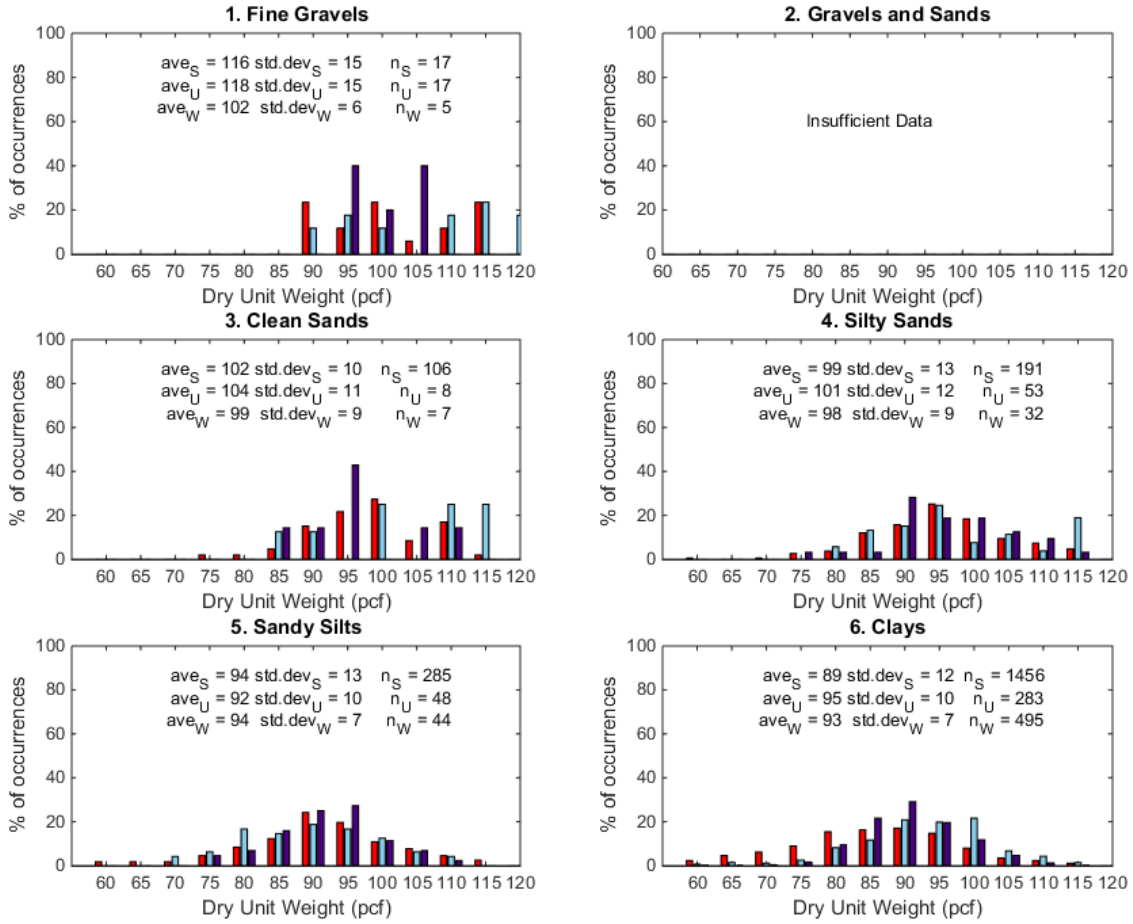

Figure 4-7: Dry unit weight distributions for samples classified by different soil types in Utah (blue), Weber (purple) and Salt Lake (red) counties.

4.6 EXAMPLE DATABASE APPLICATION

Through the development of comprehensive and readily available geotechnical databases similar to this Utah geotechnical database, important research questions such as the three introduced in this paper can be investigated. First, several examples of statistical tests were completed to discover whether it is statistically correct to group/simplify geologic groups based on whether they have common geotechnical properties (Research Question I). Next, soil properties were processed on a compiled database of the entire study area (all three counties) to express the distribution of important geotechnical parameters within different simplified geologic groups (Research Question II). Lastly, a similar approach was performed to define the distribution of geotechnical parameters on each distinct county database to carefully define and compare their distributions geographically (Research Question III).

4.6.1 Research Question *I*: Simplified Geologic Units

The first research question investigates whether the groupings performed in Table 4.2 to merge surficial geologic units into simplified geologic groups are statistically correct. Three-hundred Monte Carlo simulations were run to solve stress profile by filing in missing values in the SPT logs for moisture contents, unit weights, etc. The results were then used to calculate $\overline{N}$ values and the median of 300 simulated values were computed. Later, the medians for every borehole within each geologic group were pooled together to create samples of $\overline{N}$ median and then their average values are statistically compared.

4.6.1.1 Intra-geologic groups testing

$\overline{N}$ median values of all boreholes within every geologic unit were pooled together and samples of $\overline{N}$ median were created for each geologic unit. A null hypothesis was defined that the sample means of all $\overline{N}$ medians for all geologic units within a simplified geologic group are equal. Because several sample means with unequal variance and unequal sample sizes are compared in this analysis, a series of WelchAnova tests are performed to understand if these units are correctly grouped into a single group by determining whether there is sufficient statistical evidence to reject the null hypothesis. A 5% significance level (i.e., p-value < 0.05) was selected for rejecting the null hypothesis. After running the WelchAnova test, another statistical test (Games-Howell) was performed to compare only two units with each other in order to identify if one is different from the rest of the units.

Table 4.6: Summary of WelchAnova mean value comparison in "Stream Alluvium – Young" geologic group based on $\overline{N}$ for the borehole. (Red shading highlights units that are identified different).

Nbar	#of samples	Mean	Standard Deviation	WelchAnova Test
'Qal'	33	36	37	p = 0.10
'Qal1'	336	20	13	
'Qal2'	165	19	13	
'Qaly'	10	21	11	

P value	'Qal'	'Qal1'	'Qal2'	'Qaly'
'Qal'	NaN	0.09	0.07	0.20
'Qal1'	0.09	NaN	0.87	0.99
'Qal2'	0.07	0.87	NaN	0.93
'Qaly'	0.20	0.99	0.93	NaN

Table 4.7: Summary of WelchAnova mean value comparison in "Stream-Terrace Alluvium" geologic group based on $\bar{N}$ for the borehole. (Red shading highlights units that are identified as different).

Nbar	#of samples	Mean	Standard Deviation	WelchAnova Test
'Qat1'	7	45	23	p= 0.08
'Qat2'	10	21	29	

P value	'Qat1'	'Qat2'
'Qat1'	NaN	0.08
'Qat2'	0.08	NaN

Table 4.8: Summary of WelchAnova mean value comparison in "Alluvial Fan – Old" geologic group based on $\bar{N}$ for the borehole. (Red shading highlights units that are identified as different).

Nbar	#of samples	Mean	Standard Deviation	WelchAnova Test
'Qafb'	4	74	20	p = 0.07
'Qafm'	21	59	30	
'Qafo'	2	57	13	
'Qafp'	10	29	23	

P value	'Qafb'	'Qafm'	'Qafo'	'Qafp'
'Qafb'	NaN	0.64	0.66	0.04
'Qafm'	0.64	NaN	1.00	0.03
'Qafo'	0.66	1.00	NaN	0.28
'Qafp'	0.04	0.03	0.28	NaN

Table 4.9: Summary of WelchAnova mean value comparison in "Alluvial Fan- Young" geologic group based on $\bar{N}$ for the borehole. (Red shading highlights units that are identified as different).

Nbar	#of samples	Mean	Standard Deviation	WelchAnova Test
'Qaf'	3	9	4	p = 0.00
'Qaf1'	5	16	10	
'Qaf2'	30	50	25	
'Qafy'	178	28	25	

P value	'Qaf'	'Qaf1'	'Qaf2'	'Qafy'
'Qaf'	NaN	0.55	0.00	0.01
'Qaf1'	0.55	NaN	0.00	0.17
'Qaf2'	0.00	0.00	NaN	0.00
'Qafy'	0.01	0.17	0.00	NaN

Table 4.10: Summary of WelchAnova mean value comparison in "Delta" geologic group based on $\overline{N}$ for the borehole. (Red shading highlights units that are identified as different).

Nbar	#of samples	Mean	Standard Deviation	WelchAnova Test
'Qd3'	12	11	5	
'Qd4'	6	6	3	
'Qd5'	7	7	3	p = 0.00
'Qda'	10	13	4	
'Qdp'	13	18	16	
'Qlpd'	6	47	27	

P value	'Qd3'	'Qd4'	'Qd5'	'Qda'	'Qdp'	'Qlpd'
'Qd3'	NaN	0.21	0.37	0.65	0.61	0.12
'Qd4'	0.21	NaN	1.00	0.02	0.16	0.08
'Qd5'	0.37	1.00	NaN	0.03	0.22	0.09
'Qda'	0.65	0.02	0.03	NaN	0.91	0.16
'Qdp'	0.61	0.16	0.22	0.91	NaN	0.26
'Qlpd'	0.12	0.08	0.09	0.16	0.26	NaN

Table 4.11: Summary of WelchAnova mean value comparison in "Lacustrine Fine-Grained - Young" geologic group based on $\overline{N}$ for the borehole. (Red shading highlights units that are identified as different).

Nbar	#of samples	Mean	Standard Deviation	WelchAnova Test
'Qlf'	197	21	15	
'Qlf3'	4	25	12	p= 0.30
'Qly'	21	26	12	

P value	'Qlf'	'Qlf3'	'Qly'
'Qlf'	NaN	0.82	0.23
'Qlf3'	0.82	NaN	0.99
'Qly'	0.23	0.99	NaN

Table 4.12: Summary of WelchAnova mean value comparison in "Lacustrine Fine-Grained - Old" geologic group based on $\overline{N}$ for the borehole. (Red shading highlights units that are identified as different).

Nbar	#of samples	Mean	Standard Deviation	WelchAnova Test
'Qlbm'	3	46	12	p= 0.12
'Qlbpm'	271	28	17	

P value	'Qlbm'	'Qlbpm'
'Qlbm'	NaN	0.12
'Qlbpm'	0.12	NaN

Table 4.13: Summary of WelchAnova mean value comparison in "Lacustrine Gravel and Sand" geologic group based on $\bar{N}$ for the borehole. (Red shading highlights units that are identified as different).

Nbar	#of samples	Mean	Standard Deviation	WelchAnova Test
'Qlbpg'	16	53	38	p= 0.65
'Qlpg'	28	48	25	

P value	'Qlbpg'	'Qlpg'
'Qlbpg'	NaN	0.65
'Qlpg'	0.65	NaN

Table 4.14: Summary of WelchAnova mean value comparison in "Lacustrine and Alluvial" geologic group based on $\bar{N}$ for the borehole. (Red shading highlights units that are identified as different).

Nbar	#of samples	Mean	Standard Deviation	WelchAnova Test
'Qla'	32	30	32	p= 0.20
'Qlaly'	125	23	16	

P value	'Qla'	'Qlaly'
'Qla'	NaN	0.20
'Qlaly'	0.20	NaN

Table 4.15: Summary of WelchAnova mean value comparison in "Lacustrine Gravel" geologic group based on $\bar{N}$ for the borehole. (Red shading highlights units that are identified as different).

Nbar	#of samples	Mean	Standard Deviation	WelchAnova Test
'Qlbg'	14	66	16	p= 0.00
'Qlg'	21	40	25	

P value	'Qlbg'	'Qlg'
'Qlbg'	NaN	0.00
'Qlg'	0.00	NaN

Table 4.6 through Table 4.15 shows the results of statistical tests performed on multiple geologic groups. The rejected statistical tests in Table 4.9 and Table 4.15 (Alluvial Fan-

Young and Lacustrine Gravel) prove that there are no statistical evidence to combine the geologic units within these groups per Table 4.2 based on their distributions of $\overline{N}$. In Table 4.10, delta geologic group, Qda is the only geologic unit which is different from the rest and this is mainly because this particular unit consists of a mixture of deltaic deposits and alluvial materials which is different form all of the other Delta units. Furthermore, the modern alluvial fan located in Salt Lake County is different in terms of $\overline{N}$ parameter when compared with younger alluvial fan deposits in Utah County.

On the other hand, results from the rest of the tables demonstrate that grouping the units into the various categories was rational on the basis of $\overline{N}$, as there was lack of statistical evidence for rejecting the null hypothesis. For example, the statistical test could not separate modern stream alluvium deposits from Utah County to modern and young stream alluvium from Salt Lake County. Table 4.11 and Table 4.12 presents the results for the young and old lacustrine, fine-grained deposits, respectively. The statistical tests were not able to differentiate mixed fined grained lacustrine deposits in Utah County from young lacustrine existed in Salt Lake County, indicating that the grouping was reasonable based on $\overline{N}$ distributions.

4.6.1.2 Inter geologic groups testing

Statistical tests can also be performed between the simplified geologic groups to determine if further reduction is warranted. To this end, two simplified geologic groups with the most similar characteristics are selected: Lacustrine fine-grained-young and Lacustrine fine-grained-old. This time, the null hypothesis was defined as: “the sample mean of all $\overline{N}$

median values from young Lacustrine fine-grained geologic group is equal to that of the old Lacustrine fine-grained". A similar approach to that implemented in the previous section is applied for this analysis, and the results are presented in Table 4.16.

Table 4.16: Summary of the WelchAnova mean value comparison statistical testing between "Young Lacustrine Fine-Grained" and "Old Lacustrine Fine-Grained" simplified geologic groups based on $\overline{N}$.

Nbar	#of samples	Mean	Standard Deviation	WelchAnova Test
Lacustrine Fine-Grained - Young	226	22	15	p= 0.00
Lacustrine Fine-Grained - Old	274	29	17	

P value	Lacustrine Fine-Grained - Young	Lacustrine Fine-Grained - Old
Lacustrine Fine-Grained - Young	NaN	0.00
Lacustrine Fine-Grained - Old	0.00	NaN

This statistical test rejects the null hypothesis that two simplified geologic groups can be grouped together. While both categories contain significant clay and silt deposits related to Lake Bonneville and its successor the Great Salt Lake, their depositional time (age) are very different resulting in varying relative density, and hence, $\overline{N}$.

4.6.2 Research Question *II*: Statistical Characterization

The second research question explores the possibility of statistically describing simplified geologic groups by characterizing the distribution of various soil properties among them. Within this analysis, boreholes from all three counties in the study area were aggregated into a single database, and histograms of various geotechnical variables were produced for

each simplified geologic group. Moreover, T_{15cs} distributions for a few, representative simplified geologic groups within the database were developed.

4.6.2.1 Soil Classification

First, the range of soil types in each geologic group is described with a histogram (Figure 4-8) plotting the normalized layer thickness, the accumulated thickness of soil samples with a specific soil index (e.g. gravel, sand and etc) divided by total thickness of all soil samples residing within a given geologic group. Data with a soil index of 2 (i.e. gravels and sands) was clipped from the histograms because there are not enough samples characterized with this index inside the database. The overall soil indices percent coverage for alluvial fan and delta, young stream alluvium and several other geologic groups correlates well with the predominant soil types that would be expected based on the geology. For example, the young and old lacustrine fine-grained soils are principally composed of silts and clays and the old alluvial fan and alluvial fan and delta geologic group primarily contains gravel.

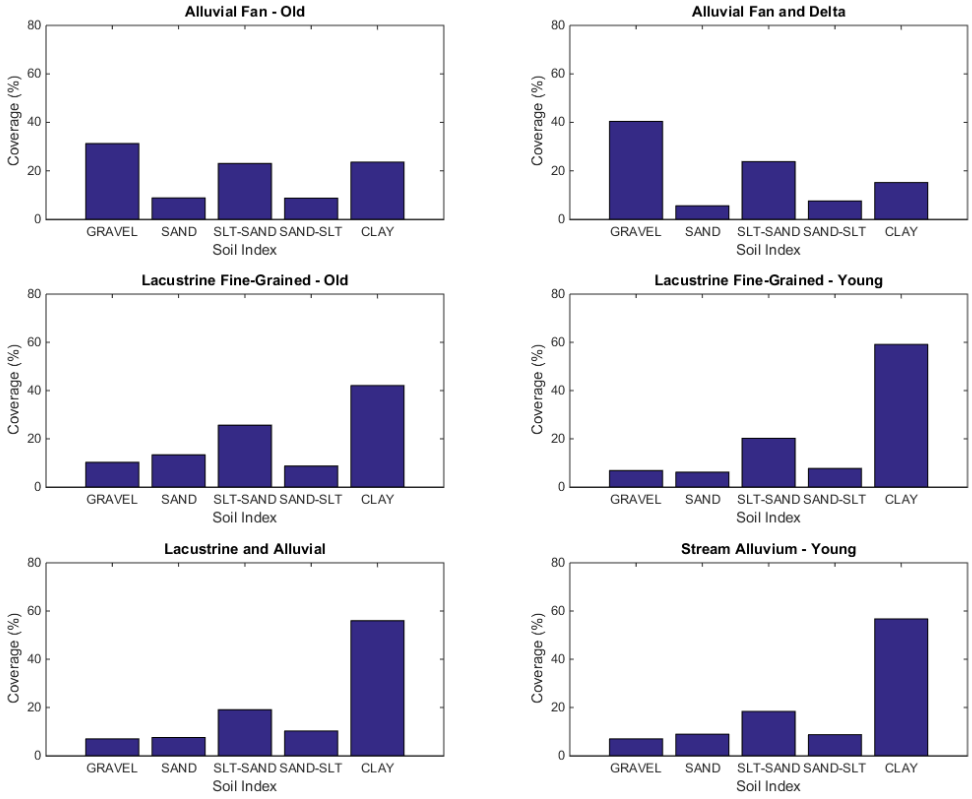

Figure 4-8: Soil type coverage within various geologic groups with all samples in the combined database.

4.6.2.2 Soil Properties

General soil properties including dry unit weight, fines content, and plasticity index histograms (Figure 4-9 to Figure 4-11) for existing geologic groups were created using all soil samples in the combined database. Note that these plots do not distinguish the results by soil index. However, for the plasticity index, these tests were only run on the fines portion of each sample.

As expected, there is not a tremendous amount of difference in dry unit weight (Figure 4-9). However, the alluvial fans tend to be significantly denser than the lacustrine or alluvial material. This makes sense since the alluvial fans tend to have more cobbles and gravels and deposit the denser materials since they occur when the material comes out of the canyon down the stream with higher energy. The alluvium and lacustrine tends to be lower energy deposition where lighter sediment tends to flocculate and accumulate in a looser, less dense configuration, resulting in a lower unit weight.

Furthermore dry unit weight is correlated with the degree of consolidation a soil profile experienced and has a direct relationship with soil stiffness and strength. The stream alluvium geologic group would be less likely to settle when compared to the alluvial fan and delta due to higher dry unit weight values. Additionally, soils with higher dry unit weight values typically have higher shear strengths and more bearing capacity. They also tend to have lower void ratios, reducing permeability and potential frost heave.

Distinctions in the distributions of fines content (Figure 4-10) and plasticity index (Figure 4-11) within each surface geologic group can be utilized to describe these soils as a clay, silt, sand or gravel. Generally, soils with lower fines contents and lower plasticity will be more susceptible to liquefaction. In this context, by comparing lacustrine and alluvial with alluvial fan and delta, the alluvial fan and delta would generally be more prone to liquefaction due to their combined and generally lower fines content and plasticity index.

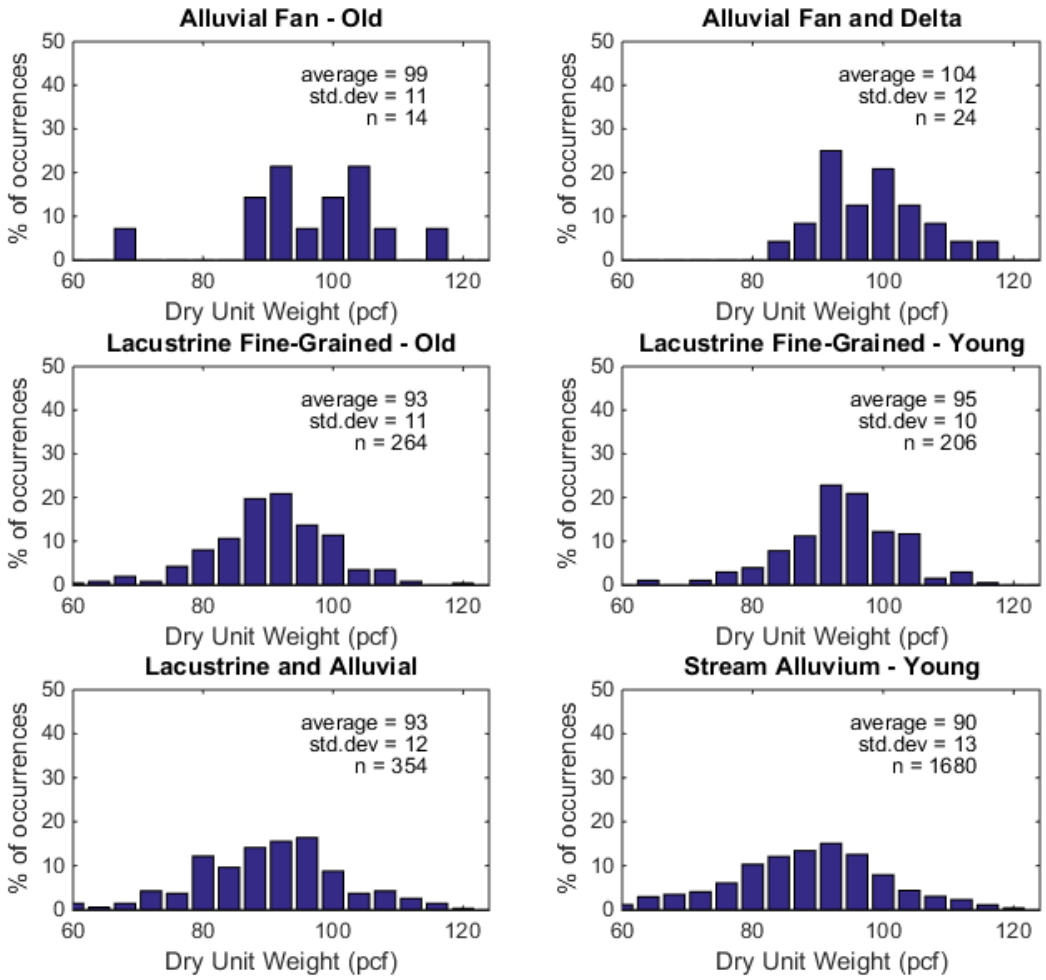

Figure 4-9: Distributions of dry unit weight for several simplified geologic groups using samples for the combined database.

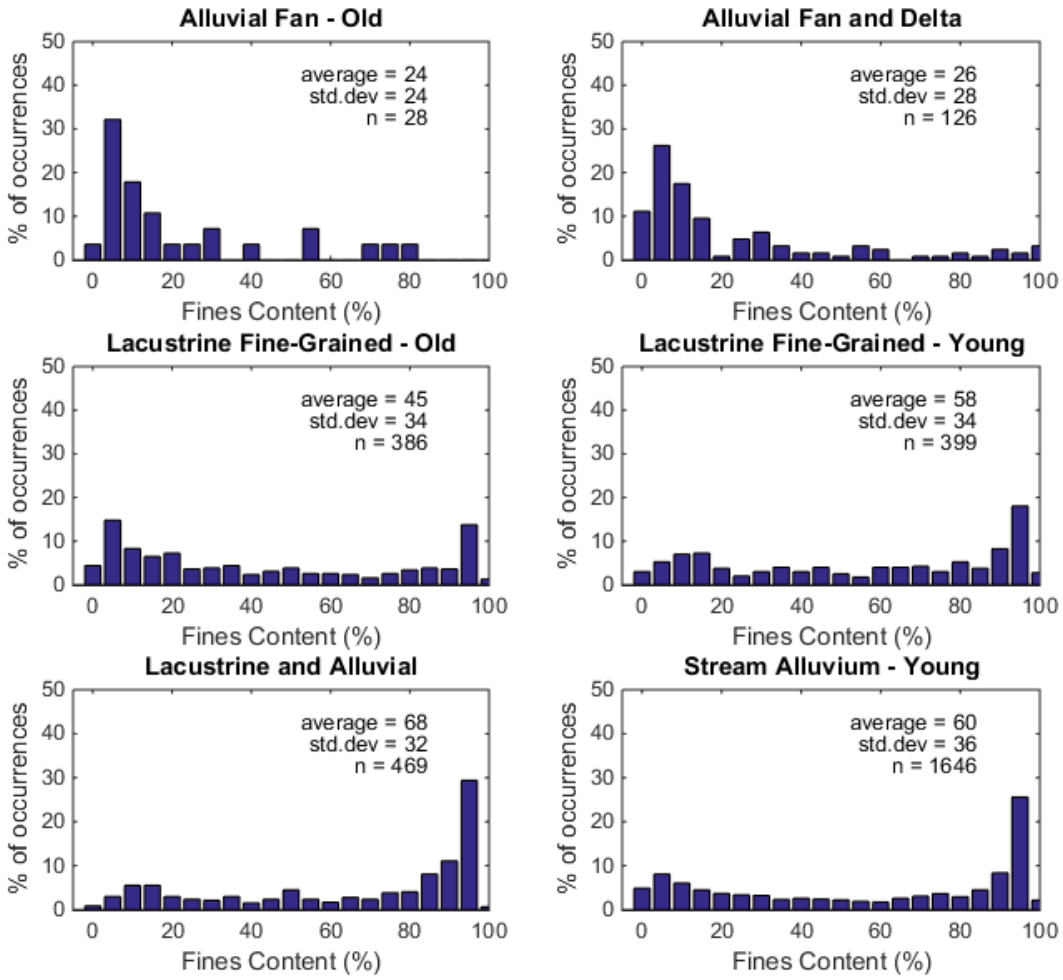

Figure 4-10: Distributions of fines content for several simplified geologic groups using samples for the combined database.

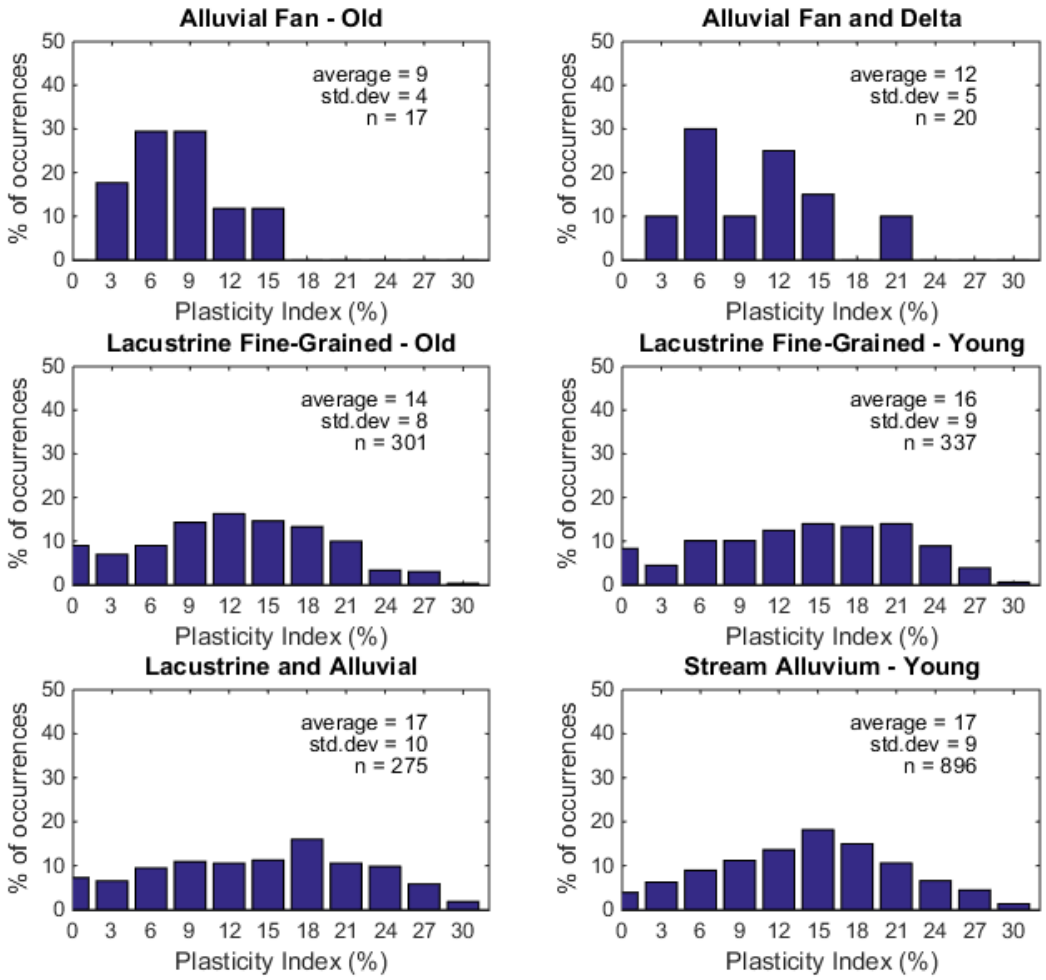

Figure 4-11: Distributions of plasticity index for several simplified geologic groups using samples for the combined database.

4.6.2.3 SPT Blow Count

The density, which strongly influences the soils' resistance to liquefaction and lateral spreading, is described by the blow counts obtained throughout each SPT borehole categorized by each geologic group. Three sets of histograms related to this parameter are

created: $(N_1)_{60}$, $(N_1)_{60cs}$ and $\bar{N}$, which are depicted in Figure 4-12 to Figure 4-14, respectively. For this analysis, as described in methodology section, we have used the results of the 300 Monte Carlo simulations for correcting the raw blow counts. Blow count values that were inflated due to sampler refusal were filtered out in the process of constructing the distributions.

Both $(N_1)_{60}$ and $(N_1)_{60cs}$ are proportional to the soil's shear strength. Higher corrected SPT blow counts, thus higher strength, are observed from the distributions of "Alluvium and Colluvium" with a peak at 20 to 25. In comparison, a weaker unit such as "Alluvial Fan – Young" peaks at 5 to 10 with lower values in its distribution. Similarly, the clean sand equivalent SPT blow count describes the relative stiffness of the soil layer. Values of $\bar{N}$ are often correlated with the shear wave velocity of the soil. A higher value (e.g., Alluvial fan and delta) indicates more shear strength (Koike et al., 1996). In contrast, young stream alluvium deposits have a $\bar{N}$ distribution indicating lower values and would have relatively lower V_{s30} values.

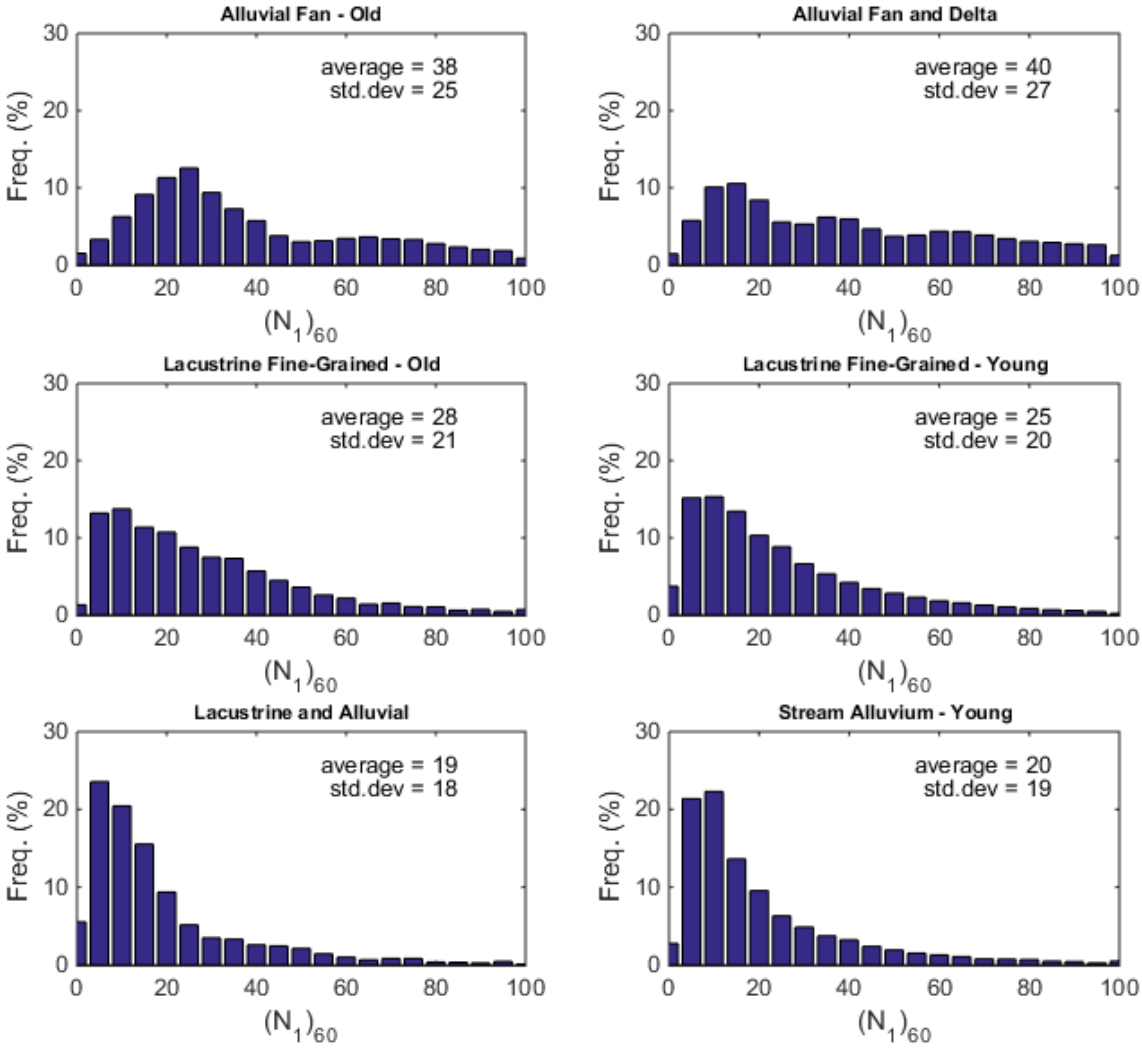

Figure 4-12: $(N_1)_{60}$ distribution of several simplified geologic groups created from the combined database.

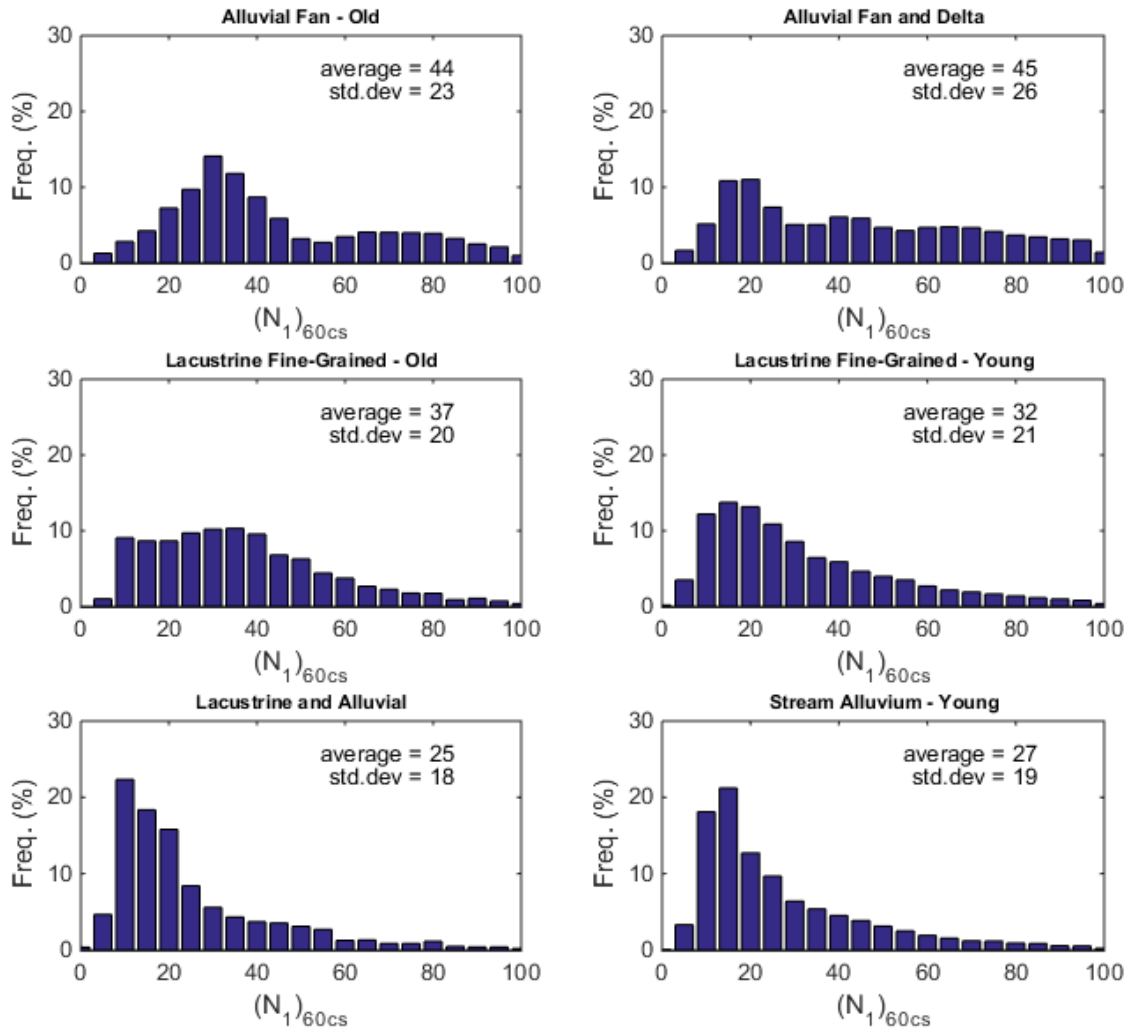

Figure 4-13: $(N_1)_{60cs}$ distribution of several simplified geologic groups created from the combined database.

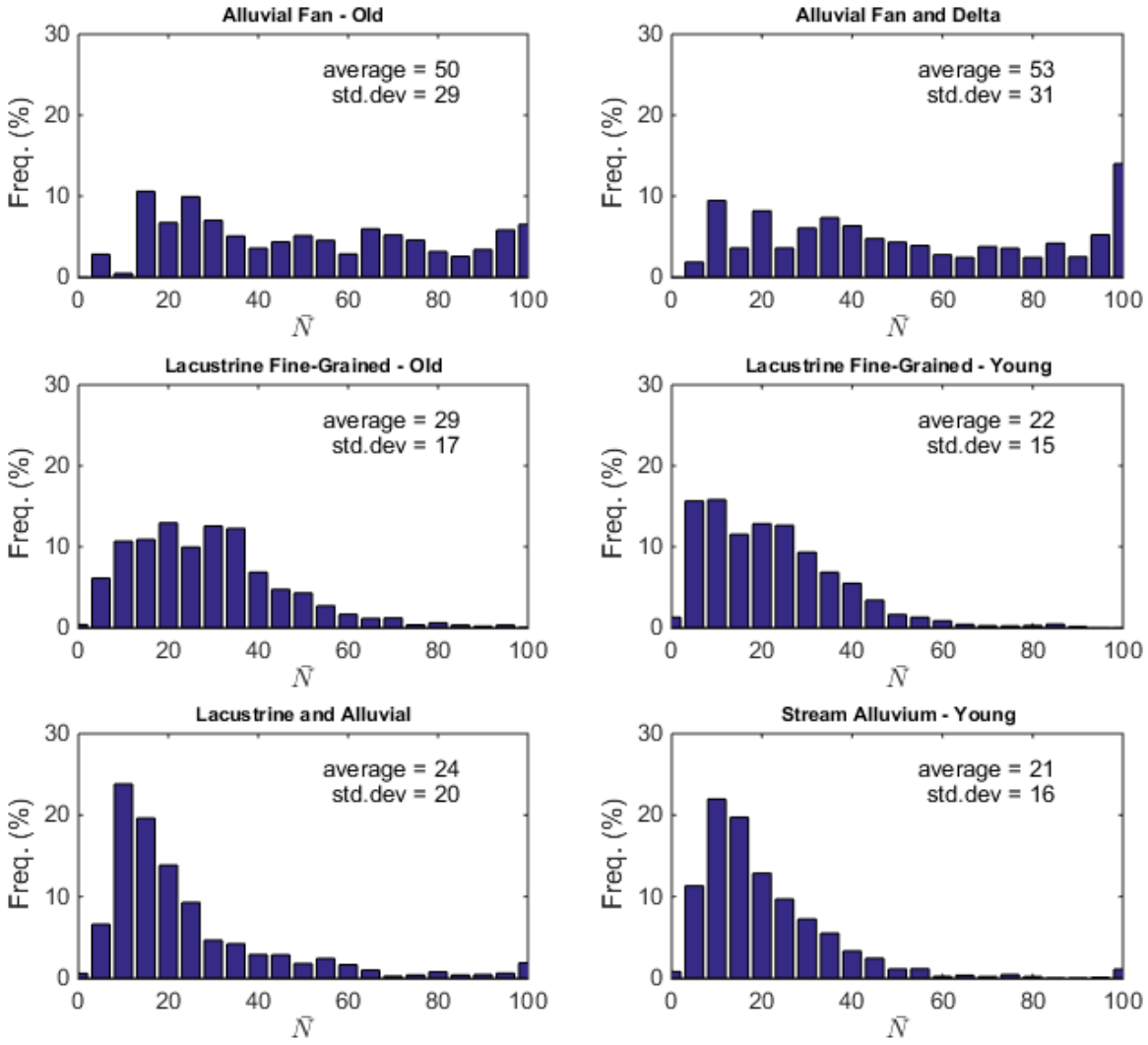

Figure 4-14: $\bar{N}$ distribution of several simplified geologic groups created from the combined database.

.

4.6.2.4 $T_{15,cs}$

Next, simulated $T_{15,cs}$ values at each boreholes located within a specific simplified geologic group were pooled together to develop distributions of $T_{15,cs}$ for each simplified geologic group.

Figure 4-15 illustrates distributions developed from these distributions of $T_{15,cs}$ for each of the simplified geologic groups within the database. In recently developed regression equations for lateral spreading, its magnitude is proportional (on a log scale) to the layer thickness (Gillins and Bartlett 2013). With the help of this plot, one can perform comparison among units to found out which unit has a higher chance of having thicker layers of soil which may undergo lateral spreading during a major or great earthquake (Sharifi-Mood et al. Under Review). In a similar situation with constant moment magnitude, distance to a seismic source and equal slope and free-face geometry, geologic groups with relatively larger values of $T_{15,cs}$ will displace more horizontally during lateral spreading. Within the database, SPT borehole logs in the lacustrine units (e.g., lacustrine and alluvial, fine-grained lacustrine) tended to show greater $T_{15,cs}$ values, whereas smaller $T_{15,cs}$ values were observed in the older alluvial fans.

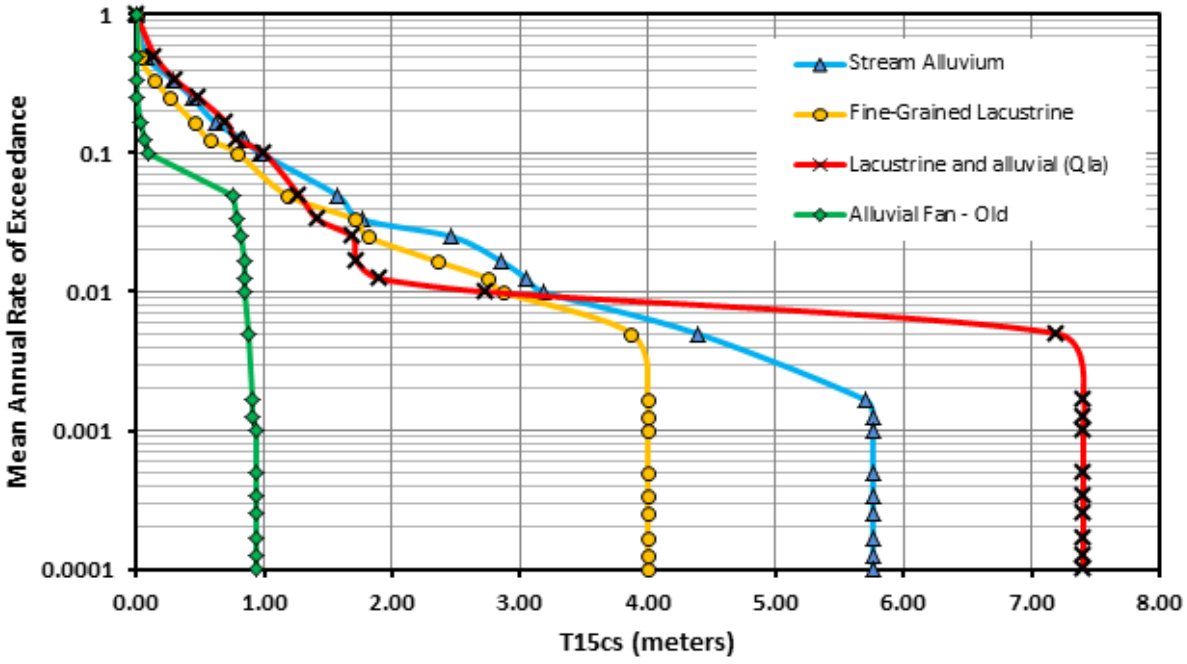

Figure 4-15: $T_{15,cs}$ distribution for several simplified geologic groups.

4.6.3 Research Question *III*: Geographical Variation Analysis

The third research question further investigated potential geographical influence on geotechnical parameters in geologic groups as well as exhibiting commonality among them. The histograms of geotechnical parameters for common simplified geologic groups were also compared for the three counties.

4.6.3.1 Soil Classification

Similar to the previous section, histograms of normalized layer thickness of various soil indices were created (Figure 4-16). It is observed that within a certain geologic group, soil indices coverage does not widely vary geographically. For example, approximately 60 and 20 percent of all samples within the surficial geologic group of young lacustrine fine-

grained in Utah, Salt Lake and Weber counties are clay and silty sands respectively. This makes sense as the geologic units consisting in this group are mainly composed of silts and clays deposited in shallow lakes and marsh deposits after the regressive phase of Lake Bonneville and the Great Salt Lake. Thus, the same geologic feature contributed to the lacustrine soils deposited in all three counties, and there is therefore limited spatial variability.

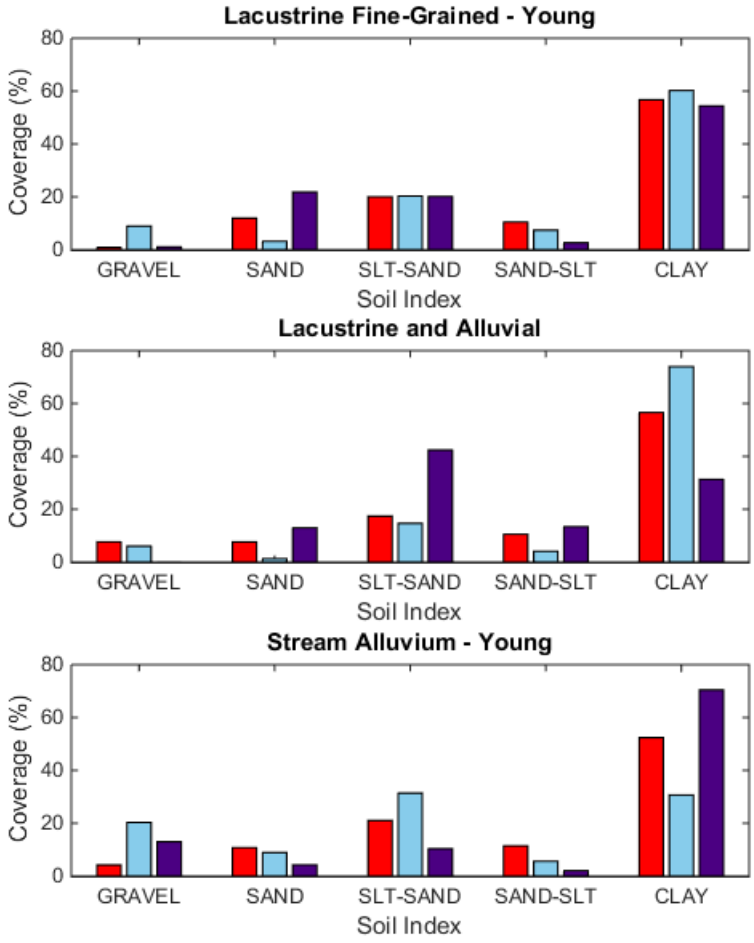

Figure 4-16: Soil type coverage within three geologic groups for Utah (blue), Weber (purple) and Salt Lake (red) counties.

4.6.3.2 Soil Properties

Soil properties such as fines content, plasticity index, and dry unit weight were selected from available information in the database to compare the distributions of simplified geologic groups in Utah, Weber and Salt Lake counties (Figure 4-17 to Figure 4-19).

Overall, comparable distributions of these properties are observed among three counties. While some of the statistics suffer from insufficient samples, the trends of comparable statistical parameters and distributions can be tracked on geotechnical information related to dry unit weight, fines content and plasticity index.

The trends of dry unit weight distribution in young lacustrine fine-grained geologic group support the third objective of this paper, proposing similar geotechnical information of common geologic groups from different locales but with similar geologic settings. A very small difference was observed among data from Utah County to those observed in Salt Lake and Weber County in fines content distributions, which may be a result of insufficient data in Utah County. Furthermore, geographically consistent, young stream alluvium tended to have several medium plastic (12-16) soils and young lacustrine fine-grained tended to have highly plastic (17-20) soils.

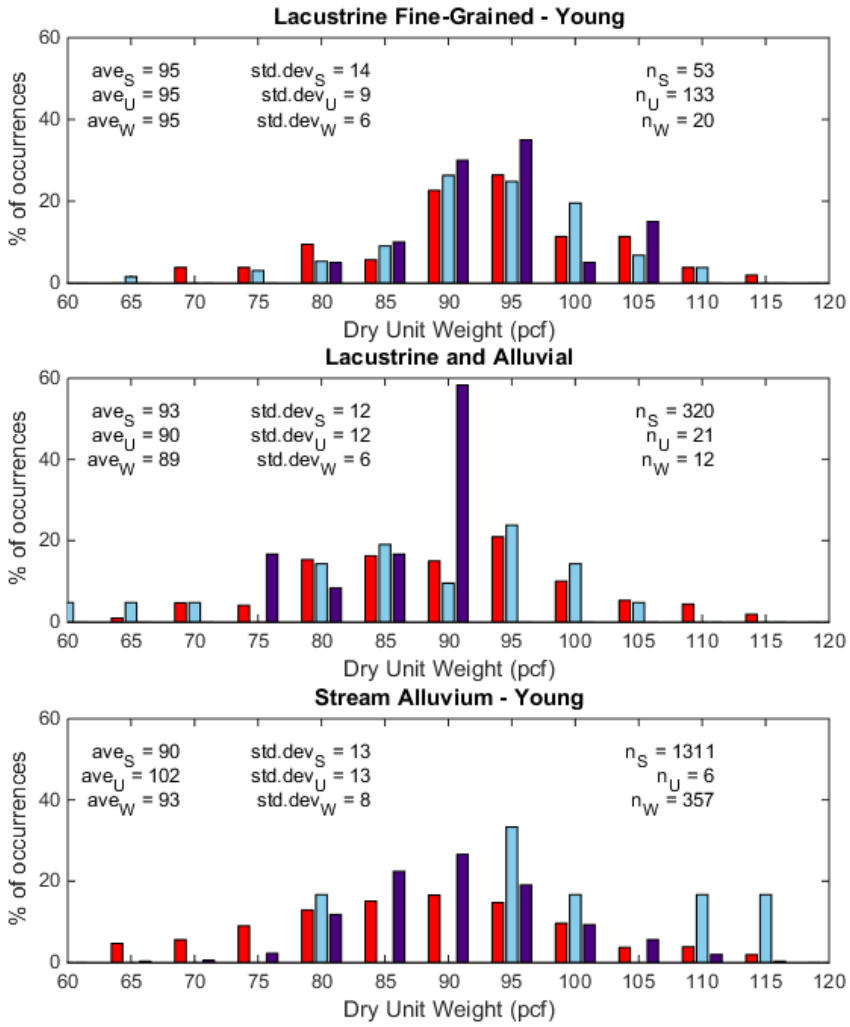

Figure 4-17: Distributions of dry unit weight from soil samples within various geologic groups for Utah (blue), Weber (purple) and Salt Lake (red) counties.

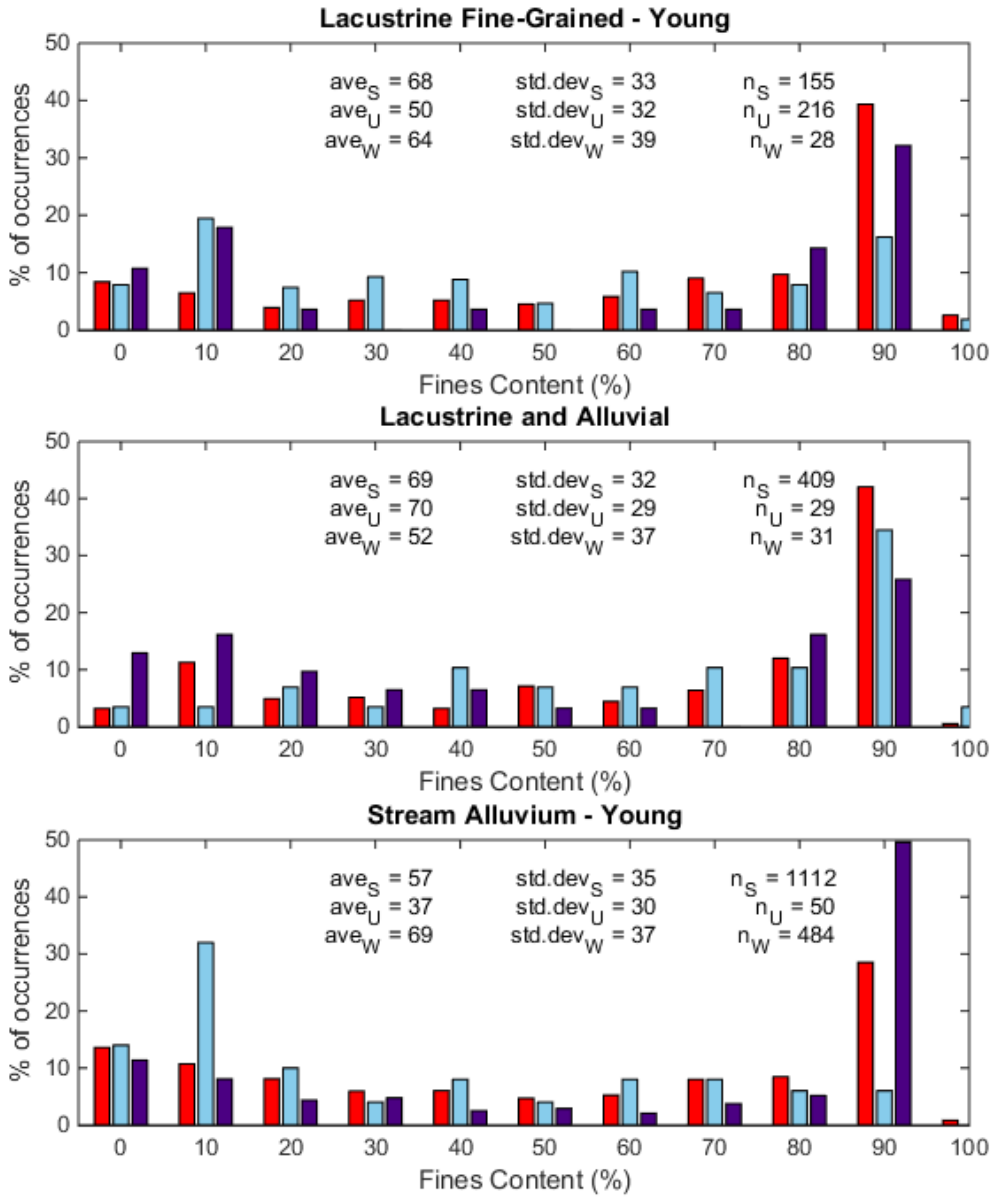

Figure 4-18: Distributions of fines content from soil samples within various geologic groups for Utah (blue), Weber (purple) and Salt Lake (red) counties.

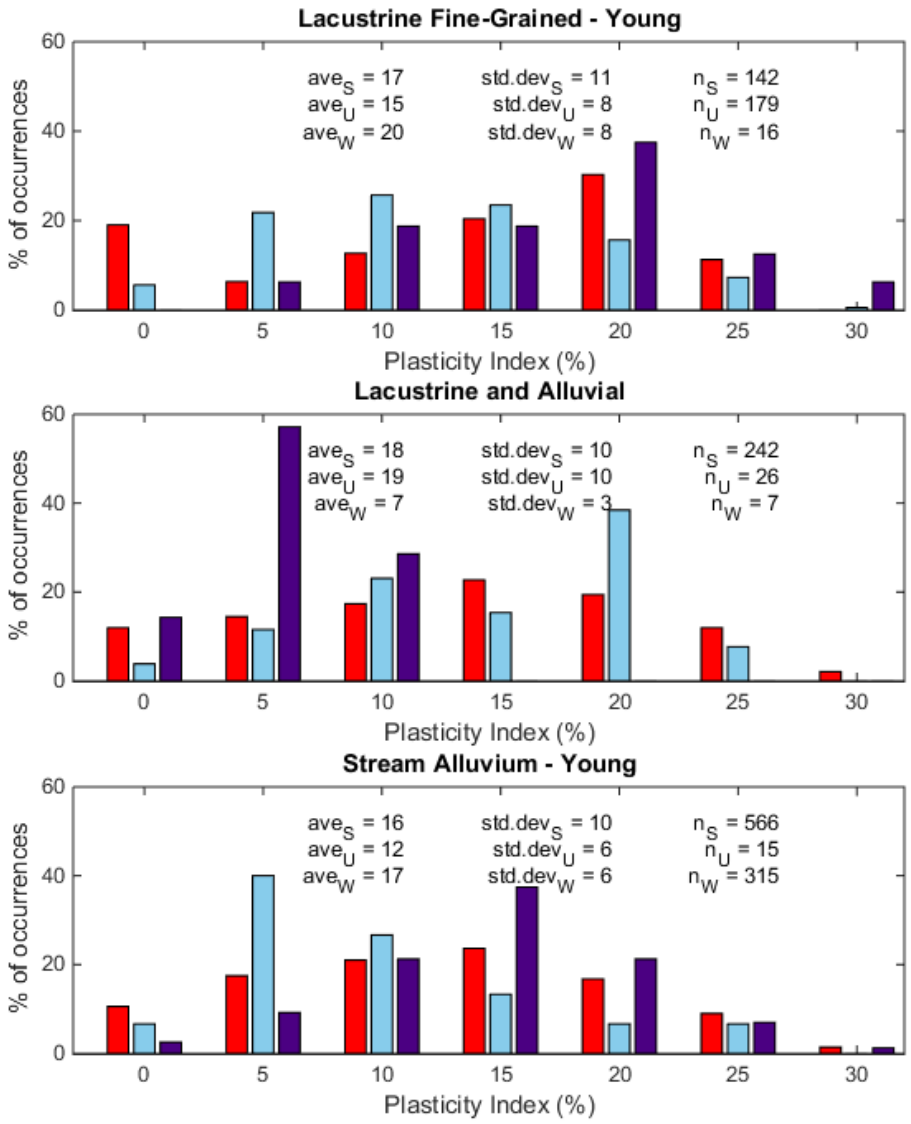

Figure 4-19: Distributions of plasticity index from soil samples within various geologic groups for Utah (blue), Weber (purple) and Salt Lake (red) counties.

4.6.3.4 SPT Blow Counts

Figure 4-20 and Figure 4-21 depict $(N_1)_{60}$, $(N_1)_{60cs}$ and $\overline{N}$ distribution at each simplified geologic group based on the above-mentioned Monte Carlo simulation to account for variation in the soil properties. A comparison of anticipated soil strength and resistance to liquefaction can be made by analyzing such histograms. The SPT blow count is directly proportional to soil packing (soil being loose or dense), relative density and soil friction angle (Meyerhoff 1956).

Young stream alluvium geologic unit are consistently medium dense with a substantial amount of very loose and loose soils which makes them very susceptible to liquefaction and lateral spreading.

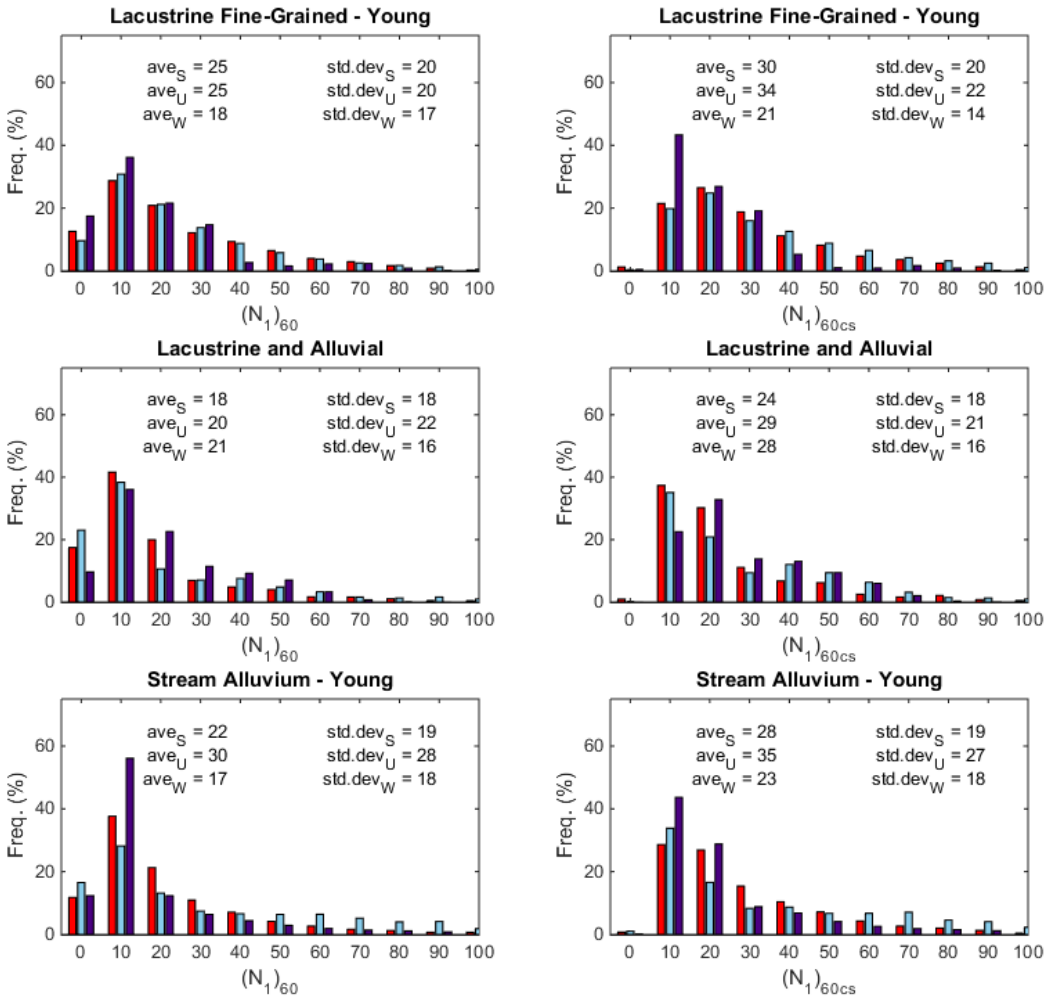

Figure 4-20: $(N_1)_{60}$ distribution (on left) and $(N_1)_{60cs}$ distribution (on right) for selected simplified geologic groups created for Utah (blue), Weber (purple) and Salt Lake (red) counties.

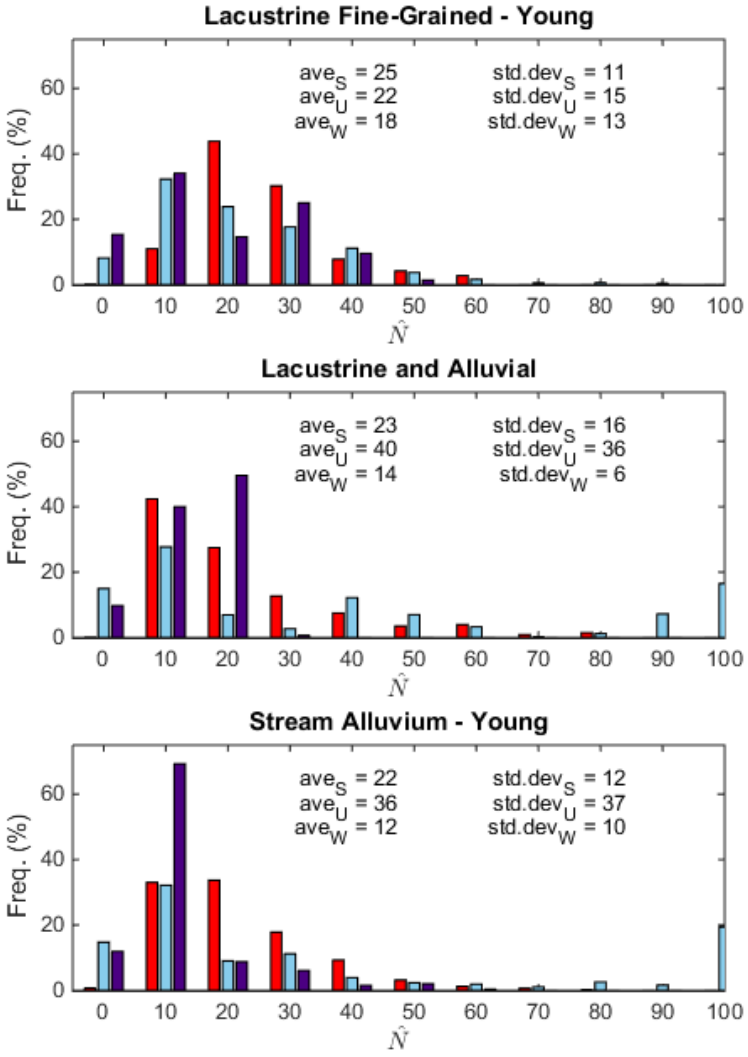

Figure 4-21: $\bar{N}$ distribution for selected simplified geologic groups created for Utah (blue), Weber (purple) and Salt Lake (red) counties.

4.6.3.5 Statistical Testing

Another statistical testing is defined to investigate whether samples from the same geologic units in the different geographical counties are similar. The null hypothesis is "the sample means of all $\overline{N}$ medians for Qal1 and Qal2 geologic units located in Weber County and Salt Lake County are equal" and the WelchAnova test is performed on a 95% confidence level. In this section, the test is performed on two geologic units within the stream alluvium geologic group (Table 4.17).

Table 4.17: Summary of WelchAnova geographical comparison for geologic units Qal1 and Qal2 in "Stream Alluvium – Young" geologic group. (Red shading highlights units that are identified as different).

Nbar	#of samples	Mean	Standard Deviation	WelchAnova Test
'Qal1_S'	277	22	13	p= 0.00
'Qal1_W'	59	11	8	
'Qal2_S'	100	23	12	
'Qal2_W'	65	13	11	

P value	'Qal1_S'	'Qal1_W'	'Qal2_S'	'Qal2_W'
'Qal1_S'	NaN	0.00	0.88	0.00
'Qal1_W'	0.00	NaN	0.00	0.52
'Qal2_S'	0.88	0.00	NaN	0.00
'Qal2_W'	0.00	0.52	0.00	NaN

While Qal1 and Qal2 are similar in a specific county, the Qal1 deposited in Salt Lake County is statistically different from the similar geologic unit residing in Weber County. These geologic units, although similar in depositional processes are deposited from different rivers running through each county, which results in these differences. For example, the stream alluvium in Salt Lake County is deposited more slowly by the Jordan River whereas the similar geologic units in Weber County are formed by the more active Weber and Ogden River. In high-flow waterways, local gravel, pebbles and small rocks are expected to

be in sediment transport. However, harder rocks are less likely to become sediment, while soft rocks erode quicker and are easily carried away by flowing water.

The result of this test does not invalidate the results for the young stream alluvium geologic group presented in Table 4.6. The previous comparison has been made among all samples acquired from combined database in Qal, Qal1, Qal2 and Qaly geologic units whereas this test specifically compares the samples of Qal1 and Qal2 located in Weber and Salt Lake counties. Combing all of the data made it more difficult to notice small, individual nuances from river to river among counties. These differences between counties are probably as a result of the underlying geologic units with possible differences in geologic interpretation between areas which is mainly a limitation of the fact that the geologic units are mapped surficial.

4.7 FUTURE APPLICATIONS

In addition to the examples presented in this paper, there are many additional applications where this database can be utilized. For instance, the database can be used for hazard mapping of expansive soils, collapsible soils, frost heave, surficial and deep seated landslides, and liquefaction and lateral spreading.

Furthermore, geotechnical records are the key part of any site investigation project. They are useful for the reconstruction of subsurface stratigraphy. In various cases where the subsurface sediment deposits are complex and require comprehensive inspection, geotechnical subsurface investigation database becomes advantageous (Raper and Wainwright, 1987). The database can be used to generate maps of average soil properties

for selected areas and to generate subsurface soil profiles. As an example, these maps and profiles can be then compared to past earthquake damages or other types of information for expedited assessment of infrastructure (Doroudian, 1997). As another example, subsurface profiles and surficial sediment classification (leading to determination of runoff coefficients, absorption and infiltration rates, etc.) can be determined with this database and combined with water quality and flow data for hydrological, hydrogeological, and ground-water resource analyses (Brandenberg et al., 2010).

The database can be also used to help in planning a geotechnical investigation campaign more efficiently and economically. The data and resulting soil profiles can assist in planning the overall site investigation, developing sampling strategies, adapting the plan when drilling in highly variable geologic units, etc. The database can also supplement the data obtained in the site investigation (after appropriate validation) as these results may provide better information than simply using a "textbook" value for further geotechnical analysis. Note that it is not the intent of this study or database to replace site investigations for engineering projects. Such usage would be reckless. Nevertheless, the database can augment and supplement those investigations. The database can continually be updated and improved as these new information are available, further enhancing this benefit.

4.8 CONCLUSION

A comprehensive database from available geotechnical subsurface investigations was compiled and evaluated. The paper demonstrates several advantages associated with this geotechnical database and applications to quantify geologic units for hazard analysis and

mapping purposes. Relationships among geologic units and geotechnical parameters are drawn through statistical analyses. The derived distributions are useful to serve as surrogate data (with uncertainty information) in areas where geotechnical subsurface investigations are not available. Additionally, these distributions quantify important properties of each geologic unit, providing valuable information to determine the susceptibility of each unit to different geo-hazards such as liquefaction and lateral spreading.

Distributions of soil properties such as those developed in this paper are very important in locales with minimal geotechnical subsurface investigations. Commonly, within a majority of regional mapping projects, a surficial geology map is available while access to SPT boreholes or CPT soundings can be much more challenging. As a result, many analyses rely on qualitative approaches rather than being able to utilize this quantitative data. One can utilize the quantitative data from the limited sampling locations to describe the larger area mapped in the same surficial geologic unit. These distributions also enable one to quantify uncertainty throughout the mapping or analysis process. For example, a reliable distribution of subsurface investigations can help to account for and accurately model the soil strength uncertainty throughout the study area (e.g. Sharifi-Mood et al. Under Review).

Analyses using this database provide the ability to distinguish geologic units from one another in terms of properties or relative hazards. As an example, histograms of a geotechnical parameter, $(N_1)_{60}$, indicates strength of a geologic unit and the resulting

distributions provide a good estimate of how soils in that geologic unit will likely behave when experiencing a strong ground motion from an earthquake.

The authors encourage the geotechnical community to take grass-roots action to build up similar databases in other locales. Having strong, comprehensive geotechnical databases that cover large extents (e.g., statewide) and later sharing them with the community can provide desirable, detailed information needed for future research in geological hazard topics, hazard analyses and mapping, and many other purposes.

4.9 ACKNOWLEDGMENTS

Financial support for this study was provided by the United States Geological Survey (USGS), Utah Department of Transportation (UDOT) and Central Utah Water Conservancy District (CUWCD). Specifically, the authors acknowledge members of UGS, UDOT, and members of ULAG for contributing borehole logs for the database and we appreciate USGS generous grants that these databases were collected under: USGS award number 04HQGR0026, 07HQGR0021, 07HQGR0024, G12AP20074 and G14AP00118. Further, we thank Griffen Erickson and Jasmyn Harper who participated in the database compilation process. We also acknowledge the support of the Cascadia Lifeline Program (CLiP) provided to the lead author`s academic studies. The authors would also like to thank Oregon State University Civil Engineering, Geomatics research lab for their assistance.

4.10 REFERENCE

Anderson, L.R., Keaton, J.R., and Eldredge, S.N., (1994), Liquefaction-potential map for a part of Utah County, Utah: Utah Geological Survey Public Information Series 28, 2 p., scale 1:365,000.

Bartlett, S. F., & Gillins, D. T. (2013). Mapping the probability and uncertainty of liquefaction-induced ground failure for Weber County, Utah. USGS External Research Award No. G12AP20074 Technical Report.

Bartlett, S. F., & Olsen, M. J. (2005). Probabilistic Liquefaction Potential and Liquefaction-induced Ground Failure Maps for the Urban Wasatch Front: Collaborative Research with the University of Utah, Utah State University and the Utah Geological Survey, Phase 1, FY2004. Department of Civil and Environmental Engineering, University of Utah.

Brandenberg S, J., Bellana, N., & Shantz, T. (2010). Shear Wave Velocity as a Statistical Function of Standard Penetration Test Resistance and Vertical Effective Stress at Caltrans Bridge Sites. Technical Report Documentation.

Constenius, K. N., Clark, D. L., & Ehler, J. B. (2011). Interim Geologic Map of the Provo 30′× 60′ Quadrangle, Salt Lake, Utah, and Wasatch Counties. Utah Geological Survey Open-File Report 586, 42 p., 2 plates, scale 1: 62: 500.

Cetin, K. O., Seed, R. B., Der Kiureghian, A., Tokimatsu, K., Harder Jr, L. F., Kayen, R. E., & Moss, R. E. (2004). Standard penetration test-based probabilistic and deterministic assessment of seismic soil liquefaction potential. Journal of Geotechnical and Geoenvironmental Engineering, 130(12), 1314-1340.

Doroudian, M. (1997). Development of 3-D geotechnical database and its application to the evaluation of nonlinear site response and seismic zonation.

El May, M., Dlala, M., & Chenini, I. (2010). Urban geological mapping: Geotechnical data analysis for rational development planning. Engineering Geology, 116(1), 129-138.

Erickson, G. L., Bartlett, S. F., Solomon, B. J., Anderson, L. R., & Olsen, M. J. (2006). Probabilistic Liquefaction Potential Mapping of Salt Lake Valley, Utah.

Gillins, D.T., (2012). Mapping the Probability and Uncertainty of Liquefaction-Induced Ground Failure, Ph.D. Dissertation, Department of Civil and Environmental Engineering, University of Utah, Salt Lake City, UT.

Gillins, D. T., & Bartlett, S. F. (2013). Multilinear Regression Equations for Predicting Lateral Spread Displacement from Soil Type and Cone Penetration Test Data. Journal of Geotechnical and Geoenvironmental Engineering, 140(4), 04013047.

Gillins, D.T., & Franke, K., 2016. Probabilistic Liquefaction Potential and Lateral Spread Hazard Maps for Utah County, Utah: Collaborative Research with Brigham Young University and Oregon State University, USGS External Research Report, USGS Award Nos. G14AP00118 and G14AP00119, Reston, VA, 89 pp.

gINT Geotechnical and Geoenvironmental Software. Available at: https://www.bentley.com/en/products/brands/gint

Harty, K. M., & Lowe, M. (2005). Interim Geologic Map of the Plain City Quadrangle, Weber and Box Elder Counties, Utah, Utah Geological Survey Open-File Report 451.

Idriss, I. M., & Boulanger, R. W. (2008). Soil liquefaction during earthquakes.

Idriss, I. M., & Boulanger, R. W. (2010). SPT-based liquefaction triggering procedures. Rep. UCD/CGM-10, 2.

Koike, K., Minta, T., Ishizaka, S., & Ohmi, M. (1996). Hydrogeological and ground-water resource analysis using a geotechnical database. Natural Resources Research, 5(1), 23-32.

Miller, R.D., (1980). Surficial geologic map along part of the Wasatch Front, Salt Lake Valley, Utah: U.S. Geological Survey Miscellaneous Field Studies Map MF-1198, scale 1:100,000.

New Zealand Geotechnical Database. Available at: https://canterburygeotechnicaldatabase.projectorbit.com

Olsen, M. J., Bartlett, S. F., and Solomon, B. J., (2007). Lateral spread hazard mapping of the Northern Salt Lake Valley, Utah for a M7.0 scenario earthquake, Earthquake Spectra 23(1), 95-113.

Personius, S.F., and Scott, W.E., (1992). Surficial geologic map of the Salt Lake City segment and parts of adjacent segments of the Wasatch fault zone, Davis, Salt Lake, and Utah Counties, Utah: U.S. Geological Survey Miscellaneous Investigations Map I-2106, scale 1:50,000.

Raper, J. F., & Wainwright, D. E. (1987). The use of the geotechnical database 'Geoshare' for site investigation data management. Quarterly Journal of Engineering Geology and Hydrogeology, 20(3), 221-230.

Roe, W. P., & Madin, I. P. (2013). 3D GEOLOGY AND SHEAR-WAVE VELOCITY MODELS OF THE PORTLAND, OREGON, METROPOLITAN AREA.

Sack, D. (2005). Geologic Map of the Roy 7.5-Minute Quadrangle, Weber and Davis Counties, Utah, Utah Geological Survey Miscellaneous Publication 05-03.

Sharifi Mood, M., Gillins, D.T., Franke, K.W (2016). Performance based liquefaction-induced lateral spreading hazard mapping of Utah County. Engineering Geology (In Preparation)

Smith, R. B., & Arabasz, W. J. (1991). Seismicity of the Intermountain seismic belt. Neotectonics of North America, 1, 185-228.

Soller, D. R., (2002), Digital Mapping Techniques '02-Workshop Proceedings, USGS Open-file Report. 02-370.

Solomon, B. J., Biek, R. F., & Smith, T. W. (2007). Geologic map of the Magna quadrangle. Salt Lake County, Utah: Utah Geological Survey Map, 216.

Stepp, J. C., Ponti, D. J., Turner, L. T., Swift, J. N., Devlin, S., Benoît, J., & Bobbitt, J. (2009). PEER Lifelines Geotechnical Virtual Data Center, PEER Report 2009/108.

Swift, J. N., Stepp, J. C., Vaughan, D., Grimes, P., & Turner, L. (2002). Collaborative research on web dissemination of geotechnical data. In Proceedings of the 2002 annual national conference on Digital government research (pp. 1-4). Digital Government Society of North America.

Utah Geological Survey (UGS), Geological Maps. Retrieved from https://geology.utah.gov/map-pub/maps/geologic-maps/

Varnes, D. J., (1974), The Logic of Geological Maps, with Reference to Their Interpretation and Use for Engineering Purposes, USGS Professional Paper 837.

Yonkee, A., & Lowe, M. (2004). Geologic Map of the Ogden 7.5-Minute Quadrangle, Weber and Davis Counties, Utah, Utah Geological Survey Map 200.

Youd, T. L., Idriss, I. M., Andrus, R. D., Arango, I., Castro, G., Christian, J. T., Dobry, R., Finn, W.L., Harder Jr, L.F., Hynes, M.E. and Ishihara, K. (2001). Liquefaction resistance of soils: summary report from the 1996 NCEER and 1998 NCEER/NSF workshops on evaluation of liquefaction resistance of soils. Journal of geotechnical and geoenvironmental engineering, 127(10), 817-833.

Youd, T. L., & Perkins, D. M. (1978). Mapping liquefaction-induced ground failure potential. Journal of the Soil Mechanics and Foundations Division, 104(4), 433-446.

Manuscript # 4

Performance-based, Liquefaction-Induced Lateral Spread Hazard Mapping and its Application to Utah County, Utah

Mahyar Sharifi-Mood, Daniel T. Gillins, Jasmyn N. Harper, Kevin W. Franke, Michael J. Olsen and Steven F. Bartlett

Target journal: Earthquake Spectra, EERI

5 PERFORMANCE-BASED, LIQUEFACTION-INDUCED LATERAL SPREAD HAZARD MAPPING AND ITS APPLICATION TO UTAH COUNTY, UTAH

5.1 ABSTRACT

Earthquake-induced liquefaction may result in the lateral spread displacement of soil down slopes or towards free-faces, causing severe and costly damage to various facilities, bridges, buildings and other critical infrastructure. In addition to analytical methods, many engineers currently use empirical regression models to estimate liquefaction-induced lateral spread displacements at specific sites. However, the application of these regression models over a large geographic area can be difficult because of the challenges associated with the accurate quantification of subsurface soil and groundwater conditions, geotechnical properties, regional topography, and uncertainties associated with the causative seismic loading. To address these challenges, this paper presents a new and fully probabilistic framework for the hazard mapping of liquefaction-induced lateral spread displacement on a regional scale. The proposed framework is demonstrated through its implementation in Utah County, Utah. The proposed framework incorporates topographical data from airborne lidar surveys and geotechnical and geological data from available maps and subsurface explorations. It accounts for uncertainties in the soil properties, seismic loading, and the empirical models for predicting lateral spread displacement by performing numerous Monte Carlo simulations. As an example, 1033 and 2475-year return period lateral spread displacement hazard maps were created for Utah County, Utah.

5.2 INTRODUCTION

Seismically-induced soil liquefaction occurs as excess pore water pressure generated by cyclic strains in loose, saturated, and cohesionless soil significantly reducing the soil's shear resistance and stiffness. A horizontal movement in the soil above a liquefied subsurface layer is called lateral spread. These type of movements generally develop on slopes or in the vicinity of free-faces, such as river channels or canals. Lateral spreads have historically resulted in excessive costs and damages to urban communities by rupturing utility lines, destroying foundations, and straining structures. Recent major earthquakes in New Zealand, Japan, Peru, Chile, China, and Haiti have highlighted the need for geotechnical engineers to be able to assess, delineate, and quantify lateral spread hazard when evaluating both new and existing facilities (Youd et al. 2001).

Engineers most commonly evaluate liquefaction and lateral spread hazard either analytically or empirically in a site-specific manner. However, researchers have attempted to quantify and map liquefaction hazard across larger regions in an effort to produce a useful preliminary hazard assessment tool for engineers, developers, emergency planners, and public officials. Early liquefaction hazard mapping studies were qualitative and based largely on liquefaction susceptibility correlations with mapped surface geology out of necessity due to insufficient subsurface soil and groundwater information (e.g., Youd and Hoose 1977; Youd and Perkins 1978). Later mapping efforts (e.g., Anderson et al. 1982; Baise et al. 2006) began considering regional seismic loading in addition to susceptibility correlations with mapped surface geology to characterize the regional liquefaction

triggering hazard. The additional consideration of available subsurface geotechnical information across a region in the liquefaction hazard mapping process (e.g., Anderson et al. 1982; Baise et al. 2006; Lenz and Baise 2007; Olsen et al. 2007; Gillins 2012) improved the characterization of the liquefaction triggering hazard, typically reporting the results for the "critical layer" (i.e., the layer of soil with the smallest factor of safety against liquefaction triggering) in the soil profile. Other researchers have quantified the liquefaction hazard with a different metric such as liquefaction potential index (LPI) (e.g., Iwasaki et al. 1982; Luna and Frost 1998; Holzer et al. 2006; and Cramer et al. 2008) or liquefaction risk index (LRI) (e.g., Lee et al. 2004; Sonmez and Gokceoglu 2005), which integrates the liquefaction triggering potential across all soil layers to produce a single hazard index.

While integrated liquefaction hazard metrics such as LPI and LRI have proven useful in mapping liquefaction triggering hazard across a region, they have been shown to correlate rather poorly with observed lateral spread displacements following major earthquake events because of other relevant factors such as site geometry that are not accounted for in their computation (Maurer et al. 2014). Other investigators have developed lateral spread displacement hazard maps using correlations with mapped surface geology (e.g., Youd and Perkins 1978; Youd and Perkins 1987) or empirical displacement prediction models in the mapping procedure (e.g., Mabey and Madin 1993, Olsen et al. 2007; Gillins 2012; Jaimes et al. 2015). These latter displacement hazard maps were developed from a single earthquake scenario developed from either a deterministic seismic hazard analysis or a probabilistic seismic hazard analysis at a single return period. However, these maps do not consider

seismic loading from multiple seismic sources and across multiple return periods, nor do they account for variation in ground motion amplification from site response effects (e.g., Bazzurro and Cornell 2004; Stewart et al. 2014).

This study presents a new and rigorous methodology to produce fully probabilistic lateral spread hazard prediction maps that account for uncertainties in ground motions, site response, subsurface geotechnical and groundwater information, and lateral spread displacement prediction models. This methodology is based on a performance-based earthquake engineering framework that incorporates probabilistic seismic hazard analysis (PSHA) of the region, site geology base maps, an extensive database of available subsurface geotechnical investigations, available groundwater data, and high-resolution lidar topographic data. The proposed methodology is demonstrated for a study area in Utah County, Utah, resulting in probabilistic lateral spread displacement hazard maps for the area corresponding to the return periods of 1033 and 2475 years.

5.3 PREDICTION OF LATERAL SPREAD DISPLACEMENTS

Currently, lateral spread displacement prediction methods can be divided into three generalized categories (Franke 2005): (1) empirical prediction models based solely on field data and observation (e.g., Hamada et al. 1986; Bartlett and Youd 1995; Rauch and Martin 2000; Bardet et al. 2002; Youd et al. 2002; Gillins and Bartlett 2013); (2) semi-empirical prediction models based on theoretical derivation that is calibrated against laboratory and/or field data (e.g., Zhang et al. 2004; Faris et al. 2006; Idriss and Boulanger 2008); and (3) analytical prediction models that numerically compute displacements and that are

based on the mechanics of the liquefaction and/or horizontal ground deformation (e.g., Bray and Travasarou 2007; Seid-Karbasi and Byrne 2007; Saygili and Rathje 2008; Lam et al. 2009). Despite the fact that the analytical methods have made and continue to make significant progress in their ability to accurately predict lateral spread displacements, empirical and semi-empirical prediction models remain the most popular method for predicting lateral spread displacements among engineering practitioners today because of their simplicity, familiarity, and basis in case histories of lateral spread displacements. However, a large amount of aleatory uncertainty is usually associated with these types of prediction models because of the complexity of the lateral spread phenomenon and the paucity of well-documented lateral spread case histories.

Bartlett and Youd (1995) originally considered lateral spread events from earthquakes in Japan and the western United States and statistically regressed an empirical prediction model from their resulting case history data that included earthquake moment magnitude, source-to-site distance, several geotechnical variables of the continuous liquefied soil layers, and slope geometry. Later, Youd et al. (2002) updated their lateral spread case history database and developed a revised multilinear regression prediction model, which remains widely used by engineering practitioners today. Gillins and Bartlett (2013) simplified the Youd et al. (2002) prediction model by consolidating some of the required geotechnical input factors such as fines content and mean grain size into a single soil classification factor. The Gillins and Bartlett (2013) model was developed for lateral spread hazard mapping applications because it does not require laboratory test results for the soil but instead uses visual soil classifications, which are more readily available in most

geotechnical field boring logs. The Gillins and Bartlett (2013) multilinear regression empirical model is given as:

$$\log D_H = b_0 + b_1 M_w + b_2 LogR^* + b_3 R + b_4 LogW + b_5 LogS + b_6 LogT_{15,cs} + 0.252 + \varepsilon \qquad (5\text{-}1)$$

where D_H is the permanent estimated horizontal lateral spread displacement in meters; M_w is the moment magnitude of the earthquake; R is the closest horizontal distance in kilometers from the site to the vertical surface projection of the fault rupture (i.e., the Joyner-Boore distance, R_{JB}); W is the free-face ratio (i.e., the ratio of the height to the horizontal distance from the site to the toe of the slope) in percent (%); S is the slope gradient in percent (%); and R^* is a distance parameter used to characterize near-source earthquakes and is computed as:

$$R^* = R + 10^{0.89 M_w - 5.64} \qquad (5\text{-}2)$$

$T_{15,cs}$, which is the only geotechnical variable in Equation (5-1), is the clean-sand equivalent value for T_{15}, and is computed as:

$$T_{15,cs} = T_{15} \cdot 10^{\left(\frac{-0.683 \cdot x_1 - 0.200 \cdot x_2 + 0.252 \cdot x_3 - 0.040 \cdot x_4 - 0.535 \cdot x_5 - 0.252}{0.592} \right)} \qquad (5\text{-}3)$$

where T_{15} is the cumulative thickness (in meters) of saturated, cohesionless, and continuous soil deposits in the upper 15 meters of the soil profile with corrected standard penetration test (SPT) resistance $(N_1)_{60} < 15$ hammer blows per 0.3 meter, and x_n is the ratio of the cumulative thickness (in meters) of soil type *n* with $(N_1)_{60} < 15$ to the total T_{15}

for the entire soil column. Thus, x_n will range between 0 and 1, and the sum of x_1 through x_5 will equal 1. Soil types *n* and their definitions are provided in Table 5.1.

Table 5.1: Soil types n and their definitions (from Gillins, 2012).

n	Definition
1	Silty gravel with sand, silty gravel, fine gravel
2	Coarse to very coarse sand, sand and gravel, gravelly sand
3	Sand, medium to fine sand, sand with some silt
4	Fine to very fine sand, sand with silt, silty sand, dirty sand
5	Sandy silt, silt with sand
6	Non-liquefiable, such as cohesive soil or soil with high plasticity

Using the Youd et al. (2002) lateral spread case history database, Gillins and Bartlett (2013) solved for the regression coefficients, b_0 to b_6, for Equation (5-1). These coefficients are given in Table 5.2 according to the topographic conditions at a site. The error for the regression model, ε, is normally distributed with a mean of 0.0 and a standard deviation, $\sigma_{\log D_H} = 0.2232$.

Table 5.2: Gillins and Bartlett (2013) empirical regression model coefficients for lateral spread displacement prediction

Model	b_0	b_1	b_2	b_3	b_4	b_5	b_6
Ground- Slope	-8.208	1.318	-1.073	-0.016	0.000	0.337	0.592
Free Face	-8.552	1.318	-1.073	-0.016	0.445	0.000	0.592

5.4 PERFORMANCE-BASED PREDICTION OF LATERAL SPREAD DISPLACEMENTS

Seismologists and engineers have long recognized that there are many uncertainties associated with predicting earthquake ground motions and their subsequent effects on the ground and structures. In response, these professionals have developed and implemented probabilistic or performance-based earthquake engineering design procedures, which quantify and account for as many of the uncertainties associated with the earthquake engineering design problem as possible. These procedures typically quantify hazards in terms of a mean annual rate of exceedance, λ.

Franke and Kramer (2013) introduced a performance-based procedure built upon the probabilistic framework introduced by the Pacific Earthquake Engineering Research Center (PEER; Cornell and Krawinkler 2000; Deierlein et al. 2003) to compute the mean annual rate of exceeding some lateral spread displacement, *d*. Their procedure modifies the Youd et al. (2002) model by grouping together all of the model variables related to seismic loading (i.e., M_w and R) and designating them as the apparent loading parameter, $\mathscr{L}$. Because $\mathscr{L}$ is a function of parameters M_w and R, it is analogous to a ground motion attenuation relationship and can be treated in a similar manner. Likewise, the Franke and Kramer procedure groups together all of the model variables related to local site conditions (i.e., S, W, T_{15}, fines content, and mean grain size) and designates them as a site parameter, *G*.

A similar modification can be applied to the Gillins and Bartlett (2013) model presented in Equation (5-1). In this modified form of the model, the apparent loading parameter is defined as:

$$\mathscr{L} = b_1 M_w + b_2 \log R^* + b_3 R \qquad (5\text{-}4)$$

The modified site parameter is defined as:

$$G = -\left(b_0 + b_4 \log W + b_5 \log S + b_6 \log T_{15,cs} + 0.252\right) \qquad (5\text{-}5)$$

The model error is defined as:

$$\varepsilon = \sigma_{\log D_H} \Phi^{-1}\left[P\right] \qquad (5\text{-}6)$$

where Φ^{-1} is the inverse standard normal cumulative distribution function, and P is the probability of exceeding the median predicted lateral spread displacement, $\hat{D}_H$. Using this modified syntax, Equation (5-1) can be re-written as:

$$\log D_H = \mathscr{L} - G + \varepsilon \qquad (5\text{-}7)$$

As demonstrated by Franke and Kramer (2013), the modified lateral spread model can now be inserted into a performance-based framework to compute the mean annual rate of exceeding a specific lateral spread displacement *d* as:

$$\lambda_{D_H|G}\left(d \mid G\right) = \sum_{i=1}^{N_{\mathscr{L}}} P\left[D_H > d \mid G, \mathscr{L}_i\right] \Delta\lambda_{\mathscr{L}_i} \qquad (5\text{-}8)$$

where $N_{\mathscr{L}}$ is the number of bins or increments associated with the seismic hazard curve for $\mathscr{L}$ developed through a probabilistic seismic hazard analysis (PSHA); $\Delta\lambda_{\mathscr{L}_i}$ is the size of each hazard increment or bin associated with the seismic hazard curve for $\mathscr{L}$; and $P\left[D_H > d \mid G, \mathscr{L}_i\right]$ is the conditional probability that the median predicted lateral spread displacement exceeds displacement *d* conditional upon seismic loading $\mathscr{L}_i$ and constant site conditions G. Ignoring the model error, *ε*, Equation (5-1) will produce the most probable value of logD_H (i.e., $\overline{\log D_H}$), and the conditional probability can be computed as:

$$P\left[D_H > d \mid G, \mathscr{L}_i\right] = 1 - \Phi\left[\frac{\log d - \overline{\log D_H}}{\sigma_{\log D_H}}\right] = 1 - \Phi\left[\frac{\log d - \overline{\log D_H}}{0.2232}\right] \qquad (5\text{-}9)$$

5.5 PROPOSED PERFORMANCE-BASED LATERAL SPREAD HAZARD MAPPING METHODOLOGY

Equation (5-9) provides a performance-based framework to compute the mean annual rate of exceeding a particular lateral spread displacement, *d*, given a site geometry, *G*. Unfortunately, when mapping a regional area using available data, *G* often has significant uncertainty due to lack or paucity of geotechnical drilling, sampling, and testing. Rather than expanding Equation (5-9) and inserting additional summations to account for uncertainty in *G*, the proposed mapping method uses Monte Carlo simulations.

The proposed lateral spread hazard mapping method requires several inputs, including: (1) a digital raster map of the geology of the project area; (2) digital raster maps of the ground slope and free-face ratios computed from a high-resolution digital elevation model (DEM); (3) available geotechnical investigation reports in the project area, such as SPT borings, laboratory data, and depths to groundwater measurements; and (4) raster maps of seismic loading, $\mathscr{L}$, at targeted return periods developed from a series of PSHAs across the project area. The incorporation of these inputs for the development of performance-based lateral spread displacement hazard mapping procedure is illustrated in a flow chart diagram in Figure 5-1. Each step of this flow chart is briefly summarized below. To offer more clarity on the proposed method, the following section of this paper presents an example implementation of each step of this workflow resulting in lateral spread displacement hazard maps in Utah County, Utah.

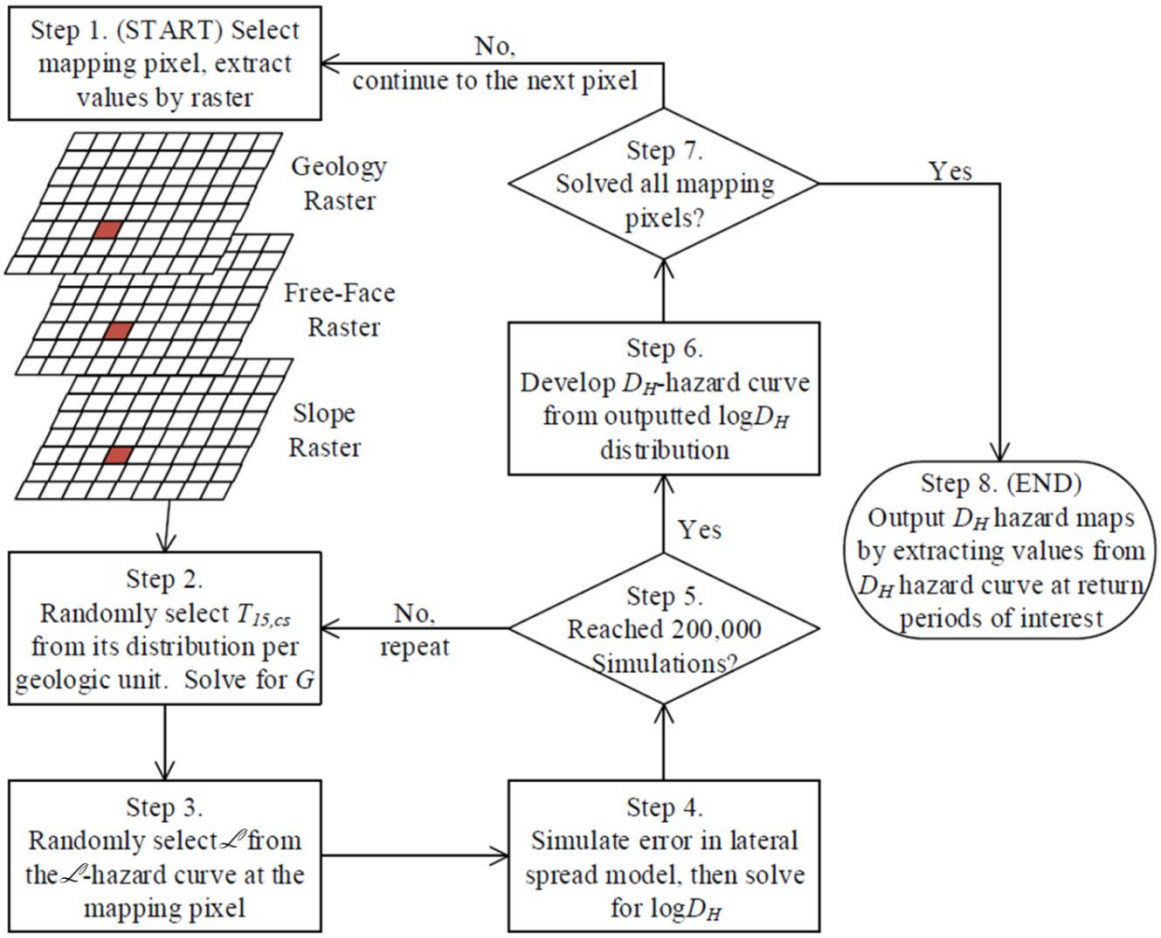

Figure 5-1: Proposed workflow for producing fully-probabilistic lateral spread displacement hazard maps.

Step 1: Extract Raster Data at a Map Pixel:

Since the geology and depositional environment significantly influences the susceptibility of the soil to liquefaction, the proposed mapping method begins by utilizing available surficial geology maps. These maps are compiled, digitized, georeferenced, and converted into a raster image for the mapping area. A raster consists of a matrix of pixels organized into rows and columns where each pixel contains a value representing information (e.g., for this case, the mapped geologic unit). The raster format is advantageous for quickly performing calculations of spatial data.

In addition to developing a raster image of the surficial geology of the mapping area, additional rasters are developed to describe the spatial variation in site geometry in the mapping area. Using a digital elevation model (DEM), raster images of the percent ground slope, and proximity and depth of free-faces are computed. (Note that an example of computing these rasters is given in the following section.)

For the proposed mapping method, the lateral spread hazard is computed for each individual pixel of a raster of the mapping area. The process is repeated for each pixel, and the results at each pixel are then combined to produce the final hazard maps. For more efficient computation, the pixels can be evaluated simultaneously using parallel processing; however, for clarity, this paper will describe the process as if solving for the hazard at each pixel sequentially. As illustrated in Figure 5-1, beginning at one pixel in the mapping area, the raster values from the surficial geology, slope (S), and free-face (W) rasters are extracted at that location.

Step 2: Begin Monte Carlo Simulations, Input $T_{15,cs}$:

Characterizing the subsurface conditions of a widespread geologic unit is challenging, particularly when using the limited data available at that scale instead of planning a geotechnical testing campaign and collecting more data by performing additional drilling, soil sampling, and laboratory testing. Accordingly, the subsurface conditions have considerable uncertainty. In order to model this uncertainty, available geotechnical data in the mapping area, such as SPT logs, are compiled and digitized, and the unit within which the SPT was conducted is recorded (see Chapter 4). Afterwards, three critical assumptions must be made: (1) the geologic units are classified appropriately such that the soil properties within each unit are relatively similar; (2) each SPT log provides geotechnical variables that can be considered independent, random variables within the geologic unit where the test was conducted; and (3) the sample size of available SPT logs are adequate to approximate the distribution of geotechnical variables in each of the geologic units in the mapping area.

Given these assumptions, the next step in the mapping process is to initiate a Monte Carlo simulation and randomly select an SPT log from the total number of SPTs in the corresponding geologic unit for the selected pixel. Afterwards, $T_{15,cs}$ for the simulation is computed using the data in the selected SPT log and Equation (5-3) and this value is input in Equation (5-5) to solve for G at the selected pixel.

Step 3: Input Apparent Loading Value, $\mathscr{L}$:

Continuing with the *i*-th simulation, the next step is to select and input an apparent loading value, $\mathscr{L}$, in order to eventually solve Equation (5-7). Of course, $\mathscr{L}$ has significant uncertainty, and in order to output fully probabilistic lateral spread hazard maps, $\mathscr{L}$ must be modeled by performing a probabilistic seismic hazard analysis (PSHA). In this step, a PSHA with $\mathscr{L}$ (i.e., Equation (5-4)) across a grid of points in the mapping study area should be performed to develop a hazard curve for $\mathscr{L}$ at every grid point. A possible grid spacing scheme that is based on a correlation with mapped probabilistic *PGA* estimates is presented in Ulmer et al. (2015).

At the selected pixel, a hazard curve for $\mathscr{L}$ is first derived by bilinear interpolation of the gridded $\mathscr{L}$ hazard curves. Afterwards, this hazard curve at the pixel is transformed into a probability density function (PDF) (Bazzurro and Cornell 2004). A value for $\mathscr{L}_i$ is then input in the Monte Carlo simulation by random sampling from the PDF.

Step 4: Compute log D_H:

The final step in *i*-th simulation is to solve Equation (5-7). The sum of G_i from Step 2 and the selected value for $\mathscr{L}_i$ from Step 3 produces $\overline{\log D_{H,i}}$ for the simulation. A value for the error in the lateral spread displacement model, ε, is then simulated using a random number generator that follows the standard normal distribution (e.g., in MATLAB, this is achieved with the function *randn*).

In other words, Equation (5-7) can be rewritten to compute $[logD_H]_i$ for the *i*-th simulation at a mapping pixel:

$$\left[\log D_H\right]_i = \overline{\log D_{H,i}} + \varepsilon = \overline{\log D_{H,i}} + \sigma_{\log D_H} \cdot K_{rand,i} = \overline{\log D_{H,i}} + 0.2232 \cdot K_{rand,i} \qquad (5\text{-}10)$$

where $K_{rand,i}$ is a random value generated from the standard normal distribution for the *i*-th simulation.

Step 5: Repeat Steps 2 – 4 for Required Number of Simulations:

The next step is to perform additional Monte Carlo simulations by repeating steps 2 through 4 until a distribution of [log D_H] is obtained at the selected pixel. An adequate number of simulations must be performed to fully characterize the major sources of uncertainty in the process. Upon completion of all of the simulations, the distribution is converted to a distribution of D_H values (in meters) at a mapping pixel by raising 10 to the $\log D_H$ values.

Step 6: Develop a D_H Hazard Curve:

Next, the D_H values at each mapping pixel are converted into a D_H-hazard curve by converting the distribution for D_H into an empirical cumulative distribution function (CDF) curve. The annual probability that D_H exceeds a displacement value, *d*, of interest (i.e., P(D_H > *d*)) is equal to 1 minus the CDF value at *d* on this curve. The annual exceedance probability can be defined using the Poisson probability model as:

$$P(D_H > d) = 1 - e^{(-\lambda t)} \quad (5\text{-}11)$$

where t is exposure period in years, and λ is the mean annual rate of exceedance whose inverse is the return period in years. The example below provides more details on how to use Equation (5-11) and an empirical CDF of D_H to compute a D_H-hazard curve.

Step 7: Repeat Previous Steps for All Mapping Pixels:

Each of the first six steps are repeated for every pixel in the mapping area, resulting in D_H-hazard curves at every pixel.

Step 8: Output Maps for Desired Return Periods:

Upon completion, values of D_H can be extracted from the hazard curves at a user-defined return period (e.g., 475, 1,033, or 2475-year return period) for each mapping pixel. The extracted value at each pixel can be aggregated into a raster image, to develop a lateral spread displacement hazard map at the desired return period.

5.6 IMPLEMENTATION OF THE MAPPING METHOD FOR UTAH COUNTY, UTAH

As an example to clarify the proposed mapping method, the flow chart (Figure 5-1) was followed to produce lateral spread displacement hazard maps in Utah County, Utah. Utah County is the second-most populous county in the state of Utah and comprises a significant portion of the overall state and regional economies. However, the liquefaction hazard is considered significant in that portion of the county along the Wasatch Front due to its close proximity to high seismic (e.g., the Wasatch fault zone) and surficial water (e.g., Utah Lake)

sources, shallow ground water tables, and widespread granular and/or silty soils in the upper 5 to 15 meters of sediments. Development of fully probabilistic liquefaction-induced lateral spread displacement hazard maps for the county will provide a tool for agencies, planners, departments, and engineers to identify and prioritize locales where future site-specific liquefaction studies should be performed.

Anderson et al. (1982) previously developed a method to map liquefaction triggering potential for urban areas in twelve counties in Utah, including Utah County (Anderson et al. 1994a,b). To produce these maps, Anderson et al. computed the potential for liquefaction triggering at available SPT borehole and CPT sounding locations. They determined critical acceleration values needed to trigger liquefaction using a method introduced by Seed (1979). They then compared these critical accelerations to probabilistic predictions from seismic hazard analyses. Using surficial geologic maps as constraints, they generalized the results at each geotechnical investigation and produced qualitative liquefaction potential maps delineating zones of *low*, *moderate*, and *high* liquefaction potential. The Anderson et al. (1994b) hazard map of Utah County (see Figure 5-2) shows high liquefaction potential for most of the urban area in the county. Although this map is a useful reference, it is desirable to produce new liquefaction hazard maps that estimate the consequences of liquefaction triggering, such as the amount of lateral spread displacement. These new maps should also be based on advancements over the past 30 years in liquefaction hazard evaluation procedures, probabilistic seismic hazard analyses, available and higher-resolution geologic and topographic maps along the Wasatch Front, and the significantly larger number of available SPT and CPT investigations.

To accomplish the 8 steps of the mapping method (Figure 5-1), available data were compiled into a geospatial database, custom MATLAB scripts were written to perform the computations, and Esri's ArcMap® was used to visualize and analyze the outputs. The following narrative provides details of each of the 8 steps of the mapping process, including the source of the data inputs and identification of any key assumptions. For additional details on the new Utah County liquefaction hazard maps, see Gillins and Franke (2016).

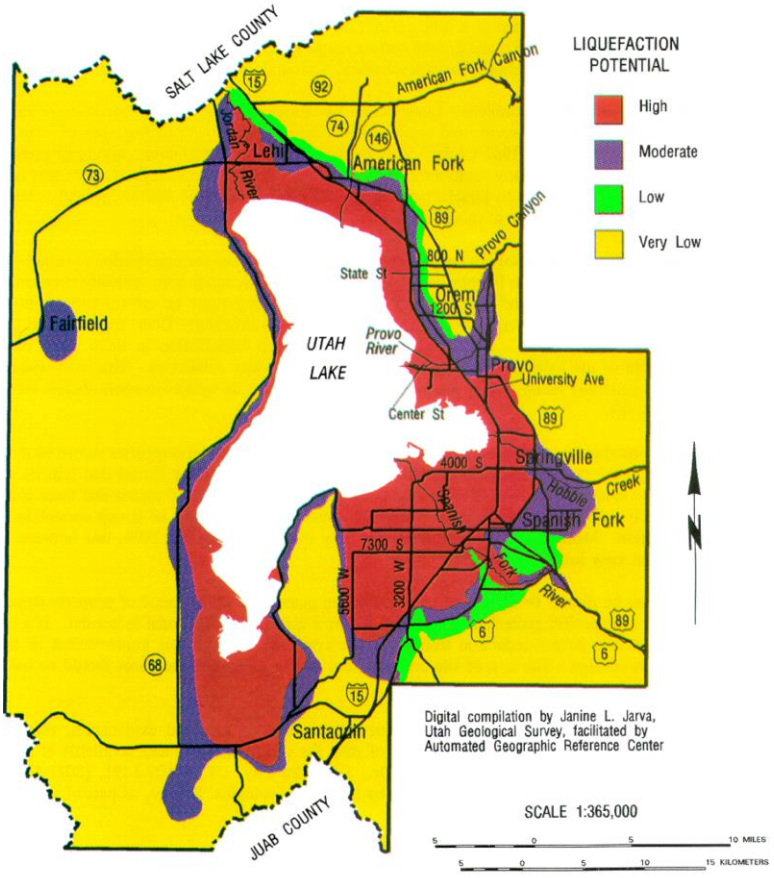

Figure 5-2: Previous qualitative liquefaction potential hazard map from Anderson et al. (1994b).

Step 1: Input Geology, Slope, and Free-Face Data:

First, a vector-based geology base map of the study area (Constenius et al. 2011) was obtained from the Utah Geological Survey and input into a geospatial database. The Constenius et al. (2011) map is a compilation of detailed and recent mapping of several 7.5-minute quadrangles at 1:24,000 to 1:50,000-scale along part of the populous Wasatch Front and Utah Valley. Figure 5-3 presents the study area in Utah County and illustrates the surficial geologic units mapped by Constenius et al. (2011). Holocene to Upper Pleistocene alluvial, lacustrine, and deltaic deposits are primarily shown on the map. Based on Youd and Perkins (1978), these deposits are moderately to very highly susceptible to liquefaction. The figure also depicts the Wasatch Mountains, which bound the study area on the east, the Utah segment of the Wasatch Fault Zone (the primary seismic threat in Utah County), the extents of Utah Lake, and West Mountain to the south of Utah Lake. The study area is also bounded on the west by the Lake Mountains.

The authors grouped the quaternary geologic units in the study area into 14 categories, as tabulated in Table 5.3. It provides the symbol, description, and age for each of the units within the 14 categories from the Constenius et al. (2011) map. Afterwards, the vector-based geologic units depicted in Figure 5-3 were converted into a raster image, with values ranging from 1 to 14 corresponding to the definitions given in Table 5.3.

Next, a 0.5-meter raster-based DEM of the study area was downloaded from the Utah Automated Geographic Research Center (AGRC) (AGRC 2014), and it was stored in the geospatial database. AGRC developed this DEM from aerial lidar data acquired in the fall of

2013 and the spring of 2014. The highly-resolute DEM was useful for identifying slopes and free-faces in the study area. The ground slope (in percent) was computed, and the locations of the major free-faces in the study area were digitized. The Jordan and Provo River and some of their tributaries were considered as free-face features. Besides these river channels, areas that showed a dramatic change in elevation, which could be readily noticed when evaluating a hillshade of the DEM, were also digitized as free-face features.

During the digitization of the free-face features, a polyline feature class was drawn along the toe of that the identified free-face, and a polygon feature class was drawn to encompass areas above and affected by this free-face feature. The polyline and polygon feature were then converted to points at a spacing less than 30 m. For each point within a polygon, multiple free-face ratios to all points along the toe were computed by dividing the difference in elevation with the horizontal distance from the site to the toe, and then the maximum free-face value was assigned as per a method in Gillins (2014). After repeating the process for all points and all free-face features in a custom MATLAB script, a natural neighbor interpolation among the points was used to output another raster that depicts the free-face ratio, W, for the study area.

Table 5.3: Geologic units in study area, descriptions, approximate age, and number of SPTs.

Deposit Symbol	Description	Age*	#SPT†
1. Stream Alluvium			
Qal	Modern stream alluvium	H	20 (33)
2. Stream-Terrace Alluvium			
Qat_1	Stream-terrace alluvium, lowest terrace levels	H - UP	4 (7)
Qat_2	Stream-terrace alluvium, medium terrace levels	H - UP	2 (4)
Qat_3	Stream-terrace alluvium, highest terrace levels	H - UP	0 (1)
3. Alluvial Fan – Old			
Qafb	Transgressive (Bonneville) Lake Bonneville-age	UP	0 (1)
Qafm	Intermediate Lake Bonneville-age alluvial fan	UP to middle P	6 (21)
Qafp	Regressive (Provo) Lake Bonneville-age alluvial fan	UP	3 (10)
4. Alluvial Fan – Young			
Qafy	Younger alluvial-fan	H	98 (171)
5. Delta			
Qdb	Near Bonneville shoreline of Lake Bonneville	UP	1 (1)
Qdp	Near and below Provo shoreline of Lake Bonneville	UP	5 (13)
6. Fine-Grained Lacustrine			
Qlf	Fine-grained lacustrine from Lake Bonneville	UP	100 (194)
Qly	Young lacustrine less than 6 m thick and overlies Qlf unit	H– UP	4 (6)
Qsm	Fine, organic-rich sediment from springs, marshes, seeps; less than 3 m thick and overlies Qlf unit	H– UP	1 (1)
7. Lacustrine Sand			
Qls	Lacustrine sand below Bonneville and Provo shorelines	UP	58 (100)
Qes	Eolian sand; 1-1.5 m thick and derived from Qls unit	H - UP	4 (7)
8. Landslides			
Qmsy	Modern landslide, currently or recently active	H	3 (6)
Qms	Modern landslide	H	2 (2)
9 – 14. Others			
Qlg	Lacustrine gravel and sand near Bonn. and Provo shorelines	Uppermost P	15 (21)
Qfdp	Lake Bonneville alluvial-fan and delta, Provo stage	Uppermost P	33 (61)
Qh	Human disturbance – fill for major interstate and highways	Historic	45 (53)
Qla	Lacustrine and alluvial, undivided	H – UP	14 (20)
Qay	Alluvial fan and terrace post-Provo shoreline of Lake Bonn.	H – UP	3 (13)
Qac	Alluvium and colluvium, undivided	Quaternary	3 (7)

* = UP = Upper Pleistocene; P = Pleistocene; H = Holocene

† = Number in parenthesis is the grand total of SPTs in the unit. Number outside of parenthesis is the total of SPTs with maximum test depths greater than 20 ft.

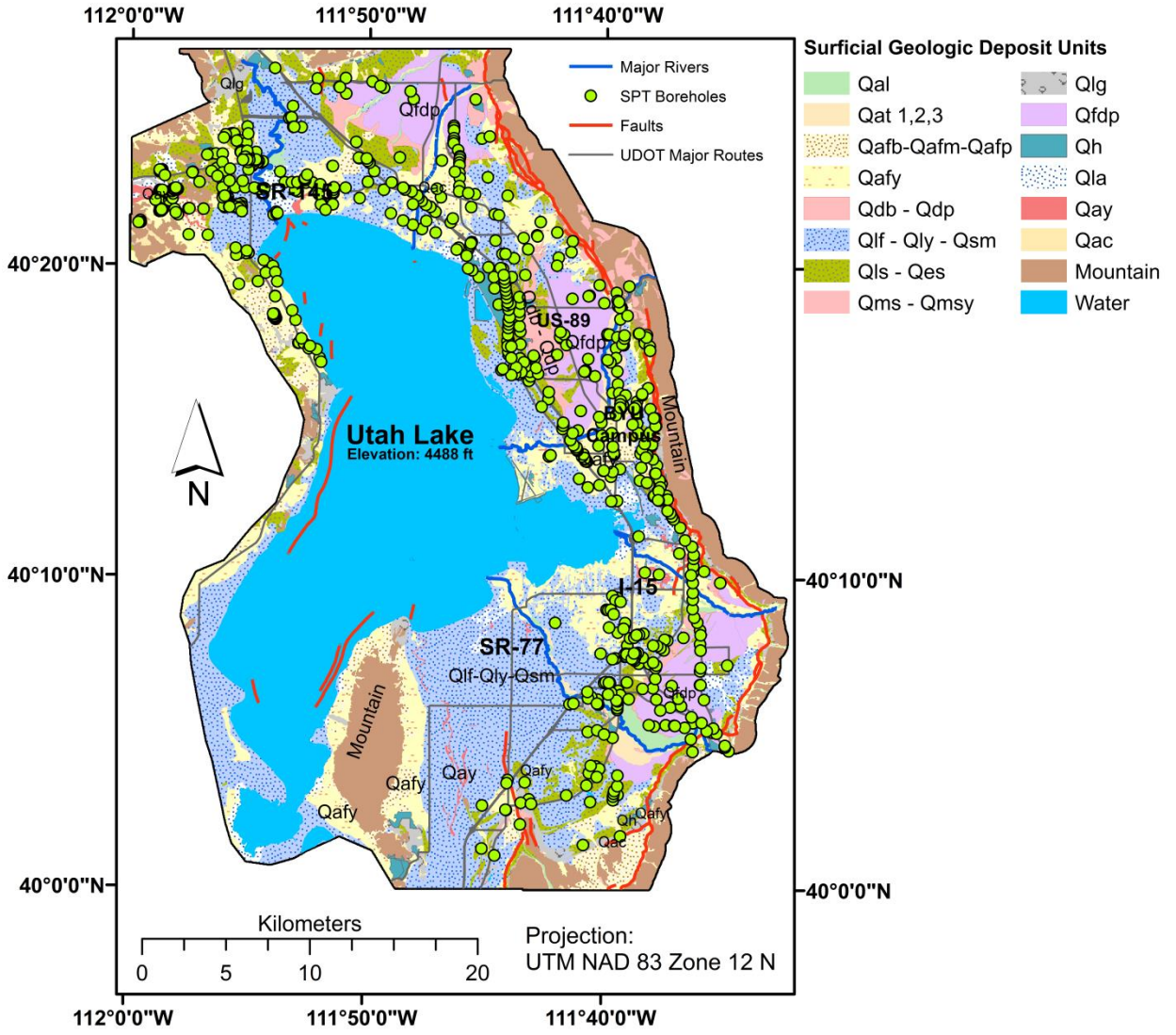

Figure 5-3: Surficial geology and location of SPT boreholes in the study area, Utah County, Utah.

The rasters of the surficial geology, slope, and free-faces were computed at a 30-m by 30-m pixel size. The lateral spread hazard was then evaluated for each individual pixel, resulting in final hazard maps.

Step 2: Input Geotechnical Data and Compute *G:*

Available geotechnical investigations were collected, digitized, and stored in a geospatial database. Both SPT borehole logs and CPT soundings were acquired from multiple engineering firms and their clients, as well as government agencies such as the Utah Department of Transportation (UDOT), Utah Geological Survey (UGS), Central Utah Water Conservancy District (CUWCD), and local city governments. Overall, 753 borehole logs and 39 CPT soundings in the study area were collected, digitized, and stored in the database. Figure 5-3 shows the spatial location of each SPT. As can be seen, the data was spaced fairly well throughout the study area, and numerous tests were found along the Interstate 15 corridor; however, some portions of the county with limited development (west and just southeast of Utah Lake) have fewer investigations.

Data from the SPT and CPT records were input into a database format that was developed and explained in Gillins (2012). Information such as soil descriptions and classifications, layer delineations, depths to groundwater, and uncorrected SPT blow counts (N_m) from the SPT logs were stored in the database. In addition, lab measurements on soil samples, such as fines contents, Atterberg limits, unit weights, and moisture contents were digitized. Friction ratio, sleeve friction, cone-tip resistance, and pore water pressure were stored from the CPT soundings. Most of the CPT soundings also had a pore-water pressure dissipation test data that gave an estimate of the depth to groundwater.

Table 5.3 shows the total number of SPT borehole logs in each of the 14 geologic categories in the study area. All 753 logs were used for characterizing the typical soil properties (e.g.,

moisture content, Atterberg limits, unit weights) for the geologic units; however, a large number of the tests (329) were quite shallow, and there was concern that some tests may not have encountered all of the soil layers at deeper depths which may liquefy and cause ground failures. Although all tests were used to characterize the geotechnical properties of the soil in Utah County, only SPTs that extended beyond a depth of 7 m were used when mapping the liquefaction hazard. A threshold depth of 7 m was selected because: (1) liquefaction most-generally occurs in the shallow layers of a soil column (i.e., < 20 m) and much of the liquefiable sediments in Utah County are in the shallow depths above layers of clay associated with a pre-historic lake; and (2) there are significantly fewer tests that reached greater depths in the database and there was concern that by setting the threshold to a deeper depth (say 10-20 m), there would be inadequate data for characterizing the variability of the soil properties for each geologic unit.

Table 5.3 provides a count of the number of SPT logs that reached a minimum depth of 7 m in all 14 geologic categories in the study area. A large number of SPT logs were available for the common units that cover the majority of the study area (e.g., Qafy, Qlf, Qfdp, Qls). Some of the units have a small number of SPT logs (e.g., Qms, Qat, Qd); however, one reason for this lack of sampling is because these units are rare in the study area. Future tests in under-developed portions of the study area, or in the geologic units with limited testing would undoubtedly improve the accuracy of the hazard maps. Future tests could be added to the Utah County geotechnical database, and new maps could then be produced that refine the maps presented in this paper.

During this step of the mapping process, a Monte Carlo simulation was initiated and a SPT borehole log was randomly selected from the total number of SPT logs that reached a minimum depth of 7 m in the geologic category for the selected pixel. For instance, if the selected pixel was located in stream alluvium (i.e., Qal), then one of the 20 SPT boreholes collected in this geologic category was randomly selected. Then, $T_{15,cs}$ was computed for the selected borehole according to Equation (5-3).

To find $T_{15,cs}$ at a borehole required several additional nested steps because only saturated soils that are susceptible to liquefaction should be considered (Boulanger and Idriss 2006). In general, clays are not susceptible to liquefaction, although some have exhibited behavior similar to liquefiable soils during major earthquakes (i.e., cyclic softening). Saturated, coarse-grained, cohesionless soils with low fines contents are widely considered susceptible to liquefaction. Clean sands are considered susceptible to liquefaction, and gravelly soils should be considered susceptible if they are bounded by materials with low permeability that allow build-up of excess pore-water pressure. It is much more difficult to define the susceptibility of soils with high fines contents (e.g., silty sands, clayey sands, sandy silts).

Boulanger and Idriss (2005) reviewed case histories and laboratory tests and identified two types of soil behavior on the basis of stress normalization and stress-strain response. Soils that exhibited *sand-like* behavior were considered susceptible to liquefaction, whereas soils that exhibited *clay-like* behavior were not considered susceptible. Boulanger and Idriss found that soil plasticity can be used to determine if the soil will exhibit sand-

like or clay-like behavior, and proposed that the soil is clearly sand-like at a plasticity index (*PI*) less than 3, and a soil is clearly clay-like at a *PI* greater than 8. Although they noted a transitional phase between 3 and 8, ultimately they recommended that engineers use a conservative guideline with *PI* = 7 as the cutoff between sand-like and clay-like behavior when detailed laboratory testing is not possible. Thus, saturated soils with high fines contents and a *PI* < 7 should be considered susceptible to liquefaction, and only layers of soil with these characteristics were considered when computing $T_{15,cs}$ at a selected borehole.

Unfortunately, values of *PI* as well as other soil properties are not reported for every layer of soil on the SPT logs in the geotechnical database. Thus, distributions of moisture contents, fines contents, and unit weights were developed using measurements recorded on *all* of the SPT logs in the database (i.e., including the shallow logs). As expected, the distributions for these properties varied by soil type. Thus, for every layer on each SPT log, a soil index value (*SI*) was first assigned per Table 5.1. Figure 5-4 shows one of the histograms of fines content, grouped according to *SI*. Refer to Gillins and Franke (2016) for other histograms of the dry unit weight, moisture content, and *PI* grouped by *SI* in Utah County. Nearly all of the soils with *SI* = 6 had a *PI* > 7, and almost all of the silts, sandy silts, and silty sands (i.e., *SI* = 4 or 5) had a *PI* < 7 in the database.

Following recommendations in Boulanger and Idriss (2005), the authors first only considered the saturated layers of soil in the SPT log with *PI* < 7 as susceptible to liquefaction when computing $T_{15,cs}$. However, some of the layers in the log lacked Atterberg

limits data, as well as measurements of soil unit weights, moisture contents, and fines contents which are necessary to correct raw SPT blow counts (N_m) to $(N_1)_{60}$ in order to find $T_{15,cs}$. To rigorously account for this uncertainty and continue with the Monte Carlo simulation, a value for the moisture content, soil unit weight, and fines content were randomly sampled from the aforementioned distributions according to the *SI* of any layer in the log which lacked these data.

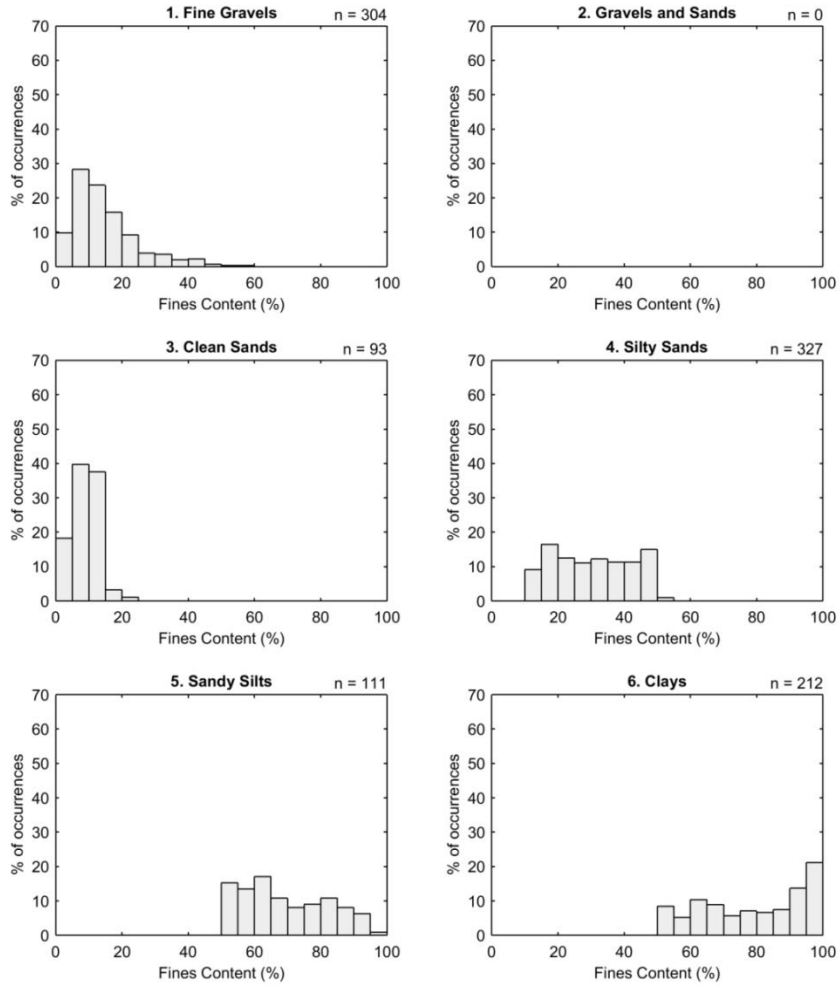

Figure 5-4: Histograms for fines content for 6 different *SI* values, Utah County.

After filling in the missing data in the SPT log by random sampling, (N_m) was corrected to $(N_1)_{60}$ per Equation (5-12).

$$(N_1)_{60} = C_E C_B C_R C_S C_N N_m \qquad (5\text{-}12)$$

where C_E is the energy ratio correction factor accounting for the high variability in the amount of energy delivered to the drill rod stem by each impact of the SPT hammer, C_B is a correction factor for the borehole diameter, C_R is a correction factor for rod length, C_S is a correction factor for a sampler that had room for liners but was used without liners, and C_N is the overburden correction meant to account for the effects of increasing confining stress.

Recommended values and equations from Idriss and Boulanger (2008) were used for each of these corrections. Borehole diameters, rod lengths, and the use of liners were reported on the SPT logs for computing C_B, C_R, and C_S, respectively. A value for C_N was computed for each simulation, since it is a function of the effective vertical stress and the soil stress profile varies according to the aforementioned, randomly selected moisture contents and unit weights for those layers in the soil profile which lacked such data.

However, many of the logs only reported the hammer release type (i.e., automatic or safety hammer) and did not include measurements of the energy delivered to the hammer for estimating C_E. Idriss and Boulanger (2008) report ranges of possible values for C_E according to the hammer type. For a safety hammer, C_E could range from 0.7 to 1.2; for an automatic hammer, C_E could range from 0.8 to 1.3. (Note that none of the logs in the geotechnical database involved the use of a doughnut hammer.) It was assumed that these possible ranges for C_E are normally distributed, with a mean equal to the middle of the range, and a

standard deviation equal to one-sixth of the range. Thus, for the *i*-th simulation, a value for C_E was estimated ($C_{E,i}$) by using Equation (5-13).

$$C_{E,i} = \overline{C_E} + \sigma_{C_E} \cdot K_{rand,i} \quad (5\text{-}13)$$

where $\overline{C_E}$ was set to 1.0 or 1.1 for the safety or automatic hammer, respectively, σ_{C_E} was set to 0.08 for both hammers, and $K_{rand,i}$ is a random number generated for the simulation that follows the standard normal distribution.

After correcting N_m to $(N_1)_{60}$ for the *i*-th simulation, $T_{15,cs,i}$ for the *i*-th simulation was next found by computing the thickness of only those saturated layers of soil with a value of $(N_1)_{60} \leq 15$ and with either: (1) a measured $PI < 7$, or (2) a value of $SI \leq 5$ if the *PI* for the layer was not recorded on the log.

Then, the computed value for $T_{15,cs,i}$ as well as *W* and *S* from the previous step were input in Equation (5-5) to compute G_i. The regression coefficients for Equation (5-5) vary depending on the topography at the point of interest. For conservatism, Equation (5-5) was solved twice—once for free-face conditions and once for ground-slope conditions. Then, the minimum value was stored as G_i for the simulation.

Step 3: Input Seismic Loading:

Continuing with the *i*-th simulation, the next step was to randomly select and input an apparent loading value, $\mathscr{L}_i$, from the PDF of $\mathscr{L}$ at the selected pixel. To develop the PDF, EZ-FRISK software (version 7.62) was used to output hazard curves for $\mathscr{L}$ from a PSHA at

grid points evenly spaced every 0.05 degrees in latitude and longitude across the study area. Franke (2005) outlined a procedure for programming EZ-FRISK to output an $\mathscr{L}$-hazard curve using its *Attenuation Table* feature. To use this table, values of $\mathscr{L}$ were entered by solving Equation (5-4) at incremented values of M from 4.6 to 8.4 (in increments of 0.2), and values of R of 1, 5, 10, 15, 20, 25, 30, 40, 50, 60, 70, 80, 90, 100, 125, 150, 175, 200, 250, and 300 km. EZ-FRISK was set to use the USGS 2008 faults, areas, and background sources to perform the PSHAs. All USGS seismic sources within 500 km of each grid point were included in the PSHAs, and hazard values for $\mathscr{L}$ were output for return periods of 100, 275, 475, 1000, 2500, 5000, and 10000 years. Figure 5-5 presents $\mathscr{L}$-hazard curves at four grid points in the study area. The location of these four grid points is shown in Figure 5-6.

Afterwards, seven 30-m resolution raster images of $\mathscr{L}$ for the above return periods were generated by bilinear interpolation of the $\mathscr{L}$-hazard curves computed at the evenly spaced grid points. Figure 5-6 illustrates three of these raster images for $\mathscr{L}$ at return periods of 1000, 2500, and 5000 years.

To perform the third step of the mapping process and continue with the i-th simulation, values for $\mathscr{L}$ were first extracted from each of the seven rasters at the selected pixel. This produced seven intermediate points on an $\mathscr{L}$-hazard curve at the pixel (similar to the points on the curves depicted in Figure 5-5). The points were then converted to units of return period so that an eighth intermediate point at (0,0) could be added. Then, a linear interpolation (in increments of 0.1) between each of the eight intermediate points was

applied to the logarithm of the return period of the points, enabling production of numerous points along the $\mathscr{L}$-hazard curve at the mapping pixel. The exceedance probability for each of the points on the hazard curve were then computed using a Poisson model, and the results were binned into a PDF for binned values of $\mathscr{L}$. Afterwards, a value for $\mathscr{L}_i$ was randomly selected from the PDF for $\mathscr{L}$ at the pixel.

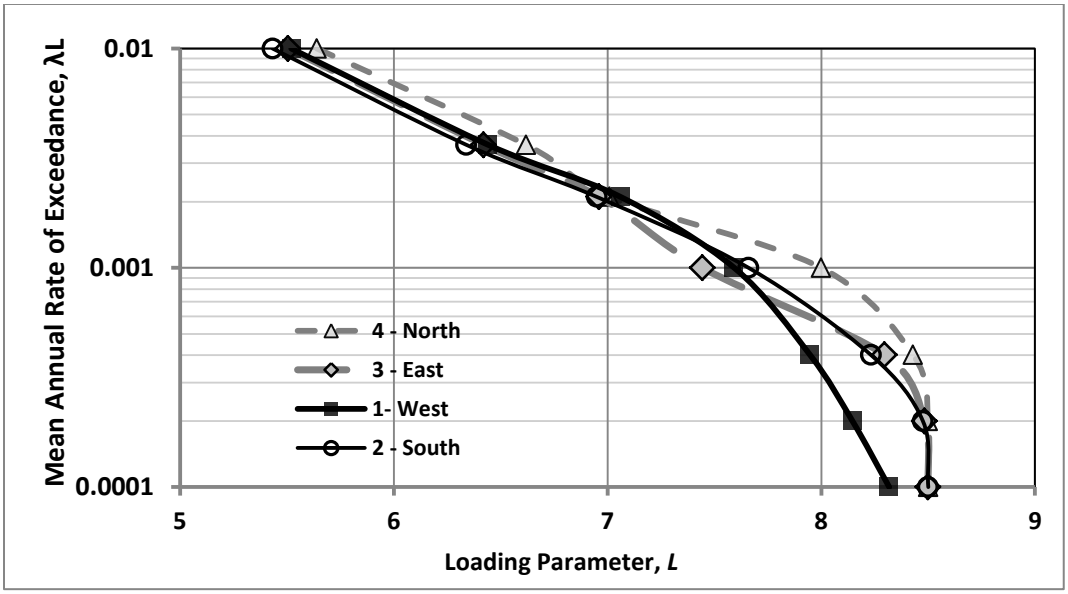

Figure 5-5: Apparent loading parameter hazard curves for four discrete locations in Utah County; which are identified in Figure 5-6.

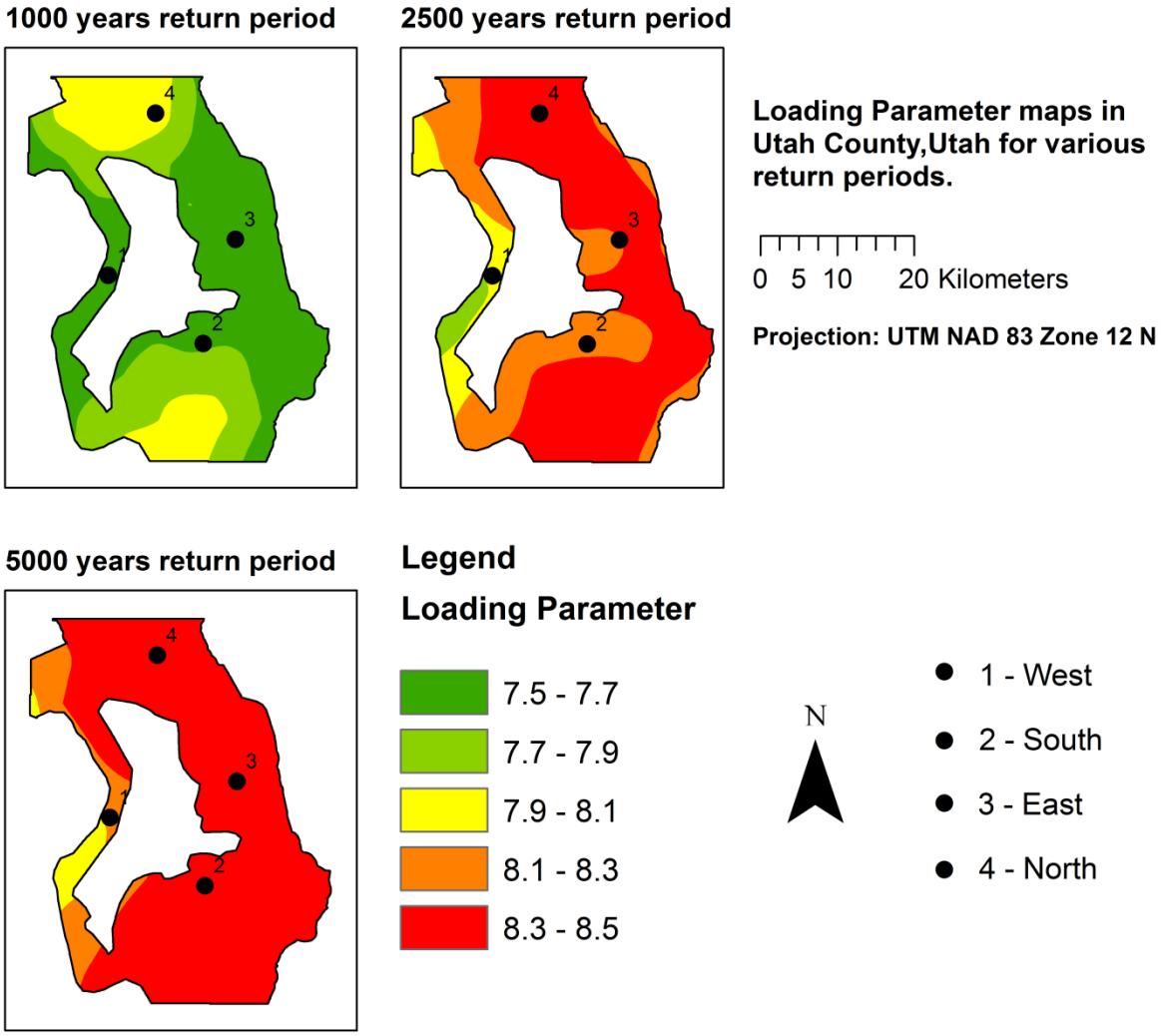

Figure 5-6: Apparent loading parameter hazard maps for a 1,000-year, 2,500-year, and 5,000-year return period in Utah County.

Step 4: Compute $logD_H$:

Continuing with the i-th simulation, G_i from Step 2 and $\mathscr{l}_i$ from Step 3 were summed to find $\overline{\log D_{H,i}}$, then error in the lateral spread displacement model was simulated by solving Equation (5-10) in order to output a value for $[\log D_H]_i$.

Step 5: Repeat Steps 2 – 4, Produce D_H Distribution:

Numerous simulations are necessary to model the several sources of uncertainty in the subsurface characterization (i.e., $(N_1)_{60}$, $T_{15,cs}$, C_E), seismic hazard (i.e., $\mathscr{l}$), and lateral spread displacement modeling error (i.e., ε). As further discussed below, Steps 2 – 4 were repeated 200,000 times for each pixel, resulting in a distribution of $logD_H$ values at each pixel. This distribution was then converted into a distribution of D_H values (in meters).

Step 6: Compute D_H Hazard Curve:

The next step in the mapping procedure was to convert the 200,000 D_H values at a pixel from the Monte Carlo simulations into a D_H-hazard curve. The distribution for D_H was first converted into an empirical cumulative distribution function (CDF) curve. The annual probability that D_H exceeds a displacement value, d, of interest (i.e., $P(D_H > d)$) is equal to *1 minus the CDF* value at d on this curve. (Note that the CDF is always equal to the non-exceedance probability; therefore, in this case, the CDF equals the probability D_H does not exceed d). The annual exceedance probability was defined using the Poisson model (Equation (5-11), where t = 1 year for an annual probability, and λ = the mean annual rate of exceedance).

Table 5.4 lists typical return periods of interest and their corresponding values of λ, annual exceedance probability, and CDF. Using the empirical CDF, points on the D_H-hazard curve at a selected pixel were developed by finding the displacement value at each of the CDF values listed in Table 5.4. As an example, the fifth column of Table 5.4 presents a set of displacement values taken from an empirical CDF at a particular pixel in the study area. Plotting λ versus d from Table 5.4, the D_H-hazard curve for this example set of data can be depicted (Figure 5-7a).

It is interesting to consider the meaning of the hazard curve depicted in Figure 5-7a and tabulated in Table 5.4. For a 475-year or 2,475-year return period hazard, the annual exceedance probability equals only 0.2% and 0.04%, respectively. Clearly, for a given year, these extreme hazard levels are highly unlikely; nonetheless, engineers are concerned with such hazard levels because the extreme events can cause significant damage. Upon further inspection of the example data in Table 5.4, 0.2% (or 400 of the 200,000 simulations) of the data in the D_H distribution at the mapping pixel exceeded a displacement value of 0.01 m, and only 0.04% (or 80 of the 200,000 simulations) exceeded a displacement value of 0.43 m. These lateral spread displacement values of 0.01 m and 0.43 m therefore correspond to the 475-year and 2475-year return period hazards, respectively.

Since the extreme values in the D_H distributions are of greatest interest when mapping the lateral spread hazard, it is important to perform many Monte Carlo simulations. In addition, numerous simulations ensure that the uncertainties in the mapping process are modeled well. The authors decided to run 200,000 simulations for each pixel. This large

number was selected because it produced a D_H-hazard curve that looked similar to a D_H-hazard curve after 300,000 or 400,000 simulations at return periods less than 2475 years, and it did not overburden the computer. For example, Figure 5-7b presents D_H-hazard curves at the same mapping pixel after running 10000, 50000, 100000, 200000, 300000, and 400000 simulations. The curve for 10000 simulations appears different than the other curves, and the authors concluded after several tests at numerous pixels that this number of simulations was inadequate. The curves appear fairly similar when N ≥ 100000 simulations, especially at return periods less than 2475 years (i.e., $\lambda < 0.0004$).

Table 5.4: Example distribution of D_H values at listed return periods.

Return Period [$1/\lambda$] (years)	Mean annual rate of exceedance, λ	Annual Exceedance Probability [$P(D_H > d)$]	CDF [$P(D_H < d)$]	d (meters)
108	0.0100	0.00900	0.99100	0.00
228	0.0040	0.00440	0.99560	0.00
475	0.0020	0.00210	0.99790	0.01
1033	0.0010	0.00100	0.99900	0.06
2475	0.0004	0.00040	0.99960	0.43
4975	0.0002	0.00020	0.99980	1.84
9975	0.0001	0.00010	0.99990	3.45

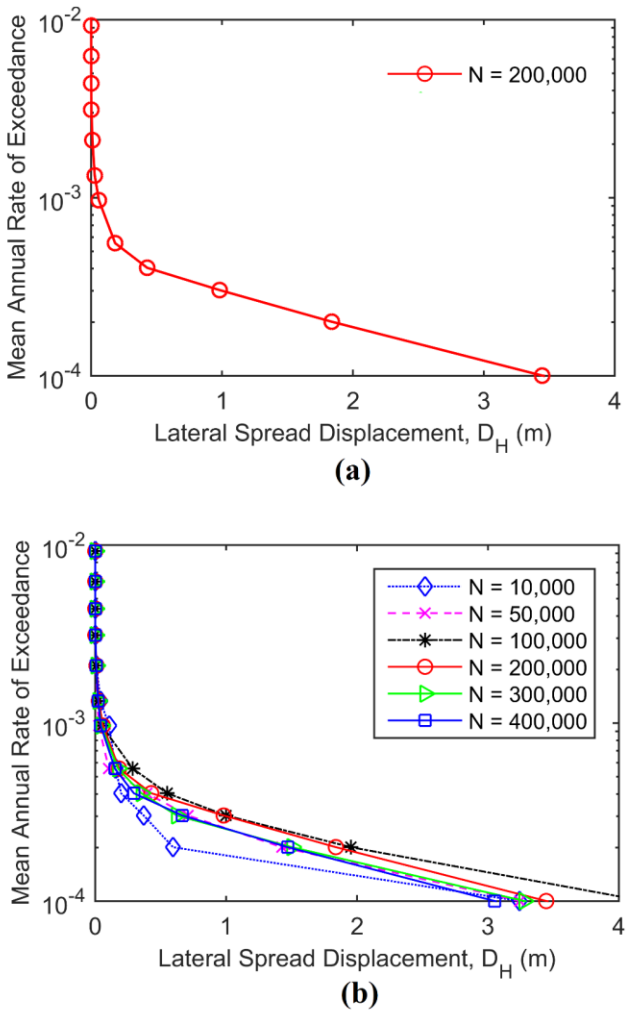

Figure 5-7: (a) Example D_H-hazard curve at a mapping pixel after 200,000 Monte Carlo simulations; (b) a set of D_H -hazard curves at the same mapping pixel after different numbers of Monte Carlo simulations.

Step 7: Repeat Steps 1-6 for All Map Pixels:

The first six steps of the mapping procedure were repeated for every pixel in the study area to generate a D_H-hazard curve similar to the one depicted in Figure 5-7a for every pixel.

Step 8: Output D_H Hazard Map:

The final step was to produce 30-m resolution raster hazard maps at the desired return periods. This was performed by simply extracting the D_H value from the D_H -hazard curve at a desired return period (e.g., 475, 1,33, or 2475-year return period) for each pixel, and then storing the extracted data as raster values in a raster image of the study area. Because the D_H -hazard curves were already computed at a resolution of 30-m for the study area, no additional interpolation was necessary. The raster images for return periods of 1033 and 2475 years were visualized in GIS to produce the final hazard maps (Figure 5-8 and Figure 5-9).

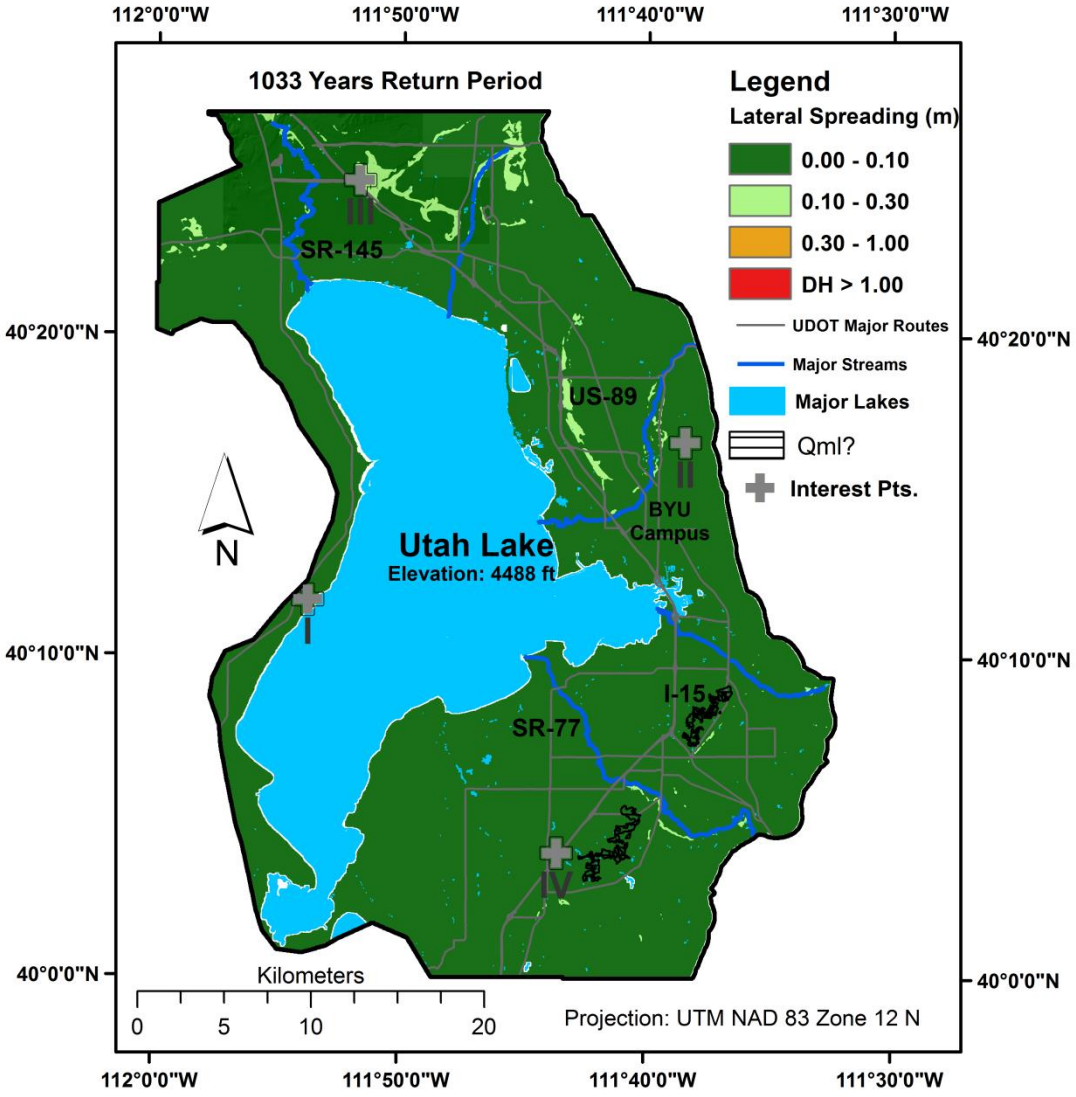

Figure 5-8: The 1,033-year return period lateral spread hazard map, Utah County, Utah.

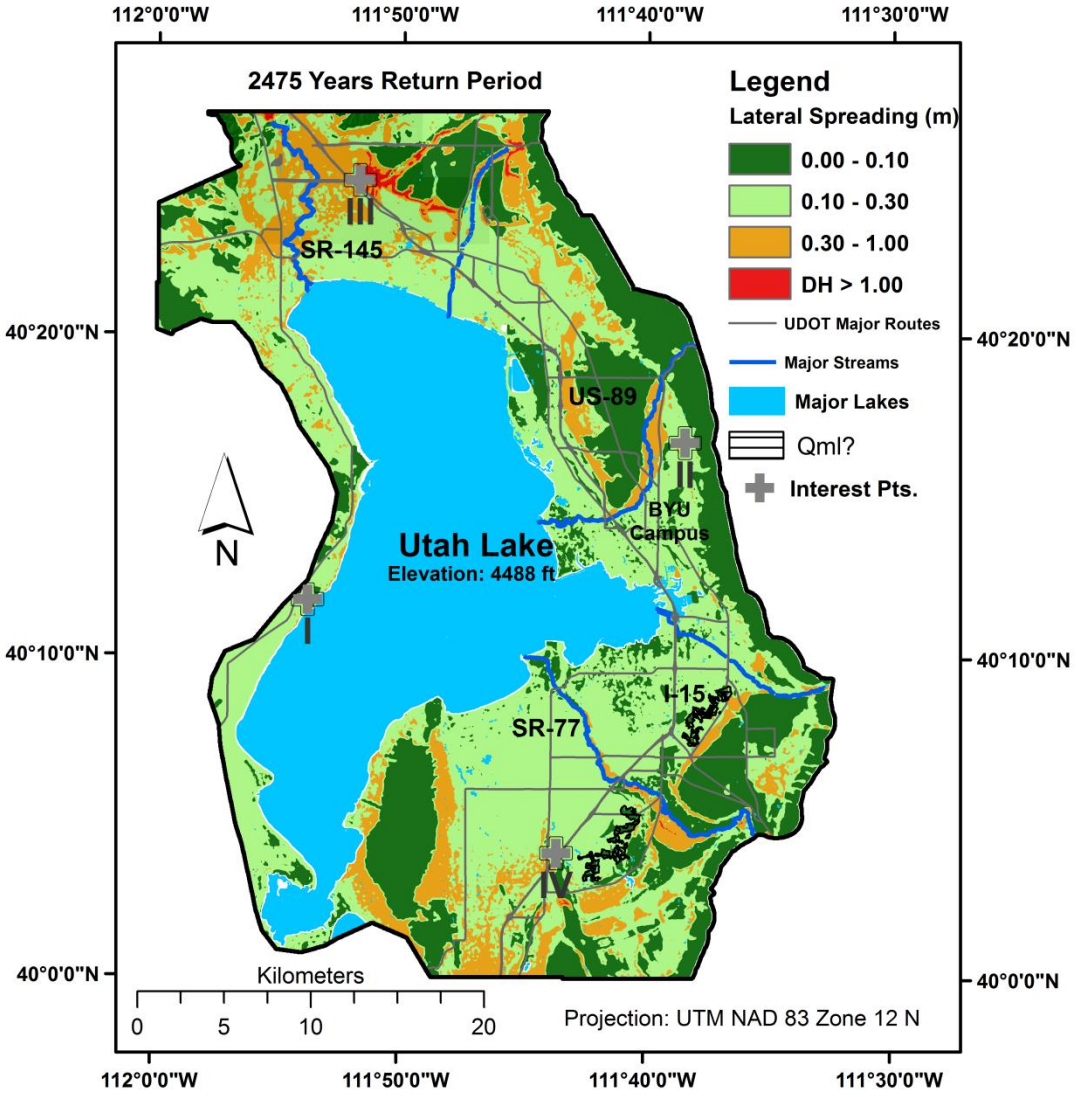

Figure 5-9: The 2,475-year return period lateral spread displacement hazard map, Utah County, Utah.

5.7 RESULTS AND DISCUSSION

The Anderson et al. (1994) map (Figure 5-2) indicates that a significant portion of the study area has *high* liquefaction potential. However, this map does not give any indication of the severity of ground failures that may result from the liquefaction. Mapping lateral spread displacements like in Figure 5-8 and Figure 5-9 is advantageous because it can be correlated with potential damage, and lateral spreading is generally considered the most pervasive type of liquefaction-induced ground failure (NRC 1985).

Figure 5-8 shows that lateral spread displacements are not generally expected to exceed 0.1 m for almost the entire study area at a return period of 1,033 years. Nevertheless, the map does show some displacements may reach up to 0.3 m in some of the lacustrine sand and young alluvial fan units with sufficient topographic relief (i.e., near a free-face or on sloping ground). Except for these small locales, it is concluded that the lateral spread hazard is generally minimal at the 1,033-year return period in most of the study area. This finding highlights one of the benefits of producing fully-probabilistic hazard maps. Some building codes require engineers to design structures, foundations, and lifelines to withstand a 475-year or 1033-year return period hazard. At this return period, significant lateral spread displacement is unlikely.

However, for more-critical infrastructure, building codes may require engineers to design for greater hazard levels. At the 2475-year return period hazard, some locations in the study area may experience significant lateral spread displacements. Figure 5-9 shows portions of the study area that may undergo displacements greater than 1 m. Locales with

the combined effect of sufficient values of $T_{15,cs}$, topographic relief, and apparent seismic loading may displace horizontally great distances during a more extreme earthquake. Even though the map does show large lateral spread hazard at some locales, the majority of the map generally shows displacements less than 0.3 m. It was found that when simulating a major earthquake (i.e., large value for $\mathscr{M}$) as a result of the nearby Utah segment of the Wasatch Fault Zone, it was so powerful and in such close proximity that it frequently produced at least a small D_H value from 0.1 to 0.3 m in geologic units with nonzero $T_{15,cs}$ values.

Figure 5-10 presents D_H-hazard curves at 4 points of interest, as located in Figure 5-8 and Figure 5-9. The Figure highlights how the displacement hazard varies in the study area. For example, Point III is near the I-15 corridor, north of Utah Lake. The lateral spread displacement hazard was greatest at this point as compared with the other points. Point I is west of Utah Lake and has the lowest displacement hazard as compared with the other points. This is likely because Point I has a lower apparent loading hazard as it is further from the Wasatch Fault Zone.

It is worth noting that the geologic map for Utah County (Figure 5-3) identifies some small deposits east of the I-15 corridor and southeasterly of Utah Lake which may have underwent lateral spreading during a prehistoric earthquake. These deposits were labeled as "*Qml? Lateral-spread deposits?*" on the Constenius et al. (2011) map. Unfortunately, none of the available investigations in the geotechnical database were within these deposits. Given that they may have underwent lateral spreading in the past, and because of a lack of

geotechnical data in these deposits, these areas were hatched in hazard maps in Figure 5-8 and Figure 5-9. Further research is needed to determine the lateral spread hazard for the *Qml?* unit.

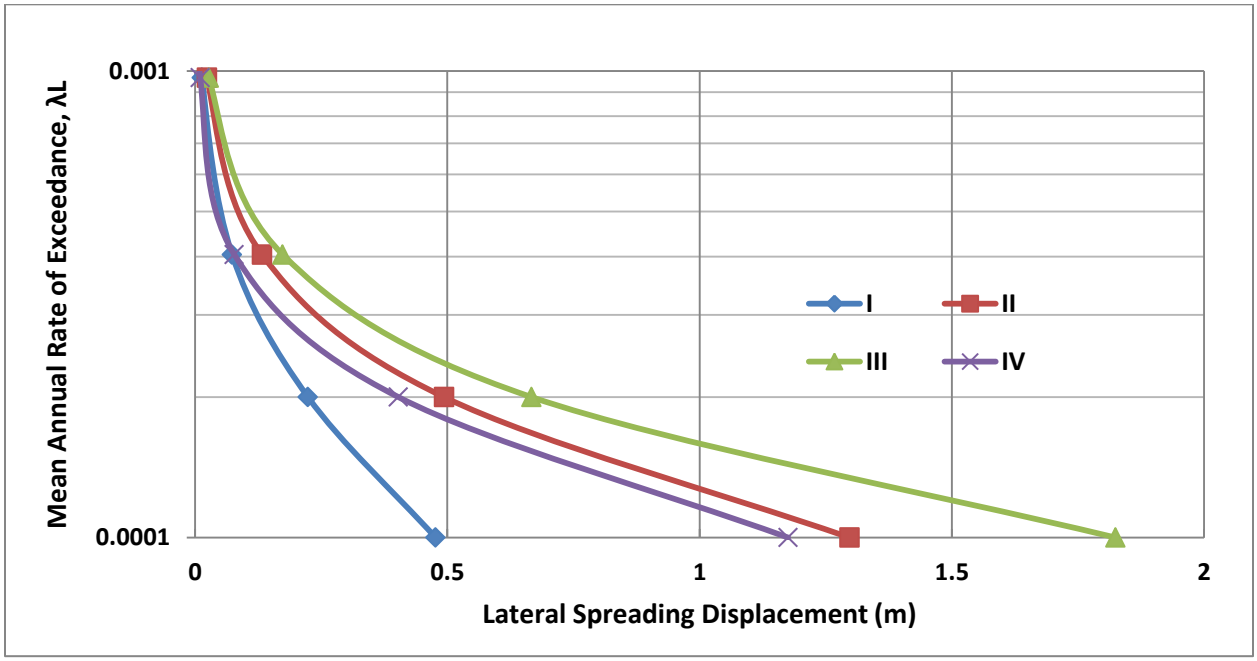

Figure 5-10: Lateral spreading displacement hazard curves for 4 points of interest in the study area.

The proposed mapping method also enables characterization of the geotechnical properties of the geologic units in the project area. As explained in the second step of the method, $T_{15,cs}$ was found for each of the SPTs that reached a minimum depth of 7 m (as listed in Table 5.3). In fact, a value for $T_{15,cs}$ was found hundreds of times for each of these SPTs as a result of the numerous Monte Carlo simulations. Computed values of T15 for SPTs located within each of the 14 geologic categories in Table 5.3 were pooled together to develop PDFs for each geologic unit. Afterwards, these PDFs were converted into $T_{15,cs}$

hazard curves in the same manner as PDFs of D_H were converted into D_H hazard curves (step 6). Figure 5-11 presents $T_{15,cs}$ distribution for each of the geologic categories. This plot provides an interesting way to compare which units are more or less likely to have thick layers of saturated, "sand-like" soil which may undergo lateral spreading during a major earthquake. Holding all other variables in Equation (5-7) constant, sites with relatively larger values of $T_{15,cs}$ will displace horizontally greater distances during lateral spreading. SPT borehole logs in the lacustrine units (e.g., lacustrine sand, fine-grained lacustrine) tended to show larger $T_{15,cs}$ values, whereas the older alluvial fans and alluvial fans and terraces tended to have smaller $T_{15,cs}$ values.

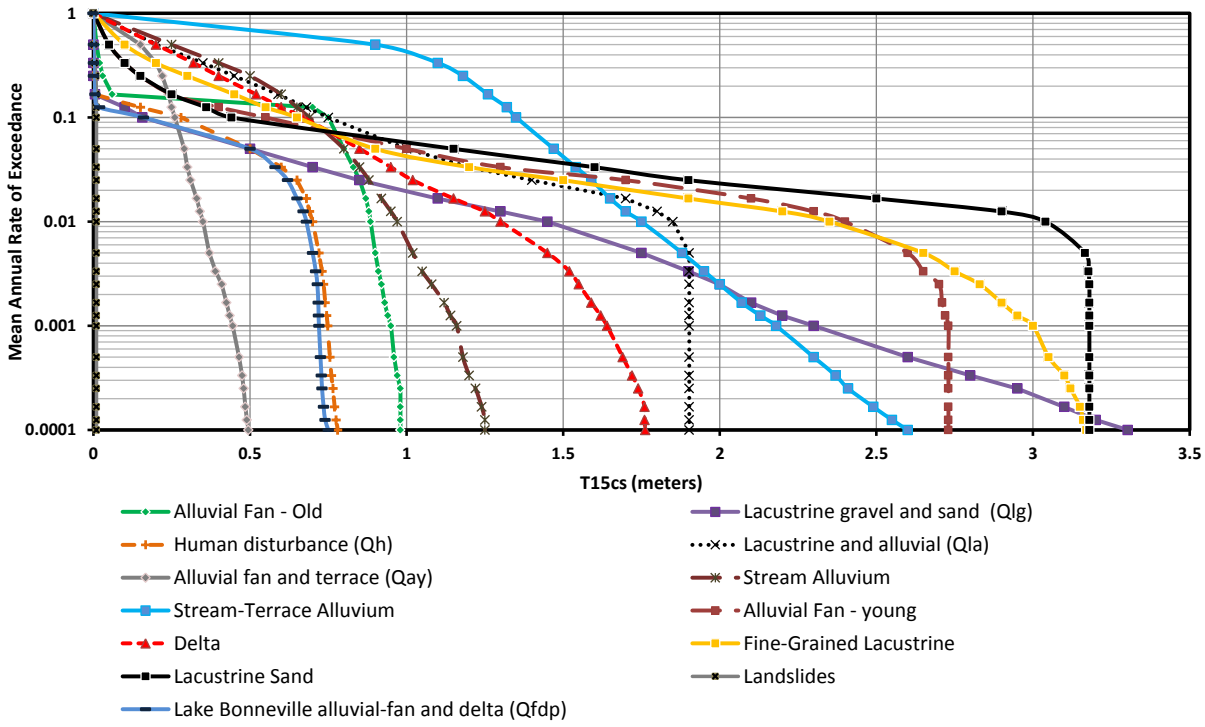

Figure 5-11: T15cs distribution for various geologic units.

5.8 CONCLUSION

This paper proposed methods to map fully probabilistic lateral spread displacement hazard maps using available seismic, geotechnical, geological and topographical data. These methods were then implemented to produce hazard maps at return periods of 1033, and 2475 years for Utah County, Utah. Although the paper focused on Utah County, other areas in the United States could also be mapped following similar procedures.

The methods presented in this paper are new and innovative. First, the hazard maps are based on seismic loading from a fully probabilistic seismic hazard analysis (PSHA). Previous liquefaction hazard mapping efforts (e.g., Anderson et al. 1982; Bartlett et al. 2005; Baise et al. 2006; Holzer et al. 2006; Olsen et al. 2007; Gillins 2012) show hazard levels given either a constant peak ground acceleration for the entire study area, a scenario or deterministic seismic event, or an event from a single return period of the deaggregation of a probabilistic seismic hazard analysis. Second, using Monte Carlo random sampling techniques, the maps presented in this paper modeled published errors in state-of-the-art liquefaction triggering (i.e., Idriss and Boulanger 2012) and lateral spread displacement (i.e., Gillins and Bartlett 2013) empirical equations as well as significant uncertainties in the subsurface characterization. Lastly, the lateral spread hazard maps modeled the spatial variation in ground slopes and free faces using a highly-resolute DEM developed from aerial lidar data collected in 2013.

The maps are intended to convey hazard information to city planners, developers, and engineers. It is hoped that engineers can begin or continue performing site-specific

analyses in areas mapped with high lateral spread hazard in order to refine the mapped estimates. Mapping liquefaction hazard for a regional area is challenging, and the authors recognize some parts of the maps likely have errors. Although the maps are based on over 750 geotechnical investigations, significant uncertainties remain in the subsurface conditions and more investigations are necessary to reduce these errors. By conducting and compiling additional investigations, it would then be possible to update and improve the maps. The maps could also be updated when new earthquake models are published by the USGS.

The authors strongly encourage people engaged in designing, building, or managing infrastructure—especially critical infrastructure—to hire an expert to perform site-specific liquefaction hazard analyses. Although the maps should be considered a step forward from previous hazard mapping efforts, the maps are still not intended nor recommended for site-specific engineering design. Local engineers should be consulted because they can provide expert knowledge of locations in the study area where they have previously conducted geotechnical investigations. Such engineers might also be able to note discrete areas on the maps that are over- or under-conservative based on their many years of experience testing and sampling the soil in these discrete locations. Nevertheless, it is highly recommended to still validate local opinions by performing site-specific testing as the authors noticed marked variability in the results of SPT investigations—even for SPT investigations in the same geologic unit within 100 m of each other. The authors attempted to account for this variability while mapping Utah County by developing distributions of geotechnical properties using tens to hundreds of available SPT investigations in each

geologic unit. It is inappropriate to assume that a few local SPT investigations at a discrete location adequately characterizes the uncertainties in subsurface conditions for an entire, widespread geologic unit.

The lateral spread hazard maps show a negligible displacement hazard at a return period of 1033 years. However, at the more-extreme 2475-year return period hazard, displacements may exceed 1 m in a few locations in the study area. This is because: (1) numerous SPT borehole logs in the geotechnical database show layers of loosely deposited, cohesionless soils; (2) a significant portion of the area has a shallow groundwater table due to its proximity to Utah Lake; and (3) the area is in very close proximity to the Utah segment of the Wasatch Fault Zone which is capable of generating a major earthquake with $M_w \geq 7$. Clearly, liquefaction should be a major concern for Utah County as well as other parts of the Wasatch Front. It is recommended to conduct additional site-specific studies at areas with high lateral spread hazard.

5.9 ACKNOWLEDGEMENTS

This research was supported by the U.S. Geological Survey (USGS), Department of the Interior, under USGS award numbers G14AP00118 and G14AP00119, as well as by the Utah Department of Transportation and the Central Utah Water Conservancy District. The views and conclusions contained in this document are those of the authors and should not be interpreted as necessarily representing the official policies, either expressed or implied, of these government agencies.

5.10 REFERENCES

Anderson, L.R., Keaton, J.R., and Bischoff, J.E. (1994a). "Liquefaction Potential Map for Utah County, Utah," Logan, Utah State University Department of Civil and Environmental Engineering and Dames and Moore unpublished Final Technical Report prepared for the U.S. Geological Survey, National Earthquake Hazards Reduction Program Award No. 14-08-0001-21359, 46 p., 1986; published as Utah Geological Survey Contract Report 94-8, 1994.

Anderson, L.R., Keaton, J.R., and Eldredge, S.N., (1994b), Liquefaction-potential map for a part of Utah County, Utah: Utah Geological Survey Public Information Series 28, 2 p., scale 1:365,000.

Anderson, L.R., Keaton, J.R., Aubrey, Kevin, and Ellis, S.J. (1982). "Liquefaction Potential Map for Davis County, Utah," Logan, Utah State University Department of Civil and Environmental Engineering and Dames and Moore unpublished Final Technical Report prepared for the U.S. Geological Survey, National Earthquake Hazards Reduction Program Award No. 14-08-0001-19127, 50 p.; published as Utah Geological Survey Contract Report 94-7, 1994.

Automated Geographic Reference Center (AGRC). (2014), Wasatch Front lidar, State of Utah, acquired from http://gis.utah.gov/data/elevation-terrain-data/2013-2014-lidar/.

Baise, L.G., Higgins, R.B., and Brankman, C.M. (2006). "Liquefaction Hazard Mapping – Statistical and Spatial Characterization of Susceptible Units." J. Geotech. & Geoenviron. Eng., Vol. 132, No. 6, 705-715.

Bardet, J.P., Tobita, T., Mace, N., and Hu, J. (2002). "Regional Modeling of Liquefaction-Induced Ground Deformation", Earthquake Spectra, 18(1), 19-46.

Bartlett S. F., Olsen, M. J., and Solomon, B. J. (2005). "Lateral Spread Hazard Mapping of Northern Salt Lake County for a Magnitude 7.0 Scenario Earthquake," Technical Report submitted to the United States Geological Survey, NERHP Award No. 04HQGR0026, 218 p.

Bartlett, S.F., and Youd, T.L. (1995). "Empirical prediction of liquefaction-induced lateral spread." J. Geotech. Eng., 121(4), 316-329.

Bazzurro, P., and Cornell, C. A. (2004). "Nonlinear soil-site effects in probabilistic seismic-hazard analysis." Bulletin of the Seismological Society of America, 94(6), 2110-2123.

Boulanger, R.W., and Idriss, I.M. (2005). "Evaluating cyclic failure in silts and clays," *Proc. of Geotechnical Earthquake Engrg. Satellite Conf. on Performance-Based Design in Earthquake Geotech. Engrg:*

Concepts and Research. Prepared by TC4 Committee of ICSMGE, Japanese Geotechnical Society, Tokyo, 78-86.

Boulanger, R. W., and Idriss, I. M. (2006). "Liquefaction susceptibility criteria for silts and clays." Journal of geotechnical and geoenvironmental engineering, 132(11), 1413-1426.

Bray, J. D., and Travasarou, T. (2007). "Simplified procedure for estimating earthquake-induced deviatoric slope displacements." J. Geotech. Geoenviron. Eng., 133(4), 381–392.

Constenius, K.N., Clark, D.L., King, J.K., and Buck Ehler, J. (2011). "Interim Geologic Map of the Provo 30' x 60' Quadrangle, Utah, Wasatch, and Salt Lake Counties, Utah," *Open-File Report 586DM*, Utah Geological Survey.

Cornell, C. A., and Krawinkler, H. (2000). "Progress and challenges in seismic performance assessment." PEER Center News, 3(2), 1–4.

Cramer, C. H., Rix, G. J., and Tucker, K. (2008). "Probabilistic liquefaction hazard maps for Memphis, Tennessee." Seismological Research Letters, 79(3), 416-423.

Deierlein, G. G., Krawinkler, H., and Cornell, C. A. (2003). "A framework for performance-based earthquake engineering." Proc., 2003 Pacific Conf. on Earthquake Engineering.

EZ-FRISK 7.60 [Computer software]. Boulder, CO, Risk Engineering

Faris, A.T., Seed, R.B., Kayen, R.E., and Wu, J. (2006). "A semi-empirical model for the estimation of maximum horizontal displacement due to liquefaction-induced lateral spreading." Vol. 3, Proc., 8th U.S. Nat. Conf. Earthquake Engrg., Earthquake Engineering Research Institute, Oakland, CA, 1584-1583.

Franke, K.W. (2005). "Development of a performance-based model for the prediction of lateral spreading displacements." M.S. thesis, Univ. of Washington, Seattle.

Franke, K.W. and Kramer, S.L. (2013). "Procedure for the Empirical Evaluation of Lateral Spread Displacment Hazard Curves." J. Geotech. & Geoenviron. Eng., 140(1), 2014.140:110-120.

Gillins, D.T. (2012). "Mapping the Probability and Uncertainty of Liquefaction-Induced Ground Failure," Ph.D. Dissertation, Univ. of Utah, Salt Lake City, 297 pp.

Gillins, D.T. and Bartlett, S.F. (2013). "Multilinear Regression Equations for Predicting Lateral Spread Displacement from Soil Type and Cone Penetration Test Data." J. Geotech. & Geoenviron. Eng., 140(4), 04013047.

Gillins, D.T., and Franke, K. (2016). "Probabilistic Liquefaction Potential and Lateral Spread Hazard Maps for Utah County, Utah: Collaborative Research with Brigham Young University and Oregon State University", *USGS External Research Report*, USGS Award Nos. G14AP00118 and G14AP00119, Reston, VA, 89 pp.

Hamada, M., Yasuda, S., Isoyama, R., and Emoto, K. (1986). "Study on liquefaction induced permanent ground displacements." *Report for the Association for the Development of Earthquake Prediction in Japan*, Tokyo, Japan, 87 pp.

Holzer, T.L., Blair, J.L., Noce, T.E., and Bennett, M.J. (2006). "LiqueMap: A Real-Time Post Earthquake Map of Liquefaction Probability." Proc., 8th US National Conference on Earthquake Eng., EERI, Oakland, CA.

Idriss, I.M., and Boulanger, R.W. (2008). *Soil liquefaction during earthquakes*, Earthquake Engineering Research Institute Monograph MNO-12, Earthquake Engineering Research Institute, Oakland, CA, 262 pp.

Idriss, I. M., and Boulanger, R. W. (2012). "Examination of SPT-based liquefaction triggering correlations." Earthquake Spectra, 28(3), 989-1018.

Iwasaki, T., Tokida, K., Tatsuoka, F., Watanabe, S., Yasuda, S., and Sato, H. (1982). "Microzonation for soil liquefaction potential using simplified methods." In Proceedings of the 3rd international conference on microzonation, Seattle, Vol. 3, pp. 1310-1330.

Jaimes, M. A., Niño, M., & Reinoso, E. (2015). "Regional map of earthquake-induced liquefaction hazard using the lateral spreading displacement index D LL." Natural Hazards, 77(3), 1595-1618.

Lam, I., Arduino, P., and Mackenzie-Helnwein, P. (2009). "OpenSees soilpile interation study under lateral spread loading." Int. Foundation Congress & Equipment Expo '09, ASCE, Reston, VA, 206–213.

Lee, D. H., Ku, C. S., and Yuan, H. (2004). "A study of the liquefaction risk potential at Yuanlin, Taiwan." Engineering Geology, 71(1), 97-117.

Lenz, J. A., and Baise, L. G. (2007). "Spatial variability of liquefaction potential in regional mapping using CPT and SPT data." Soil Dynamics and Earthquake Engineering, 27(7), 690-702.

Luna, R., and Frost, J. D. (1998). "Spatial liquefaction analysis system." Journal of Computing in Civil Engineering, 12(1), 48-56.

Mabey, M. A., and Madin, I. (1993). *Relative Earthquake Hazard Map: Portland, Oregon 7-1/2 Minute Quadrangle*. Oregon Department of Geology and Mineral Industries.

Maurer, B. W., Green, R. A., Cubrinovski, M., and Bradley, B. A. (2014). "Evaluation of the Liquefaction Potential Index for Assessing Liquefaction Hazard in Christchurch, New Zealand." Journal of Geotechnical and Geoenvironmental Engineering.

National Research Council (NRC) (1985). Liquefaction of Soils During Earthquakes, National Academy Press, Washington D.C., 240 p.

Olsen, M. J., Bartlett, S. F., and Solomon, B. J., (2007). "Lateral Spread Hazard Mapping of the Northern Salt Lake Valley, Utah, for M7.0 Scenario Earthquake," Earthquake Spectra, 23(1), 95-113.

Rauch, A.F., and Martin, J.R. (2000). "EPOLLS Model for Predicting Average Displacements on Lateral Spreads", J. Geotech. & Geoenviron. Eng., ASCE, 126(4), 360-371.

Saygili, G., and Rathje, E. M. (2008). Empirical predictive models for earthquake-induced sliding displacements of slopes. *J. Geotech. Geoenviron. Eng*., 134(6), 790–803.

Seed, H.B. (1979). "Soil liquefaction and cyclic mobility evaluation for level ground during earthquakes," *Journal of Geotechnical Engineering Div.* 105(2), 201-255.

Seid-Karbasi, M., and Byrne, P. M. (2007). "Seismic liquefaction, lateral spreading and flow slides: A numerical investigation into void redistribution." Can. Geotech. J., 44(7), 873–890.

Sonmez, H., and Gokceoglu, C. (2005). "A liquefaction severity index suggested for engineering practice." Environmental Geology, 48(1), 81-91.

Stewart, J. P., Afshari, K., & Hashash, Y. M. (2014). "Guidelines for performing hazard-consistent one-dimensional ground response analysis for ground motion prediction." PEER Rep, 16.

Ulmer, K., Ekstrom, L., & Franke, K. (2015). "Optimum Grid Spacing for Simplified Performance-based Liquefaction and Lateral Spread Displacement Parameter Maps." In 6th International Conference on Earthquake Geotechnical Engineering.

Youd, T. L., and Hoose, S. N. (1977). "Liquefaction susceptibility and geologic setting." In Proc., 6th World Conf. on Earthquake Engineering, Vol. 6, pp. 37-42. Roorkee, India: Indian Society of Earthquake Technology.

Youd, T. L., Hansen, C. M., and Bartlett S. F. (2002). Revised multilinear regression equations for prediction of lateral spread displacement." J. Geotech. Geoenviron. Eng. 128(12), 1007-1017.

Youd, T. L., Idriss, I. M., Andrus, R. D., Arango, I., Castro, G., Christian, J. T., Dobry R., Finn W.L., Harder Jr L.F., Hynes M.E., Ishihara K. (2001). Liquefaction resistance of soils: summary report from the 1996 NCEER and 1998 NCEER/NSF workshops on evaluation of liquefaction resistance of soils. Journal of geotechnical and geoenvironmental engineering, 127(10), 817-833.

Youd, T.L., and Perkins, D.M. (1978). Mapping liquefaction-induced ground failure potential, *Journal of the Geotechnical Engineering Division* 104, No. GT4, 433-446.

Youd, T.L., and Perkins, D.M. (1987). "Mapping of liquefaction severity index." J. Geotech. Eng. 113(11), 1374-1392.

Zhang, G., Robertson, P. K., and Brachman, R. W. (2004). "Estimating liquefaction-induced lateral displacements using the standard penetration test or cone penetration test." J. Geotech. Geoenviron. Eng. 130(8), 861-871.

6 CONCLUSIONS AND FUTURE WORK

6.1 CONCLUSION

This dissertation presented innovative research on development of regional geological hazard maps. The dissertation focuses on landslide displacement, liquefaction, and lateral spreading. The methodologies employed a full seismic hazard curve on a performance based approach to probabilistically detect these ground failures and displacement parameters in regional scale.

Herein, a summary of the challenges addressed by this work in geo-hazard mapping is presented to highlight the research contribution of each manuscript:

Within Chapter 2, a procedure and an efficient computational framework is demonstrated to accurately analyze multiple deterministic scenarios of CSZ and produce a suite of descriptive hazard maps. Unlike previous efforts, the procedure is developed as an automated, adaptive and stand-alone application, which later can be used for other study areas or with updated data. A series of ground deformation maps corresponding to deterministic scenarios of CSZ as input datasets are produced, which can support engineering analysis.

In Chapter 3, soil strength correlations to geologic units are produced after performing a statistical analysis of slope at failures. The results demonstrated distinctive geological features among existing geologic units which later were used in computation of landslide hazard and displacement. The Newmark sliding block analyses is used to assess landslide

hazard and its displacement where subsurface data is not available. The paper utilizes an innovative performance based methodology and considers all known seismic sources at different ground motion hazard levels to probabilistically calculate the landslide hazard level across a large area. The implemented technique can successfully be applied to other regions if similar data are available.

In Chapter 4, a compiled geotechnical subsurface database is developed from available borehole data in three counties within the state of Utah. The possibility of generalizing geological units to larger groups were investigated and further histograms of different soil properties and geotechnical parameters were produced. Further, the possibilities of using geotechnical information available from one locale to another area based on common geologic unit were explored by performing statistical tests on important geotechnical parameters. This study provides a useful link between surficial geology and quantifiable geotechnical data, which can be effectively utilized to improve hazard mapping efforts.

In Chapter 5, state of the art lateral spreading displacement empirical models were used to produce lateral spreading hazard maps of a Utah County, Utah. The maps are created based on apparent seismic loading from a fully probabilistic seismic hazard analysis (PSHA) whereas all previous efforts were used on a constant PGA, a seismic scenario event, or a single event from de-aggregation of PSHA. The methodology models spatial variation in ground slopes and free-faces using high resolution DEMs developed from lidar. Furthermore, it accounts for major sources of uncertainties including the empirical lateral spreading displacement model uncertainty which was used to create the output maps.

6.2 FUTURE WORK

This research has enabled and identified several future possibilities of study, which are defined as below:

In Chapter 2, the maps currently use HAZUS-MH recommendations for the geo-hazard ground failure maps. The deterministic maps can be updated with newer and state of the art practices. HAZUS-MH typically utilizes older, more conservative models.

In Chapter 3, the seismically induced landslide methodology currently utilize the USGS 2008 seismic hazard data, we encourage researchers to use the newer and updated version of the seismic hazard data released by USGS in the future. Besides this, many of the other datasets can be updated and modernized. Landslide inventories will continue to be enriched as higher resolution lidar data becomes available (e.g., Burns and Madin 2009). A comprehensive landslide inventory database will directly affect the accuracy of distinguishing geologic features and shear strength estimation. The developed routines can be further used for other regions where similar datasets are available. To make the model more sophisticated, additional factors can be modeled. For example, the probability of soil being saturated enough for landslide to occur can be added to the probability chain equation. Furthermore, uncertainty in some of the factors can be modeled in great detail. For instance, the uncertainty in the NEHRP site classification maps, which are based on shear wave velocity data can be incorporated into the model. Last but not least, an improved validation methodology can be performed using recent case histories of

landslides triggered from major to great earthquakes such as Tohoku, Japan, earthquake of 2011 database.

In Chapter 4, the compiled database includes many CPT and shear wave velocity tests as well as the SPT data. As a future effort, one can use these data in combination to SPT data to better delineate the geologic units in state of Utah. Many other geotechnical information can be modeled within both geologic units and geologic groups, which can be useful for future applications. Many other statistical testing on a broader range of parameters can be performed to prove if generalization of geologic units can be possibly further achieved.

In Chapter 5, the introduced methodology can successfully be implemented for other regions where available data is present. A future work will be to incorporate the detailed CPT and shear wave tests within the Utah County to better delineate the geotechnical parameter present in the lateral spreading equation.

This work can play an important role in future research in natural hazard mapping and brings attention to the effects of seismic activities and geotechnical related hazards that are associated with them. The results of this study will be useful in future mapping, assessments and analysis of ground failures and can result in less social and economic impacts by addressing challenges in developing sustainable infrastructures against earthquakes.

7 APPENDICES

7.1 APPENDIX A – CSZ-SCENARIO MODULES INSTRUCTIONS

There are two programs developed, each designed to output Band Interleaved by Line image files (.bil) results. Directory paths to inputs required for each program should be written in a text file which will then be dragged and dropped on the relevant executable. Below are the details of the input files each program needs.

7.1.1 Module 1 – Re-projection and site amplification

This program requires 4 inputs all of which should have (.bil) extensions. The paths to each of these four image files should be given as a separate line in a text file. Inputs are NEHRP, PGA_760(Rock), Spectral acceleration (0.3 second period) and Spectral acceleration (1 second period) for an specific moment magnitude earthquake scenario(e.g. 8.1). A lookup table designed as a comma separated value (.csv) file is also given. The directory path to this look up table should be given either.

Path file to these inputs should be typed *in order with no line missing*. A valid directory path to store the results should be given in **fifth** line. CSV file path is given in the **sixth** line.

ORDER: (Following paths are examples, please revise accordingly.)

K:\\DOGAMI\\CODE\\Test\\NEHRP_O_13_6_12_SSNA.bil

K:\\DOGAMI\\CODE\\Test\\M8.1_PGA_760.bil

K:\\DOGAMI\\CODE\\Test\\M8.1_SA03_760.bil

K:\\DOGAMI\\CODE\\Test\\M8.1_SA10_760.bil

K:\\DOGAMI\\CODE\\Test\\RESULT_RASTERS\\M8.1_760_Output

K:\\DOGAMI\\CODE\\lookup.csv

7.1.2 Module 2 – Hazard map generator

This program requires four inputs with BIL extensions and one valid directory path to store the outputs. Inputs are PGA_Soil for a specific moment magnitude earthquake scenario (e.g. 8.1). HAZUS geology group raster file, Landslide slope map, liquefaction susceptibility raster (all in BIL extension).

Path file to these inputs should be typed *in order with no line missing*. A valid directory path to store the results should be given in **fifth** line.

Please note that besides the text file, when using this program, user should type in the moment magnitude scenario they are analyzing in the command window upon request.

ORDER: (Following paths are examples, please revise accordingly.)

K:\\DOGAMI\\CODE\\HAZUS_Results\\M8P1_PGA_Soil.bil

K:\\DOGAMI\\CODE\\HAZUS_Results\\GEN_INPUTS\\HAZUS_LS_GROUP.bil

K:\\DOGAMI\\CODE\\HAZUS_Results\\GEN_INPUTS\\Landslide_Slope_Map.bil

K:\\DOGAMI\\CODE\\HAZUS_Results\\GEN_INPUTS\\LIQ_SUSC.bil

K:\\DOGAMI\\CODE\\HAZUS_Results\\OUTPUTS

7.1.3 Important tips

Do not use very long directory paths.

It is good practice to do not use space in directory and file names.

Order of the inputs in the text file is really important. Any typos can result to crash the program.

Do not forget to have consistent inputs with the Moment magnitude value inserted in Module 2.

Please make sure directories and folders mentioned in the paths exist, because programs will not create folders.

The program will create output bil files with their header, projection and statistics files.

Please refer to text file examples for orders and structures.

For questions and concerns please email: **sharifim@oregonstate.edu**

7.2 APPENDIX B – 3D MAPS

Probability of Landslide Hazard

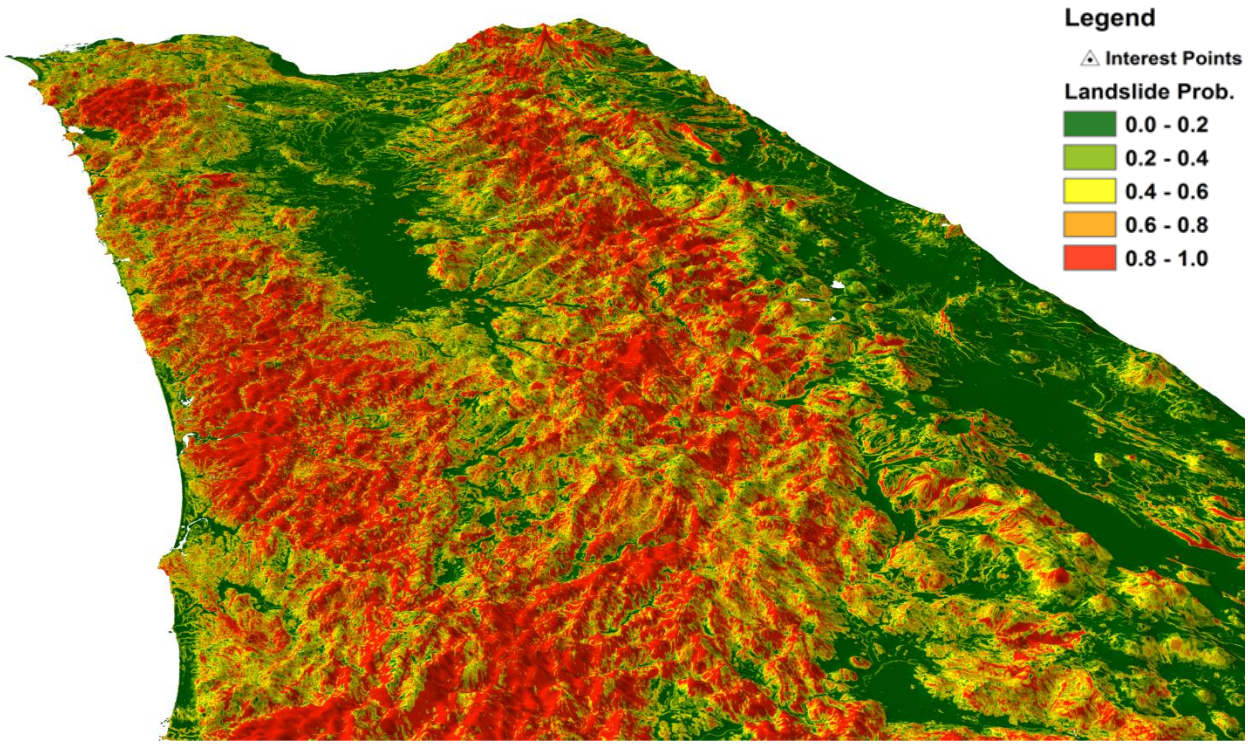

Probability of Landslide Displacement Exceeding 10 cm

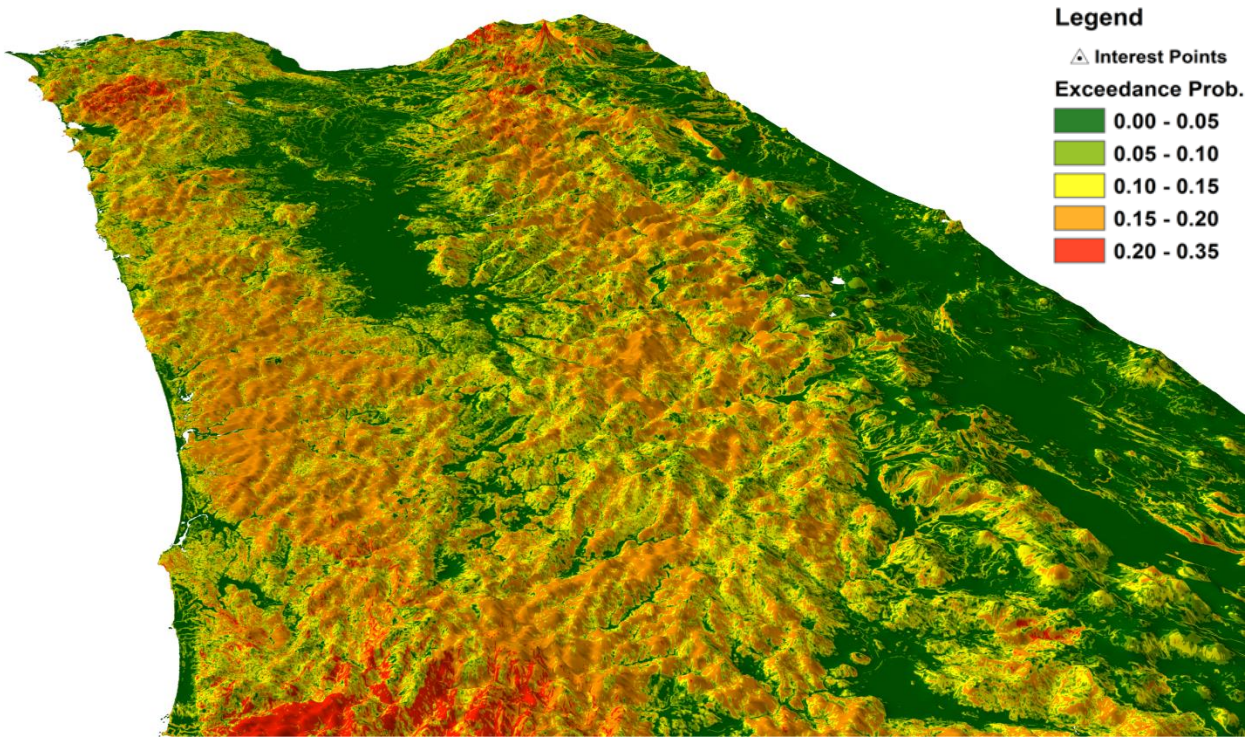

Surficial Geologic map of Utah County, Utah

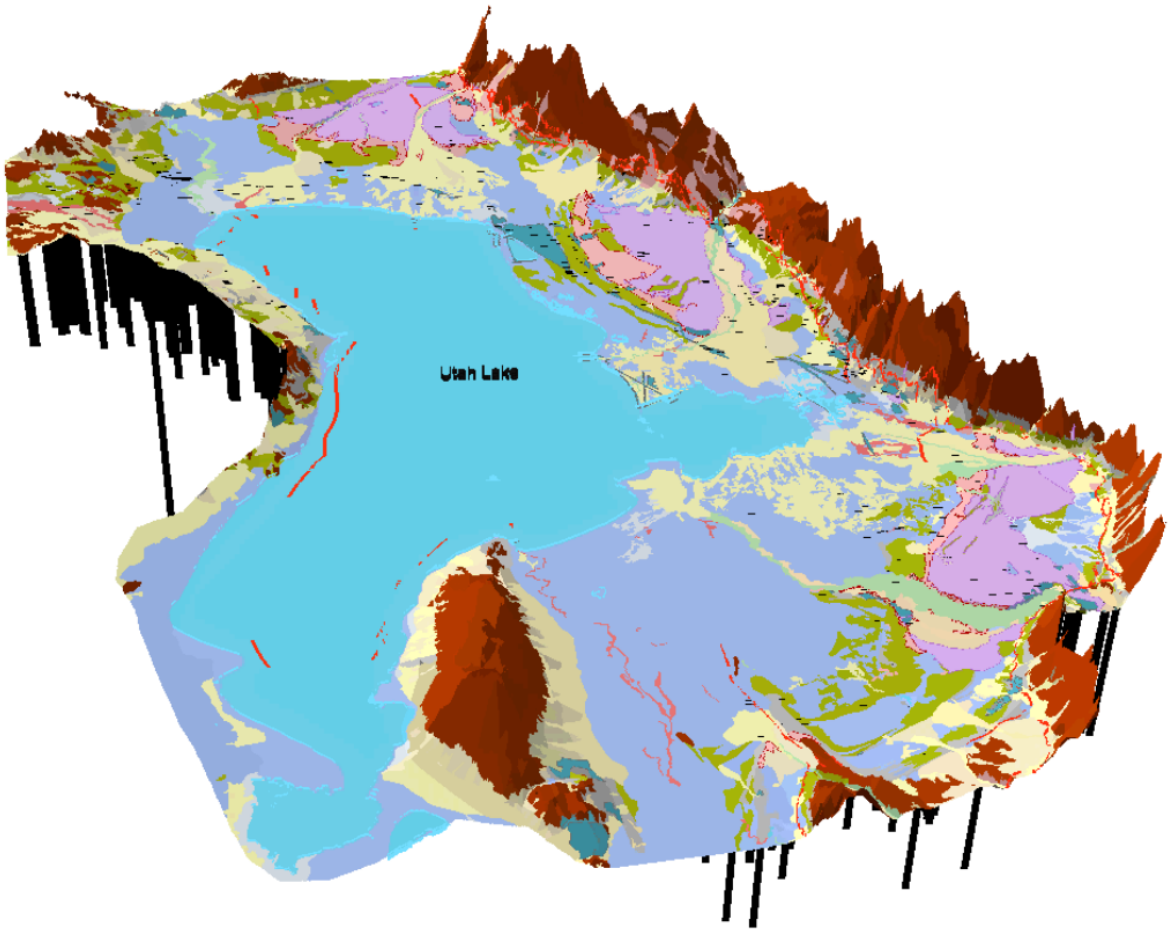

2475 years return period lateral spread hazard map for Utah County, Utah.